UNIVERSITY OF DERBY

Pressure Gain Combustion: Fuel Spray and Shockwave Interaction

Solomon Onwuegbu

Doctor of Philosophy 2023

Abstract

Pressure gain combustion can attain higher thermodynamic cycle efficiency in gas turbine power systems, resulting in the reduction of specific fuel consumption/fuel burn and Carbon dioxide emissions. There are many ways to achieve pressure gain and the present research investigates pressure gain through shock bubble (gas and liquid bubble) interaction (SBI) using computational fluid dynamics (CFD) simulations. The numerical simulations have been performed in 2D and 3D representations of the shock tube to depict the interaction of a planar shock wave with distinct gas and liquid inhomogeneities. The three scenarios considered cover the interaction of a planar shock wave in air with: spherical helium bubble (Mach number, Ma = 1.25); cylindrical helium bubble (Ma = 1.22) and cylindrical water bubble (Ma = 1.47). To perform these simulations, the Unsteady Reynolds-Averaged Navier-Stokes (URANS) mathematical model and the coupled level set and VOF method within the commercial CFD code, ANSYS FLUENT, have been applied. A finite volume method (FVM) is also employed to solve the governing equations. For the spherical and cylindrical gas bubble cases, various quantitative analyses are presented and compared to the experimental work of Haas and Sturtevant (1987). These include: refracted wave, transmitted wave, upstream interface, downstream interface, jet, vortex filament, non-dimensional bubble, and vortex velocities. The predicted non-dimensional bubble and vortex velocities have also been compared with experimental data, a simple model of shock-induced Rayleigh-Taylor (RT) instability and other theoretical models. Comparisons are also shown between the predicted bubble length/width and the experimentally measured results to elucidate changes in the shape and size of the 2D and 3D bubbles. Additional quantitative analyses are also presented for the spherical bubble involving the size estimation of the vortex pair as well as their spacing. For the shock cylindrical water bubble interaction case, the quantitative predictions include: displacement/drift, acceleration, distortion in the lateral direction, distortion in flow direction, area variation from bubble distortion, as well as drag coefficient and are compared to the experimental measurements of Igra et al. (2002). It has been demonstrated that 3D simulations compare very well with the experimental data, suggesting that 3D simulations are necessary to capture SBI process accurately. Finally, comprehensive flow visualization has been used to elucidate the shock-bubble interaction (SBI) process from bubble compression to the formation of the vortex filaments (cylindrical helium bubble), vortex rings (spherical helium bubble), vortices (cylindrical water bubble) as well as the production and distribution of vorticity. It is demonstrated for the first time that turbulence is generated at the early phase of the SBI process, with the maximum turbulence intensity reaching about 20% around the vortex filaments/vortex rings regions for the cylindrical/spherical helium bubble cases respectively and about 22% for the cylindrical water bubble case at the later phase of the interaction process.

Acknowledgements

I would like to immensely thank God who has granted me the grace to complete this PhD. Even with the health struggles, You were my strength and guide. I would also like express my sincere gratitude to my supervisors, Prof. Zhiyin Yang and Dr. Jianfei Xie, for their consistent support during this project. Thank you, Prof. Zhiyin, for all your unwavering support throughout my PhD studies. I would particularly like to thank you for all the times you went out of your way to answer all the technical questions I asked regarding my PhD as well as your impeccable understanding of the health struggles I had. I would especially like to appreciate my beautiful wife, Emmanuella Onwuegbu. Thank you for all you do and your support. I would also like to thank my family and friends (Seyi, Bamidele, etc.) who supported me throughout my PhD. I would also like to thank my grandma for all she did for me when I was a child and how she always encouraged me to chase my academic dreams. I would also like to appreciate Prof. Farid Meziane for the incredible support he also rendered coupled with the invaluable advice he gave me regarding my PhD. To the University of Derby, I am extremely appreciative of the facilities which you provided as well as the computational resources. I would also like to thank IT services for all the support they rendered particularly when my office computer crashed. I also appreciate all the help and support provided by Mr Birol Gundogdu. I really appreciate your patience and thoroughness particularly with respect to explaining the key details that are relevant to shock bubble/flame interaction. Rest on Great Man!!!

Table of Contents

List of Figures

List of Tables

Publications

Isehunwa, S. O., Ogunkunle, T.F., Onwuegbu, S.M. and Akinsete, O.O (2017) 'Prediction of sand production in gas and gas condensate wells', Journal of Petroleum and Gas Engineering, Vol. 8(4), pp. 29 – 35. Doi: 10.5897/Jpge2016.0259.

Onwuegbu S, Yang Z. (2022) 'Numerical analysis of shock interaction with a spherical bubble', AIP Advances, Vol. 12, pp. 025215/1 – 025215/15. https://doi.org/10.1063/5.0084349.

Onwuegbu, S., Yang, Z. and Xie, J. 'A computational study of shock wave interaction with a cylindrical bubble', Submitted to Modelling Journal.

1. Introduction

In this chapter, a brief outline of the motivation for this research, a detailed introduction to the research topics and the structure of the thesis are presented.

1.1. Motivation

Pressure gain combustion (PGC) possesses the required potential to hugely boost combined cycle performance when implemented in combustion gas turbines. PGC has the ability to replace the steady, isobaric (which mainly results in a total pressure loss), subsonic combustion exhibited by conventional gas turbine engines with a number of physical phenomena such as resonant pulsed combustion, isochoric combustion or supersonic exothermic combustion with front propagating shock wave (detonation). PGC principally aims to cause a rise in effective pressure across the combustor while utilizing the same volume of fuel as the constant pressure combustor. This technique has been adopted from the Humphrey (or Atkinson) cycle and is highly regarded as having a likelihood to achieve higher efficiency in gas turbine power systems, potentially attaining up to 4-6% for simple cycle systems and 2-4% in combined cycle systems[1]. These improvements will also prove pivotal for the power system level as this efficiency boost would help alleviate associated cost by efficiently trapping carbon.

This project is also useful as it represents an approach to the 65% combustion turbine combined cycle efficiency goal as research shows that efficiency boosts in combustion turbines have not been met by constantly increasing turbine inlet temperatures[1]. The PGC concept thus creates an alternative route to the ultrahigh efficiency target which certainly is not inhibited by the turbine material limitations currently encountered by technology developers. Very interestingly, this technology does not prevent further research from being conducted on novel turbine materials and advanced cooling techniques particularly for the Integrated Gasification Combined Cycle (IGCC). However, this technology could potentially be faced with technical issues like fuel injection, fuel and air mixing, backflow avoidance, detonation onset, controlling wave direction, pressure rise maintenance, emissions (CO and NOx) control, transient heat transfer, combustor wall cooling and flow (injections and spray) and combustion temperature maintenance. Issues related to combustion temperature maintenance is attributable to the expansion of the turbine's hot gas path components. These challenges require commensurate research to help curb/prevent these problems.

A PGC system describes a method where the combustion process generates final stagnation pressure which is greater than the original stagnation pressure. A particularly useful illustration is the constant volume combustion process within the ideal spark-ignited engine (Gemmen et al., 1995). This constant volume combustion (CVC) systems yield more available energy in the final state gas compared to the constant pressure combustion (CPC) systems (Gemmen et al., 1995). The adoption of this technology for gas turbine cycles under ideal conditions with a pressure ratio of 10:1 and turbine inlet pressure of 1200K, revealed that efficiency of a CVC system (54%) bettered that of a CPC system (48%) (Gemmen et al., 1994). Several authors (e.g., Thring, 1961; Muller, 1971; Kentfield and O'Blenes, 1987a; 1987b) have tried to adopt this technology with different levels of success achieved. While their studies have shown that huge possibilities abound for the attainment of pressure gain, the combined challenge of pressure gain, pollutant reduction and engine reliability has not been extensively studied (Gemmen et al., 1995).

Pressure gain in gas turbines is a well-recognized combustion technology which promises to provide a huge increase in gas turbine efficiency by replacing the conventional constant-pressure heat addition process with a constant volume process. This represents a deviation from the conventional gas turbine cycle i.e., the Brayton cycle, and a utilization of the Atkinson (Humphrey) thermodynamic cycle. This results in a reduced entropy rise thus ensuring that more work is extracted at the turbine and less required fuel input for a constant work output. The motivation for this technology follows from the fact that for a conventional gas turbine engine, overall pressure loss in the range of 4 – 8% of the stagnation pressure delivered by the compressor (without inclusion of pressure loss from isobaric combustion) results from the complex fluid flow paths required for flame stabilization, increasing turbulence, and

[1] https://www.netl.doe.gov/research/coal/energy-systems/turbines/pressure-gain-combustion

dilution schemes for cooling of the combustion products and combustor occurring as the density of the working fluid is decreased and velocity increased due to heating (Lefebvre, 2010). Pressure gain combustion (PGC), which then seeks to not only eradicate this loss but also substitute it with a net rise in stagnation pressure, can be defined as "*a fundamentally unsteady process whereby gas expansion by heat release is constrained, causing a rise in stagnation pressure and allowing work extraction by expansion to the initial pressure"* (Paxson, 2017).

Fig. 1.1 shows the real Brayton and Humphrey Cycles with process 2-3 corresponding to compression losses i.e., where ambient air is pressurized adiabatically in the compressor and process 4-5 corresponding to an adiabatic fluid expansion i.e., where the heated pressurized air gives up its energy while expanding in the turbine with no heat addition. The third cycle diagrammatically shown in Fig. 1.1 corresponds to the PGC cycle which denotes a real gas turbine cycle within which a PGC process has been incorporated.

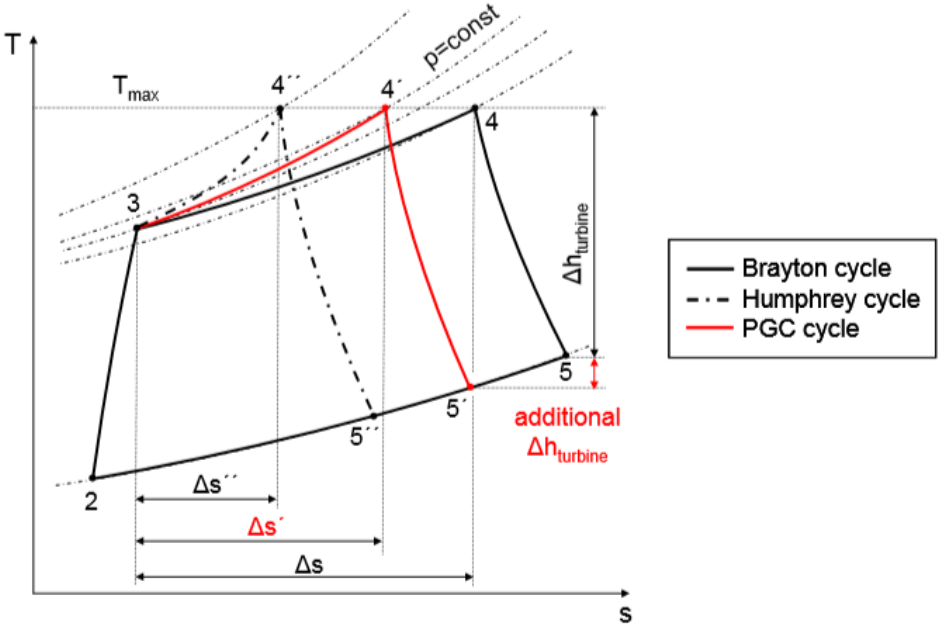

Figure 1.1: A Temperature-entropy (T-s) diagram showing the Real Brayton, Humphrey and PGC Cycles (Eugen, 2014).

The highest temperature for the cycle, T_{max}, is equivalent to the Turbine Entry Temperature/Turbine Inlet Temperature (TET) for all three cycles. Also, TET and the combustion end pressure i.e., states $4'$ and $4''$ are assumed to have quasi-steady, time-averaged values from an investigation of unsteady CVC and PGC processes. The thermal efficiencies for an idealised, loss-free Brayton and Humphrey cycles are given as Eqs. (1.1) and (1.2) respectively (Kruggel-Emden et al., 2004):

$$\eta_{th} = 1 - \frac{T_2}{T_3} = 1 - \frac{1}{\Pi_C^{(\gamma-1/\gamma)}} \tag{1.1}$$

$$\eta_{th} = 1 - \gamma \frac{\left((T_4/T_2)^{(1/\gamma)}\ \Pi_C^{(1-\gamma/\gamma^2)} - 1\right)}{T_4/T_2 - \Pi_C^{(\gamma-1/\gamma)}} \tag{1.2}$$

where Π_C and γ denote the compression ratio and ratio of specific heat capacities or adiabatic exponent. The thermal efficiency of the ideal Brayton cycle is dependent on the compressor ratio while there is an extra reliance on the maximum cycle temperature, T_4 or TET for the ideal Humphrey cycle. Fig. 1.2 shows a plot of the thermal efficiency of the ideal Brayton and Humphrey cycles which is dependent on the compressor pressure ratio. The computation also utilised an initial cycle temperature, T_2 of 300K.

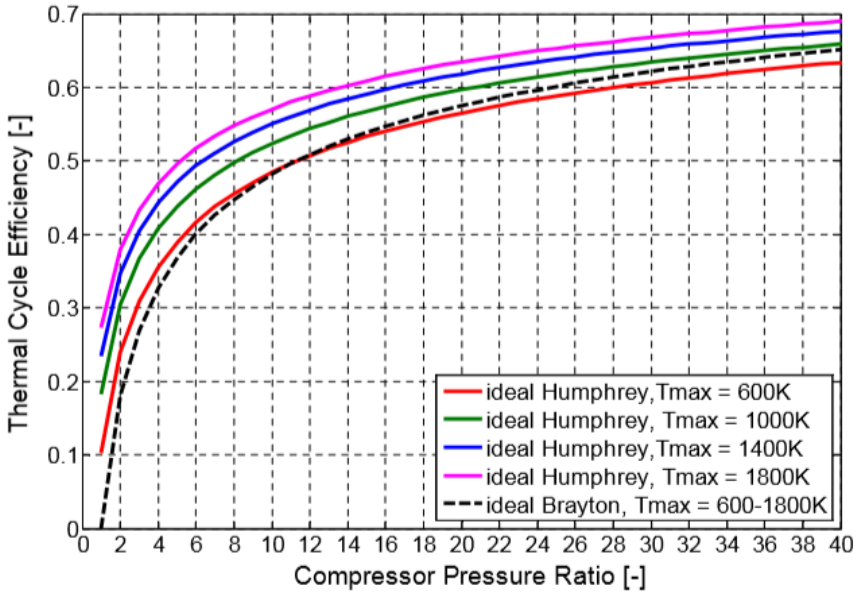

Figure 1.2: Thermal efficiency of the ideal Brayton and Humphrey cycles against compressor pressure ratio computed at different TET (Eugen, 2014).

The ideal Humphrey cycle has a greater thermal efficiency in comparison to the ideal Brayton cycle principally attributable to a reduced entropy increase during CVC. This is particularly true at low compression ratios and at high turbine entry temperatures (Heiser and Pratt, 2002; Kruggel-Emden et al., 2004; Wintenberger and Shepherd, 2004; Wu et al., 2003). However, as the compressor pressure ratio rises, the thermal efficiency of the Humphrey cycle gets closer to the thermal efficiency of the Brayton Cycle and when the temperature, T_3, at the close of the compression process, becomes equal to the fixed TET, the efficiency of both cycles become identical as it then becomes impossible for any additional heat to be added to the combustor.

Comparing the thermal efficiency of real PGC cycle to the previously discussed cycles shows that the time averaged pressure gain of the unsteady PGC process, as shown by process 3-4′ in Fig. 1.1, is assumed to be located somewhere between those of the CPC and CVC. Based on this assumption and procedure, a reduced level of entropy is produced during the PGC process compared to the CPC of the Brayton cycle thus yielding a higher possible temperature reduction across the expansion process. Assuming the compressor power demand requirement stays constant, this results in an extra work output (Δh) in the turbine. Furthermore, because of the compression throughout the combustion process, a reduced amount of fuel is needed for heat addition to the fluid from a fixed temperature T_3 to T_{max}. Following from this, the real PGC cycle thermal efficiency, dependent on the averaged pressure rise in the combustor, $\Pi = p_4/p_3$, can be expressed as (Kruggel-Emden et al., 2004; Probst, 2002):

$$\eta_{th} = 1 - \frac{T_4/T_2\left(1-\left(1-(1/\pi_C\,\Pi)^{(\gamma-1/\gamma)}\right)\eta_T\right)-1}{\left(T_4/T_2-\left(1+\left(\pi_C^{(\gamma-1/\gamma)}-1\right)/\eta_C\right)\right)} \tag{1.3}$$

The thermal efficiency of the real Humphrey cycle is given by Eq. (1.4) below (Kruggel-Emden et al., 2004):

$$\eta_{th} = 1 - \gamma\frac{T_4/T_2\left(1-\left(1-\left(T_2/T_4\,\pi_C\left(1+\left(\pi_C^{(\gamma-1/\gamma)}\right)/\eta_C\right)\right)^{(\gamma-1/\gamma)}\right)\eta_T\right)-1}{\left(T_4/T_2-\left(1+\left(\pi_C^{(\gamma-1/\gamma)}-1\right)/\eta_C\right)\right)} \tag{1.4}$$

From Eqs. (1.3) and (1.4) above, η_C and η_T denote the compressor and the turbine isentropic efficiencies respectively. Fig. 1.3 shows the thermal efficiencies of the real Brayton and PGC cycle for different values of Π plotted against compressor pressure ratio. The thermal efficiency of the real Humphrey cycle is also illustrated for comparison. Eugen (2014) assigned 300K, 1700K, 1.4, 0.86 and 0.9 as values for T_2, T_4, γ, η_C and η_T respectively. From Fig. 1.3, the PGC cycles have a better efficiency than the Brayton cycle for the various pressure ratios investigated with maximum advantage experienced by small engines with a low compressor pressure ratio. This advantage drops for rising compression and cycle temperature ratios with these findings conforming with previous research work (Kentfield and O'Blenes, 1987; Lampinen and Turunen, 1992; Welch et al., 1997; Akbari and Müller, 2003; Li et al., 2007). The real Humphrey cycle shows better performance than the PGC cycle just at very low compressor pressure ratios i.e., $\Pi < 6$. This real Humphrey cycle's thermal efficiency rapidly declines with rising Π and drops below the Brayton cycle's thermal efficiency at $\Pi = 14$.

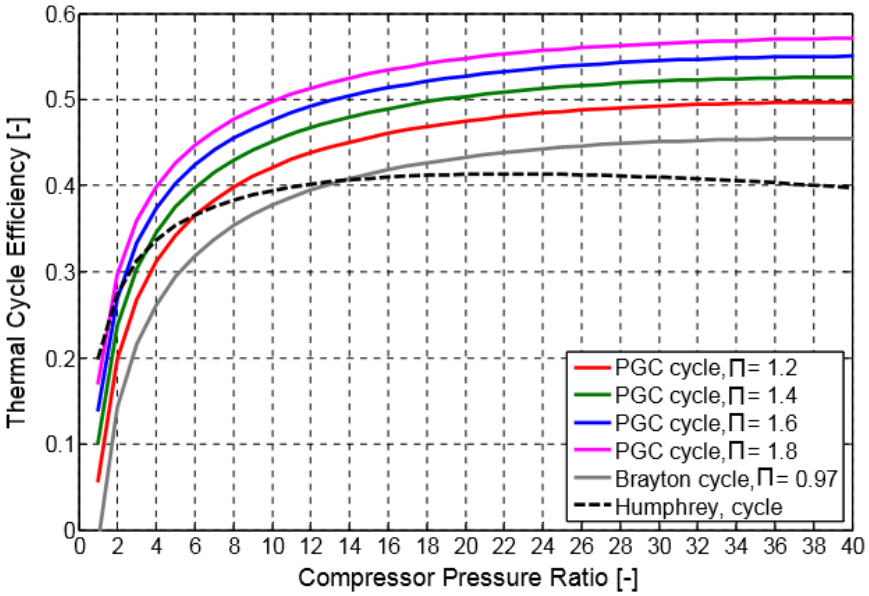

Figure 1.3: Thermal efficiency against compressor pressure ratio for real Brayton, Humphrey and PGC cycles (Eugen, 2014).

Eugen (2014) also investigated three representative types of engines by studying the impact of a 20% combustor pressure-gain i.e., $\Pi = 1.2$ with the aim of clarifying the theoretical capability of PGC. Following from this, a micro-jet engine operating at a compressor pressure of 4 and TET of 1000K is estimated to have a theoretical rise in cycle efficiency of 30%. A turboshaft-type engine with Π_C and TET of 20 and 1500K respectively is estimated to attain a 11.4% rise in cycle efficiency while a turbojet with Π_C and TET of 38 and 1800K shows an improved capacity of 8.4%. Thus, a subsequent rise in the specific power and specific fuel consumption is estimated to be in an identical range of values (Kentfield et al., 1980; Kentfield and O'Blenes; 1990; Akbari and Müller, 2003). Eugen (2014) noted that the computations as shown in Fig. 1.3 denote a higher range of likely advancements as they have ignored the details of how PGC is attained.

Fig. 1.4 shows an optional implementation of PGC to a gas turbine cycle where the turbine work output is identical to that of the reference Brayton cycle. In addition to the improvements in thermal efficiency and specific fuel consumption (SFC) as explained previously, the cycle offers an added benefit of decreased TET (Eugen, 2014). The pressure gain in the combustor can also be modified by reducing

the cycle pre-compression, i.e., lowering the number of compressor stages. These two variations result in a low-weight, increased dependability, additional efficiency, and reduced cost engine.

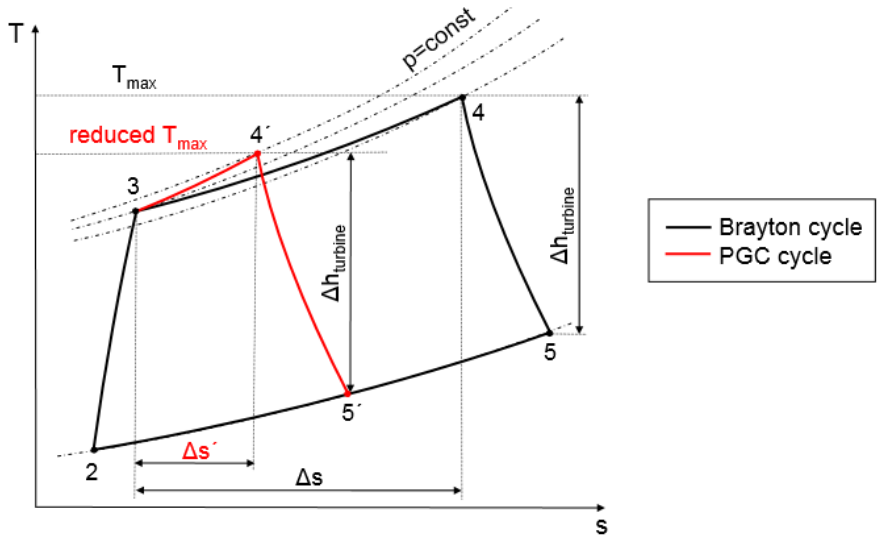

Figure 1.4: Temperature-entropy diagram for a conventional Brayton and PGC gas turbine cycles for an identical turbine work output (Eugen, 2014).

This PGC technology provides a massive, thermodynamically verified development capability for gas turbine efficiency. A major highlight of this technology is the Vulcan project of the US government's Defense Advanced Research Projects Agency (DARPA). This project was initiated to aid in achieving the Department of Defence's goal of reducing energy consumption throughout the agency[2]. The project will also see that a full-scale CVC power generation turbine engine is devised, fabricated, and established with an expectation that the adoption of this technology will lower the fuel consumption of fuel gas turbine engines by 20% leading to almost 65 gallons per hour fuel savings in comparison to the existing DDG-51 Class gas turbine generator sets[2]. However, there exists some unsolved challenges from the introduction of the PGC. These include: stability and dynamics of the unsteady combustion mode, cooling of the combustor and turbine, interaction of compressor and turbine with unsteady flow, mechanical and thermal stresses etc.

In the last hundred years, there has been an abundance of different PGC concepts for adoption in gas turbines (e.g., Bauer, 1958; Kentfield and O'Blenes, 1987; Sabatiuk, 1987; Whurr, 1997; Norris and Twelves Jr., 2005; Sammann et al., 2005; Murrow et al., 2009). Eugen (2014) explained that all these concepts involve unsteady processes during combustion to produce a total pressure gain from inlet to outlet. Kentfield & O'Blenes (1987a) and Paxson (2010) also explained that the detonation wave combustors, wave rotors, and valveless pulse combustors have been recognised as the PGC concepts with the most viability and potential. These PGC concepts also presently establish the basis for different industrial and academic research works (e.g., Roy et al., 2004; Offord et al., 2008; Akbari and Nalim, 2009; Heffer and Miller, 2009). As Kentfield and O'Blenes (1987a) rightly established that all practical pressure gain systems require some form of unsteady fluid mechanics and combustion, the pulse combustion (which represents a general category of combustion system) depends on the characteristic unsteadiness of resonant chambers. Within the combustion chamber, the periodic injection and consumption of air and fuel preserves the resonant mode for the oscillation of fluid in an

[2] DARPA Announces Phase II of its Vulcan Program. Available at: http://www.deagel.com/news/DARPA-Announces-Phase-II-of-its-Vulcan-Program_n000007701.aspx. (Accessed: 26 August 2023)

attached tube. Kentfield and Fernandes (1990) revealed some certain configurations of these sort of devices capable of generating up to 4% pressure rise.

Resonant combustion systems possess three advantageous features that make them possible options for first-generation pressure gain combustors (Gemmen et al., 1995). Firstly, they do not need any mechanical mechanism to generate unsteady fluid mechanics and combustion as they are propelled in a natural mode of instability. Also, as their oscillations are almost sinusoidal, there is a huge possibility for pairs of these systems to be run anti-phased with the sole aim of attaining wave attenuation (Gemmen et al., 1995). In the same vein, there stands a massive chance to minimise the effects of fluid oscillations on gas turbine reliability particularly with the prospects of wave cancellation. Lastly, George and Corliss (1988) explained that particular styles of resonant systems like the aerovalve pulse combustors have been fabricated without any mechanically moving components like the flapper valves and rotary valves. The absence of these mechanically moving components ensure that detrimental impacts on gas turbine dependability, accessibility and sustainability are prevented (Gemmen et al., 1995). Gemmen et al. (1995) mainly adopted the aerovalved Helmholtz-type resonator while Eugene (2014) classified the PGC concepts into five main groups based on the mechanism through which PGC is attained namely; Elementary CVCs, Combustors dependent on Reciprocating Internal Combustion Engines, Detonation Wave Combustors, Pulse Combustors and External and Internal Combustion Wave Rotors.

More recently, Lutoschkin et al. (2013) studied the possibility of applying shock interaction with a flame to attain pressure gain combustion. They explained that this method was very useful in considerably enhancing the performance of gas turbine engines as pressure rise could be achieved by employing the thermodynamically more efficient unsteady combustion. Using a quasi-one-dimensional model, they computed a fully defined one-dimensional flow-field produced at the end of a single shock-flame interaction process which they validated utilising experimental data on methane-oxygen-argon flames. Their works went to show that a single process of shock-flame interaction yielded a dramatic rise in pressure with time in comparison to a constant pressure combustion using the same unburned gas conditions. Heiser and Pratt (2002) described the Humphrey cycle as a thermodynamic cycle consisting of compression and ‘idealised’ isochoric combustion succeeded by the expansion of the working fluid. This cycle compared to a conventional Brayton cycle as shown in Fig. 1.1 for a fixed maximum cycle temperature and compressor discharge pressure show that turbine power output as well as thermal cycle efficiency are increased for an equal combustion energy. Shock flame interaction can have the same positive effects for gas turbine engines as the propagation of shock wave via a wavy flame front leads to an increase in gas temperature and pressure as well as an increase in turbulence intensity, flame stretch and flame surface area (Ju et al., 1998; Khokhlov et al., 1999; Kilchyk, 2009; Lutoschkin et al., 2013).

This project intends to investigate pressure gain using shock-bubble (gas and liquid bubble) interaction (SBI). When vorticity or velocity shear is deposited on a bubble surface by a shock wave due to SBI, the bubble surface (represented by the interface across which gases of different densities exist) deforms resulting in a change in its surface area. An intensification of this distortion because of shock refraction of any disturbance previously existent in the gas interface is termed the Richtmyer–Meshkov instability (RMI). Velocity shear is the local variation of velocity across the material interface and is induced by the RMI (Diegelmann et al., 2017). This RMI with growing interface distortion leads to secondary instabilities like the Kelvin–Helmholtz shear instability which further develop to improve mixing and turbulence (Batley et al., 1996). This research then intends to preliminarily study and understand shock wave interaction (with a gas and liquid bubble) via a detailed computational fluid dynamics (CFD) investigation. From a SBI perspective, positive impacts can be achieved for gas turbine engines particularly with respect to a rise in gas pressure as well as an increase in turbulence intensity.

1.2. Compressible shockwave propagation through a medium

For the case of an inviscid adiabatic flow of a perfect gas in a constant area insulated duct as provided by Houghton and Brock (1993), the model was reduced to the scenario of an adiabatic flow of a compressible fluid through a unit area stream tube as they did not consider wall effects. This is shown in Fig. 1.5.

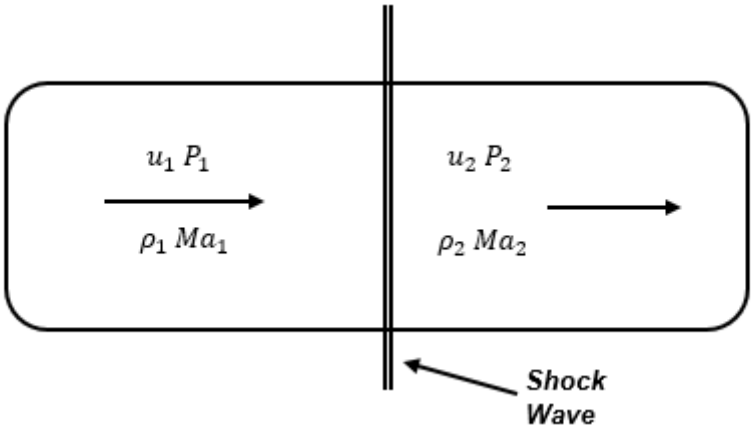

Figure 1.5: Normal Shock waves for compressible fluid flow through an insulated duct (Houghton and Brock, 1993).

From Fig. 1.5, u, P, ρ and Ma represent the velocity, static pressure, density, and Mach number respectively. Subscripts 1 and 2 denote sections 1 and 2 respectively. They also revealed that the only flow possible in a frictionless tube of constant area, except for the scenario where the flow is uniform i.e., $u_1 = u_2$; $P_1 = P_2$; $\rho_1 = \rho_2$, is a compressible flow (see Eqs. (1.21) and 1.25)) which is originally under supersonic conditions but is finally characterised by subsonic conditions subsequently followed by a rise in entropy. This compressive flow can abruptly occur requiring that the governing equations are obtained assuming that a 'non-impulsive, insulated' discontinuity occurs between the left and right sections shown in Fig. 1.5 with the flows before and after this discontinuity being uniform.

This discontinuity is termed a shock wave. Shock waves have several applications but of particular significance is its use for such purposes as boosting pressure for an '*airbreathing*' scramjet and producing lift via the wave rider structure (Wu et al., 2013). Wu et al. (2013) explained that shock waves can be grouped into four classes which include; attached shock wave, e.g. when a supersonic flow meets an inward corner; detached shock wave e.g. when a supersonic flow goes past a blunt body; recompression shock wave produced for modification to farfield pressure e.g. when a transonic flow goes past the upper surface of an airfoil or supersonic flow past a nozzle with high back pressure; and secondary induced shock wave from various scenarios e.g. reflection of shock, interaction between/among several shock waves, interaction between shock-wave and boundary layer, lateral jet flow etc. Wu et al. (2013) also explain that shock waves can be produced from explosion, combustion or lightning strike, followed by the appearance of a local high-pressure region characterised by strong shock propagating at supersonic speed with Ma in the range $1.2 \leq Ma \leq 5$.

Wu et al. (2013) also highlighted some characteristics of shock waves as shown below:

- The extent of a shock wave is in the range of the local mean free path of fluid particles. This then means that the shock wave can be referred to as a sharp discontinuity in normal aerodynamic flow.
- The pressure, density, temperature and entropy rise across a shock wave in the streamwise direction.
- The Mach number, velocity and normal velocity component decrease across a shock wave in the

streamwise direction.

- The total temperature and tangential velocity component stay constant for a calorically perfect gas across a shock in the streamwise direction.
- The inherent difference between the shock wave and other discontinuities in the fluid flow e.g., a slip surface for a 3D geometry or a slip line for a 2D geometry defines a plane across which the tangent velocity is discontinuous, but the pressure and normal velocity are continuous. The pressure and velocity are continuous while the density is discontinuous across a contact discontinuity.
- The shock wave, as a discontinuity in the flow field, has the contour line of Mach number, pressure, density, temperature concentrating close to it as shown in Fig. 1.6. On the other hand, the pressure contour lines for a slip plane and contact discontinuity do not concentrate in the region of these discontinuities.

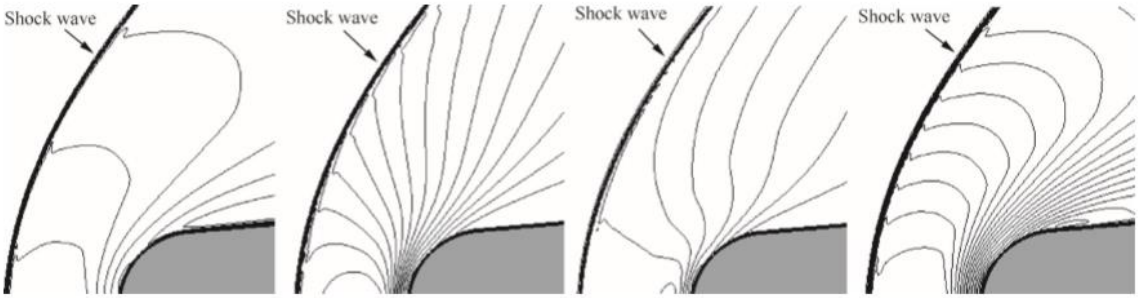

Figure 1.6: Illustration for Concentration of contour at Ma = 5 for Mach number, pressure, density and temperature contour respectively (Wu et al., 2013).

- The numerical simulation of fluid flow with discontinuities like shock waves, contact discontinuity and slip line presents the resolution of this challenge using shock capturing techniques whereby the shock wave can be smoothed adopting low-order scheme or high-order scheme when there are spurious oscillations close to the shock surface (Toro, 2009; see Fig. 1.7).

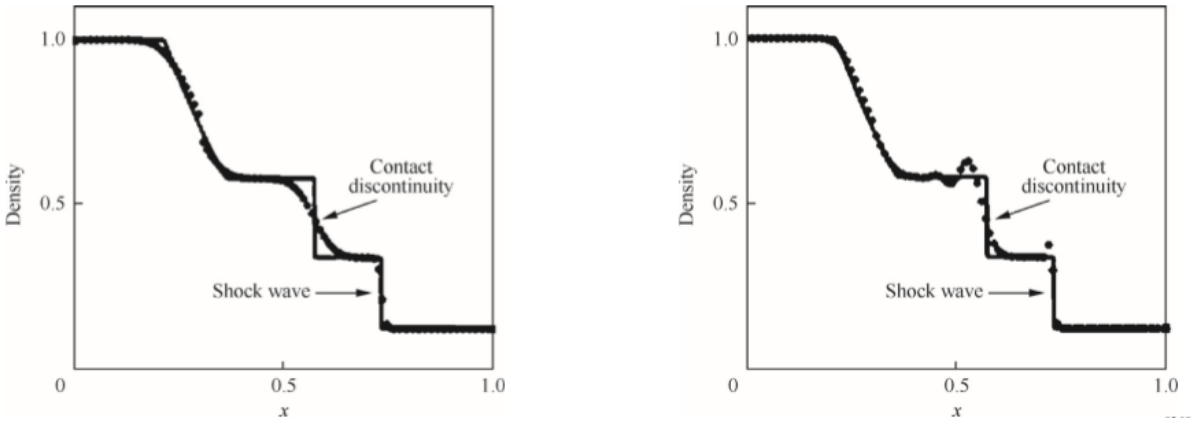

Figure 1.7: Solution of Sod challenge for Euler equations calculated with; first-order Godunov's method; and second-order two-step Lax-Wendroff technique (Toro, 2009).

The Sod shock tube challenge, named after Gary A. Sod, is a test for the accuracy of computational fluid codes like Riemann solvers. For this challenge, the shock tube is divided into two parts by a central diaphragm which splits the fluid within the tube into two different states of varying density, velocity, and pressure. The sudden withdrawal of this diaphragm leads to the appearance of different forms of waves i.e., shock wave, rarefaction wave and contact discontinuity, in the flow field (Sod, 1978). From Fig. 1.7, the dotted lines denote the calculated result while the solid lines denote the analytical solution. Adopting the classical boundary shock-

fitting techniques presents a method where the shock wave is introduced explicitly as outer flow boundary based on experimental, theoretical, or numerical-centered knowledge on shock shape and location (Salas, 2011). Finally, the floating shock-fitting method as presented by Moretti (Moretti, 1973) can be used to identify shock waves via the Rankine–Hugoniot jump condition and the technique of characteristics which may be relevant to post-processing shock detection.

1.3. Governing equations for shock wave propagation

Houghton and Brock (1993) stated that the suitable equations for a compressible flow assuming that a shock discontinuity lies in the flow are obtained from; the perfect gas Equation of State, Conservation of momentum as well as Conservation of energy and are given below[3];

$$\frac{P_1}{\rho_1 T_1} = \frac{P_2}{\rho_2 T_2} \tag{1.5}$$

$$\dot{m} = \rho_1 u_1 = \rho_2 u_2 \tag{1.6}$$

$$\rho_1 {u_1}^2 - \rho_2 {u_2}^2 + (P_1 - P_2) = 0 \tag{1.7}$$

$$c_p T_1 + \frac{1}{2}{u_1}^2 = c_p T_2 + \frac{1}{2}{u_2}^2 = c_p T_0 \tag{1.8}$$

Replacing $c_p T$ with $\{\gamma/(\gamma-1)\}\,P/\rho$ and rearranging Eq. (1.8) above gives:

$$\frac{\gamma}{\gamma-1}\left(\frac{P_1}{\rho_1} - \frac{P_2}{\rho_2}\right) = \frac{1}{2}(u_2 - u_1)(u_2 + u_1) \tag{1.9}$$

Simplifying Eq. (1.9) using Eqs. (1.6) and (1.7) yields:

$$\frac{\gamma}{\gamma-1}\left(\frac{P_1}{\rho_1} - \frac{P_2}{\rho_2}\right) = \frac{1}{2}(P_1 - P_2)\left(\frac{1}{\rho_2} + \frac{1}{\rho_1}\right) \tag{1.10}$$

Rearranging Eq. (1.10), the Rankine-Hugoniot relationships are obtained as shown below:

$$\frac{P_2}{P_1} = \frac{\frac{\gamma+1}{\gamma-1}\left(\frac{\rho_2}{\rho_1}\right) - 1}{\frac{\gamma+1}{\gamma-1} - \left(\frac{\rho_2}{\rho_1}\right)} \tag{1.11}$$

$$\frac{\rho_2}{\rho_1} = \frac{\frac{\gamma+1}{\gamma-1}\left(\frac{P_2}{P_1}\right) + 1}{\frac{\gamma+1}{\gamma-1} + \left(\frac{P_2}{P_1}\right)} \tag{1.12}$$

These relationships then ensure that the pressure ratio, exit Mach number, density ratio, temperature ratio, entropy and velocity change across a shock are obtained.

1.3.1. Pressure ratio through shock

From the momentum and continuity equations (Eqs. (1.7) and (1.6)), Eq. (1.13) can be obtained:

$$\frac{P_2 - P_1}{P_1} = \frac{\rho_1 {u_1}^2 - \rho_2 {u_2}^2}{P_1} = \gamma {Ma_1}^2\left(1 - \frac{u_2}{u_1}\right) \tag{1.13}$$

Replacing $\rho_2/\rho_1\ (= u_1/u_2)$ from Eq. (1.12) and simplifying gives:

[3] The fact that a shock wave has a finite thickness and its own typical properties do not discredit the developed governing equations for a compressible flow from previously supersonic state to a finally subsonic state.

$$\frac{P_2}{P_1} = \frac{2\gamma}{\gamma+1} {Ma_1}^2 - \frac{\gamma-1}{\gamma+1} \tag{1.14}$$

1.3.2. Exit mach number

From Eq. (1.14) and by switching the order of the variables, Eq. (1.15) is derived:

$$\frac{P_1}{P_2} = \frac{2\gamma}{\gamma+1} {Ma_2}^2 - \frac{\gamma-1}{\gamma+1} \tag{1.15}$$

Multiplying Eqs. (1.14) and (1.15) produces:

$${Ma_2}^2 = \frac{(\gamma-1){Ma_1}^2 + 2}{2\gamma {Ma_1}^2 - (\gamma-1)} \tag{1.16}$$

1.3.3. Density ratio through shock

Replacing P_2/P_1 in Eq. (1.12) with Eq. (1.14) gives:

$$\frac{\rho_2}{\rho_1} = \frac{(\gamma+1){Ma_1}^2}{2 + (\gamma-1){Ma_1}^2} \tag{1.17}$$

1.3.4. Temperature ratio through shock

Since $T_2/T_1 = (P_2/P_1)\,/(\rho_2/\rho_1)$, Eq. (1.18) can then be obtained:

$$\frac{T_2}{T_1} = \left(\frac{2\gamma {Ma_1}^2 - (\gamma-1)}{\gamma+1}\right)\left(\frac{2 + (\gamma-1){Ma_1}^2}{(\gamma+1){Ma_1}^2}\right) \tag{1.18}$$

1.3.5. Entropy change through shock

From the Second Law of Thermodynamics, the entropy, S, of a system must increase in a real (irreversible) process and is constant only in an ideal (reversible) process. This can be expressed below:

$$\frac{\Delta S}{c_v} = \gamma log \frac{T_2}{T_1} + (\gamma-1) log \frac{P_1}{P_2} \tag{1.19}$$

Replacing T_2/T_1 and P_1/P_2 in Eq. (1.19) with Eqs. (1.18) and (1.15) gives:

$$\frac{\Delta S}{c_v} = log\left\{\left(\frac{2 + (\gamma-1){Ma_1}^2}{(\gamma+1){Ma_1}^2}\right)^{\gamma}\left(\frac{2\gamma {Ma_1}^2 - (\gamma-1)}{\gamma+1}\right)^{\gamma-1}\right\} \tag{1.20}$$

Expanding Eq. (1.20) gives the first term of a series as shown below:

$$\frac{\Delta S}{c_v} = \frac{2\gamma(\gamma-1)}{(\gamma+1)^2} * \frac{\left({Ma_1}^2 - 1\right)^3}{3} \tag{1.21}$$

When $Ma_1 > 1$, $\Delta S > 0$, there is a dissipation flow

And $Ma_1 < 1$, $\Delta S < 0$ is disallowed by the Second Law of Thermodynamics.

Putting $c_p T_1 = \frac{\gamma}{\gamma-1} * \frac{P_1}{\rho_1}$ into Eq. (1.8) yields,

$$\frac{P_1}{\rho_1} = \frac{\gamma-1}{\gamma}\left\{c_p T_0 - \frac{{u_1}^2}{2}\right\}, \qquad \frac{P_2}{\rho_2} = \frac{\gamma-1}{\gamma}\left\{c_p T_0 - \frac{{u_2}^2}{2}\right\}, \tag{1.22}$$

And from Eqs. (1.7) and (1.6), Eq. (1.23) is obtained:

$$u_1 - u_2 = \frac{P_2}{\rho_2 u_2} - \frac{P_1}{\rho_1 u_1} \tag{1.23}$$

Substituting the expressions for P_1/ρ_1 and P_2/ρ_2 from Eq. (1.22) above, Eq. (1.24) is derived:

$$u_1 - u_2 = \frac{\gamma - 1}{\gamma}\left\{(u_1 - u_2)\left(\frac{1}{2} + \frac{c_p T_0}{u_1 u_2}\right)\right\} \tag{1.24}$$

The trivial solution $u_1 = u_2$ can be ignored and Eq. (1.25) is obtained:

$$u_1 u_2 = \frac{2(\gamma - 1)}{\gamma + 1} c_p T_0 = {a_{Ma=unity}}^2 \tag{1.25}$$

Eq. (1.25) describes the limiting case of Sonic flow when Ma_1 =1, $u_1 = u_2 = a_{Ma=unity}$

1.3.6. The velocity change across shock

From the continuity equation, $u_2/u_1 = \rho_1/\rho_2$. Therefore, from Eq (1.17), Eq. (1.26) is derived:

$$\frac{u_2}{u_1} = \frac{2 + (\gamma - 1){Ma_1}^2}{(\gamma + 1){Ma_1}^2} \tag{1.26}$$

1.3.7. Pressure recovery

This is represented by $R_{0,1} = P_{0,2}/P_{0,1}$ and can also be re-expressed as $R_{0,1} = (P_{0,2}/P_1) \cdot (P_1/P_{0,1})$. This concept can be effectively visualised from a tube closed at one end, by a pressure measuring device, with its other end open into the supersonic flow stream. In this case, the pressure recovery is modified by the presence of a curved shock wave in front of the tube, which close to the axial streamline could be termed a plane as shown below:

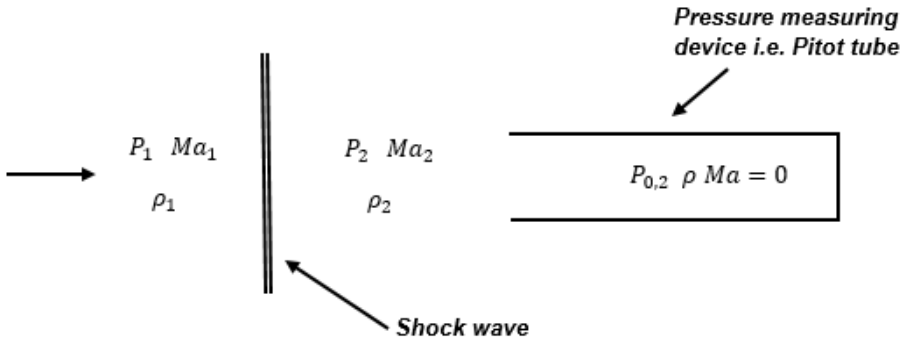

Figure 1.8: The Assumed Bow shock plane which is normal to the axial flow.

From Fig. 1.8, the axial flow into the pressure measuring device can be assumed to stop at pressure, P_{02} from the subsonic region behind the shock (P_2), after supersonic compression (P_1) by the shock wave. Following from this and applying the isentropic pressure ratio between the region behind the shock wave and the position of the pressure measuring device, Eq. (1.27) is derived:

$$\frac{P_{02}}{P_2} = \left[1 + \frac{\gamma - 1}{2}{Ma_2}^2\right]^{\gamma/\gamma - 1} \tag{1.27}$$

1.4. Governing equations for a moving shock wave

Having dealt with all these fundamental theories of Shock-wave propagation, this research has further investigated the physics behind a moving shock. A moving shock deals with a shock wave that propagates through a fluid with a velocity relative to the velocity of the fluid that constitutes the medium. This then necessitates the modification of the normal shock relationships previously discussed to effectively calculate the properties before and after the moving shock. This theory is also very important to this research as the principal objective of this PhD is to investigate the effects of a moving shock wave on a gas and liquid bubble.

Shapiro (1983) derived the theoretical equations for a moving shock wave by considering the gas-relative and shock-relative velocities as shown in Fig. 1.9.

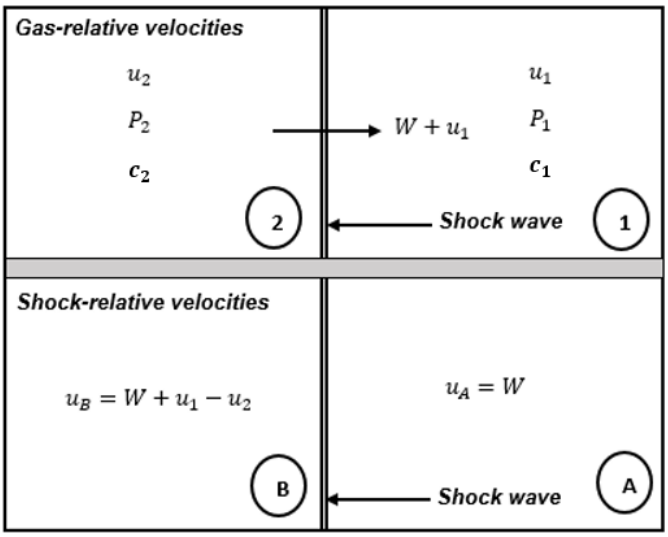

Figure 1.9: Gas-relative and shock-relative velocities for derivation of moving shock waves equations.

From Fig. 1.9, the shock wave propagates from left to right and the region 1 is ahead of the shock wave while the region 2 is behind the shock wave. The velocity, pressure and local speed of sound are represented by u, P and c respectively. As the speed of the shock wave relative to the gas is W, the total velocity thus equates $W + u_1$.

Shapiro (1983) then assumed that a reference frame was then fixed to the shock as shown in Fig. 1.9 to create an appearance of a stationary shock as the gas in regions 1 and 2 travel with a velocity relative to it. This was followed by a representation of region 1 as A and region 2 as B resulting in the following shock-relative velocities:

$$u_B = W + u_1 - u_2 \tag{1.28}$$

$$u_A = W \tag{1.29}$$

Based on these shock-relative velocities, the properties of the regimes before and after the shock can be defined as shown below while introducing temperature (T), density (ρ) and the Mach number (Ma):

$$P_1 = P_A \;\; ; \;\; P_2 = P_B \;\; ; \;\; T_1 = T_A \;\; ; \;\; T_2 = T_B$$

$$\rho_1 = \rho_A \;\; ; \;\; \rho_2 = \rho_B \;\; ; \;\; c_1 = c_A \;\; ; \;\; c_2 = c_B$$

$$Ma_A = \frac{u_A}{c_A} = \frac{W}{c_1} \tag{1.30}$$

$$Ma_B = \frac{u_B}{c_B} = \frac{W + u_1 - u_2}{c_2} \tag{1.31}$$

Introducing the ratio of specific heat at constant pressure to specific heat at constant volume allows the ratios of sound speed, density, and pressure to be obtained as shown below:

$$\frac{c_2}{c_1} = \sqrt{1 + \frac{2(\gamma - 1)}{(\gamma + 1)^2}\left[\gamma {Ma_A}^2 - \frac{1}{{Ma_A}^2} - (\gamma - 1)\right]} \tag{1.32}$$

$$\frac{\rho_2}{\rho_1} = \frac{1}{1 - \frac{2}{\gamma + 1}\left[1 - \frac{1}{{Ma_A}^2}\right]} \tag{1.33}$$

$$\frac{P_2}{P_1} = 1 + \frac{2\gamma}{\gamma + 1}\left[{Ma_A}^2 - 1\right] \tag{1.34}$$

However, for a shock propagating from right to left, the subscripts A and B must be alternated thus giving:

$$u_B = W - u_1 + u_2 \tag{1.35}$$

$$Ma_B = \frac{W - u_1 + u_2}{c_2} \tag{1.36}$$

In order to determine required parameters for the simulation, this research has reviewed several key definitions and equations starting with the Mach number which is a dimensionless quantity that represents the ratio of velocity of flow (u) past a boundary to the local speed of sounds (c) represented as:

$$Ma = \frac{u}{c} \tag{1.37}$$

c can be derived as:

$$c = \sqrt{\gamma RT} \tag{1.38}$$

where, γ is the ratio of specific heats and R is the gas constant.

Eq. (1.30) can then be rewritten as:

$$W = Ma_A c_1 = Ma_A \sqrt{\gamma RT_1} \tag{1.39}$$

1.5. Shock/gas bubble interaction

Shock-bubble interaction (SBI) is an unsteady flow created by shock wave propagation through a distinct round inhomogeneity surrounded by ambient fluid in a uniform medium (Niederhaus et al., 2008). During shock wave propagation through a material of non-uniform thermodynamic properties, various processes take place concurrently that change the geometry of the shock wave and the thermodynamic state of the medium. These include shock compression and acceleration of the material, shock refraction and production of vorticity within the material. Ranjan et al. (2011) explain that the simplest configuration through which all these processes can be studied in detail is the interaction of the shock wave with a cylindrical or spherical bubble. Their work also showed that shock acceleration results in an initial bubble compression and deformation after which a vortex pair or a vortex ring is formed for a two-dimensional (2D) or three-dimensional (3D) scenario respectively. As the interaction progresses, and with the correct blends of the incident shock strength and variation in

density between the bubble and the surrounding fluid, there is a formation of secondary vortices, stripping of original bubble's mass as well as bubble and surrounding fluid mixing (Ranjan et al., 2011).

Shock interaction with a geometrically distinct density inhomogeneity (like a gas or liquid bubble) creates a flow field. This flow field is characterised by the intense coupling of various types of fluid dynamic phenomena such as shock wave refraction and reflection; vorticity generation and transport; as well as turbulence mixing. This interaction leads to a complex configuration of shock and rarefaction waves mainly through focusing and scattering with the concurrent production of characteristic vortices and frequent mixing of the surrounding gas with the gas inhomogeneity (Niederhaus et al., 2008). This physical phenomenon is preliminarily essential for the studies and investigation of complex challenges related to shock travel through an arbitrary material with varying density, temperature, and other thermodynamic state variables. SBI thus represents a fundamental pattern for understanding the more robust cases of shock accelerated inhomogeneous flows, SAIFs (Zabusky, 1999) with strong similarities noticeable in comparison with perturbations from the evolution of Richtmyer-Meshkov instability on spontaneously accelerated fluid interfaces (Brouillette, 2002).

Considering the specific situation where a planar incident shock wave interacts with a discrete sharply well-defined spherical gas bubble surrounded by ambient gas. Assuming the surrounding unshocked gas has a density and speed of sound of ρ_1 and c_1 respectively while the density and speed of sound of the unshocked bubble gas corresponds to ρ_2 and c_2 respectively, a parameter called the Atwood number (A) can be defined as (Niederhaus et al., 2008):

$$A = \frac{(\rho_2 - \rho_1)}{(\rho_2 + \rho_1)} \tag{1.40}$$

From Eq. (1.40), Niederhaus et al. (2008) explained that two scenarios may be defined corresponding to the light bubble case where $A < 0$ and the heavy bubble case where $A > 0$. Zabusky and Zeng (1998) had previously distinguished these two cases with respect to the variation in the ideal gas speed of sound by stating that for a fixed uniform specific heats ratio, γ, the light bubble case implied that $c_2 > c_1$ while the heavy bubble case meant that $c_2 < c_1$. Based on this finding, they called the light bubble case the 'slow-fast-slow' (SFS) scenario and the heavy bubble case the 'fast-slow-fast (FSF) scenario. They also explained that the sign of A determined the configuration of the shock refraction patterns which were generated in the SBI. These patterns, configurations and related bubble distortions are shown in Fig. 1.10.

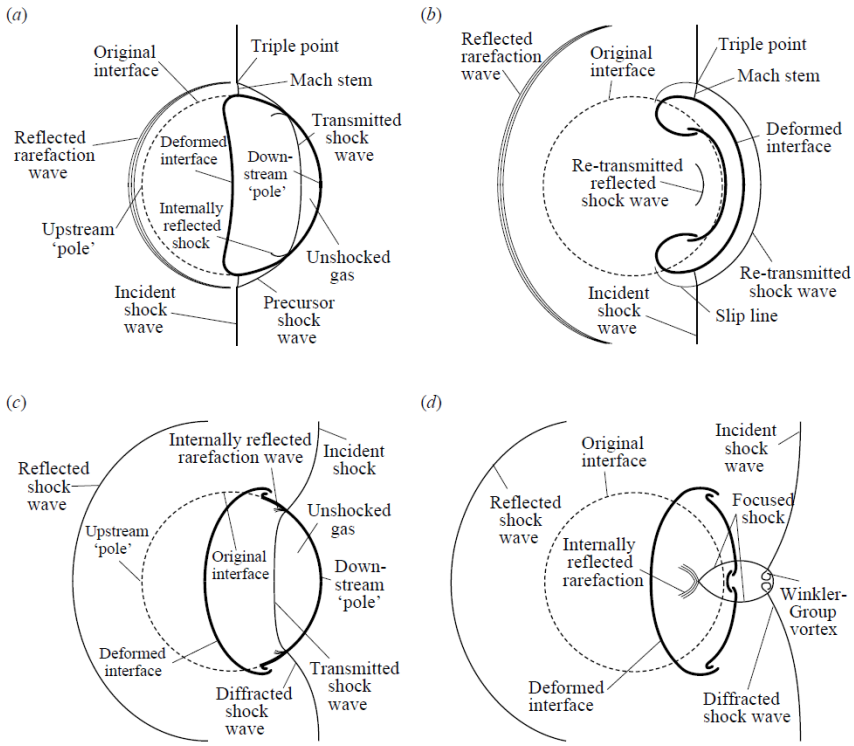

Figure 1.10: Representation of SBI flow field with shock wave travelling from left to right. Light bubble case, A < 0 (a) during the initial shock wave propagation, and (b) immediately after initial shock wave travel. Heavy bubble case A > 0 (c) during the initial shock wave propagation and (d) immediately after the initial shock wave travel (Nierderhaus et al., 2008).

For the two scenarios, the incident shock wave is refracted while propagating through the curved upstream bubble surface due to the variation in the speed of sound. For the case where A < 0, this refraction is divergent resulting in a transmitted shock wave with a convex curvature (see Fig. 1.10(a), (b)). Following from this, an upstream moving reflected rarefaction arises in the surrounding gas with the sole aim of conserving mechanical equilibrium. This then leads to the transmitted shock wave generating an internally reflected shock wave which impacts the downstream surface of the interior of the bubble thus moving the bubble upstream. Henderson (1966, 1989) explains that an irregular shock refraction pattern is developed on the bubble exterior as the transmitted shock wave travels in the downstream direction in front of the external incident shock. This process creates a Mach Stem, triple point, and precursor shock (Niederhaus et al., 2008) and it is possible to trace a slip surface in the flow across the path transited by the triple point. Haas & Sturtevant (1987) and Jacobs (1993) essentially state that vorticity is intensely placed on the bubble gas/ambient gas interface by the baroclinic mechanism (measure of misalignment between the pressure gradient of the interacting shock waves and density gradient in the bubble gas) throughout the propagation of the shock wave which leads to the overturning of the interface's upper section and the subsequent production of a vortex ring.

For the A > 0 case, refraction is convergent which means that the transmitted shock wave has a concave curvature. Here, mechanical equilibrium is preserved after shock impact by the production of an upstream-directed reflected shock wave after which the transmitted shock wave travels through the bubble and produces an internally reflected rarefaction wave. This internally reflected rarefaction wave impacts the downstream interior bubble surface (Niederhaus et al., 2008). If A as well as the variation in speed of sound are high enough, sections of the shock front sweeping around the bubble edge are diffracted (Haas and Sturtevant 1987; Quirk & Karni 1996) which implies that these front sweeping shock portions are inverted towards the axis such that the surface of discontinuity stays approximately

normal to the interface. These diffracted shock waves may then meet with the transmitted shock wave at the downstream pole leading to shock focusing and the motion of secondary shock waves both laterally and upstream. During this time, vorticity is deposited baroclinically on the interface during the propagation of the primary and secondary shocks leading to rotation predominantly in a reverse sense to the light bubble scenario.

There also exists a formation of the supersonic vortex ring analogous to those noticeable in the simulations of Winkler et al. (1987) which is produced following the re-transmitted shock front in the surrounding gas with the upstream- or downstream positioned perturbations emerging at the bubble's downstream pole. Niederhaus et al. (2008) pointed out very essentially that the convergence or divergence related with shock refraction through the bubble is decided by the acoustic impedance disparity at the interface. Following from this, it can thus be inferred that SBIs will exhibit; a divergent, 'light bubble' (A < 0) refraction behaviour in the non-uniform-specific heat ratio scenario for $\rho_2 c_2/(\rho_1 c_1) < 1$ or a convergent, 'heavy bubble' (A > 0) refraction behaviour for $\rho_2 c_2/(\rho_1 c_1) > 1$. However, some anomalies could exist where the SBIs will reveal a refraction pattern synonymous to divergent light-bubble in the non-uniform-specific heat ratio scenario for $\rho_2 c_2/(\rho_1 c_1) < 1$ although A > 0 with the reverse situation also possible. This indicates that there is a chance that externally reflected shock waves could exist in some divergent bubble scenario i.e., A < 0 due to the offsetting effects of the variation in the specific heat ratio on the density variation while externally reflected rarefaction waves could also appear for the convergent 'heavy-bubble' scenario i.e., A > 0.

1.5.1. Generation and evolution of vorticity with associated vortex strength

SBI has been previously studied experimentally by Rudinger & Somers (1960) and Haas & Sturtevant (1987) with the latter proposing that this interaction be adopted as a model problem for studying vorticity and creation of turbulence in compressible flows with shock-wave propagation. Shock wave propagation across a non-uniform gas leads to refraction, diffraction and reflection of the shock wave impacting/interacting with inhomogeneities. These processes or deviations from the global symmetry alter the shock's transmission across the gas. Picone and Boris (1983) explained that the interactions of pressure waves with density fluctuations in a fluid are the principal basis for vorticity formation and turbulbent motion. These rotational flows develop on more extended periods compared to shock passage across the local non-uniformity thus resulting in major lasting impacts on the composition and characteristics of the fluid (Picone and Boris, 1983).

Rotational motion has been mainly created from shock-tube experiments primarily via the interaction of shocks with inhomogeneous gases thus creating the foundation for shock-bubble interaction (Haas, 1983; Haas, 1984; Haas and Sturtevant, 1987) and shock-flame interaction (Markstein, 1957a, b). Haas and Sturtevant (1987) have investigated shock interaction with single or multiple bubbles while Picone and Boris (1988) investigated spherical flame and single-bubble experiments of the earlier mentioned authors with their research representing limiting cases of a fluid in which ambient variations are localised and widely separated with respect to their representative spatial scales. The experiments of Haas and Sturtevant (1987) created a good foundation for studying vorticity generation by shock interactions with discrete density fluctuations in a fluid as they have used non-reactive gases. In their research, they used air as the ambient gas while the bubble contained a mixture of air and one of helium or Freon-22. Their research also investigated geometrical impacts utilising cylindrical or spherical-shaped bubbles. For the axisymmetric spherical bubble geometry, they detected the appearance of a vortex ring with Markstein (1957a, b) similarly noticing the emergence of a vortex ring but for the axisymmetric spherical flame geometry. Haas (1983) indicated that there was a previous challenge associated with the discernment of vortex structures in shadowgraphs from experimental analysis with cylindrical bubbles. Markstein (1957a, b), Haas (1984) and Haas & Sturtevant (1987) also examined the linearized impulsive Rayleigh-Taylor instability theory (Richtmyer, 1960) for the purpose of inspecting the flame or bubble behaviour post shock propagation. Following from this,

Haas and Sturtevant (1987) used more advanced models credited to Rudinger & Somers (1960) and Taylor (1953), as the first model group, and Maxworthy (1977) and Didden (1979) as the other model group with the second model group initially handling vortex generation using an analogy of an impulsive motion of a piston that emitted fluid from the mouth of a diminutive cylindrical chamber.

A non-linear theory for the creation of vorticity using shock wave propagation was established by Picone and Boris (1983) with Picone et al. (1985) applying this theory to the experiments conducted by Markstein (1957a, b), where a planar shock impacted a spherical flame. The resulting numerical simulations of the shock-flame interaction assumed a smoothly varying radial density distribution (Bennett profile) for the flame as shown below:

$$\rho(r) = \rho_\infty + \frac{\rho_0 - \rho_\infty}{[1 + (r/S_0)^2]^2} \tag{1.41}$$

where ρ_∞, ρ_0, r and S_0 denote the density of the surrounding air, flame centre density, distance from the flame centre, and flame boundary radius. There was a variation between the Bennett distribution and the expected steep gradient at a flame or bubble edge but the timescales and velocities in their conducted simulations matched with the experimental values. Their research, from the theory and the simulations, showed that the progression of the system is inherently nonlinear from the inception of the shock-flame/bubble interaction.

Picone and Boris (1988) based their theory on the equation that describes the progression of vorticity, ω, as given below:

$$\frac{d\omega}{dt} + \omega\nabla.v = \omega.\nabla v + \frac{\nabla\rho\ x\ \nabla P}{\rho^2} \tag{1.42}$$

where v, P and ρ represent the velocity, pressure, and mass density of the fluid. Eq. (1.42) also shows that the disparity between the local gradients for pressure and density would result to the non-zero source term, for the creation of vorticity, given below:

$$S = \frac{\nabla\rho\ x\ \nabla P}{\rho^2} \tag{1.43}$$

Picone and Boris (1988) then went on to explain the mechanism that involves the propagation of a planar shock wave across a gas as well as the impact of such shock wave on a bubble with a circular geometry assuming that the bubble has a constant density varying from the ambient air/gas density. Their research revealed that the interaction leads to a transmitted shock through the inside of the bubble with a part of the incident shock diffracting around the edge of the bubble. They also showed that there existed a difference in the timing of the impacts for the various parts of incident shock at different parts of the bubble solely attributable to the curved surface of the bubble. This meant that the refracted shock within the bubble interior will be curved. There was also going to be a distinction between the travel speed of the refracted (interior) shock and the diffracted (exterior) shock due to the variation between the bubble density and the density of the ambient gas.

Haas and Sturtevant (1987) used ray tracing and geometric acoustics to create a valid picture of the qualitative characteristics of the physical process described by Picone and Borris (1988). Picone and Borris (1988) also provided a very valid picture of this interaction when they defined the x-axis as a line parallel to the direction of incident shock travel and passed through the centre of the circular cross-section of the bubble. Their illustration also explained that as the incident shock reached the bubble, the pressure and density gradient of the shock and bubble respectively at the contact point corresponded with the x-axis. From Eqs (1.42) and (1.43) above, it is clear that little or no vorticity will be created at this point. However, as the interaction evolves, the diffracted incident shock and the refracted interior shock will have pressure gradients misaligned with the bubble density gradient with the bubble's density gradient appearing radially away from the centre of the bubble. At this point, the vorticity source term (Eq. (1.43)) is significant and as a result,

substantial vorticity is created at the edge of the bubble, where the density gradient is no longer zero. There is another shift in the physics of this process as the diffracted and refracted shocks arrive the bubble downstream side. Here, the pressure gradients of the shocks and the density gradient of the bubbles again almost match with the source term again becoming insignificant at the point of the bubble's intersection with the x-axis. There also exists a perpendicularity of the vorticity vector to the plane defined by the circular geometry of the bubble. The sign of the vorticity created along the bubble edge in this plane is opposite on the reverse sides of the x-axis. This further explains how the rotational motion induced by the significant vorticity alters the bubble and circulation of vorticity. As the interaction progresses, the distribution of vorticity rolls up into one of two vortex structures depending on the preliminary symmetry/shape of the bubble i.e., a cylindrical bubble will roll into a pair of vortex filaments while a spherical bubble will roll into a vortex ring.

Picone and Borris (1988) further defined the vortex strength along the x-axis stating that for a system which varied only in the (x-y)-plane, the vortex strength in the location, $y \geq 0$, covering the top half of the bubble solves Eq. (1.44) below:

$$\frac{dx}{dt} = \int_{A(t)} \frac{\nabla\rho \times \nabla P}{\rho^2} dA(t) \tag{1.44}$$

Eq. (1.44) was gotten by integrating Eq. (1.42) in a Lagrangian manner over the area A(t) which covers the upper half of the bubble and translates with the bubble. The vortex strength (also called circulation, *k*) can be numerically calculated by integrating over the shock travel time across the bubble as shown below:

$$k \approx 2V_2\left(1 - \frac{V_2}{2W}\right) S_0 ln\left(\frac{\rho_\infty}{\rho_b}\right) \tag{1.45}$$

where V_2, W, S_0 , ρ_∞ , $and\ \rho_b$ represent the velocity of flow behind the shock in the laboratory frame, shock velocity, cross-sectional radius of the bubble, density of surrounding gas and bubble gas density respectively. They also did not consider the impacts of curvature and variation in the strengths of the incident, refracted and diffracted shocks while representing the shock as a planar discontinuity to perform this integration. Their work also revealed that the decrease in vortex strength compared to what is provided by Eq. (1.45) was predominantly caused by the distortion and interaction of the different shocks. Their prediction was confirmed from the estimations of the vortex strength using simulation data. Nonetheless, scaling arguments by Picone and Boris (1983) show that the functional variations and trends e.g., with V_2 and $W$are accurate. Picone and Boris (1988) stated that equation (1.45) can provide precise scaling correlations among the different parameters and is very important in comprehending both the laboratory experiments and the numerical evaluations. An experimental instance exists when analysing the speed at which the vortex structures and the bubble travel moments after SBI has ended. Very interestingly, their work showed that the propagation velocities of a vortex filament pair or a vortex ring is directly related to the vortex strength. Eq. (1.45) also reveals that the normalisation of the velocity using V_2 will reduce as the Ma rises. This is because the ratio of V_2 to W rises as Mach number rises. This has been experimentally verified by Haas and Sturtevant (1987).

The source term of the vorticity evolution equation (Eq. (1.43)) also provides the generalisation of the normal propagation of the Rayleigh-Taylor instability to a whole possible range of space scales, timescales and geometry of perturbation (Picone et al., 1985). Picone and Boris (1988) explained that the conventional Rayleigh-Taylor instability theory starts with an infinitesimal spatial perturbation which occurs for an unlimited period with respect to the perturbation growth rate. Picone and Boris (1988) considered a finite perturbation scenario in form of the gas bubble as well as a finite period over which the shock wave propagates through the bubble thus creating vorticity. They discovered that this finite perturbation in form of a bubble yields a different outcome attributable to the behaviour of the perturbation which is not sinusoidal. This created a deviation from the impulsive Rayleigh-Taylor or Richtmyer-Meshkov instability exhibited during the

translation of a planar shock across a rippled interface or propagation of a perturbed shock through a planar interface which would previously reveal a linear growth (Richtmyer, 1960; Meshkov, 1970). Conversely, Picone and Boris' (1988) work revealed that SBI associated with the consequent development of the flow-field represented a nonlinear process from the onset as initially explained. However, there has been contentions that the linear theory would fit the shock bubble challenge by representing the bubble side facing the propagating shock as a component of a sinusoidal density discontinuity with a wavelength equivalent to $2\pi R$ where R represents the bubble radius. However, these arguments have been clearly countered by the experimental works of Haas and Sturtevant (1987) and the numerical computations of Picone and Boris (1988) where they showed that the subsequent deformation of the upstream edge of the bubble by the vorticity field has an evident wavelength expressed approximately as $^{4}/_{3}\,R$. These two ideas thus create an ambiguity related with the choice of wavelength for the linear theory, but the linear theory has generally provided valuable understanding (Markstein,1957a, b; Haas & Sturtevant, 1987**)** with Haas and Sturtevant (1987) discussing the relationship between the linear theory and experiment in detail as well as detailed pros and cons of the theory.

Haas and Sturtevant also discussed two further models associated with the production of vortex and linked them to the numerical simulations of Picone and Boris (1988). The first as purported by Rudinger and Somers (1960) defines the vortex formation process as an acceleration of the gas bubble during the initial transients and conversion into a vortex ring closely matched by Taylor's (1953) 'dissolved' vortex-generating disk. The second model represents Haas and Sturtevant's revision of Kulkarny's (see Haas and Sturtevant, p. 72), Maxworthy's (1977), and Didden's (1979) illustration of vortex-ring formation by impulsive fluid flow through a tube's mouth. These interesting adaptations led to Haas and Sturtevant's (1987) treatment of the air jet observed in the two helium cases as a vorticity generating piston. However, Picone and Boris (1988) have since stated that both models do not sufficiently describe the real physical process as seen from the dynamics of vorticity generation which their simulations showed. Their work also revealed that the principal focus should be at the bubble's edge where the vorticity is situated from the time of interaction between the incident shock and the bubble. Also, their simulation showed a subsequent interaction of the vorticity with the surrounding fluid, to create a jet, and with itself across the fluid medium to yield filaments or a ring. Lamb (1945) and Picone & Boris (1988) clarified the meaning of 'vortex filament' to represent a fluid within the vortex tube with a finite cross-section different from a vortex line. Within a two-dimensional (x, y) Cartesian system, a finite vortex would typify a vortex filament's cross-section whose axis is a straight line perpendicular to the (x, y) plane. Based on these invaluable findings, Picone and Boris (1988) summarized that the bubble's spontaneously produced movement across the surrounding gas did not by itself create the vorticity and that the jet was a sign/result of the produced vorticity as opposed to initiating it.

1.5.2. Description of wave effects and acoustic wave processes

During shock interaction with a spherical or cylindrical volume of gas of varying density and/or speed of sound, it is useful that reflection, refraction, diffraction and focusing of waves be closely investigated (Haas and Sturtevant, 1987). Several authors (e.g., Jahn, 1956; Abd-el-Fattah et al. 1976; Abd-el-Fattah and Henderson 1978a, b; Catherasoo & Sturtevant, 1983) have investigated shock waves refraction at gas interfaces. Depending on the shock wave incidence angle at the interface as well as on the shock strength, the refraction can be regular i.e., intersection of the incident, reflected and refracted waves at the same point on the interface, or irregular i.e., an intersection of the refracted shock with the interface in front of the incident shock. For the slow-fast case i.e., light bubble case (where the gas ahead of the interface has a greater speed of sound than the gas behind the interface), the transmitted wave can travel in front of the initial disruption in the heavier material resulting in a precursor configuration. Shock refraction from a cylindrical or spherical interface includes the complete range of incidence angles and by implication all refraction

categories. With respect to the plane refraction challenge and its associated difficulty, it is no wonder that minimal consideration has been given to plane shock waves interaction with curved gas interfaces. Similarly, Markstein (1957a, b) and Rudinger (1958) investigated shock waves interaction with curved flame fronts thus considering the curved slow-fast case from where they recognised precursors and lateral shocks related with the irregular refraction phenomenon. The works of Pierce (1981) and Friedlander (1958) present a useful foundation for studying the deformation of weak shocks by fluid inhomogeneities (which function as lenses). They provided a robust literature on the refraction, reflection, and diffraction of waves with extremely small amplitudes. There are also close comparisons in the nonlinear case from seldom observed effects like tunnelling or glory (see Jones, 1978; Marston and Kingsbury, 1981; Marston and Langley, 1983). Typical areas where considerable research has been performed include; Ultrasonics field where characteristics of cylindrical and spherical sonar targets has been investigated; identification of transmitted waves geometry in the liquid-filled cylinders' scenario (Brill and Überall, 1970) and in the metal cylinders' scenario (Neubauer & Dragonette, 1970); identification of reflected waves geometry (Folds 1971); configuration of the internal refracted and reflected waves noticed in the scenario of mechanical impact of the liquid-filled cylinder containers (Bockhoff and Rauch, 1973); and the documentation of the comparable occurrences of light wave interaction with spherical particles (Van de Hulst 1957).

Haas and Sturtevant (1987) acoustically described the wave processes involving the exhibition and classification of wavefronts, to a first approximation, produced by the weak plane shock interaction with a cylindrical or spherical inhomogeneity. They then explained that the experiment function where finite-amplitude wave exists is to explain the impacts of nonlinear motion and volume distortion. They then explained that the impact of the perturbing gas is analogous to an acoustic lens with index of refraction given as:

$$n = \frac{a_1}{a_2} \tag{1.46}$$

where a_1 and a_2 represent the speed of sound in the external air and the speed of sound in the bubble gas while the rays of the acoustic wavesfronts are straight lines in the regions of the constant speed of sound. The rays also refract at the boundaries of these constant sound speed regions following Snell's law as given below:

$$sin\theta_i = nsin\theta_r \tag{1.47}$$

where θ_i denotes the incident ray angle and θ_r represents the refracted ray angle. There exists a rays' reflection at the boundaries ensuring that the reflection angle is same as the incidence angle.

Haas and Sturtevant (1987) showed the rays resulting from the incident wave interaction with the top half of the volume as shown in Figs.1.11 and 1.12.

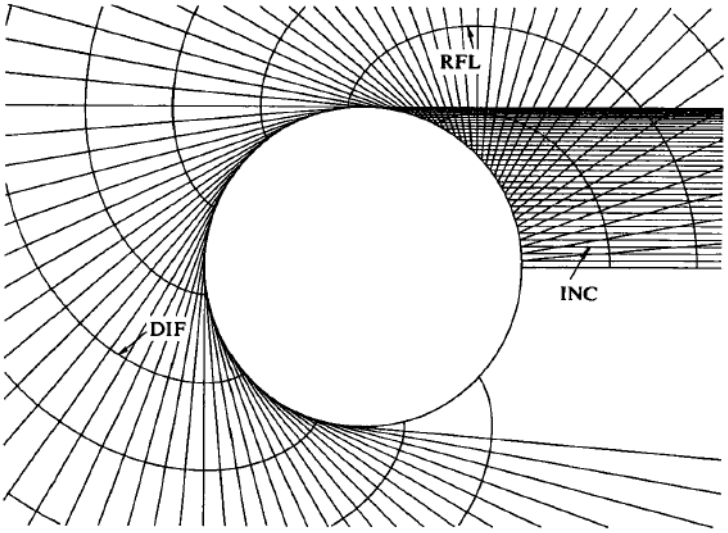

Figure 1.11: External reflected and diffracted rays and wavefronts; where INC denotes incident ray; RFL represents reflected and DIF represents diffracted (Haas and Sturtevant, 1987).

As shown in Fig. 1.11, the incident wave is illustrated by a group of parallel lines incident from the right up to the circular boundary at incidence angles rising at intervals of 5 degrees. For Fig. 1.12, the intervals are 1 degree apart. The wavefront spacing is selected to correspond to a time step of 40 microseconds for an interaction of shock waves with a 50-millimetre diameter cylinder. For Fig. 1.12, the time intervals are 20 microseconds. Fig. 1.11 shows the externally reflected and diffracted rays as well as wavefronts.

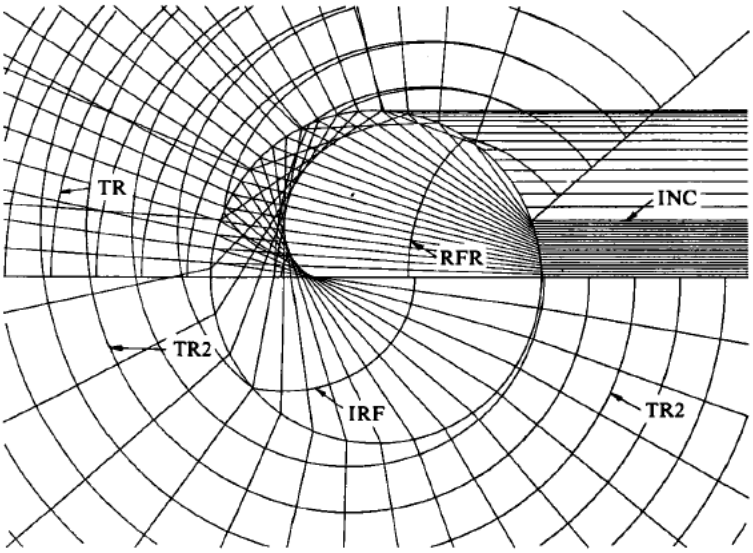

Figure 1.12: Rays and wavefronts typical of the divergent scenario; RFR, IRF, TR and TR2 represent the refracted, internally reflected, transmitted and secondary transmitted waves respectively (Haas and Sturtevant, 1987).

Based on the geometrical theory of diffraction (Keller, 1955; 1958), the diffracted wave into the shadow region arises from a curved diffracted ray on the boundary which delivers straight diffracted rays tangentially into the shadow region. The amplitude of the surface diffracted wave is previously a proportion of the amplitude of the incident wave. This depends on the material characteristics and problem geometry. The surface diffracted wave amplitude also exponentially drops as it travels

across the surface. The tangentially shed diffracted wave has an amplitude which is also some fraction of the amplitude of the local surface wave.

1.5.3. Representation of the shocked interface system

Fig. 1.13 below describes the five various regions of the shocked interface system. Regions 1, 2, $1'$, $2'$ and $1''$ correspond to the unshocked surrounding gas, unshocked bubble gas, shocked surrounding gas, shocked bubble gas after the propagation of the transmitted shock and shocked surrounding gas after the propagation of the initial shock and the reflected shock or rarefaction wave. The flow variables for each region are separated using subscripts 1 for the ambient fluid and subscript 2 for the fluid in the bubble while single quotations are used to represent the number of shock or rarefaction waves that have travelled across the fluid. Following from this, p_1 represents the pressure of surrounding gas before SBI, p_2 represents the pressure of the fluids in the bubble before SBI while p_1' and p_2' denote the pressures after the first shock travel.

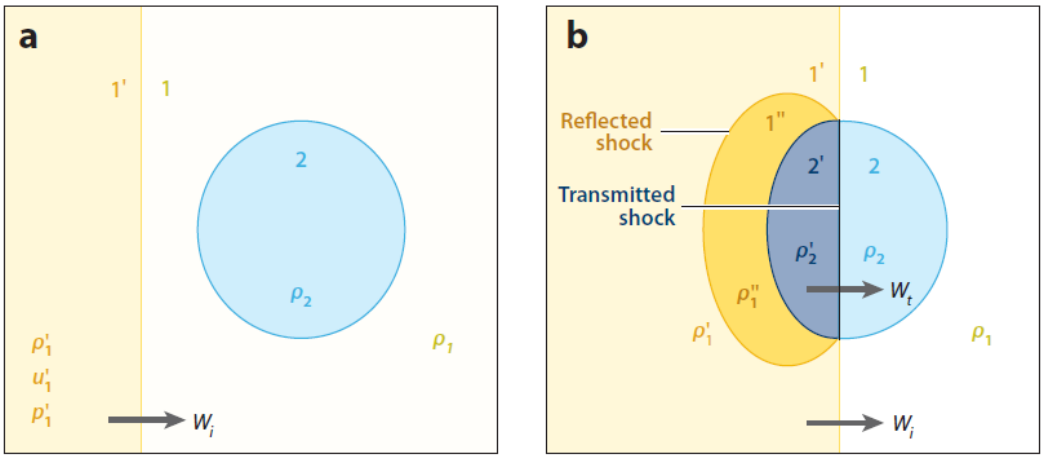

Figure 1.13: Diagrammatic representation of shocked interface system for SBI; (a) before shock interaction with bubble, and (b) during and after shock interaction with bubble (Ranjan et al., 2011).

1.5.4. First aspect of shock bubble interaction: shock compression and acceleration

Shock propagation across a bubble results in bubble compression and an accelerated jump in fundamental thermodynamic properties like pressure, temperature and density. Based on this, these properties together with the translational velocity must also rise in accordance with the Rankine-Hugonoit conditions because the transmitted shock waves travel through the bubble.

Ranjan et al. (2011) assumed an adiabatic flow through the shock wave without any heat addition or removal at the boundary and derived the rise in the fundamental variables from the equations for conservation of mass, momentum and energy. Along the shock-wave reference frame, the shock relations are given as:

$$\rho W = \rho'(W - u') \tag{1.48}$$

$$p + \rho W^2 = p' + \rho'(W - u')^2 \tag{1.49}$$

$$h + \frac{W^2}{2} = h' + \frac{(W - u')^2}{2} \tag{1.50}$$

Eqs. (1.48), (1.49) and (1.50) represent the Continuity, Momentum and Energy equations with respect to the normal shock relations where, W, u', h and h' represent the velocity of the shock

wave, velocity of fluid behind the shock wave, enthalpy of the fluid infront of the shock wave and enthalpy of the fluid behind the shock wave respectively. For a calorically perfect gas with a defined specific heat ratio, γ, the thermodynamic relations can thus be summed up as shown below:

$$p = \rho RT \tag{1.51}$$

$$h = \frac{\gamma RT}{(\gamma - 1)} \tag{1.52}$$

where R denotes the specific gas constant. Eqs. (1.48) to (1.52) have five variables; $\rho', u', p', h' \; and \; T'$; which are unknown and must be solved algebraically to derive the shocked state variables applicable for the motion of a normal shock wave across a gaseous interface (Liepmann and Roshko, 1957; Anderson, 2003). T' denotes the temperature after the first shock travel.

1.5.5. Second aspect of shock bubble interaction: nonlinear acoustic impacts

The next phase of SBI involves nonlinear acoustic impacts which deals with refraction, reflection and diffraction of the incident shock wave by the bubble. This process also involves a subsequent change in the shape and motion configuration of the shock wave by the bubble. This is attributable to interface curvature and disparity of the acoustic impedance, R, (defined as the product of the gas density, ρ, and speed of sound, c, in the medium) at the interface (Ranjan et al., 2011). This acoustic impedance disparity makes the bubble behave as a diverging or converging lens (Dimotakis and Samtaney, 2006). A useful explanation to this is obtained from a brief description of acoustic impedance as a; thermodynamic property unusual to the medium of propagation as well as being a measure of a material's stiffness as it is a proportionality constant between impressed velocity and applied pressure. It is different from the normal elastic moduli and is derived as ρc^2 (Thompson, 1984). A variation of acoustic impedance between two media is termed as impedance mismatch and can be represented as:

$$\delta R = R_2 - R_1 \tag{1.53}$$

$$\delta R = \rho_2 c_2 - \rho_1 c_1; \quad (R = \rho c) \tag{1.54}$$

Shock passage over the bubble surface can be investigated conveniently using a 1D method by neglecting the bubble interface's curvature (Ranjan et al., 2011). Shock wave transmission and reflection in a gas slab (chosen as fluid 2, see Ranjan et al. (2011)) has been shown in Fig. 1.14.

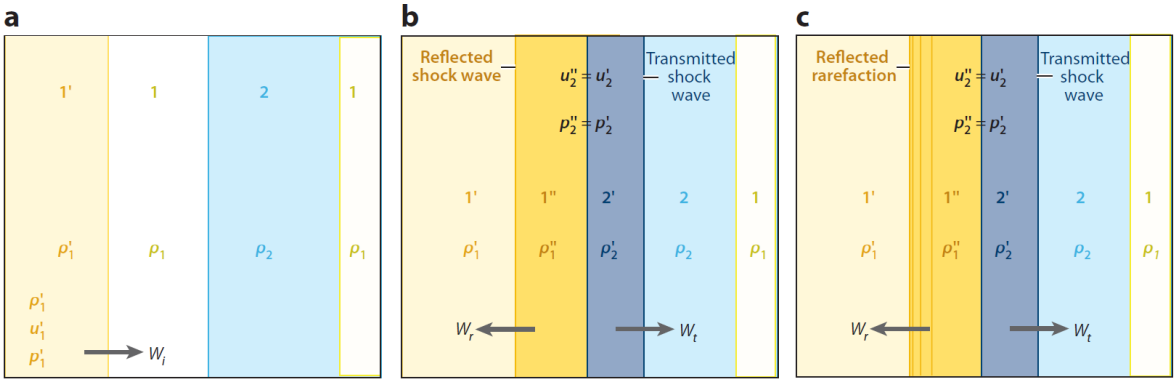

Figure 1.14: Diagrammatic representation of 1D shock-wave transmission and reflection in a gas slab (a) before shock interaction (b) after shock interaction with $\rho_2 c_2 > \rho_1 c_1$, and (c) after shock interaction with $\rho_2 c_2 < \rho_1 c_1$ (Ranjan et al., 2011).

Following from Fig. 1.14, two dissimilar after shock cases are investigated based on the sign of the impedance mismatch term (δR) at the interface. For the case where $\delta R > 0$, there is reduction in the shock wave speed after propagation followed by a contraction of the initial gas in order to

maintain mechanical equilibrium at the interface which implies that the reflected wave is a shock wave (see Fig. 1.14 (b)). On the flip side, $\delta R < 0$ implies that there is a rise in the shock speed after propagation followed by an expansion of the initial gas in order to maintain mechanical equilibrium at the interface which implies that the reflected gas is a rarefaction wave (see Fig. 1.14 (c)). The wave diagram for both scenarios is shown in Fig. 1.15.

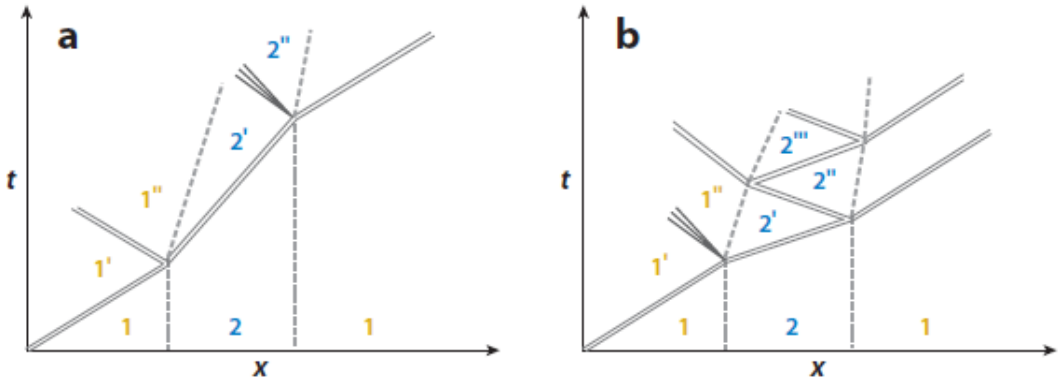

Figure 1.15: Representation of 1D shock propagation and reflection in gas slab (a) after shock interaction with $\rho_2 c_2 > \rho_1 c_1$ and (b) after shock interaction with $\rho_2 c_2 < \rho_1 c_1$ (Niederhaus 2007; Ranjan et al., 2011).

From Fig. 1.15, the solid double lines, dashed lines and triple diverging solid lines represent shock waves, fluid interfaces and rarefaction waves respectively (Niederhaus 2007). For the two scenarios described, it is useful to understand that the transmitted shock is permanently independent of the impedance of the medium as well as the interface's shape. Ranjan et al. (2011) then explained that shock travel across a bubble can be thought of as an extension of the gas-slab challenge. Ranjan et al. (2011) considered the case where the gas slab is a cylindrical or spherical bubble. Just as Niederhaus at al. (2008) had used the sign of the A to determine the configuration of the shock refraction pattern, Ranjan et al. (2007) explained the impacts of the bubble interface curvature on the shock refraction pattern for the previously discussed impedance-mismatch cases. For the case where $\rho_2 c_2 > \rho_1 c_1$, the transmitted shock wave is concave in shape and runs behind the exterior incident shock and the reflected shock is a shock wave. This case is termed the convergent geometry (see Fig. 1.16 (a)). For the case where $\rho_2 c_2 < \rho_1 c_1$, the reflected wave is a rarefaction wave. Regular refraction happens at the interface (at small angles of incidence) where the transmitted wave and incident wave meet the interface at the same point while irregular refraction patterns are observed at higher angles (Henderson 1989, Henderson et al. 1991). This case is referred to the divergent geometry (see Fig. 1.16 (b)) and the transmitted shock wave quickly travels across the bubble subsequently followed by the formation of a Mach stem, precursor shock and triple point located just outside the interface (non-existent in the convergent geometry case).

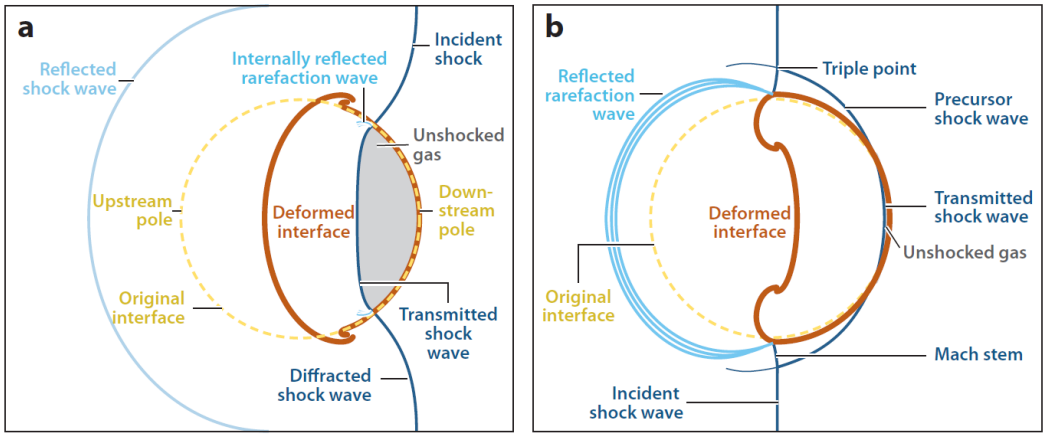

Figure 1.16: Diagrammatic representation of the flow-field for shock-bubble interaction as well as shock refraction patterns for a; (a) convergent case, $\rho_2 c_2 > \rho_1 c_1$ and (b) divergent case, $\rho_2 c_2 < \rho_1 c_1$ immediately after initial shock wave propagation with incident shock travelling from left to right (Niederhaus, 2007).

Also, for the divergent geometry case, higher density contrast i.e., density ratio in excess of 1.5 are characterised by irregular refraction of the shock wave resulting in shock focusing. There also exists a diffraction of a section of the shock wave front sweeping around the bubble periphery thus implying that the bubble is inverted facing the axis such that the discontinuous surface remains almost normal to the interface (Haas & Sturtevant 1987, Niederhaus et al. 2008). Following from this, the diffracted shock waves intersect at the downstream pole. Ranjan et al. (2011) presented an excellent depiction of shock focusing on the downstream pole of a bubble resulting from the different phases of shock refraction for the convergent geometry scenario (see Fig. (1.17)). The collision of the diffracted shock waves together with the focusing of the transmitted shock wave, generates an intense pressure jump and induces an added baroclinic vorticity deposition. Shock focusing, in turn, can lead to the production of secondary shock waves which can also result in intense deviations from the observed late time flow fields comparable to a reshock phenomenon. This is analogous to the Richtmyer-Meshkov flows in shock tubes.

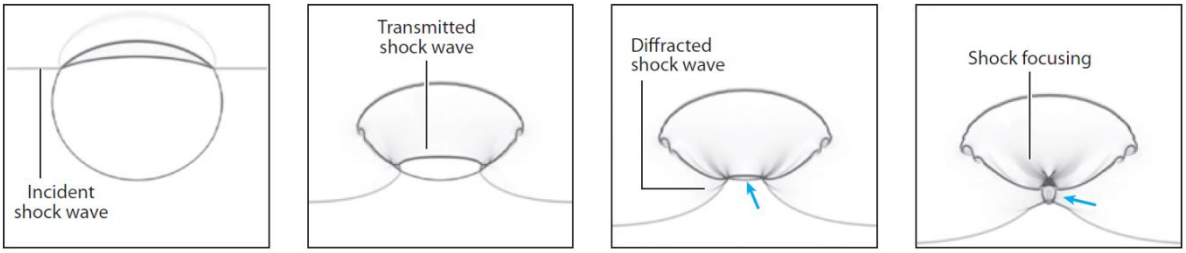

Figure 1.17: Representative, schematic view of shock focusing for the convergent geometry scenario. Incident shock motion is from top to bottom and the arrows represent position of the shock focusing (Ranjan et al., 2011).

1.5.6. Third aspect of shock bubble interaction: vorticity production and transport

The third and most essential phase of SBIs is the vorticity deposition as a result of disparity between pressure and density gradients. As the shock waves (primary incident shock wave, together with the secondary refracted, reflected, diffracted and focused waves) propagates through the bubble, vorticity is generated in the flow. Ranjan et al. (2011) therefore defined vorticity as the curl of the velocity and is given as:

$$\omega \equiv \nabla X U \tag{1.55}$$

They then replaced the curl of the momentum equation with a compressible flow and derived the vorticity transport equation given below:

$$\frac{D\omega}{Dt} = (\omega \cdot \nabla)U - \omega(\nabla \cdot U) + \frac{1}{\rho^2}(\nabla\rho\ X\ \nabla p) + v\nabla^2\omega \tag{1.56}$$

The first term on the right-hand side of Eq. (1.56), $(\omega \cdot \nabla)U$, denotes to the vortex-stretching term. This term is important particularly with respect to 3D turbulence and mixing. It also denotes the stretching as well as the turning and tilting of the vortex lines by gradients in the velocity field. The principle of conservation of angular momentum is also revealed in vortex stretching which reduces the moment of inertia of fluid elements that make up a vortex line subsequently increasing their angular speed. It is useful to understand that this vortex stretching and tilting term are non-existent in 2D flows where ω is perpendicular to the flow.

The next term on the right-hand side, $\omega(\nabla \cdot U)$, denotes the vortex dilation term which is essential just for highly compressible fluids. The last term on the right-hand side, $v\nabla^2\omega$, represents the rate of change of ω as a result of molecular diffusion of vorticity in a similar fashion to how $v\nabla^2 U$ denotes the acceleration attributable to velocity diffusion. The negligible physical viscosities of the fluids considered, in the range of 10^{-5} Pa.s, and the short timescales, in the range of 10^{-3} s, within which the evolution of flow is investigated mean that the dissipative effects can be neglected. The third term on the right-hand side, $\frac{1}{\rho^2}(\nabla\rho\ X\ \nabla p)$, represents the baroclinic term which denotes the vorticity production rate as a result of flow baroclinity. This term just shows that the disparity of the local pressure from the density gradients results in the production of vorticity in the flow field.

For a SBI scenario, ω is previously zero at all locations and as result, the vortex stretching and dilation term in Eq. (1.56) above can be ignored. This then means that dissipative effects can be ignored and Eq. (1.56) becomes:

$$\frac{D\omega}{Dt} = \frac{1}{\rho^2}(\nabla\rho\ X\ \nabla p) \tag{1.57}$$

Eq. (1.57) suggests that the baroclinicity is the only source for the generation of vorticity in the flow field when time = 0. Fig. 1.18 then shows the early time vorticity distribution:

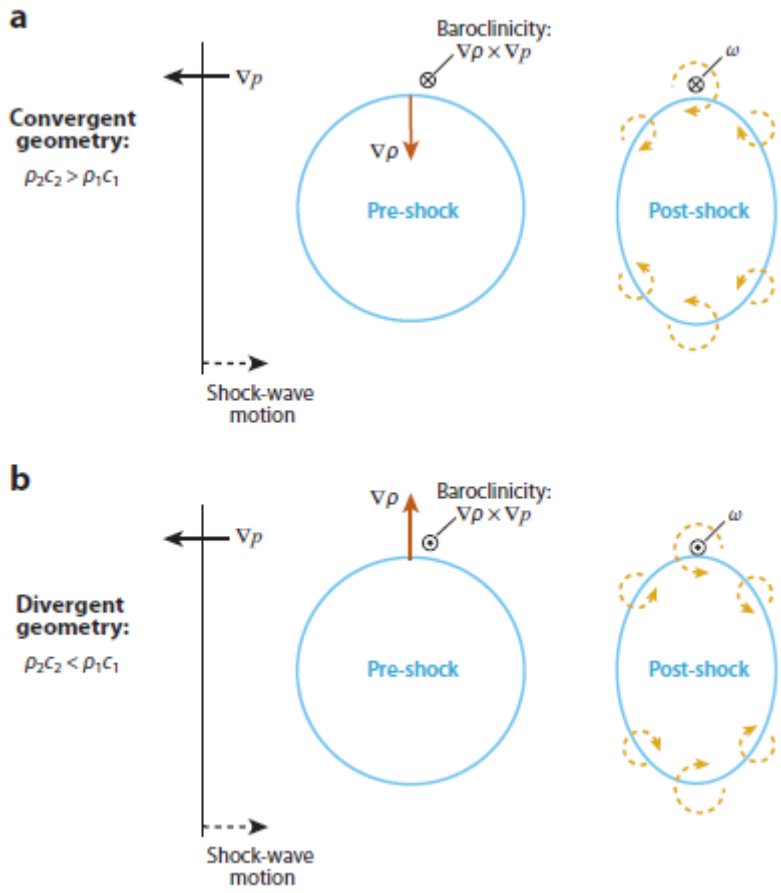

Figure 1.18: Diagrammatic representation of the configuration of vectors in baroclinic vorticity deposition during and after initial shock propagation in SBI for the; (a) convergent geometry case, $\rho_2 c_2 > \rho_1 c_1$ and (b) divergent geometry case, $\rho_2 c_2 < \rho_1 c_1$ (Ranjan et al., 2011)

During SBI, vorticity is deposited locally on the fluid interface across the bubble with the magnitude dependent on the noncollinearity of $\nabla\rho$ and ∇p. The highest misalignment occurs at the diametral plane depending on if the inhomogeneity is 2D i.e., cylindrical, or 3D i.e., spherical. The vortices' rotation is dependent on the orientation of the density gradient at the bubble interface. This is shown on Fig. 1.18 for the direction of rotation of the convergent and divergent geometry scenarios thus creating sufficient proof that these vortices are the dominant feature of the flow.

This process of vorticity production is analogous to the Richtmeyer-Meshkov instability. It is useful to understand that although the shock refraction pattern is determined by the impedance mismatch at the interface, this concept only exists in the early phase of the flow (Ranjan et al., 2011). Subsequent to numerous shock travel times, the characteristics noticed in the flow field are dominated by the vortical movement. Ranjan et al. (2011) then adopted the concept of A as in Niederhaus et al. (2008) to illustrate the impact of a variation in density at the bubble interface as opposed to the impedance mismatch. Following from this, they have then stated, for the gas pairs they chose, that $A > 0$ corresponds with the convergent geometry case ($\rho_2 c_2 > \rho_1 c_1$) and $A < 0$ denotes the divergent geometry scenario ($\rho_2 c_2 < \rho_1 c_1$). Thompson (1984) explained that there was a possibility that convergent refraction ($\rho_2 c_2 > \rho_1 c_1$) could occur even when $A < 0$ and vice versa if the impact from the specific heat ratios disrupts the density variations. From the discussed phases for SBI, it is then clear that these three fundamental processes are nonlinearly coupled together and their concurrent actions in SBI results in the generation of extremely complex sections of strong, disorderly rotating motion and mixing[4].

[4] Ranjan et al. (2011) categorised both shock-accelerated cylinders and spheres as SBIs with the cylinder representing a 2D bubble while a sphere represented a 3D bubble.

1.6. Shock/liquid bubble interaction

Liquid droplets breakup has a range of applications like rain erosion damage, combustion and detonation of multi-phase mixtures, atomization of liquid jet, atmospheric distribution of liquid agents dispersed at supersonic speeds, and heat recovery applications for geothermal waste. Droplet breakup mode can be categorized into five regimes based on the initial Weber number (We). These regimes are: vibrational, bag, bag and stamen, stripping and catastrophic breakup with the initial We range corresponding to these regimes being ≤12, 12-50, 50-100, 100-350, and >350 respectively (Pilch and Erdman, 1987; Hsiang and Faeth, 1992). Theofanous et al. (2004) went ahead to reclassify these regimes into the Rayleigh-Taylor Piercing (RTP), which happens in the range $10 < We < 10^2$, and the shear-induced entrainment (SIE), which occurs in the range $We > 10^3$. They also described a transition phase which exists in the range $10^2 < We < 10^3$. There has been several opinions which have been fused into the previously described classifications i.e., some classical works (e.g., Engel, 1958; Ranger and Nicholls, 1969; Simpkins and Bales, 1972; Waldman et al., 1972; Harper et al., 1972) as well as some past and more current studies (e.g., Pilch and Erdman, 1987; Wierzba and Takayama, 1988; Hsiang and Faeth, 1992; Hsiang and Faeth, 1995; Chou and Faeth, 1998; Joseph et al., 1999; Dai and Faeth, 2001; Theofanous et al., 2004; Theofanous and Li, 2008).

Thefanous et al. (2004) explained that when a liquid bubble is subjected to a gas flow, it becomes distorted and disintegrates into a 'cloud' of tinier droplets at rates and sizes dependent mainly on the We given below:

$$We = \frac{\rho U^2 D}{\sigma} \tag{1.58}$$

where ρ, U, D, and σ denote the gas density, initial relative velocity between the gas and bubble, initial liquid bubble diameter, and the bubble surface tension respectively. This process of distortion and fragmentation consists of several detailed features with Hinze (1955) explaining that a We greater than a critical value of approximately 10 is required for instability (also see Theofanous et al., 2004). The different regimes and respective studies that created their definitions is given in Fig. 1.19. Related to We is the Reynolds number (Re) which is very important for liquid bubble breakup. Both dimensionless numbers are represented by the ratio of the inertial (aerodynamic) force to either the capillary (surface tension) force i.e., We or the viscous force i.e., Re.

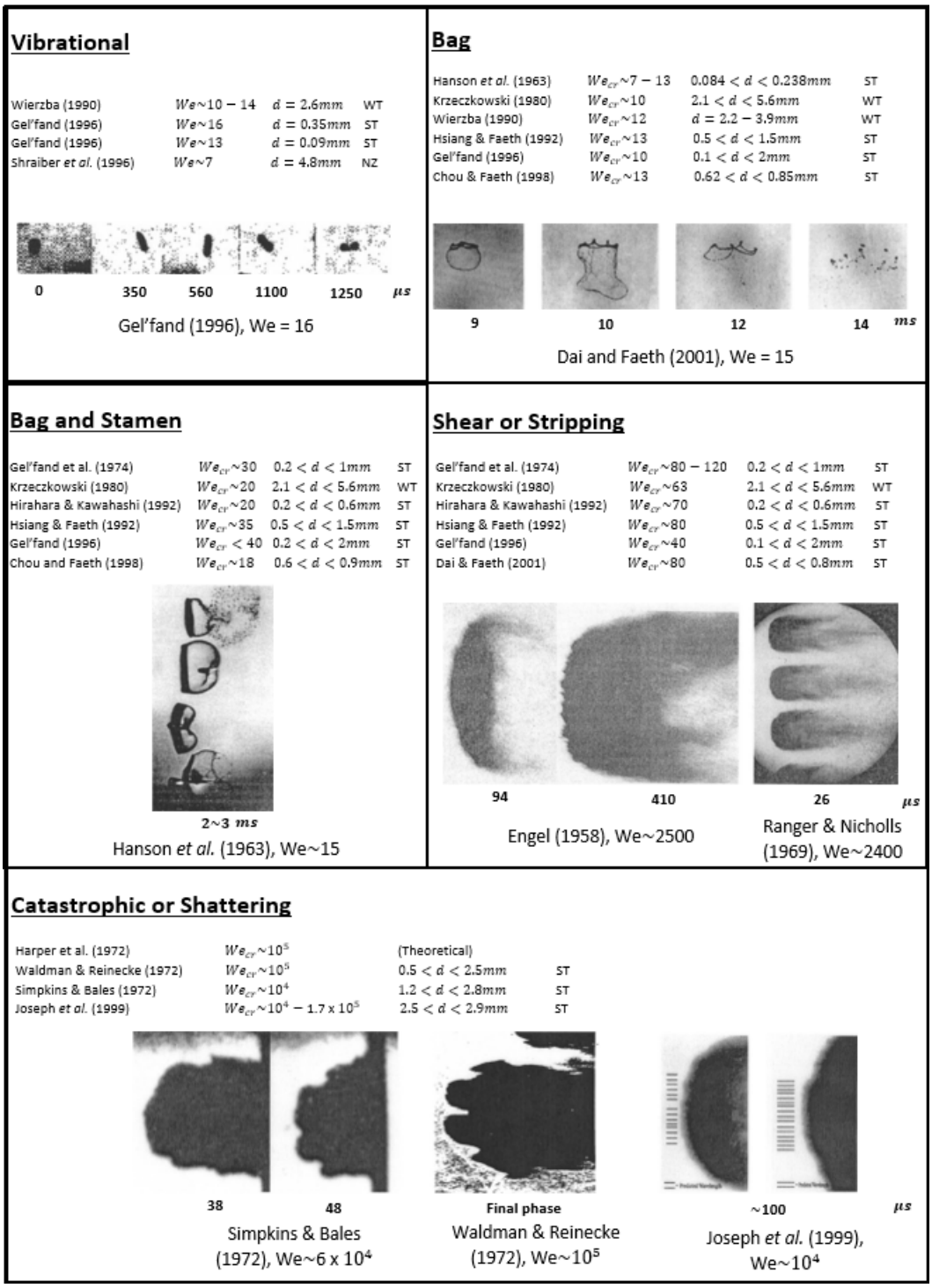

Figure 1.19: Breakup regimes obtained at or near atmospheric conditions. All experiments were carried out at subsonic or mildly supersonic flow conditions. ST - shock tube, WT - Wind tunnel, NZ – Nozzle (Theofanous et al., 2004).

Pilch and Erdman (1987) explained that when the relative velocity between the bubble and the flow field i.e., gas, is considerable, there is a production of mist on the windward (upstream) interface of the bubble. This mist is transferred into the bubble's wake and totally eclipses the bubble in experimental shadowgraphs as it is observed as a dark shadow. Thus, Pilch and Erdman (1987) explained that breakup time and deformation data derived from shadowgraphs can be misleading as this mist makes the bubble appear bigger than it is. Previously, derived data have not been shown in

a coherent way. Following from this, several independent variables have been employed to analyze breakup and bubble deformation properties like breakup times. These include: We, Bond number (Bo), Reynolds number (Re), free stream velocity, dynamic pressure, shock Mach number and pressure ratio. Several past and current works have used We as it represents the ratio of unsettling hydrodynamic forces (shown as the numerator of Eq. (1.58)) and the steadying surface tension force (shown as denominator of Eq. (1.58)). Viscous effects on bubble breakup are associated with the Ohnesorge number (On) shown below:

$$On = \frac{\mu_d}{(\rho_d D\sigma)^{1/2}} \tag{1.59}$$

where μ_d and ρ_d denote the bubble dynamic viscosity and density respectively. As On considers only bubble characteristics, Pilch and Erdman (1987) explained that there is then an applied assumption that the continuous fluid i.e., gas is insignificant in comparison to the bubble viscosity. A dimensionless time property of bubble breakup by Rayleigh-Taylor or Kelvin-Helmhotlz instabilities is given below as:

$$t = T\frac{U\ \in^{1/2}}{D} \tag{1.60}$$

where T and $\in$ correspond to the dimensional time and flow field/drop density ratio respectively. $\in$ can be expressed as:

$$\in = \frac{\rho}{\rho_d} \tag{1.61}$$

1.6.1. Qualitative explanation of breakup mechanisms

Several past researchers have been unsuccessful at making a clear distinction between the different liquid bubble breakup mechanisms (Pilch and Erdman, 1987). There are five different mechanisms of liquid breakup based on the initial We. These mechanisms are listed below and represented pictorially in Fig. 1.20.

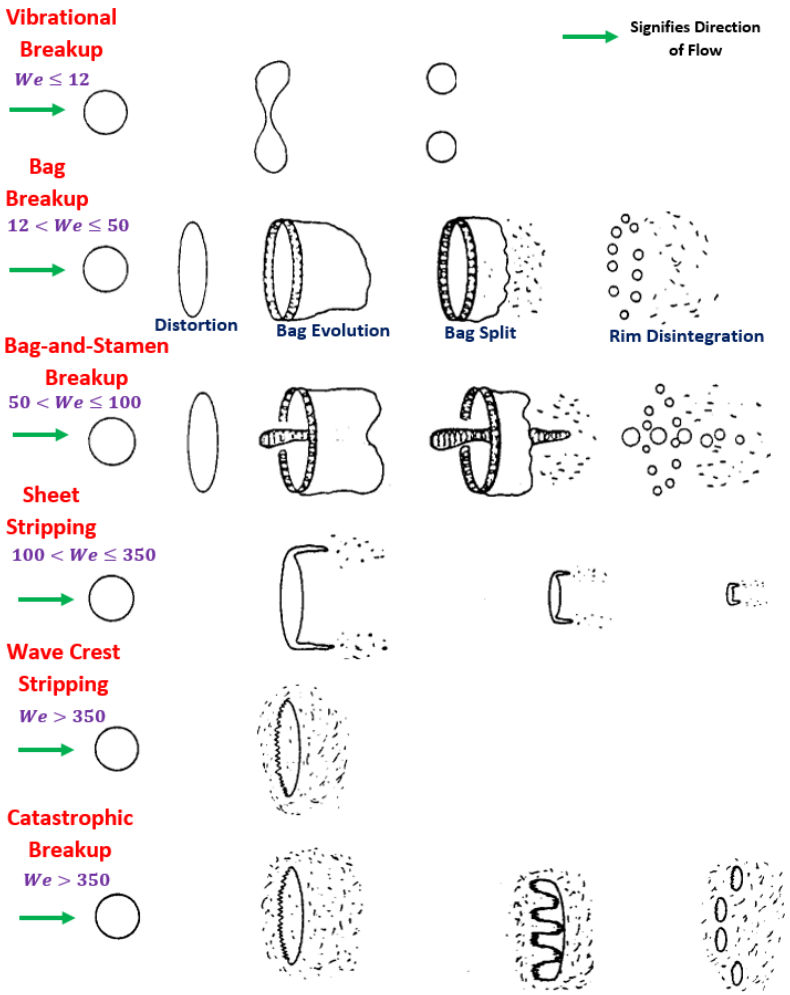

Figure 1.20: Breakup mechanisms (Pilch and Erdman, 1987).

Vibrational breakup happens when the We is small i.e., $We \leq 12$ and is characterized by oscillations which evolve at the natural frequency of the bubble. Under certain conditions, the flow field interacts with the drop in a manner that leads to an increase in the oscillation amplitude. This leads to the decomposition of the bubble into a few large fragments. Pilch and Erdman (1987) clarified that this type of breakup mechanism does not automatically take place in all instances and the overall breakup time is extended in comparison to the other breakup mechanisms.

Bag breakup is similar to the rupturing of soap bubbles from a soap film connected to a ring. Pilch and Erdman (1987) likened this breakup mechanism to a thin hollow bag that is 'blown' downstream while connected to a more massive toroidal rim after which the bag eventually ruptures. This creates several small fragments. This is followed by the disintegration of the rim after a brief period generating a small amount of large fragments. This mechanism occurs in the range: $12 < We \leq 50$.

Bag-and-Stamen breakup represents a transition mechanism which possesses many characteristics similar to the bag breakup and takes place in the range: $50 < We \leq 100$. A thin bag is driven downstream while being attached to a massive toroidal rim as in the Bag breakup mechanism. A column of liquid or stamen is then produced along the bubble's axis parallel to the oncoming flow. The bag then ruptures before rim and stamen fragmentation takes place.

Sheet stripping, unlike the Bag & Bag and Stamen breakup mechanisms where bags are produced, involves the constant withdrawal of a thin sheet from the edge/interface of the distorting bubble at We in the range: $100 < We \leq 350$. This is followed by the disintegration of the sheet at a small

distance in the downstream direction from the bubble. Pilch and Erdman (1987) explained that a 'coherent residual' bubble exists throughout the whole breakup process.

At higher We i.e., $We > 350$, large-amplitude and small wavelength waves are produced on the upstream interface of the bubble with the wave crests continuously eroded by the flowfield i.e., gas flow over the bubble surface. This creates the wave crest stripping breakup mechanism.

For the Catastrophic breakup mechanism, large amplitude, long wavelength waves finally pierce the bubble producing many large fragments before wave crest stripping can significantly decrease the mass of the bubble. This breakup mechanism causes fragments as well as fragments of these fragments to be exposed to more breakup. Pilch and Erdman (1987) explained that this process continues until all the fragments have We less than the critical value.

As presented above, Pilch & Erdman (1987) provided an excellent summary and synthesis on bubble breakup. Gel'fand (1996) also provided a comprehensively significant assessment of the subject. Hsiang & Faeth (1992), Chou & Faeth (1998) and Dai & Faeth (2001) performed comprehensive experiments that focused on a lower We range i.e., approximately between 10 and 10^2 while Joseph et al. (1999; 2002) conducted experiments that focused on the higher We range i.e., approximately between 10^4 and 10^5). There are also classical works on the subject conducted by Engel (1958), Ranger and Nicholls (1969), Simpkins and Bales (1972), Waldman and Reinecke (1972), and theoretical findings of Harper et al. (1972). The experiments were conducted in shock tubes and at pressures close to atmospheric conditions. In a few other scenarios, wind tunnels were used. Due to the long lengths of the shock tubes, they were set horizontally which created constraints on the injection technique and the drop sizes that could be derived. On the flip side, a wind tunnel, which was operated at steady state, required that the liquid be injected via the wall boundary layer. Theofanous et al. (2004) explained that this created obstacles to data analysis and constrained the conditions available to such experiments. They then added that asides small and typically unrecorded differences, the complete regime classification scheme that emerges from all this work is summarized in Fig. 1.19.

The vibrational, bag and bag-and-stamen regimes are clearly detectable and rather well defined with respect to the critical We needed for their initiation. The Bag regime was investigated comprehensively, and it was proved that resulting droplet distribution is bimodal i.e., shattering of the bag creates one size and the capillary breakup of the bubble circumference produces larger sizes. Theofanous et al. (2004) added that no extensive theoretical interpretation of these regimes has been documented in the past. They continued by explaining that the shear or stripping regime developed from $We{\sim}10^2$ while the catastrophic or shattering regimes become the prevailing mechanism from $We{\sim}10^4$ to 10^5. They also explained that the shear or stripping regime entailed a fine mist of liquid originating from the equator seemingly as a result of a shear-induced boundary layer on the liquid surface as shown in Fig. 1.19. Taylor (1949) and Ranger & Nicholls (1969) provided a simplified viscous description of this regime without taking into consideration the interfacial instabilities and its subsequent roughness. Conversely, Harper et al. (1972) and Joseph et al. (1999) accounted for interfacial instability without considering shear. Harper et al. (1972) provided the first theoretical analysis of the catastrophic regime and considered it to entail penetration by Rayleigh-Taylor waves. More recently, Joseph et al. (1999) investigated this regime from a similar basis. Very interestingly, Harper et al. (1972) claimed that when $We{\sim}10^5$, there is a change in behavior from algebraic to exponential for the growth of instabilities while Joseph et al. (1999) claimed that the waves observed on the images in Fig. 1.19 agree with the quickly evolving Rayleigh Taylor waves for We ranging from 10^4 to $\sim 2\,x\,10^5$. Waldman & Reinecke (1972) and Simpkins & Bales (1972) quantitatively compared their experimental findings to Harper et al.'s (1972) work on the catastrophic regime.

1.7. Aims and objectives of this research

Pressure gain combustion (PGC) possesses the needed ability to hugely boost combined cycle efficiency and performance when incorporated into the combustion gas turbines. Gulen (2017) explains that the only possibility for an isentropic and steady flow process characterised by pressure gain is a supersonic flow with a standing shock wave idealised as a discontinuity in the flow field. This has then been used as an efficient basis for investigating pressure gain via the interaction of a moving shock waves with a gas or liquid bubble. The overall aim of this research is to advance our current understanding of shock-bubble-interaction with the following objectives:

- Carrying out a detailed numerical study of the interaction of a shockwave with a single spherical gas bubble to improve our understanding of the physical mechanisms of such a complex process.
- Carrying out a detailed numerical study of the interaction of shockwaves with a single cylindrical gas bubble to advance our understanding of the physical mechanisms of such a complex process.
- Carrying out a detailed numerical study of the interaction of a shockwave with a single water bubble to improve our understanding of the physical mechanisms of such a complex process.

1.8. Thesis outline

Chapter one presented the motivation for research, brief description of shock wave propagation, brief description of shock interaction with gas/liquid bubble, as well as the aims and objectives. Chapter two detailed the literature review of relevant experimental and theoretical studies. The review of experimental performance of shock gas/liquid bubble interaction helped identify suitable data sets for CFD model validation. Chapter three explained governing equations and numerical methods used in the present study. Chapter four examined shock interaction with a spherical helium bubble with in-depth analysis of results and discussion. Chapter four examined shock interaction with a cylindrical helium bubble with a thorough analysis of results and discussion. Chapter six examined shock interaction with a water bubble with comprehensive analysis of results and discussion. Chapter seven presented the conclusions and future work recommendations.

2. Literature Review

This chapter provides a comprehensive literature review on shock-gas bubble and shock-liquid bubble interactions in both two- (2D) and three-dimensional (3D) cases. Previous experimental investigations in these research fields are also presented along with the numerical methods adopted in the treatment and accurate resolution of shock-gas and shock-liquid interfaces.

2.1. Experimental investigation of shock bubble interaction (SBI)

Markstein (1957a, b) and Rudinger (1958) investigated the shock interaction with a flame front which has an almost spherical shape. Their works formed the basis for the experimental investigations of shock waves interaction with curved interfaces although their main aim of study was to evaluate the impacts of shock on the volumetric ignition rates. The interaction of pressure waves with density gradients is an underlying cause of long-lived vorticity in fluids and is particularly essential in combustion due to the emission of chemical energy which creates both pressure and density disturbances in fluids. These disturbances subsequently interact yielding a significant vorticity in the flow field. Markstein (1957b) illustrated in his classic experiments how the acceleration of an initially curved flame surface by a shock wave was succeeded by ignition intensification. His work explained that heavy distortions (like inflection and spike formation) were experienced by curved flame fronts when accelerated by a shock wave and the volumetric combustion rate was intensified after the shock flame interaction. Fig. 2.1 shows the schlieren images from one of his experiments where a weak shock propagated through a roughly spherical flame located at about 15cm from the bottom of the combustion chamber containing a stoichiometric mixture of n-butane and air.

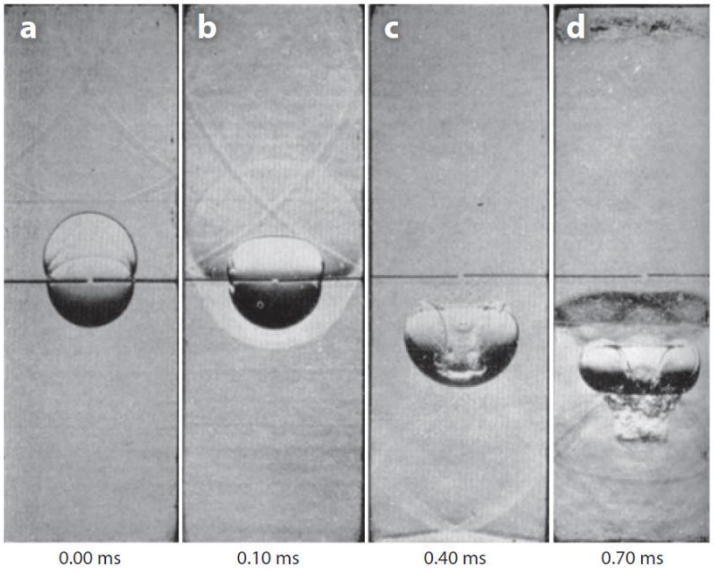

Figure 2.1: Shock interaction with a flame that was initially roughly spherical. For this experiment, the pressure ratio of incident shock wave is 1.3; and the stoichiometric butane-air mixture is burned at the middle of the combustion chamber at a time of 8.70 ms before the origin of the timescale (Markstein, 1957b; Rudinger, 1958). The times with respect to the initial shock-wave impact are: (a) 0.00 ms, (b) 0.10 ms, (c) 0.40 ms, and (d) 0.70 ms.

In Fig. 2.1(a), the distance of the shock wave from the flame boundary is less than 1cm with the flame actually appearing more oblong than spherical. In Fig. 2.1(b), the compression of the flame front as well as the upward-moving curved rarefaction wave is clearly seen. The central spike of the unburned gases crossing the lower portion of the flame front is shown in Fig. 2.1(c) thus initiating the generation of a vortex ring. This accelerated flow attributed to the vortex ring results in the production of a very-fine-grained turbulent ignition zone. Vorticity generation was also studied in a nonreactive medium to investigate the fluid dynamic dimensions of this phenomenon. A very interesting technique to boost the volumetric burning rate is discovered when a discontinuous flame contains isolated regions of ignited or unburned gas surrounded by gases with varying density noticeable in evaporating fuel droplets. Rudinger and Somers (1960) considered the reaction of such distinct pockets of varying density to impulsive acceleration without added complications to the combustion process. Following from this research, they considered a more fundamental challenge related to the interaction of a planar

shock wave with a light or heavy gas (either spherical or cylindrical inhomogeneities) generated using either a spark discharge or small jets or hydrogen, helium or SF_6. In these experiments, they found that after acceleration by a shock wave, the small spaces in the flow with varying density compared to the ambient gas propagated faster or slower than the later depending on if their density was lower or higher than the main flow. Their verifications of these impacts were attributable to the instabilities induced by the vortices which were stimulated during the shock-wave passage over the spark column. This led them to present a simple model for the relative velocity of the shocked bubble. SBI was thus obtained as the interaction of a shock wave with a cylindrical or spherical gas inhomogeneity. Their work has inspired an enormous amount of work as well as a rich database of available literature as regards SBI.

Haas and Sturtevant (1987) performed experiments in a horizontal shock tube while studying the planar shock interaction with a light or heavy gas bubble. They produced the spherical shapes using soap bubbles filled with either a light or a heavy gas while the cylindrical structures were enclosed, compressed and formed in thin nitrocellulose membranes. They used shadowgraph photography to envision and image the wave-front geometry and the distortion of the gas volume. They also compared wave patterns predicted with geometrical acoustics such as impacts of refraction, reflection and diffraction with the observed flow field. Their research also revealed that for a cylindrical or spherical volume occupied by a heavy, low sound speed gas, the wave which transverses the inside focuses only on the downstream pole of the cylinder while there is a divergence of a wave propagating through a light, high sound speed gas. The deformation of the helium cylinder surrounded by ambient air at late times revealed that shock interaction with a light gas resulted in the formation of a pair of vortices which propagates faster than the surrounding fluid. In this particular case study of helium, they discovered that the primary vortex ring splits off from the main inhomogeneity and travels along the axis of symmetry.

Jacobs (1992, 1993) discovered a novel method where a laminar jet was utilised to create the gas cylinder in a horizontal shock tube meaning that there was no requirement for encapsulation of the heavy or light gas as done by Haas and Sturtevant (1987). There was also no need for shadowgraph photography which was replaced with the planar laser-induced fluorescence (PLIF). Sulfur hexafluoride or helium, used as the experiment testing gas, was seeded with a small quantity of biacetyl while the jet of the test gas was accelerated by a planar shock wave propagating in a perpendicular direction to the jet axis and a cross-section of the flow illuminated with a laser sheet which led to the fluorescence of the biacetyl. This experiment along with the improvements from Haas and Sturtevant's (1987) work, as shown in Fig. 2.2, led to a higher quality for flow visualisation as well as enabled assessment of species concentration and shock-cylinder interaction induced mixing.

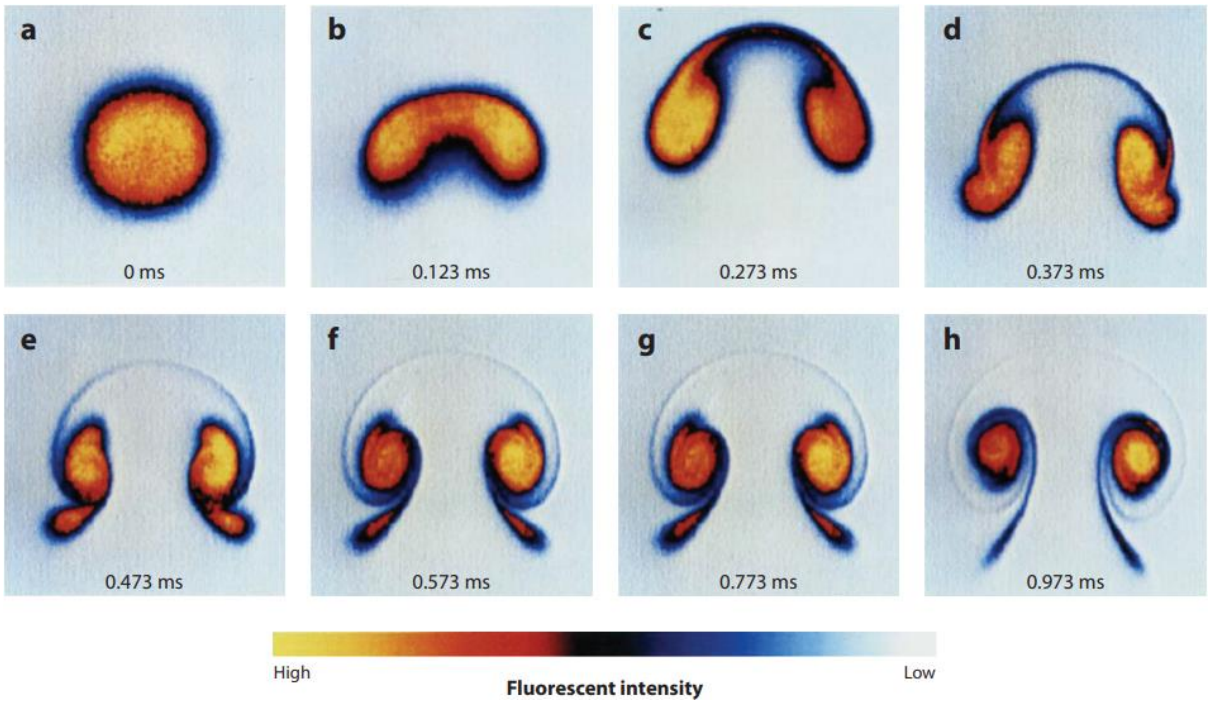

Figure 2.2: Development of flow-field from a shock interaction with a cylindrical helium inhomogeneity (Jacobs, 1992) with shock strength equivalent to Ma = 1.093. The PLIF images creates a cross-sectional view of the evolving structure showing (a) the initial jet, (b) t = 0.123 ms after propagation of the shock wave, (c) t = 0.273 ms, (d) t = 0.373 ms, (e) t = 0.473 ms, (f) t = 0.573 ms, (g) 0.773 ms, and (h) 0.973 ms.

The development of two SF_6 cylinders accelerated and impacted by a moving shock was investigated by Tomkins et al. (2003) to broaden the existing scope for the single-cylinder configuration. Here, they used the Planar Mie scattering for the flow visualization. The light scattered by the bubble gas, which were seeded with a minute amount of glycol/water fog droplets, was captured with a strengthened charge-coupled device (CCD) which was aligned normal to the laser sheet. Digital particle image velocimetry (PIV) was used to conduct velocity measurements. From the flow visualisation, they were able to show that the flow morphology is highly sensitive to the initial cylinder separation. Kumar et al. (2005) then extended the two-cylinder scenario to a three or more-cylinder system in which one of the five various systems of SF6 cylinders in ambient air was spontaneously accelerated to yield one or more pairs of interacting vortex columns. They also used PLIF in the normal plane to the cylinder's axes for flow visualisation. They discovered that the shock-influenced mixing, from an interfacial area generation viewpoint, was affected by the quantity, alignment and positioning of the gaseous cylinders. Kumar et al. (2005) had principally conducted this research to understand fluid mixing in SAIFs so as to preliminarily study material lines' stretching at early timescales which exists approximately during the first 220μs after the shock impact. These kinds of flows are characterised by a Schmidt number of nearly 1 and a Re of almost 25,000 depending on the circulation and mean kinematic viscosity. These (Schmidt and Re) ensure that these studies are possible just at early times. Yang et al. (1993) defined a specific stretching rate exponent, λ, which is given below:

$$\frac{L(t)}{L(t=0)} = Aexp\left(\frac{\lambda t}{t_0}\right) \tag{2.1}$$

From Eq. (2.1), $L(t)$ denotes the length of a marked material line at time t, $L(t=0)$ denotes the length of the interface at t = 0 i.e., the time the shock first propagates the gaseous cylindrical inhomogeneity, A represents a constant, and t_0= D/2c_1 which is the time needed for sound to transit the radius of the nozzle and is used for the time normalisation. The integral mixing width of these five configurations

were also measured revealing that the integral widths collapsed at early times and thus not an ideal measurement of the impact of the initial conditions on the flow mixing. On the flip side, λ, appeared to be a satisfactory measurement and evidently separated the different configurations in examination.

Kumar et al. (2007) experimentally and numerically investigated shock interaction with three gaseous SF_6 cylinders differentiated in the spanwise direction at a 1.5 spacing ratio. The shock strength they used is equivalent to Mach number of 1.2 and their work aimed to understand the sensitivity of subsequent flow configurations to relatively small perturbations i.e., alterations in the diffused material's structure between the gaseous cylinders, in the initial conditions where the flow is visualised using PLIF. From their research, they obtained four different postshock morphologies as a result of the perturbations in the nominally exact initial conditions as they were created by the same nozzle. Their study was then different from the two-cylinder configuration investigated by Tomkins et al. (2003) as their study revealed that the system's complexity considerably rises with the number of gaseous cylinders in the spanwise direction attributable to increased interactions of the vortices.

Jacobs et al. (1993); Budzinski et al. (1994); Baltrusaitis et al. (1996) and Prestridge et al. (2001) investigated an established issue known as the gas curtain useful for the studying and subsequent understanding of mixing induced by the Richtmyer-Meshov instability. This research is very important particularly because the gas curtain can be considered a difficult phenomenon with various, narrowly spread out, gaseous cylinders in the spanwise direction. Tomkins et al. (2008) investigated the problematic situation of fluid mixing following the interaction of a shock wave with strength Ma = 1.2 with one gaseous cylinder utilising quantitative PLIF. Fig. 2.3 shows the results from the experimental measurements of the spatial distribution of the rates of instantaneous scalar dissipation. This instantaneous scalar dissipation rates, which were gotten for the first time at various times after shock impact, is given as:

$$X(x,t) \equiv D(\nabla c.\nabla c) \tag{2.2}$$

From Eq. (2.2), D denotes the molecular diffusivity between the gases. Their analysis showed comprehensive mixing mechanisms which were not supplied by the traditional integral mixing width measurements.

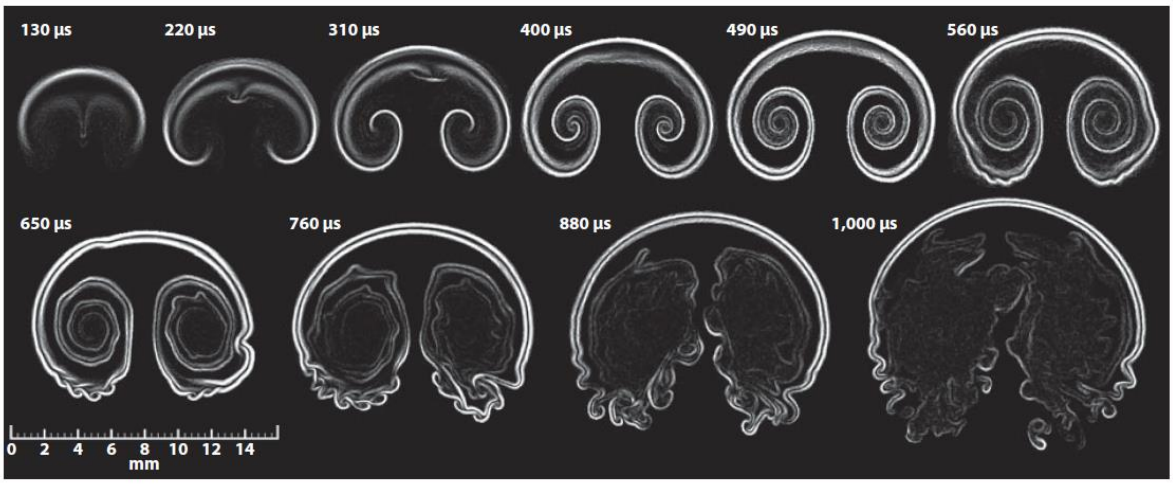

Figure 2.3: Representation of spatial maps for the mixing rate (scalar dissipation rate) of a heavy gas, $X/{c^2}_{max}$ at different timescales, t (Tomkins et al. 2008).

Tomkins et al. (2008) also detected three regions of mixing in such a flow which include the bridge connecting the two primary vortices, the vortex cores and the Kelvin-Helmholtz (KH) region. In the bridge region, mixing is linked to gradient strengthening as a result of straining velocity field. The bridge region looks like a rather smooth and non-turbulent stretch of material connecting both primary

vortices in the visualisation images and unexpectedly provides 40% to the mixing up to a late timescale of approximately 1,000 μs after shock impact. The distribution of instantaneous scalar dissipation rates reveals that the bridge i.e., the primary instability, plays a key role in supplying the highest values of these rates thus resulting in the most intense mixing in the flow. In the regions on the outer surfaces where KH rollers are observable as well as in regions near the middle of the core where secondary instabilities and spiral roll up exist i.e., the vortex cores, the mixing is influenced by large scale strain fields at early times. This is the case notwithstanding that the induced motions resulting from vorticity produce both gradient intensification and rise in surface area as a result of evolving spirals. The KH instability is located along outer regions of the flow at transitional times and a mix of Rayleigh-Taylor (RT) and KH instabilities develops in the cores. The mixing becomes primarily linked with stretching and folding of the concentration fields mainly attributable to motions influenced by the secondary instabilities.

More recently, Layes et al. (2003; 2005; 2009) experimentally investigated a planar shock interaction with a spherical gas inhomogeneity formed as a soap bubble. Their pioneering works used high-speed shadowgraph imaging to visualise the interaction of shock waves (strengths equivalent to $Ma \leq 1.25$), in air, with spherical bubbles occupied by one of krypton, nitrogen, or helium. The pioneering feature in their work is the use of high-speed rotating camera shadowgraph technique which was synchronized with a stroboscopic nanolite flash lamp. This enabled them to reconstruct the experimental history for the movement and distortion of the gaseous inhomogeneity by processing the successive frames derived throughout one experiment. They did more work to qualitatively characterise the flow progression for SBIs and revealed that for all the cases examined, the streamwise dimension of the bubble developed at a constant rate and the shocked bubble propagated at a non-changing translational speed at late timescales. Layes' (2005) dissertation as well as the research works of Giordano & Burtschell (2006) and Layes & LeMetayer (2007) showed more detailed investigation of these results and the data employed for shock strength was less than or equal to 1.68. SBIs at a higher strength (increased Mach numbers) have been studied by Ranjan et al. (2005) where they examined the scenario of a soap bubble occupied by argon. This argon-filled soap bubble is then impacted and accelerated by a shock with strength equivalent to $Ma = 2.88$. They used nitrogen as the ambient fluid through which the bubble propagated. In their study, the planar laser diagnostics were used to visualise the development of the flow-field in a region close to the bubble's midplane. In the same vein, Ranjan et al. (2007, 2008a) employed analogous diagnostic mechanism to investigate the scenario of a helium-filled bubble accelerated by a shock wave with strength equivalent to $Ma = 2.95$. Both scenarios were characterised by the shocked bubble reaching a uniform translational velocity at late times (Layes et al. 2003; 2005). Discrete secondary vortex rings were created at later times too. These findings were not noticeable in the lower Ma experiments. Fig. 2.4 shows the prolonged secondary vortex rings that had been captured using the planar laser illuminated experimental images.

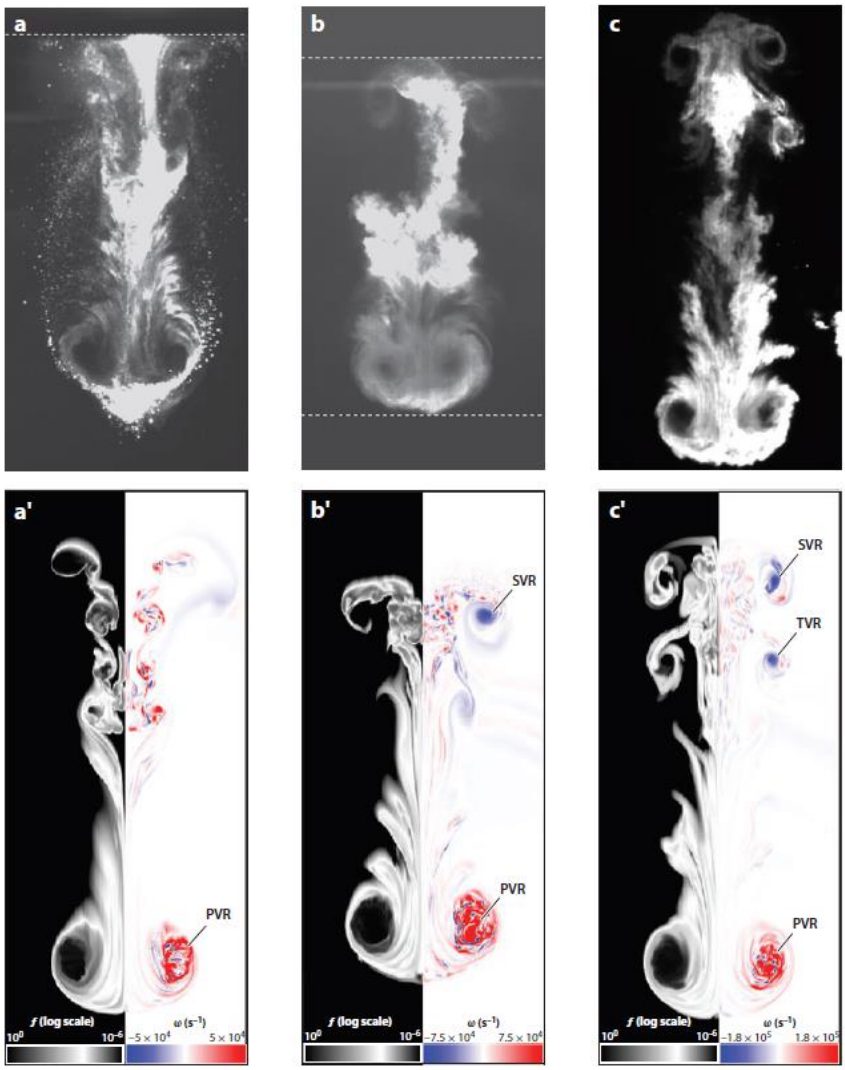

Figure 2.4: Long-lived secondary vortex rings with their counterparts as depicted using planar laser illuminated experimental images (Ranjan et al., 2005; 2007; 2008a).

The appearance of these secondary vortices is essential because they aid the elongation of the mixing region as the two counter-rotating vortex rings are more inclined to spraining apart from each other subsequently followed by a pinching off. Also, vortex rings are stable coherent structures that continue for very late times and travel downstream at an almost uniform velocity. Following from this, they expected that in SAIFs, within which strong irregular shock refraction happens in the inhomogeineities, prolonged vortex projectiles, like those previously highlighted, will appear in the flow as products of shock refraction and should continue to very late timescales after shock interaction (Ranjan, 2007).

Ding et al. (2017) carried out experimental studies on a planar shock wave interacting with 2D and 3D gas cylinders. Their research highlighted the impacts of initial interface curvature on flow morphology, wave pattern, distribution of vorticity, and interface movement. In their experiments, they utilized a wire-restriction technique based on the soap film method to generate the nitrogen cylinders with sulphur hexafluoride as the ambient gas. The 3D cylinders had either convex or concave shapes with a minimum surface characteristic. Their work showed, via a high-speed schlieren images, that not many disturbance waves exist in the flow field with the changing interfaces developing in a more symmetrical manner. Very interestingly, they showed that the shape and size of the 3D cylinders in various planes along the vertical direction altered slowly as a result of the presence of the horizontal and vertical velocities of the flow. They also explained that pressure oscillations, generated by complex

waves, in the surrounding area of the developing interfaces contributed significantly to the deformation of the 3D gas cylinders at early stages of the shock bubble interaction while as time progresses, the shocked bubble development was dominated by the baroclinic vorticity deposition on the interface. Finally, they compared their 3D with 2D results and explained that the opposite (or identically) signed principal curvatures of the concave or (convex) sulphur hexafluoride/nitrogen boundary leads to complex high-pressure zones and added vorticity deposition while the upstream interface from the symmetric slice of the concave (or convex) nitrogen cylinder travels with an inhibition (or promotion).

2.2. Laser-driven experiments

Different shock-accelerated experiments have been performed for a spherical inhomogeneity at high Ma (with values up to 10) utilising the Omega laser at the Laboratory of Laser Energetics (Robey et al., 2002; Hansen et al., 2007) as well as at the NOVA laser at the Lawrence Livermore National Laboratory (Klein et al., 2000, 2003). The Nova laser had been used by Klein et al. (2000) to produce a strong shock with Ma = 10 which moved through a small beryllium shock tube about 750microns in diameter occupied by plastic with low density. Within the plastic was a 100 microns diameter copper sphere. This research used a side-on radiography to diagnose the morphology and progression of the inhomogeneity as well as the shock path. The need for the shock tube wall materials to be made from Beryllium is based on the requirement for the X-rays to pass through a transparent material for diagnostics of the observed development. The experiments revealed the initial deformation of the copper sphere into vortex-ring structures. Klein et al. (2003) likened their past experimental results in Klein et al. (2000) to detailed 2D and 3D radiation hydrodynamic simulations. These simulations showed the initial distortion of the bubble into a vortex ring and the subsequent breakup of the vortex ring due to the azimuthal bending mode instability as previously investigated by Widnall et al. (1974).

In 2002, Robey et al. carried out a comparable set of experiments on the Omega laser. They concurrently conducted side-on and face-on radiography to restructure the 3D topology of the interaction. This ensured that they were able to visualise both the initial deformation of the copper sphere into two vortex ring structures and the onset of the azimuthal instability. Hansen et al. (2007) extended the Omega experiments by substituting the area-radiography method (adopted by Robey et al. (2002)) with a point-projection radiography system. This process ensured that the number of shock tube illuminating photons increased thus leading to an improved signal to noise ratio. This new method also ensured that the derived images allowed better estimation of the cloud mass as the time dependent variable. For the experiments, they substituted the copper sphere, used in previous experiments, with an aluminium sphere to investigate the quicker hydrodynamic development for the lighter material. This ensured that the material's deformation was examined for a lengthier time. Their experiment also revealed that the variation of cloud mass with time corresponded to a turbulent mass stripping model. This firmly indicated the essential function turbulence plays in the evolution at delayed timescales. Hansen et al. (2007) also used X-ray radiographs to reveal the 3D structure development and mass-stripping impacts as shown below:

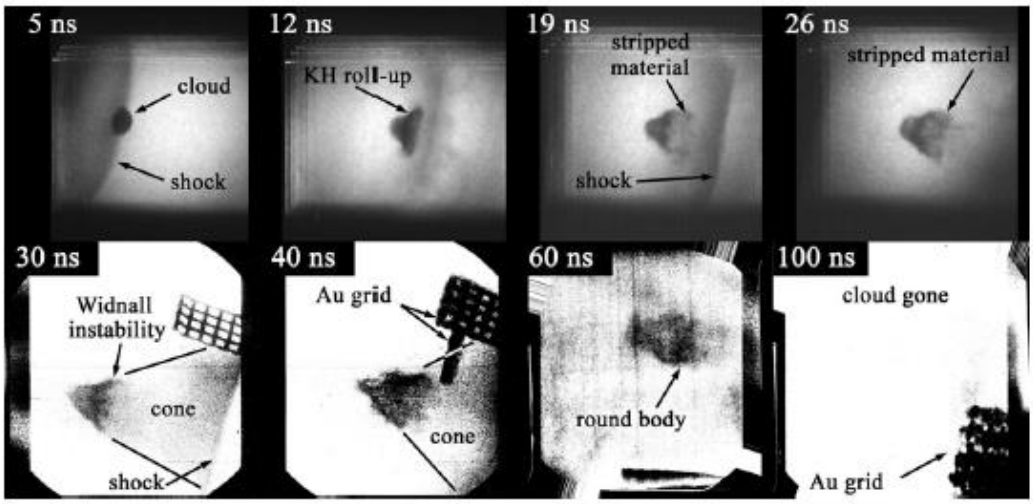

Figure 2.5: X-ray radiograph which reveals the evolution of the cloud with time after the propagation of shock waves in form of a blast wave as a rarefaction follows the shock. The direction of the shock wave travel is from left to right; perpendicular to the imaged shock particularly at times, t = 19 ns and 30 ns and in accordance with the orientation of the Au grids in the images at t= 30 ns and 40 ns. Area backlighters were used to derive the first four images while point projection radiography were used to obtain the last four images (Hansen et al., 2007).

From the Fig. 2.5, at time 5 ns as seen from the first image, the shock meets the cloud, and the left-hand side of the cloud is compressed by a factor of 4. This represents the strong shock limit for a polytropic gas with an adiabatic constant of 1.67. Following from this, the cloud suffers a classical Kelvin-Helmholtz roll-up as seen from the second image (t = 12 ns) and upwards. From here, material is stripped from the cloud and stripped material is clearly evidenced following the cloud at times greater than or equal to 19ns resulting in a cone-shaped structure which extends all the way to the shock or outside the view of the flow field (t = 40 ns). There is also a change in the direction of the ambient flow when the time nears 40 ns by the rarefaction while at time 60 ns, the right-hand side of the cloud becomes fairly round attributable to the developed reverse flow. When the time progresses to 100 ns, the cloud fades. Generally, their work, as seen from the deformation of the cloud, agreed mostly with the shock tube experiments described by Ranjan et al. (2005) with respect to the scaled lengthwise growth of the bubble.

2.3. Analytical and numerical modelling of SBI

Klein et al. (1994) created simple models for several flow field characteristics. However, typical experimental diagnostics do not supply access to many of these features such as the velocity dispersion and the mean pressure in the bubble. Based on this, Ranjan et al. (2011) focused on variables which are quantifiable either directly or indirectly from shock tube experiments such as translational vortex velocity and circulation models. Rudinger and Somers (1960) developed a simplified theoretical model for SBI which results in the computation of the initial bubble velocity denoted as V_b and final vortex velocity denoted as V_v. Their model assumed that the bubble is primarily accelerated by the shock to a velocity, V_b, different from the surrounding shocked gas velocity denoted as u'_1. At the early phase, they considered the bubble to be a solid particle and stated the computation assumed an impulsive, principally incompressible acceleration. The impulse per unit volume, I, transmitted by the shock to the gas bubble is exactly the same as what the surrounding gas experiences and given below as:

$$I = \rho'_1 u'_1 = \rho'_2 V_b + k\rho'_1 (V_b - u^1_1) \tag{2.3}$$

where ρ'_2 and ρ'_1 represent the aftershock density of the gas bubble and aftershock density of the surrounding gas respectively. The last term on the right-hand side $k\rho'_1(V_b - u^1_1)$ denotes the impulse transmitted to the surrounding gas around the bubble as a result of the movement of the bubble. k represents the inertial coefficient or apparent additional mass fraction. k = 0.5 for a spherical bubble and k = 1 for an infinitely long cylinder travelling at right angles to its axis (Lamb, 1945). From equation (2.3), the velocity of the bubble shortly after the propagation of the shock is given as:

$$V_b = \left(\frac{1+k}{\sigma+k}\right) u'_1 \tag{2.4}$$

where $\sigma = \rho'_2/\rho'_1$ is the aftershock density ratio. They then analysed the transformation of the gas bubble into a vortex where the energy trapped by the vortex is supplied by the kinetic energy of the initial motion thus resulting in a drop of the relative velocity. This is given below:

$$V_v - u'_1 = \beta(V_b - u'_1) \tag{2.5}$$

Adopting a computation by Taylor (1953) for the generation of a vortex ring by the impulsive acceleration of a disk, they were able to compute the vortex velocity as shown below:

$$V_v = \left(1 + \beta\frac{1-\sigma}{\sigma+k}\right) u'_1 \tag{2.6}$$

Taylor (1953) provided typical values for β = 0.436 for the vortex ring i.e., spherical bubble case and β = 0.203 for the infinitely long vortex pair i.e., cylindrical bubble case (Rudinger and Somers, 1960). The Rudinger and Somers vortex-ring velocity model is simple as well as useful. For a fixed aftershock velocity ratio, it produces a normalised velocity V_v/u'_1 which remains constant with the Mach number. As there is a degree of certainty in the effective shape of the bubbles in the experiments, Rudinger and Somers found that measured velocities of the vortex had values predicted by Eq. (2.6) with β values agreeing with the values for spheres and cylinders.

Piccone and Boris (1988) performed the first comprehensive numerical study of SBI in 2D following the experiments performed by Haas and Sturtevant (1987) for spheres and cylinders. Even though their 2D simulations only reached a grid resolution of fewer than 50 cells per bubble radius (R50), they still manage to represent the evolution of the vortical features observed by Haas and Sturtevant (1987). Their work also presented a model for the computation of the late-time bubble velocity and vortex strength magnitude, Γ. Piccone and Boris (1988) also used this estimate to define adaptive gridding parameter in Eulerian simulations for SBIs. However, they gave no information on the accuracy of the model compared with experimental or numerical outcome. This approximation is also valuable as a model of the vortex itself even though it was originally meant for the detection of the motion of the entire shocked bubble. The circulation, Γ, is a scalar quantity which has considerable importance in the description of the vertical flows. It is defined around a simple closed curve C as a line integral of the velocity as given as follows:

$$\Gamma = \oint_C U.ds \tag{2.7}$$

From Stokes's theorem, it can then be inferred that the circulation around a reducible curve is equivalent to the vorticity flux via an open surface A bounded by the curve as shown below:

$$\Gamma = \int_A \omega.dS \tag{2.8}$$

The circulation model provided by Piccone and Boris (1988) is dependent on the initial properties of the shocked gas, unshocked ambient gas and the bubble. They then used Eq. (2.8) to compute the

circulation in half of the bubble with the baroclinic term being the lone source term for the vorticity. Their circulation model is derived as:

$$\Gamma_{PB} \approx 2u'_1\left(1-\frac{u'_1}{2W_i}\right)\left(\frac{D}{2}\right)ln\left(\frac{\rho_1}{\rho_2}\right) \tag{2.9}$$

They also expressed the vortex velocity as:

$$V_v \approx u'_1 + \frac{\Gamma_{PB}}{2\pi D_v} \tag{2.10}$$

From Eq. (2.10), D_v is the major diameter of the vortex ring, and D is the initial bubble diameter. Yang et al. (1994) numerically examined the shock-cylinder interaction and adopted a similar technique as Piccone and Boris (1988) in calculating the circulation. Yang et al. (1994) predicted the circulation model (YKZ model) given as:

$$\Gamma_{YKZ} \approx \frac{2D}{W_i}\frac{p'_1 - p_1}{\rho'_1}\left(\frac{\rho_2-\rho_1}{\rho_2+\rho_1}\right) \tag{2.11}$$

They also presented results from 2D simulations for shock interaction with a cylindrical helium bubble surrounded by ambient air with Ma number ranging from 1.05 to 2.0. They also investigated and simulated different cases with larger density ratios (χ as denoted by Ranjan et al. (2011) in their review paper) less than 1. The simulations utilised a Eulerian flux-corrected-transport method as well as a spatial resolution of R_{20} with the results revealing that the model predicted the circulation obtained from simulations to a precision level of almost 85% while Piccone and Boris (1988) were discovered to have overvalued the circulation.

Quirk and Karni (1996) described a comprehensive numerical investigation of SBI using a sophisticated adaptive mesh refinement algorithm, with a non-conservative shock-capturing scheme. The adaptive mesh refinement technique allowed them to yield outcomes with high resolution at low computational cost and there was an effective resolution of the shock refraction pattern and vortical features noticed by Haas and Sturtevant (1987). Winkler et al. (1987) also conducted some numerical simulations based on the experimental studies of Haas and Sturtevant (1987). In their numerical studies, they simulated shock interaction (Ma = 2) with a spherical bubble of a relatively dense gas in order to underline the detected evolution of a supersonic vortex ring downstream from the bubble in the aftershock flow. Following from this, Cowperthwaite (1989) also created 2D simulations of the deformation and movement of a previously spherical mass of Freon 12 gas surrounded by an ambient fluid, either air or helium, with computations continued to late times and the velocity of the bubble's center of mass computed as a function of time. The bubble velocity obtained from their simulations showed agreement with simple models for drag, added mass and entrainment.

Samteney and Zabusky (1994) described a detailed analysis of the baroclinic vorticity deposition on a planar interface utilising shock polar analysis. This finding was applied to the spherical scenario using a near-normality condition given below:

$$\Gamma_{SZ} = \left(1+\frac{\pi}{2}\right)\left(\frac{2}{1+\gamma}\right)(1-\chi)(1+M^{-1}+2M^{-2})(M-1)(D/2)c_1 \tag{2.12}$$

From Eq. (2.12), χ denotes the density ratio across the interface. Their model revealed that for large χ, the circulation does not rely on the density ratio. Also, for flows at high Ma, they showed that the circulation behaves linearly with Ma. They also proved that their model was effective for the convergent-geometry SBI i.e., A > 0, $\rho_2 c_2 > \rho_1 c_1$. Zabusky and Zeng (1998) also described their numerical study of the shock interaction of planar shocks with a Freon 12 axisymmetric spherical

bubble surrounded by ambient air. In their research work, they applied the early axisymmetric simulations by Piccone and Boris (1998) to flows with high Mach number (up to 5). They discovered that the creation of a secondary vortex ring at the bubble apex was as a result of the secondary shocks that appear in the higher-shock-strength-case. Levy et al. (2003) applied an interface-tracking 2D ALE hydrodynamic code to simulate the SBI. They had earlier conducted some experimental analysis which inspired the numerical simulations that followed. Their numerical model was also an extension of Samteney and Zabusky's (1994) circulation model to the velocity field scaling. Their model revealed that the bubble velocity does not rely on the radius of the bubble and the velocity scaling failed for Ma > 2.

Layes et al.'s (2003) experiments have also been numerically investigated by Giordano & Burtschell (2006) and Layes & LeMetayer (2007) with both agreeing closely with the experiments. A small secondary vortex ring at the bubble's apex was formed as depicted by the numerical schlieren image for the acceleration of shock (with strength Ma = 1.7) on a krypton bubble (Giordano and Burtschell, 2006). An analytical method for the computation of the final volume of the inhomogeneity after it is accelerated by a shock was described by Giordano and Burtschell (2006). Ranjan et al. (2011) also explained that extensive work has been numerically performed on shock-cylinder interaction with Marquina and Mulet (2003) simulating the experiments of Haas and Sturtevant (1987) utilising very high spatial resolution Their work revealed the evolution of distinctive turbulent features in the flow field during delayed timescales.

Greenough and Jacobs (1996) executed a high-order Godunov implementation of the multifluid equations in an adaptive mesh refinement environment (AMR) to investigate as well as successfully resolve the challenges related with fine-scale details of the complex, highly vortical flow field detected in the experiments conducted by Jacobs (1993). Their system accurately modelled multiple component mixtures by considering varying compressibility effects with the embedment of AMR. This ensured effective rise in resolution by the concentration of computational effort where high accuracy or higher resolution are needed. They also qualitatively and quantitatively compared their results to past experimental data which revealed excellent concordance. Some of their key results revealed; deposition of counter sign vortex blobs in the jet core by baroclinic production of the curved shock wave as it propagates the bubble and the jet; and three stages of bubble development (weak deformation, strong deformation, relaxation/reorganization (RR)). They explained that the weak deformation stage is characterised by a weak distortion of the helium jet as a result of insubstantial vorticity stimulated velocity effects while the strong distortion stage is characterised by large deformation of the jet and the vortex blobs influenced by strong vorticity stimulated velocity effects. Finally, they explained that the RR stage involved a reorganization of the vorticity field into 'point-like' pair of vortices.

Bagabir and Drikakis (2001) investigated the impact of the strength of the incident shock on the cylindrical behaviour with similar characteristics as in the experiments conducted by Haas and Sturtevant (1987). They carried out these experiments using the Euler equations for different incident shock Ma ranging from 1.22 to 6. They also adopted high-resolution Godunov-type methods as well as an implicit solver. Their results showed good concordance with past experimental investigations as well as further revealing more gasdynamic characteristics with increasing Ma. Their numerical studies showed that larger bubble distortions were discovered at higher Ma with circular-shaped structure, observed at these higher Ma, replacing the 'c-shaped' vortical structure that was seen at Ma = 1.22. Finally, their work revealed that with rising Ma, the jet speed emerging at the centre of the bubble during SBI was also increased.

Robey et al. (2002) ensured that they were able to visualise both the initial deformation of a copper sphere into two vortex ring structures and the onset of the azimuthal instability by performing a comprehensive numerical investigation using a 3D Eulerian adaptive mesh refinement code, which is an identical code adopted by Niederhaus (2007) to conduct a parametric investigation for SBI

challenge. Their numerical study also revealed that 2D codes are entirely insufficient for fixing the noticed azimuthal mode structures. Finally, their paper showed an accurate agreement with the noticed deformation of the copper sphere. Their simulations also depicted the breakup of the vortex ring as a result of the beginning of bending-mode instabilities. Wang et al. (2018) numerically investigated the vortex breakdown behaviour of the scaling criterion in the interaction between an incident shock and cylindrical bubbles. Their work laid emphasis on the vortex breakdown phenomenon described by the specific stretching factor which directly indicates the drop in normalised circulation. They also numerically showed the appearance of vortex breakdown in terms of bubble morphology and interface stretching before going on to explain that additional insight into the physical mechanism of reduced circulation shows that the impact of viscous dissipation versus baroclinic production is strengthened in microscale interactions. Very interestingly, they stated that there exists an impedance to roll up (into the vortex structure) for the cylindrical bubble in a microscale interaction with the interface deformation not as efficient compared to a macroscale interaction and explained that this situation can be elucidated by normalised circulation. To evaluate the level of vortex breakdown, their research proposed a dimensionless scaling vortex breakdown number, μ^*, via order-of-magnitude analysis, which indicates the conflicting contribution from dissipation and baroclinity i.e., the ratio of baroclinic to viscous terms. Depending on the viscous effect on the formation of vortex, μ^* is classified under three flow categories i.e., $\mu^* < 10^{-3}, 10^{-3} < \mu^* < 10^{-1}, \mu^* > 10^{-1}$, which represent inviscid, transient and viscous regimes respectively. Finally, they explained that the introduction of the nonlinear factor such as viscous dissipation in flow development leads to scaling breakdown with the exact modelling and simulation of the nonlinear factor posing the main difficulties in comprehending the microscale dynamics.

Chen et al. (2021) numerically studied the interaction of shock waves with circular or elliptic bubbles in an air medium. They used a five-equation model and the finite volume method (FVM) to numerically examine the generation and distribution of vorticity. They also examined its impact on the deformation of the bubble interface and acceleration of turbulent mixing of the two-phase gases. Their research showed that the time needed to generate the transverse jet and vortex structure reduces while the deformation degree and the collapse speed rise as the aspect ratio of the horizontally aligned elliptic bubbles is increased. They went forward to state that for vertically aligned elliptic bubbles, the location of the transverse jet is linked to the aspect ratio i.e., the more the aspect ratio, the greater the distance between the jet position and the centreline. Singh et al. (2021) numerically studied the effect of bulk viscosity on flow morphology of shock-accelerated cylindrical light bubble in diatomic and polyatomic gases. They adopted an explicit mixed-type modal discontinuous Galerkin scheme with uniform meshes to solve a 2D system of unsteady physical conservation laws developed from the Boltzmann-Curtiss kinetic equations. They also obtained a new complete viscous compressible vorticity transport equation including the bulk viscosity. Their result revealed that during the interaction of the shock wave with the cylindrical light bubble, the bulk viscosity linked to the viscous excess normal stress in diatomic and polyatomic gases play a major role. Their research explained that the diatomic and polyatomic gases initiate major significant changes in flow morphology, leading to complex wave patterns, production of vorticity, formation of vortex, and bubble distortion. They compared their results with monoatomic gases and elucidated that both diatomic and polyatomic gases produce bigger rolled-up vortex chains, different inward jet formations, and sizeable mixing zones with intense large-scale expansion. Finally, they investigated the impacts of diatomic and polyatomic gases via various occurrences like vorticity generation, degree of non-equilibrium, enstrophy, and dissipation rate.

Following a massive improvement in computational resources over the years, there is added competence to simulate SBIs numerically in three spatial dimensions at suitable grid resolutions. This has proven to be very expedient as most preliminary aspects of the flow-field developments for SBIs are mainly 3D, especially at increased Ma and A. However, there is a limited scope for numerical investigation of 3D SBIs with the first complete 3D simulations for SBIs examined by Stone and Norman (1992). Their simulations were conducted at a simple spatial resolution of R60 showing that

vortex rings produced in SBIs from an astrophysical viewpoint (Ma approximately 10) are unsteady in three dimensions. This leads to a break-up at late times into fragments. Fig. 2.6 shows their 3D rendered images for the distribution of vorticity of SBIs at high Ma.

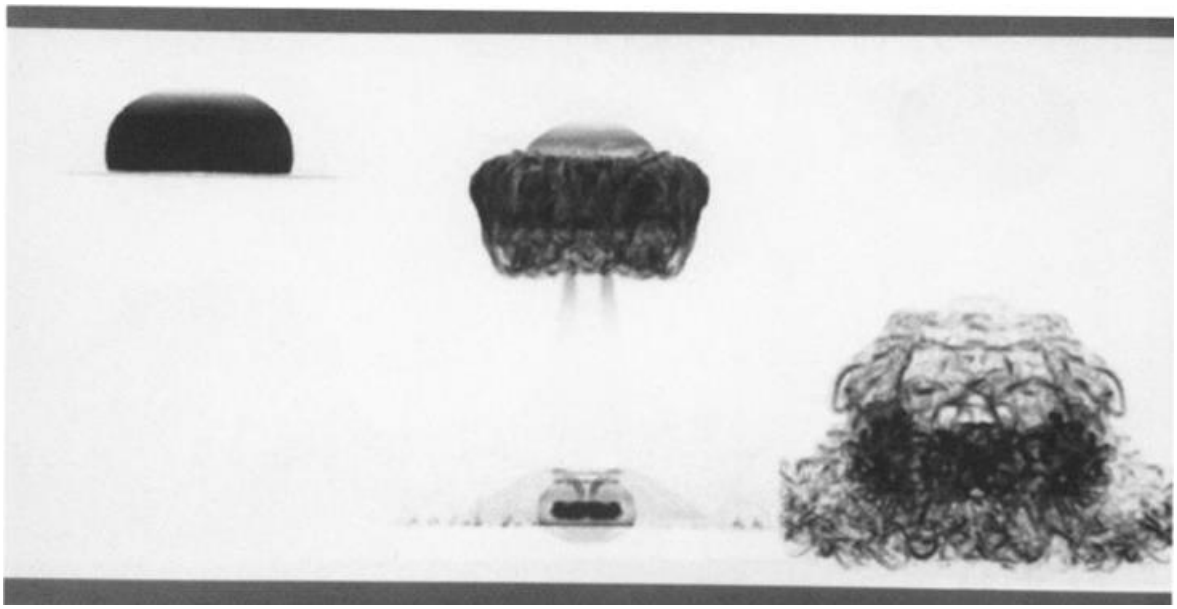

Figure 2.6: Cloud fragmentation and 3D distribution of the vorticity magnitude as shown at different time scales (with respect to the cloud-crushing time, t_c). The left gray-scale image corresponds to t = $0.5t_c$, the middle image corresponds to t = $2.0t_c$ and the last image corresponding to $4.5t_c$ (Stone and Norman, 1992).

Klein et al. (2003) also described a 3D adaptive mesh refinement simulation for shock interaction (Ma approximately equal to 10) with a solid copper sphere in a low-density foam medium. Their simulation revealed that an azimuthal bending-mode instability analogous to Widnall instability for incompressible flows (Widnall et al., 1974) is present which breaks up the primary vortex ring created during the SBI. This azimuthal redistribution of the sphere mass accounted for characteristics of the experimental data which could not be completely depicted in 2D simulations. Fig. 2.7 reveals the 3D-rendered image of the multimode channelled azimuthal structure visible on the shocked sphere at late times.

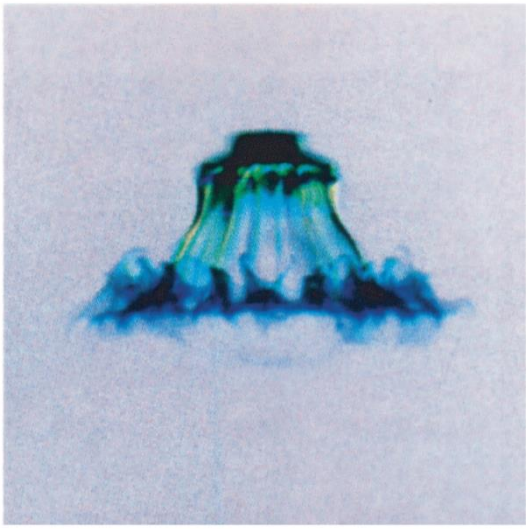

Figure 2.7: Three-dimensional adaptive mesh refinement simulation of shock sphere at late times shown by volume rendering. The shock propagates from top to bottom (Klein et al., 2003)

Klein et al. (2003) used an ideal gas equation of state and scale-free calculation, and Fig. 2.7 shows the impact of vortex ring instabilities on sphere breakup as well as the unsteady lower ring-like structure attributed to Widnall instability. The most robust numerical study of SBIs was conducted by Nierderhaus (2007) who utilised a range of 3D multifluid Eulerian simulations. Niederhaus et al. (2008) also comprehensively investigated SBIs across an extensive range of Ma and A. Their work also thoroughly examined different essential characteristics of the SBI, and their work revealed that the mean density and bubble velocity can be scaled over a broad range of Ma for a fixed value of A using quantities predetermined from the 1D gas dynamics. This is irrespective of the fact that this problem displays a complex flow field. There have been some remarkable deviations from a characteristic SBI morphology described by both Niederhaus et al. (2008) and Ranjan et al. (2008b) for cases with Ma and A greater than 2 and 0.5, respectively. They discovered that the flow field mainly showed a diffuse turbulent plume at delayed timescales as opposed to the expected discrete vortex rings and vortex projectiles. This is shown below:

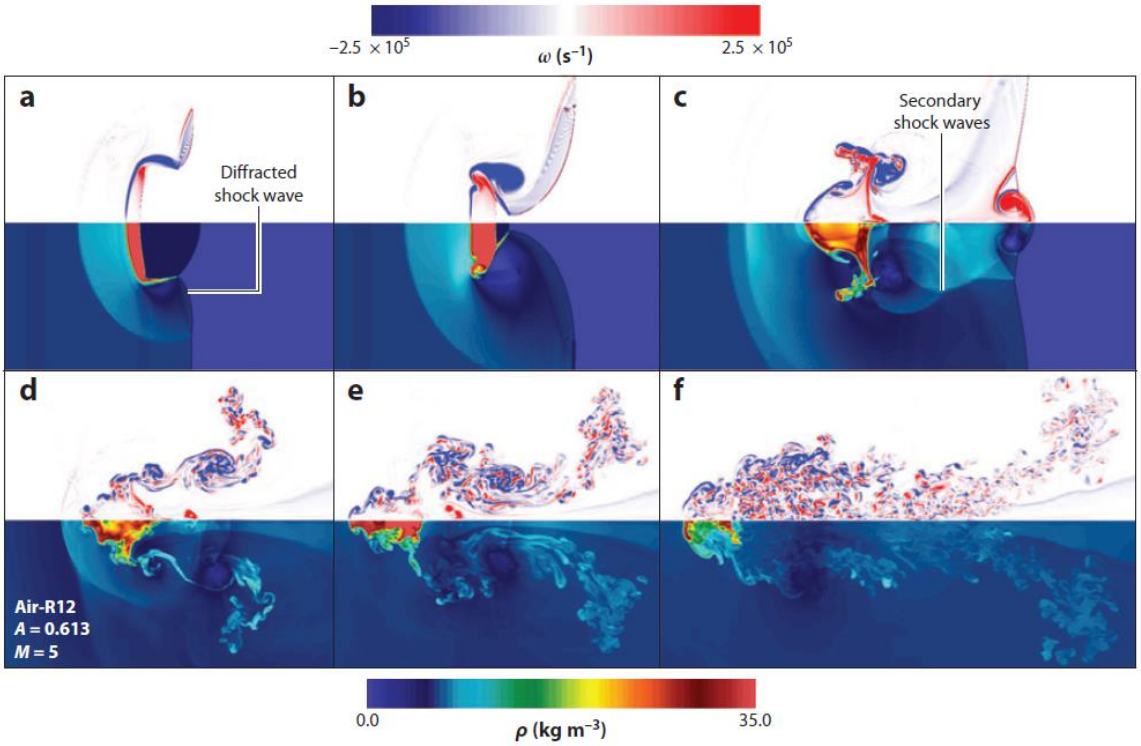

Figure 2.8: Schlieren images for shock interaction with Freon 12 bubbles surrounded by air with shock strength equivalent to Ma = 5. The shock is propagating from left to right, A = 0.613 and the upper images correspond to the vorticity magnitude while the bottom images correspond to density at (a) $\tau = 1.5$ (b) $\tau = 2.5$ (c) $\tau = 5.0$ (d) $\tau = 10.1$ (e) $\tau = 15.0$ (f) $\tau = 25.0$, where $\tau = tW_i/R$ and W_i is the lab-frame speed of the incident shock waves and R is the radius of the Freon 12 bubble (Niederhaus, 2007).

Niederhaus et al. (2008) proposed an approach to model the circulation where the velocity field during shock propagation is remodelled using one-dimensional gasdynamics parameters. Accordingly, they obtained an estimate of the circulation in accordance with one-dimensional gasdynamics reconstruction as shown below:

$$\Gamma_R = u'_1 y_1 + \frac{1}{3} R(u'_1 - u'_2)\left(\frac{-y_1}{R}\right)^3 + u'_2 y_2 - u'_1(W_i t^* + y_3) \tag{2.13}$$

where y represents a line = 2R, and the lengths of the line segments y_1, y_2, y_3, and y_4 obtained from 1D gasdynamics are given below:

$$y_1 = \frac{1}{\sqrt{Ma_r}}(u'_2 + W_r)t^* \tag{2.14}$$

$$y_2 = (W_t - u'_2)t^* \tag{2.15}$$

$$y_3 = \frac{W_r t^*}{\sqrt{Ma_r}} \tag{2.16}$$

$$y_4 = W_i t^* \tag{2.17}$$

$$t^* = \frac{2R}{\widetilde{W}} \tag{2.18}$$

where Ma_r, W_r, W_t, u'_2 and $\widetilde{W}$ represent the Ma for the reflected shock wave, reflected shock wave speed, transmitted shock wave speed, speed of particle behind the transmitted shock wave, and the effective shock wave speed (as defined by Zabusky and Zeng (1998)) respectively.

Eq. (2.14) represents the distance between the bubble apex and the reflected shock wave as it transverses the bubble's axis. It can be modified by replacing t^* in it with equation (2.18) as given below:

$$y_1 = \frac{2R}{\widetilde{W}\sqrt{Ma_r}}(u'_2 + W_r) \tag{2.19}$$

Their circulation results from the 3D simulations against the model values for Γ_{SZ}, Γ_{YKZ}, Γ_{PB}, and Γ_R revealed that the Γ_R gave the most excellent conformity from the wide range of Ma and density ratios studied. Based on this, Γ_R is suggested as the best initial approximation when there is a lack of 3D simulation data for circulation.

Ding et al. (2017) completed numerical simulations to examine the interaction between a planar shock wave and cylindrical (both 2D and 3D) bubbles. Their numerical research combined the high-order weighted essentially non-oscillatory construction with the double-flux scheme to study the detailed 3D flow structures. They came up with a generalised 3D theoretical model for predicting the upstream interface movements of different gas cylinders. They showed that subsequent to when the shock propagates through the cylinder, baroclinic vorticity deposited at the gas cylinder controls the deformation of the interface. They continued by explaining that for the 2D case, the vorticity mainly has the direction normal to the horizontal plane as opposed to the 3D case where the curved catenary leads to further baroclinic vorticity parallel to the horizontal plane. Very importantly, they stressed that the interface deformations in the symmetric and boundary slices of the concave and convex cylinders suffer from similar 3D effects as a result of their differing principal curvatures of initial interfaces in comparison with the 2D scenario. Finally, they showed that the upstream interface along the symmetric slice of the convex cylinder travels quicker than the 2D scenario as opposed to the concave upstream end which moves slower. The interface velocities were calculated using a generalised 3D high amplitude theoretical model.

2.4. Applications of SBI and SAIFS

Shock wave propagation through gas inhomogeneities is driven by the wide applicable areas in which this phenomenon occurs together with the requirement to understand the preliminary mechanisms related to turbulence creation and mixing. Such applications include, but not limited to; supersonic combustion (Marble et al., 1987; Yang et al. 1993, 1994), detonation (Madar, 1965), inertial confinement fusion (Zhang and Graham 1997; Lindl et al. 1992), fragmentation of cancer cells (Takayama 1999), cavitation damage to human tissues during diagnostic ultrasound or lithotripsy

(Takayama 1999; Tamagawa and Akamatsu 1999), shock-boundary layer interaction (Delery 1983), instability of collapsing gas bubbles in liquids (Ding and Gracewski 1996), cooling of lightening channels (Picone et al. 1981) and astrophysics (Arnett et al. 1989).

SBI has direct relevance as well as exists in natural and man-induced activities. They can also be used as a vital tool in the investigation of complex flow scenarios in which a shock wave interacts with an inhomogeneity within which acoustic impedance variation exists (Ranjan et al., 2011). A lot of progress has been made particularly with respect to measurement and estimation of macroscopic geometrical, kinematic and integral characteristics. This progress has also seen the evolution of dimensionless scaling laws between these integral characteristics and the flow-governing parameters. There has also been research related to measurement and estimation of flow variables like velocity, density and pressure as well as the fusion of other physical techniques like chemical reactions and plasma physics with the fluid dynamics aspect of this research (Ranjan et al., 2011).

Niederhaus et al. (2008) also followed the work of Rudinger and Somers (1960) on shock-bubble interaction where they stated that a shock wave interaction with a density inhomogeneity produced perturbations which were non-existent under constant-entropy acceleration. These perturbations drastically change the shape of the inhomogeneity and the wavefront of the shock wave thus resulting in the generation of distinctive vortices and sometimes, regions of intense mixing. They also explained that such interactions could range from the simple case for the propagation of a planar shock wave through a uniform medium (without considering variations resulting from a spherical or cylindrical density inhomogeneity) to shock-accelerated inhomogeneous flows where a shock wave travels in a medium characterised by a variation in density, temperature and other state variables. The later kind of flows have extensive applications in broad energy and spatial scales such as shock propagation in the interstellar and intergalactic medium (e.g., Klein et al., 1994), sonic boom propagation (e.g., Davy & Blackstock, 1971), supersonic combustion (e.g., Yang et al., 1994), shock mitigation in foams (e.g., Delale et al., 2005), and shock-wave lithotripsy (e.g., Jamaluddin et al., 2005). Niederhaus et al. (2008) also referenced Haas and Sturtevant's (1987) work when they referred to the shock-bubble interaction as a 'finite-mass high-interface-curvature' like the Richtmyer–Meshkov instability (Richtmyer 1960; Meshkov 1970), which can limit the driven compression efficiency in inertial confinement fusion implosions (Lindl, 1995). Following from this, Niederhaus et al. (2008) have considered this shock-accelerated inhomogeneous flows as a density-interface perturbation whose distortion is influenced by an impulsive acceleration.

SAIFs are applicable in a broad range of physical situations across various spatial, temporal and energy scales such as astrophysical flows (Arnett, 2000); the interaction of supernova remnants with interstellar clouds (Hwang et al., 2005; Klein et al., 1994); atmospheric sonic boom propagation (Davy & Blackstock 1971), supersonic combustion systems (Marble et al. 1990, Yang et al. 1994), shock travel through foams and bubbly liquids (Ball & East, 1999; Collins et al., 2005; Delale et al., 2005), the fragmentation of gallstones or kidney stones by shock waves (Delius et al., 1998; Eisenmenger, 2001; Gracewski et al. 1993), and high-energy-density systems such as inertial confinement fusion devices (Lindl et al., 1992; Lindl, 1995). Ranjan et al. (2011) explained that the dynamics of the interstellar medium in spiral galaxies is considerably impacted by the strong shock waves created by supernovae explosion, stellar winds, expanding HII regions and spiral density waves (Klein et al., 1994). Their work also showed that it is widely accepted that the produced shock waves considerably change the morphology of the high-density cloud thus resulting in a turbulent exchange of material and energy between interstellar gases of varying temperatures and densities. One such example, as shown by Hwang et al. (2005), is the remnant of the bright eastern knot of the Puppis A supernova. This Puppis A supernova is responsible for the deformation of shock front as a result of the cloud-shock interaction as seen from the Chandra X-ray telescope. Klein et al. (1994) and Hansen et al. (2007) explained the physics of mass stripping from the cloud; energy and momentum transfer to the shocked cloud; as well as the instabilities generated by shocks at the cloud boundary which they

modelled after laser-driven high-energy-density SBI experiments. SAIFs are also seen in shock-mitigation systems based on two-phase flows in which bubbly liquids and aqueous foam barriers are utilised to dissipate the impulse of the shock waves (Ball and East, 1999; Collins et al., 2005; Delale et al., 2005). This redistribution is mainly due to heat transfer at the interface as well as small-scale internal processes on the foam interior. Ball and East (1999) also showed that aqueous foams displayed high acoustic impedance and low speed of sound which subjects the shock and blast waves to refraction. This incomplete transmission at foam/air interfaces is subsequently delayed within the foam.

Another useful application is found in inertial confinement fusion experiments (where temperature and density of the thermonuclear fuel confined in a small capsule is elevated to values required for a fusion reaction). This is usually done by imploding the capsule with a convergent spherical shock wave produced by direct or indirect illumination of the capsule using several high-power laser beams (Ranjan et al., 2011). Lindl et al. (1992) and Lindl (1995) noticed that as the shock wave travelled across the solid capsule, the shock-induced turbulent mixing[5] resulted in the intermingling of the shell material with the energy source i.e., fuel, which could hugely reduce the generation of energy from the fusion reaction.

Piccone and Boris (1983) argued that pressure waves interactions with fluid density oscillations are a principal cause of vorticity and turbulent motion. They explained that these rotational flows developed on a significantly lengthier period compared to shock propagation across the density inhomogeneity. They indicated that production of vorticity by rotational flow and strongly associated processes has demonstrated to be important in investigations related to; ramjet engines' operation (Rudinger, 1958), inertial confinement fusion efficiency (Emery et al., 1984), and lightening channel cooling rates (Picone et al., 1981). The wide application and usefulness of this vorticity generation can be linked to the essential lasting impacts which rotational flows have on the structure and properties of the fluid (Picone and Boris, 1983).

2.5. Experimental investigation of shock/liquid bubble interaction

Most of the initial experimental investigations regarding bubble breakup by stripping was performed by Ranger and Nicholls (1969; 1972). They investigated the interaction between the shock wave and the liquid column at various phases of the breakup procedures utilizing streak photography. Joseph et al. (1999) carried out similar experiments utilizing a high-speed camera. Their findings were finished from a series of experiments in which different liquids were applied. Their experiments also produced incident shock waves with strengths of 2 and 3. Their work only examined the shock liquid droplet interaction and the waves produced around the bubble. Similar experiments for stripping type breakup were performed by Simpkins and Bales (1972), Krzeczkowski (1980), Yoshida & Takayama (1990), Hirahara & Kawahashi (1992), and Theofanous & Li (2008).

Ranger and Nicholls (1969) presented experimental and analytical results for liquid bubble disintegration. They noticed breakup to take place due to the interaction between the bubble and the convective flowfield created by the propagation of shock wave over it. The aim of their work was to establish the breakup rate and the time required for disintegration to take place. They presented photographs as well as results on bubble displacement and disintegration time for various scenarios involving shock waves travelling in air at Mach numbers ranging from 1.5 to 3.5. Their experiment used water bubbles with diameters ranging from 750 to 4000 microns. They also formulated a model for the disintegration process by considering that breakup occurs from 'boundary-layer stripping' as the shearing effects induced by the high-speed flow leads to the creation of a boundary layer in the bubble surface. Their work showed that the stripping away of this layer accounts for this breakup. They combined their experimental measurement of the changes in bubble shape and variations in bubble

[5] Shock-induced turbulent mixing is attributable to the perfectly non-spherical shape of the shock wave; the small amplitude contained within the capsule surface; and the high wave number manufacturing imperfections.

velocity (with time) together with their analytical findings to calculate the rate of fragmentation. With respect to changes in bubble shape, they discovered that the initially spherical drop is distorted into a planetary ellipsoid having its major axis perpendicular to the flow direction. From an analytical viewpoint, their work showed that breakup time is directly related to the bubble diameter and the square root of the liquid to gas density ratio but inversely related to the velocity.

Simpkins and Bales (1972) experimentally investigated the distortion of originally spherical bubbles subjected to an external flow for wide range of We and Bo. They compared their observed variation in bubble 'response' with analytical predictions. Their results revealed that beyond a We_{cr}, the 'response' is no longer vibratory and becomes monotonic with time. They then observed that even though the 'response' is erratic, the distortion exerted by the external aerodynamic pressure distribution is still the principal factor. Their measurements of the drag coefficient (C_D) produced an average value of 2.5 over a wide range of *Re*. Finally, their measurements of bubble acceleration showed a good agreement with Taylor's prediction for a lenticular bubble and their work revealed that the time at which Taylor instability takes place is inversely related to the *Bo* to a quarter power.

Waldman and Reinecke (1972) experimentally examined the challenge of determining raindrop breakup impacts in the shock layer of a high-speed automobile. Their research aimed to compute the surface damage on automobiles induced raindrops. They derived their experimental data in a shock tube using shadowgraphy and x-ray photography. They showed these data as correlations of non-dimensional time required for the disintegration of the raindrops. They also expressed the We combined with the raindrop mass change and trajectory as a function of non-dimensional time. Their work also expressed the connection between the experimental scenario and the flight case which they used to describe the stagnation and downstream conical flow regions of a high-speed shock layer. They used their experimental correlations to perform computations for the mass fraction of the impacting raindrop, velocities, and impact angles for an automobile travelling through a rainstorm. Following from these experimental data correlations and the histories of actual drop mass, their computations revealed that both the stripping and catastrophic breakup modes are significant in the stagnation area of the automobile while only the stripping breakup mechanism is important in the downstream conical flow region. Finally, they concluded by stating that bubble breakup is a significantly more dominant mechanism than deceleration or deflection with respect to the protection of the surface of a high-speed automobile from the approaching rain.

Wierzba and Takayama (1988) experimentally examined the stripping-type breakup of water bubbles. They performed their experiments in a 60 x 150 mm cross-sectional shock tube equipped with pulsed laser holographic interferometry. They used water bubbles with diameters of 1,030 and 4,300 microns. The shock wave (having strengths of 1.3 and 1.5) was produced in atmospheric air. The We and Re for these scenarios ranged from 600 to 7600 and 1.38 to 10.4 x 10^4 respectively. Their images were very conspicuous to allow the observation of the droplet structure during the different distortion phases of the breakup procedure in comparison to past experimental data for stripping-type breakup. These images were derived by spark shadowgraphs, streak schlieren methods and high-speed movies. Their work noted that past experimental works were also impaired because the structure of the fragmenting bubble could not be visualized properly. This was due to the impact of light scattering through the micromist. Wierzba and Takayama (1988) then aimed to use the holographic interferometry to re-evaluate the classical challenge of the stripping-type breakup of the liquid bubble. They then established a four-stage mechanism of the stripping type breakup of liquid bubbles.

Yoshida and Takayama (1990) revealed that various droplet breakup patterns were noticed when adopting various techniques for flow visualization. For instance, their work revealed that the droplet fragmentation pattern detected while utilizing the double-exposure image holographic interferometry were distinct from those noted on the unconstructed holograms i.e., equivalent to a direct shadowgraph. To support their argument, Igra and Sun (2010) explained that the results of Ranger & Nicholls (1969), Simpkins & Bales (1972) and Joseph et al. (1999) showed that the disintegrating spherical droplets looked like fireballs. Based on these images, Igra and Sun (2010) further inferred

that it was difficult to differentiate the internal structure of the fragmenting spherical droplets i.e., the shattering mists clouds and wakes. On the other hand, utilizing holographic interferometry revealed that the derived somewhat 3D images indicated mist clouds and wakes that were distinct from those detected in schlieren and shadowgraph photographs. Very interestingly, Igra and Sun (2010) also pointed out that the distinct images produced by the holographic interferometry is attributable to their object beams that convey phase information, generated by the scattered light, from the micromist particles to the holofilm. Via reconstruction, the phase information was partly recovered but could not be captured in the schlieren or shadowgraph technique. Nevertheless, most of the documented experiments utilized schlieren or shadowgraph techniques to image the droplet breakup process.

Hirahara and Kawahashi (1992) experimentally examined the distortion and breakup of water as well as silicone oil droplets within a shock tube. Their bubbles, which varied from 200 to 500 microns in diameter, were produced by an oscillatory capillary. The diameter of the water bubbles ranged from 220 to 390 microns (We from 7.1 to 13) while that of the silicone oil ranged from 380 to 590 microns (We from 20 to 65). Their experimental examinations were performed close to the We_{cr}. They used the shadowgraph technique to optically visualize their results. They explained the impact of the liquid viscosity on the breakup mechanism as well as on the breakup time. Their research also revealed that the smallest We approached the breakup We_{cr} and the bubbles fragmented in the stamen or bag mechanism for moderate We values. Also, they showed that the distortion time until a bubble fragments into small particles is not reliant on the magnitude of the We for the liquid droplets they employed. According to their findings, this distortion time depended on the pressure distribution in the vicinity of the bubble as well as the shearing stress induced by bubble distortion. They detected several breakup mechanisms like the Bag, Bag-and-stamen and the Chaotic mode and presented their reliance on the We and On. Finally, they revealed that the non-dimensional distortion time for silicon bubbles is more prolonged than the water bubbles' and the silicon oil droplets were more deformed than the water droplets because of the viscosity effects.

Hsiang and Faeth (1992) experimentally discovered the characteristics of drop distortion and secondary breakup for air disturbances at normal temperature and pressure induced by a shock wave. They utilized several liquids like water, glycerol solutions, n-heptane, ethyl alcohol and mercury to yield We in the range of 0.5 to 1000, On in the range of 0.0006 to 4, liquid/gas density ratios in the range of 580 to 12,000 as well as Re in the range of 300 to 16,000. They also employed several measurements like the pulsed shadowgraphy and holography to derive bubble distortion characteristics before breakup as well as size distribution of the bubble after breakup. Their work showed that drop deformation and breakup existed at We > 1. They also detected various distortion and breakup regimes like no deformation, non-oscillatory deformation, oscillatory deformation, bag breakup, multimode breakup and shear breakup. These distortion and bubble disintegration modes have been listed in order of rising We at On < 1. Their work also revealed that at the start of bubble distortion and disintegration, We rises with increasing On and no breakup is noticed when On > 4 as a result of the 'stabilizing' impact of the liquid viscosity. Drop sizes were also shown to reduce after secondary breakup as We increased. Finally, they explained that bubble characteristics following secondary breakup at high We showed a potential for the ensuing breakup of the biggest drops in the size distribution provided relative velocities remained the same during breakup.

Hsiang and Faeth (1995) experimentally investigated the distortion characteristics of a bubble caused by a shock wave and steady 'disturbances'. They used three test equipment which include: a shock tube to measure the impacts of shock wave 'disturbances' on bubbles travelling in gases; a 10m high drop tube facility to measure the impacts of steady 'disturbances' on bubbles propagating in gases; and a 1m high drop tube equipment to measure the impacts of 'steady disturbances' on bubbles in liquids. They also used different dispersed and continuous phase gases and liquids to obtain dispersed/continuous phase density ratios of 1.15 – 12,000, On of 0.0006 – 600, We of 0.004 – 700 and Re of 0.03 – 16,000. They showed that at low On, e.g., < 1, and for all types of disturbances, substantial bubble distortion (estimated at 5%) started at We with values approximately equal to one.

They also recorded that the distortion subsequently stopped because of the inception of breakup at We ranging from 10 to 20. These shifts were not impacted by the On for steady 'disturbances' but a rise in the On led to a progressive rise in the We range for the distortion and breakup regimes for shock wave 'disturbances'. Another shift from the dome-shaped to the bowl-shaped bubbles (which they linked to the shift between the bag and shear breakup) was correlated primarily with respect to the We and Re for the selected conditions. Finally, they showed that bubble distortion for steady 'disturbances' was not reliant on dispersed/continuous phase density ratios but was largely less than that of shock wave 'disturbances' at comparable conditions because of the lack of 'overshoots' from inertial impacts. On the other hand, they explained that bubble C_D, normalized by the C_D of a solid sphere at an identical Re, correlated reasonably well based solely on the extent of bubble distortion.

Joseph et al. (1999) experimentally investigated the breakup of viscous and viscoelastic drops in the high-speed airstream following a shock wave in a shock tube. The interaction was visualized using a rotating drum camera which provides one photograph every 5 μs. They created movies for the bubble disintegration history of different viscous bubbles (of varying viscosity) and viscoelastic bubbles at very high We and Re using the derived photographs. Their results also revealed that bubbles in the range of 1mm are diminished to droplet clouds and even to vapor in times < 500 μs. Their movies showed Bag and Bag & Stamen breakup at very high We, in the regime previously classified as 'Catastrophic'. Essentially, they explained that the movies enabled them to create accurate graphs that depict the relationship between displacement and time. They then used the graph to calculate precise values of acceleration ranging from 10^4 to 10^5 multiplied by the gravity acceleration. They stated that these high values of the acceleration from the gas to the liquid exposes the flattened bubbles to a high risk of RT instabilities. Finally, they revealed that the most unstable Rayleigh Taylor wave fits almost 'perfectly' with waves measured on the improved images of bubbles from the movies, but the impacts of viscosity cannot be ignored.

Dai and Faeth (2001) experimentally examined the secondary bubble breakup induced by shock wave disturbances for the multimode breakup regime. They performed their measurements in a shock tube utilizing pulsed shadowgraphy and holography to detect the mechanism and breakup results. They used water and ethanol drops with liquid/gas density ratios more than 500, On less than 0.1 and We ranging from 15 to 150. The development of the characteristics in the multimode breakup regime with rising We started when the bag breakup regime ends, and plume bubble emerged at the apex of the bag. They stated that this plume drop is noticed at a We of approximately 15 which continues in a bag/plume breakup regime characterized by the appearance of both bag-like structures and plume bubbles. This is followed by a shift to the absence of bags at a We of approximately 40 finishing with a plume/shear breakup regime which entails the evolution of plume-like structures. These plume-like structures gradually developed into a parent bubble and ligament system as the shear breakup regime is approached at a We of approximately 80. Finally, their work provided measurements for breakup times, bubble distortion characteristics and C_D before breakup starts, distribution of resulting bubble sizes for different breakup structures, bubble velocities succeeding breakup, and rates of liquid removal as breakup takes place. They provided these characteristics as a function of the We in the multimode breakup regime with their results conforming with the findings of Hsiang and Faeth (1992) at equivalent We.

Igra and Takayama (2001) experimentally examined the distortion and breakup of a cylindrical water bubble impacted by a planar shock wave. They performed their experiments in a shock tube which had a double-exposure holographic interferometer to ensure qualitative imaging of the gas and liquid phases. The cylindrical water column had a diameter and height of 4.8 mm and 4 mm respectively and was subjected to a planar shock wave with strength of 1.47 in atmospheric air. The We and Re relating to these conditions were 6.9 x 10^3 and 1.12 x 10^5 respectively. Their work evaluated density variations and wave interaction within the water bubble using interferometric fringes after which they discussed the impact of these examinations on the bubble breakup. They also estimated the distortion and disintegration processes of the bubble using interferograms. Their results revealed that the

pressure distribution within the water droplet impacted mainly the distortion in the first and second stages of the breakup after which it became irrelevant at later stages as boundary layer stripping took over as the dominant factor. Finally, their experimental findings which investigated the stripping type breakup mechanism were concordant with the explanations offered by Wierzba and Takayama (1988) for the stripping type breakup of spherical bubbles.

Igra et al. (2002) performed experiments in a shock tube to study water droplet distortion and breakup from shock wave loading. They produced a 6.4 mm diameter water bubble inside the test section of the shock tube. They also generated a shock wave (Mach number of 1.3) at atmospheric air. They then used a double exposure finite-fringe holographic interferometry with a double path arrangement for visualization. To validate their findings, they collected and compared their interferograms of the bubble breakup process with past experiments performed at the Shock Wave Research Centre (SWRC) for various diameters and *Ma*. They showed their results in a non-dimensional manner. They then evaluated the C_D and compared it with that of spherical droplets taking into consideration the distortion of the water bubble. They observed identical trends for the spherical bubbles. Interestingly, their work revealed that the C_D reduces with a rise in the incident shock Mach number which was contrary to the findings of Ranger and Nicholls (1969), Simpkins and Bales (1972), Pilch and Erdman (1987). These authors explained that the C_D of a spherical bubble is constant over a broad range of Mach numbers. Their work computed the C_D of the water bubble for different scenarios employing different assumptions. Finally, they evaluated the C_D of the water bubble for different scenarios based on several assumptions. They explained that the C_D can be estimated more precisely by considering the mass, frontal area and velocity variations which would produce a lesser value than what was estimated without these assumptions.

Igra and Takayama (2003) experimentally examined the interaction between two cylindrical bubbles and a planar shock wave. These two water droplets had a diameter of 4.8 mm and were positioned 30 mm apart within a shock tube test section. These two bubbles were then impinged by a shock wave (Ma = 1.47) which was generated in atmospheric air. The We and Re corresponding to these flow conditions were 6.9 x 10^3 and 1.12 x 10^5 respectively. They then utilized double exposure holographic interferometry to visualize the shock/water bubble interaction. They were able to estimate the C_D of the shock impacted water bubbles from the effective visualization of the water droplets' distortion, drift, and acceleration. Their work showed that the front water bubble acted the same way a solitary water droplet would react given similar flow conditions. In contrast, the drift and acceleration of the rear water bubble was less substantial in comparison to the front droplet thus implying that the C_D of the rear bubble was less than that of the front one. This revealed that the front bubble had impacted the flow field in the vicinity of the rear water drop.

Theofanous et al. (2004) produced experimental measurements on interfacial instabilities and breakup of Newtonian liquid bubbles that had been suddenly subjected to rarefied, high speed air flows with Ma = 3. Their experimental method ensured a comprehensive observation of interfacial features and mixing for the entire duration of the breakup cycle performed for a broad span of We. They discovered that the RT instability is the active mechanism for freestream We as small as 28 (for low viscosity liquids). They also showed that stripping instead of piercing is the asymptotic regime as *We* approaches infinity. Their work proved that comprehensive visual evidence for We over 26 but less than 2600 is particularly useful for performing CFD simulations in a bid to provide and improve fundamental understanding of aero-breakup over a wide range of conditions.

Theofanous and Li (2008) utilized laser-induced fluorescence to image the experimental procedure involving the exposure of liquid drops to supersonic gas streams. Their experimental findings achieved quality images. Their experimental results revealed that past documented findings, which used the shadowgraph technique, permitted misconceptions that resulted in erroneous conceptualizations and theory of the physics that control bubble disintegration at high We > 10^3. Contrary to previous results, they explained that the governing mechanism at these high We is the shear-induced motion characterized by a major radial component and instabilities on the subsequently produced elongated

liquid sheet. On the other hand, at low $We < 10^2$, their data showed the quantitative characteristics of 'multiwave' bubble piercing induced by RT instabilities. Finally, their well resolved images present exceptionally appropriate benchmarks for Direct Numerical Simulations (DNS) of interfacial instabilities and specifically of bubble disintegration.

Theofanous et al. (2012) performed experiments and direct numerical simulations to develop the work of Theofanous and Li (2008) which concerned aerobreakup physics of water-like, low viscosity liquid bubbles to Newtonian liquids with any viscosity. Their work dealt with a broad range of aerodynamics from almost incompressible to high Mach number flows. They then validated and measured the principal physics of the Rayleigh-Taylor piercing (RTP) and Shear-Induced Entrainment (SIE) using viscosity and capillary based scalings for fluids of varying viscosity. Interestingly, their work established the importance and predictive power of linear stability analysis of the Rayleigh-Taylor and Kelvin-Helmholtz challenges for the RTP and the SIE regimes. Finally, they examined the advanced phases of bubble disintegration and the resulting particle-clouds whilst providing a distinct description and measurement of breakup times.

Theofanous et al. (2013) conducted experiments and direct numerical simulations to develop the works of Theofanous and Li (2008) which concerned aerobreakup physics of water-like, low viscosity liquid bubbles and of Theofanous et al. (2012) for Newtonian liquids of varying viscosity, to polymer-thickened liquids over a broad range of viscoelasticity. Their work dealt with a broad range of aerodynamics from almost incompressible to supersonic flows. They recorded their visualizations using $\mu s/\mu m$ resolutions. They adopted a similar scaling technique as documented in their previous research i.e., Theofanous et al. (2012) which was modified to validate and measure the key physics of the RTP and SIE regimes. The modifications are based on the shear thinning and elastic behavior of these liquids. They explained that even at conditions beyond the RTP regime, there is no breakup or observed 'particulation' but an apparent unstable bubble which have been elongated into sheets and recovered elastically to re-form an integral mass. They continued by explaining that this resistance to breakup is discovered beyond the SIE regime which is now characterized by the generation of an extensive filament which sustains a considerable level of cohesiveness until the dynamic pressure of the gas is sufficient enough to lead to filament ruptures. This then led them to define a third regime particularly for viscoelastic liquids. They called this regime the SIE for ruptures (or the SIER). They stated that beyond this regime, the degree of 'particulation' rises and the characteristic dimension of produced fragments reduces in an unending manner with rising dynamic pressure. Finally, they outlined a rheology-based scaling method for elasticity regulated 'phenomena' and proposed a way for similar representations (using polymer and solvent variations) with respect to critical rupture stress that can be quantified separately. As in their previous publication i.e., Theofanous et al. (2012), they examined the advanced phases of bubble disintegration and the resulting particle-clouds as well as provided a distinct description and measurement of breakup times.

Sembien et al. (2016) experimentally examined a complex system of waves travelling within a water column because of the impact of a plane shock wave. In their studies, they qualitatively and quantitatively studied flow characteristics like large negative pressure created by expansion wave focusing, cavitation bubble nucleation and a re-circulation zone. Several methods have been adopted to generate the water bubbles (see Joseph et al., 1999; Hirahara and Kawahashi, 1992; Igra and Takayama, 2001) but the diameter had continually been constrained to a few millimeters. Sembien et al. (2016) explained that the production of large diameter water droplets is essential for the comprehensive analysis of wave movements within the bubble, but it is difficult to maintain a cylindrical geometry of a large water bubble as the water is likely to 'splash' sideways. They overcame this challenge by applying an external force to hold the bubble walls in place. They clarified that this method would not impact the flow and test chamber transparency characteristics. They also adopted the super-hydrophobic coating methods with the coating used on a finite area of the bottom window of the test chamber. The hydrophobicity level was also selected to prevent the water from gliding sideways on the bottom window at static 'unperturbed' requirements. They then pushed an O-ring of 22mm diameter against the bottom window after which the hydrophobic coating was cautiously put on the

ambient region. The coating layer thickness was small in comparison to the channel thickness. They then utilized an air gun to accelerate the drying procedure followed by the removal of the O-ring after half an hour. The top window was then positioned in place and secured. Finally, the 22mm diameter water column was created by injecting water from a syringe inserted through a small hole positioned at the rear end of the test chamber.

2.6. Numerical investigation of shock/liquid bubble interaction

Harper et al. (1972) theoretically and numerically investigated the breakup of accelerating liquid drops. They showed that an accelerating liquid bubble under the influence of surface tension is unstable to small disturbances that are greater than the first critical value of the Bo. They used numerical and second order asymptotic techniques to characterize the normal mode reaction/behaviour and the neutral stable modes at greater Bo. They also used the initial-value challenge to study the unsteady reaction of an originally spherical bubble accelerated by an ambient gas flow. This then led them to present a theory that incorporated acceleration and aerodynamic impacts to enable them to take into consideration the complete dynamic range of We and Bo. Finally, they compared their findings with experimental measurements that comprised of nonstop vibration, permanent aerodynamic deformation and erratic fragmentation with good agreements observed.

Igra and Takayama (2001) numerically investigated the distortion and breakup of a cylindrical water drop to further elucidate the breakup process of spherical liquid bubbles by shock wave loading. They derived their numerical results by solving the Euler equations utilizing the Cubic Interpolated Pseudo-particle (CIP) technique to handle a two-phase flow field comprising of compressible and incompressible fluids. They also modified this scheme to adequately describe the gas/liquid interface and prevent any density jump from smearing across the interface. They were able to achieve this by computing the density independently for each phase independently. They estimated the density at every grid point by employing a density function in a similar manner to the CIP. Following from this, they derived a sharp density gradient for the entirety of the flow field which meant that the scheme could adequately treat gas/liquid interfaces characterized by a huge density ratio. Their numerical findings, after comparison with the suitable interferograms, revealed good quantitative agreement for the density variation in air while only qualitative concordance was obtained for water with respect to the numerical density distributions. They also compared the results they derived for the cylindrical water drop with a similar solid cylinder case. They discovered that only at the preliminary phases did the flow surrounding the water bubble resemble that noticed on a solid cylinder. Their research then showed that at approximately 40 μs, after the shock wave had impinged on the water column, some variation was noticed in the flow field close to the back of the droplet which were not observed in the numerical results produced from shock interaction with the solid cylinder. Following from this, they then concluded that the water bubble had undergone some deformation at the preliminary phase.

Quan and Schmidt (2006) numerically simulated the impulsive acceleration of a liquid spherical bubble by a gaseous flow. Their numerical studies aimed to examine drag force and bubble distortion. They studied the dynamics of this interaction by solving the incompressible Navier-Stokes equations utilizing a finite volume staggered mesh method combined with a moving mesh interface tracking scheme. They explained that the advantage of this scheme is the direct application of the interface conditions on an explicitly located interface with no thickness. Their work also showed that the bubble shape altered during droplet acceleration and the factor of distortion of the bubble is as tiny as 0.2. This then meant that they applied mesh adaption techniques to attain satisfactory mesh quality as well as effectively capture the interface curvature. Very usefully, their research showed that the total C_D was greater than the characteristic steady state C_D of solid spheres at similar Re. This conformed with the observation of Temkin and Kim (1980) whose work revealed that the unsteady drag of decelerating relative flows is always greater than the steady drag. Quan and Schmidt (2006) believed that this greater drag force could be attributed to the large recirculation region preceding the distorted bubble. They then examined the impacts of the viscosity and density ratios as well as that of the initial We on

the dynamics of the bubble. Their results showed that the initial We and viscosity ratio have considerable impacts on the bubble dynamics, but the density ratio does not. Finally, they discovered that a reduction of the surface tension resulted in a greater bubble deformation and drag force while a rise in the bubble viscosity led to smaller distortions and a reduced drag force.

Chen (2008) carried out two dimensional simulations to investigate the stripping breakup of a water droplet. They explained that the disintegration of a liquid bubble subjected to a high-speed gas flow is a popular multiphase flow problem and that the stripping breakup mechanism occurs over a broad range of We i.e., from 100 to nearly 20,000. They adopted a multiphase flow solver with a five-equation model to examine the development of the stripping breakup process for a water bubble. They carried out various test scenarios like the gas-gas shock tube, water-air shock tube, and the underwater explosion challenges to validate their numerical techniques. For comparison of their work with experimental measurements, they used water bubbles with diameters of 6.4 mm and 4.8 mm and Ma of 1.3 and 1.47. They examined the stripping breakup of a water bubble and discussed shape distortion, vortex shedding, unsteady drag force as well as flow instability. Their work showed good agreement with the experimental data in dimensionless form with respect to the bubble drift, acceleration and change in volume. Finally, they used flow visualization to display the development of a water bubble during the stripping breakup process for an inviscid flow.

Igra and Sun (2010) performed a numerical study for the loading of cylindrical water column with shock waves adopting a fully conservative scheme. This scheme, which considered subcell-sized particles like water ligaments, was applied to capture gas-liquid interfaces sharply without any difficulties associated with spurious pressure oscillations or density diffusion. The scheme could also resolve fragments smaller than 1 grid-cell size. Their results conformed well with experimental measurements with respect to the distortion and shape of the water droplet impacted by a planar shock wave with varying strengths i.e., 1.3 and 1.47. Also, good concordance was derived from the experimental analysis for changes in the shock wave location. They also revealed that it was possible to notice the beginning of fragmentation of the water bubble located at the same position as in the experimental results. Their work usefully pointed out that previously published CFD works did not consider bubble distortion but just the simulation of the early impingement of the shock wave on the water droplet. They also examined results derived from the interaction of supersonic shock wave (Ma = 3) with the water bubble. All their results revealed stripping breakup but no Rayleigh-Taylor-type oscillations/piercing thus proving that the principal mechanism for water droplet breakup is boundary-layer stripping as a result of high velocity shear flow and the gradual motion of the distorting water bubble. Finally, Igra and Sun (2010) noticed that a 2D cylindrical water column acted in the same way as a spherical bubble after they compared bubble distortion and fragmentation. They further explained that the 2D scenario allows for a more straightforward visualization when conventional methods like shadowgraph, Schlieren, and/or interferometry are applied.

Meng and Colonius (2015) numerically simulated the interaction between water cylinders and normal shocks by solving the multicomponent, compressible Euler equations. They aimed to examine the preliminary phases of break up in the cylindrical water bubbles. They set up their simulations to match and compare their findings to the experimental system of Igra and Takayama (2001). Generally, their work was able to correctly compute the cylindrical bubble's center of mass velocity, acceleration, and unsteady C_D. Their numerical work noticed qualitative breakup characteristics like original streamwise flattening of the bubble and the generation of tips at the cylinder's boundary which verified past experimental observations of stripping breakup mechanism. Interestingly, their work showed and explained the existence of a 'transitory recirculation' area at the bubble's equator and a continuous upstream jet in the wake. They investigated the impacts of the shift between subsonic and supersonic post-shock flow by broadening the incident shock Mach strengths beyond the ones that had been previously examined in experiments. They observed that velocities in the supersonic post-shock flow region did not considerably change the bubble's behavior as they were able to efficiently 'collapse' the drift, acceleration, and drag curves for all the shock Mach numbers that were simulated. They then

adopted a technique which reduced 'noise errors' to compute the cylindrical bubble's acceleration. Afterwards, they collapsed all the shock Mach numbers using the approach of scaling with the pressure ratio across the incident shock. Although they had shown that the unsteady C_D increases with time when calculated utilizing the constant initial bubble diameter, their work came up with a useful approximation as regards the computation of this parameter. This related with the estimation of the C_D as a constant throughout the initial breakup phase by adopting the cylindrical bubble's distorted diameter. Finally, they explained that within the characteristic ambiguity of the various techniques utilized to extract measurements from past experimental and numerical findings, their comparisons with different experimental bubble distortion measurements revealed good concordance.

Sembien et al. (2016) numerically investigated the interaction of a planar shock wave with a 22 mm diametrical water column. Their simulations enabled them to study the wave motions within the water bubble as well as estimate the spatial location of the expansion wave focusing point and the corresponding negative peak pressures. They concentrated on the wave propagation within the 2D water droplet during the preliminary phases of SBI following their comprehensive experimental visualization and pressure measurements. They adopted a modern method of specifically handling the test chamber windows where symmetric cylindrical water droplets of relatively large diameters were generated. The water bubble is then impacted by a shock wave produced adopting the exploding wire (EW) methods with visualization performed utilizing the shadowgraph technique. They then adopted Star-CCM+ CFD solver to conduct numerical simulations which allowed them to explicate and investigate the flow characteristics noticed in their experiments.

Xiang and Wang (2017) conducted numerical analysis on the interaction of a planar shock wave with a water bubble embedded with and without a cavity of varying sizes at higher We. They calculated their numerical fluxes using the Godunov-type Harten-Lax-van Leer contact Riemann solver together with an incremental fifth order weighted essentially non-oscillatory (WENO) scheme. WENO schemes are well-known high-order schemes for solving hyperbolic conservation laws (Lin et al., 2023) and was first presented by Liu et al. (1994). WENO schemes are particularly relevant for numerical challenges consisting of strong discontinuities and complicated smooth solution structures (Zhang and Shu, 2016). Xiang and Wang (2017) then adopted a third-order Total Variation Diminishing (TVD) Runge-Kutta scheme to advance the solution in time. A TVD scheme was first presented by Harten (1983) and can serve as a high-resolution scheme for computing the solutions of hyperbolic conservation laws. A TVD scheme is thus employed to capture sharper shock predictions and suppress spurious oscillations of the solution (Kupka et al., 2012). The research work of Xiang and Wang (2017) qualitatively and quantitatively investigated the morphology and dynamical features of the bubble deformation process to determine the disintegration mechanism as well as to show the development of transverse jets under various incident shock intensities and embedded-cavity sizes. Afterwards, they obtained the jet tip velocities by examining the evolution of the interface. Their work revealed that the liquid bubble is susceptible to aerodynamic disintegration characterized by the generation of micro-mist at advanced phases as opposed to liquid evaporation due to the insufficient heating impacts of the ambient air. They then numerically proved that the liquid-phase pressure will reduce lower than the saturated vapor pressure with this low pressure maintained for a certain time due to the expansion wave focusing. This expansion wave focusing accounted for the cavitation within the water bubble. With respect to measurements, their work identified the geometrical parameters of the distorted water bubble revealing that the centerline width reduces as opposed to the transverse height which rises in a non-linear manner with time. Interestingly, their research showed that the distortion rates compared non-linearly under various Ma with the initial transverse jet observed for a water bubble with an embedded cavity. This contrasted with the water hammer shock and the second jet which did not appear under the impact of incident shock waves with low intensity. Their recorded x-velocity component at the rear stagnation point stayed constant at the rear stagnation location for a 'comparable' time after a deteriorated development. This showed that the downstream wall of the shocked water ring somehow travelled in a uniform manner. They then clarified that the acceleration of the downstream wall is stabilized by the trailing shedding vortex. They claimed that this effect is

clearer under higher *Ma*. Finally, they compared the entire field enstrophy and discovered that the rising 'trend' is characterized by the contributed production of a vortex because of the baroclinic impacts of the shock wave's interaction on the two-phase interfaces.

Liu et al. (2018) numerically simulated liquid bubble disintegration in supersonic flows. They employed a five-equation model based on the finite-difference technique. They then used an anti-diffusion technique to improve the interface capturing quality. This anti-diffusion approach was presented as a correction of volume fraction after every computation step to sharpen the interface. They confirmed the 'robustness' of this method using the hybrid variable reconstruction in which the second order and high-order techniques were adopted in discontinuous and continuous flow fields respectively. Following the recent classification of droplet breakup regimes, their simulations fell within the shear induced entrainment regime. They stated that surface tension and viscid forces were insignificant for both 2D and 3D simulations in comparison to the momentum of the high-speed air flows. Their simulations set the inflow parameters corresponding to Ma of 1.2, 1.5 and 1.8 to attain various dynamic pressures while an initial liquid to gas density ratio of 1000 was used. Their findings revealed that the breakup process was broken into three phases which they thoroughly examined considering the gas/liquid interactions. Interestingly, their research showed that the shear between the high-speed gas flow and the liquid bubble led to surface instabilities on the windward side of the bubble while the instabilities on the leeward side was induced by vortices. They investigated the motion of the liquid center mass and examined the unsteady acceleration. Finally, they showed that the characteristic breakup time was around 1.0 using either the criterion of bubble thickness or liquid volume fraction.

Meng and Colonius (2018) performed a three-dimensional numerical simulation examining the disintegration of a spherical water bubble in the flow following a normal shock wave. Their studies employed the compressible multicomponent Euler equations in a finite-volume scheme combined with shock and interface capturing to simulate the bubble and ambient gas flow. Their work discussed the characteristics of the bubble distortion and disintegration in the stripping breakup regime as well as offered descriptions of the surrounding gas flow. Their studies of observed surface instabilities and a Fourier decomposition of the flow field showed asymmetrical azimuthal modulations and broadband instability growth which led to disordered flow inside the wake area. Finally, they compared their breakup process with available experimental visualizations which showed good qualitative agreement with respect to the bubble's early distortion and transformation into a muffin-like shape. This was succeeded by the breakup of the liquid sheet which envelops a cavity in the near -field wake area.

Kaiser et al. (2020) numerically examined the interface distortion during the early phases of the breakup of a water bubble in a surrounding flow field. They used high resolution numerical simulations taking into account the compressible Navier-Stokes equations (which control the movement of the two fluids) as well as considering capillary forces and impacts of viscosity. They modelled the multiphase flow using a level set based sharp interface method with conservative interface interaction. They then discretized the governing equations using FVM with low dissipation flux reconstruction at cell faces following a fifth-order WENO scheme and a third-order Runge-Kutta TVD explicit time integration scheme. Their results showed that they were able to attain a precise estimation of wave dynamics and interface distortion of the liquid bubble. The first and second phases of bubble deformation corresponding to flattening of the cylinder and sheet shearing at the bubble equator respectively were also successfully replicated. They revealed the formation of a clear pressure-wave pattern in the supersonic flow area close to the cylindrical bubble's equator post shock propagation. They explained that these waves interacted with the phase interface leading to the local interface disturbances which formed at the same period as the beginning of the second phase. They continued by stating that it was expedient to attain a resolution of these waves to allow for an effective 'prediction' of the hat-like structure at the upstream face of the cylinder during the second phase of the bubble disintegration which had only been noticed in experimental visualizations of this specific breakup mechanism. Their findings supported the connection of the sheet stripping mode with the local formation of recirculation zones. They pointed out that, at very preliminary phases of the shock bubble interaction, a correct prediction of the interaction between the secondary wave system and the interface instabilities is

crucial to attain a qualitative concordance between their simulations and the experimental results of Igra and Takayama (2001). Finally, their high-resolution findings showed that recirculation zones existed at several positions along the interface and are directly linked to the growth of water sheet-forming interface disturbances.

2.7. Bubble shapes employed in shock/liquid bubble interaction

Several experimental analyses (e.g., Ranger and Nicholls, 1969; 1972; Simpkins and Bales, 1972; Krzeczkowski, 1980; Wierzba and Takayama, 1988; Yoshida and Takayama, 1990; Hirahara and Kawahashi, 1992; Hsiang and Faeth, 1992; Joseph et al., 1999; Theofanous et al., 2004; Theofanous and Li, 2008; Theofanous et al., 2012; Theofanous et al., 2013) have utilized a spherical liquid bubble to visualize the 3D interaction between the travelling shock wave and the liquid column in question. However, Igra and Sun (2010) explained that 3D visualization is still evolving and wave interactions within the bubble and the wake structure have certainly not been accurately imaged. On the flip side, the interaction between a planar shock wave and a cylindrical liquid droplet, which Igra and Sun (2010) described as a 2D bubble, can be correctly studied. In order to consider the fragmentation process and elucidate the impact of wave movements within the bubble, it is essential that the head-on impingement of the liquid bubble by the shock wave is effectively visualized. The findings of such imaging can be accurately broadened to clarify complex 3D bubble fragmentation processes. Igra & Takayama (2001) and Igra et al. (2002) performed experiments detailing shock interaction with a cylindrical water droplet for various Ma and with several bubble diameters. They stated that on evaluation and comparison of the bubble distortion with that of a spherical droplet, similarities were observed. They also reported that due to the distinctive experimental set-up, the distortion of the water bubble preceding its full breakup is approximately half of what is observed in a comparable spherical droplet scenario. Igra and Takayama (2003) performed experimental analysis of two cylindrical water bubbles exposed to the loading of a planar shock wave. More recently, Sembian et al. (2016) conducted experiments involving the interaction of a planar shock wave with a cylindrical water droplet. From a numerical standpoint, several authors (e.g., Igra and Sun, 2010; Meng and Colonius, 2015; Sembien et al., 2016; Kaiser et al., 2020) have used a cylindrical droplet geometry while others (e.g., Quan and Schmidt, 2006; Theofanous et al., 2012; Theofanous et al., 2013; Meng and Colonius, 2018) have utilized a spherical bubble shape.

2.8. Conclusions

An extensive literature review has been performed to: advance the current understanding of SBI, identify suitable experimental data sets for CFD model validation, and gain the necessary knowledge for the execution of the CFD simulations. Although several past experimental works have been studied and presented in this chapter, the main experimental studies that have been adopted for the numerical model validation are: Haas and Sturtevant (1987) for shock helium bubble interaction and; Igra & Takayama (2001) & Igra et al. (2002) for shock water bubble interaction. The findings from this literature review can then be applied to simulate shock-gas and shock liquid-bubble interaction capable of attaining pressure gain in gas turbines which possesses the needed ability to hugely boost combined cycle efficiency and performance. Therefore, these investigated shock bubble interaction studies are very relevant as they have served as an efficient basis for investigating pressure gain via the interaction of a moving shock wave with a gas or liquid bubble.

3. Methodology

This chapter outlines the conservation laws/equations and the various approaches available to modelling turbulence. Detailed explanations are also provided for various simulation techniques and numerical methods available to solve shock-gas and shock-liquid problems. These include the different turbulent models, interface tracking techniques like the Volume-of-Fluid (VOF) and Level-set methods etc. This chapter thus presents a theoretical context for the understanding and applicability of the adopted numerical methods accessible on the ANSYS Fluent package.

3.1. Governing equations: general form, control volume approach

If $\phi\ (x,t)$ represents any conserved intensive property in a control volume (CV), the total amount of ϕ in CV can be expressed as:

$$\int_{CV(t)} \rho\phi(x,t)dV \tag{3.1}$$

Taking into account the fixed CV, the rate of change of ϕ in the CV with time can be described using Eq. (3.2):

$$\frac{d}{dt}\int_{CV(t)} \rho\phi(x,t)dV = \frac{\partial}{\partial t}\int_{CV(t)} \rho\phi(x,t)dV + \oint_{CS(t)}\rho\phi(x,t)\left(\vec{U}\right).ndS \tag{3.2}$$

where $\vec{U}$ and n denote the velocity vector and unit vector normal to the control surface (CS). Eq. (3.2) explains that the change in ϕ in the CV is given a property change in the CV together with its flux across the CS.

The rate of change of ϕ in the fixed CV is same as its volume and surface sources. This is shown below:

$$\frac{\partial}{\partial t}\int_{CV(t)} \rho\phi(x,t)dV + \oint_{CS(t)}\rho\phi(x,t)\left(\vec{U}\right).ndS = \int_{CV(t)} S_v(\phi)dV + \oint_{CS(t)}S_S(\phi).ndS \tag{3.3}$$

Accounting for an infinitesimal CV, Eq. (3.3) can be shown in differential form as seen below:

$$\frac{\partial\rho\phi}{\partial t} + \nabla.\left(\rho\phi\vec{U}\right) = S_V(\phi) + \nabla.S_S(\phi) \tag{3.4}$$

or

$$\frac{\partial\rho\phi}{\partial t} + \nabla.\left(\rho\phi\vec{U}\right) = S(\phi) \tag{3.5}$$

where;

$$S(\phi) = S_V(\phi) + \nabla.S_S(\phi) \tag{3.6}$$

Several authors (e.g., Batchelor, 2000; Ferziger and Peric, 2012; Aris, 2012) have expressed the governing equations of continuum mechanics in the form of Eq. (3.5)

3.1.1. Continuity/conservation of mass equation

Mass conservation in infinitesimal fluid element can be illustrated by the following equation:

$$\underbrace{\frac{\partial\rho}{\partial t}}_{\substack{rate\ of\ change\\ of\ mass\ per\ unit\\ volume\ with\ time}} + \underbrace{\nabla.\left(\rho\vec{U}\right)}_{\substack{net\ fluid\ flow\\ across\ fluid\\ element\ boundary}} = 0 \tag{3.7}$$

3.1.2. Conservation of momentum equation

Momentum conservation in infinitesimal fluid element can be illustrated by the following equation:

$$\underbrace{\frac{\partial\rho\vec{U}}{\partial t}}_{\substack{rate\ of\ change\\ of\ momentum\\ with\ time}} + \underbrace{\nabla.\left(\rho\vec{U}\otimes\vec{U}\right)}_{\substack{net\ convective\ inflow\\ of\ momentum\ due\ to\\ a\ change\ in\\ veolcity\ position}} = \underbrace{-\nabla p}_{\substack{momentum\ change\\ due\ to\ pressure}} + \underbrace{\nabla.(\bar{\bar{\tau}})}_{\substack{diffusion\ influenced\\ by\ viscous\ forces}} + \underbrace{\rho S_M}_{source\ term} \tag{3.8}$$

where $\bar{\bar{\tau}}$ denotes the viscous stress tensor, S_M is a source term that may comprise of the body forces i.e., gravity force, centrifugal force, Coriolis force and electromagnetic force.

The viscous stress tensor, $\bar{\bar{\tau}}$, is expressed below:

$$\bar{\bar{\tau}} = \mu \left[\underbrace{\left(\nabla\vec{U} + \left(\nabla\vec{U}\right)^T\right)}_{\substack{momentum\ diffusion \\ due\ to \\ linear\ deformation}} - \underbrace{\frac{2}{3}\nabla.\vec{U}I}_{\substack{momentum\ diffusion \\ due\ to \\ volume\ dilation}} \right] \tag{3.9}$$

where μ and I denote the molecular viscosity and unit tensor respectively.

3.1.3. Conservation of energy equation

Energy conservation within an infinitesimal fluid element can be illustrated below:

$$\underbrace{\frac{\partial \rho E}{\partial t}}_{\substack{rate\ of\ change \\ of\ energy \\ with\ time}} + \underbrace{\nabla.\left(\rho E\vec{U}\right)}_{\substack{rate\ of\ change \\ of\ energy\ caused \\ by\ a\ change\ in \\ velocity\ over\ location}} = \overbrace{\underbrace{-\nabla.\left(p\vec{U}\right)}_{\substack{rate\ of\ work \\ done\ induced \\ by\ pressure\ force}} + \underbrace{\nabla.\left[\mu\left(\nabla\vec{U} + \left(\nabla\vec{U}\right)^T\right)\vec{U} - \left(\frac{2}{3}\mu\left(\nabla.\vec{U}I\right)\vec{U}\right)\right]}_{\substack{rate\ of\ work \\ done\ induced \\ by\ viscous\ forces}}}^{rate\ of\ work\ done\ induced\ by\ surface\ forces} +$$

$$\underbrace{\rho\dot{q} + \nabla.\left(k\nabla T\right)}_{\substack{net\ heat\ influx \\ into\ element}} + \underbrace{\rho\vec{U}S_E}_{\substack{source \\ term}} \tag{3.10}$$

where k, $\dot{q}$, and T represent the thermal conductivity, rate of volumetric heat addition per unit mass and temperature respectively. E denotes the total energy equivalent to the addition of the internal energy e (per unit mass) and kinetic energy $\vec{U}^2/2$ (per unit mass). Source term, S_E, may comprise of body forces which influence total energy. Therefore, Eq. (3.10) can also be expressed as:

$$\frac{\partial\left(\rho\left(e + \left(\vec{U}^2/2\right)\right)\right)}{\partial t} + \nabla.\left(\rho\left(e + \frac{\vec{U}^2}{2}\right)\vec{U}\right) = \nabla.\left(p\vec{U}\right) + \nabla.\left[\mu\left(\nabla\vec{U} + \left(\nabla\vec{U}\right)^T\right)\vec{U} - \left(\frac{2}{3}\mu\left(\nabla.\vec{U}I\right)\right)\vec{U}\right] + \rho\dot{q} + \nabla.\left(k\nabla T\right) + \rho\vec{U}S_E \tag{3.11}$$

Anderson (1995) also explained that with some manipulations and algebra, Eq. (3.11) can be used to obtain the transport equation for kinetic energy, internal energy and enthalpy equation. Anderson (1995) also explained that the continuity, momentum and energy conservation equations are coupled system of non-linear partial differential equations (PDEs) and hence are quite complicated to solve analytically. As such, there is no overall closed form of solution to the governing equations above. Eqs. (3.7), (3.8) and (3.10) reveal several unknown and dependent variables i.e., five equations and six unknown flow-field variables (ρ, p, U_x, U_y, U_z, and e). Several authors (e.g., Anderson, 1995; Versteeg and Malalasekera, 2007) explained that the Navier-Stokes equation system can be closed by introducing the equation of state for pressure i.e., $p = p(\rho, T)$ and internal energy, $i = i(\rho, T)$ which presents seven equations and one extra variable (seven equations and seven flow field variables).

3.2. Approaches to modelling turbulence

Turbulence leads to the appearance of eddies in the flow with a broad range of length and time scales that interact in a dynamically complicated manner. In this regard, a huge level of research has been directed at the development of numerical methods that capture the essential impact of turbulence. The methods can be categorized into the following three classes:

3.2.1. Turbulence models for Reynolds-averaged Navier-Stokes (RANS) equations

These models lay emphasis on the mean flow and the impacts of turbulence on mean flow characteristics. Before the application of numerical methods, the Navier-Stokes equations are time averaged, or ensemble averaged in flows with time dependent boundary conditions. Additional terms appear in the time-averaged (or Reynolds-Averaged) flow equations because of the interactions between different turbulent fluctuations. These additional terms are modelled with classical turbulence models with $k-\varepsilon$ and the Reynolds stress turbulence models being the most popularly common ones. They also require modest computing resources to attain a relatively precise flow simulation. As a result, this approach has been the basis for most engineering flow computations in the past three decades (Versteeg and Malalasekera, 2007).

3.2.2. Large eddy simulations (LES)

This approach represents the intermediate form of turbulence computations which focuses on the behavior of the larger eddies. This technique entails the space filtering of the unsteady Navier-Stokes equations before computations are performed. This filtering process permits the larger eddies and discards the smaller ones. The sub-grid scale model introduces this impact on the resolved flow i.e., mean flow together with the large eddies as a result of the smallest, unresolved eddies. It can be used to treat Unsteady CFD challenges with complex geometry but places a high strain on computing resources with respect to large storage requirement and the constraint of a huge volume of computations (Versteeg and Malalasekera, 2007).

3.2.3. Direct numerical simulations (DNS)

These approaches calculate the mean flow and all turbulent velocity fluctuations. They solve the unsteady Navier-Stokes equations on spatial grids which are adequately fine to resolve the Kolmogorov length scales. There is also dissipation of energy and the need for appropriately small-time steps to resolve the period of the quickest fluctuations. These computations are very expensive with respect to computing resources and as a result, this approach is not readily applied for industrial flow simulations (Versteeg and Malalasekera, 2007).

Based on these three approaches, this research has adopted and tested turbulence models for unsteady RANS equations (URANS). This is because the RANS approach is uncomplicated, computationally cheap and more economical than more detailed techniques like the LES, hybrid RANS/LES and DNS. As a result, it has been widely applied in industry for different applications like design, assessment and optimization, prediction of off-design performance (Hanjalic, 2005) etc.

3.3. The governing equations for URANS

Generally, the RANS model, which represents the most extensively adopted approach for computing industrial flows, solves the ensemble-/time-averaged Navier-Stokes equations (ANSYS, 2018). Yang (2014) expressed the URANS governing equations as shown below:

$$\frac{\partial \overline{U}_i}{\partial x_i} = 0 \tag{3.12}$$

$$\frac{\partial \overline{U}_i}{\partial t} + \frac{\partial \left(\overline{U}_i \overline{U}_j\right)}{\partial x_j} = -\frac{1}{\rho}\frac{\partial \bar{P}_i}{\partial x_j} + \frac{\partial}{\partial x_j}\left[\nu \frac{\partial (\overline{U}_i)}{\partial x_j}\right] - \frac{\partial \left(\overline{u_i u_j}\right)}{\partial x_j} \tag{3.13}$$

ANSYS (2018) also explains that in Reynolds averaging, the solution variables in the instantaneous (exact) Navier-Stokes equations are decomposed into the mean i.e., ensemble-averaged or time-averaged and fluctuating components. The velocity components can be expressed as shown below;

$$u_i = \bar{u}_i + u_i' \,, \tag{3.14}$$

where $\bar{u}_i$ represents the mean velocity component and u_1' represents the fluctuating velocity component. i can take values from 1 to 3. Similarly, for pressure and other scalar parameters, the representation below can be used:

$$\varphi = \bar{\varphi} + \varphi' \,, \tag{3.15}$$

where φ represents any scalar quantity such as pressure, energy, or species concentration. Placing expressions in the form of Eq. (3.14) and (3.15) into the instantaneous continuity and momentum equations, performing a time average and dropping the overbar on the mean velocity gives the ensemble-averaged momentum equations, which is expressed in Cartesian tensor form as:

$$\frac{\partial \rho}{\partial t} + \frac{\partial}{\partial x_i}(\rho u_i) = 0 \tag{3.16}$$

$$\frac{\partial}{\partial t}(\rho u_i) + \frac{\partial}{\partial x_j}(\rho u_i u_j) = -\frac{\partial p}{\partial x_i} + \frac{\partial}{\partial x_j}\left[\mu\left(\frac{\partial u_i}{\partial x_j} + \frac{\partial u_j}{\partial x_j} - \frac{2}{3}\delta_{ij}\frac{\partial u_i}{\partial x_j}\right)\right] + \frac{\partial}{\partial x_j}\left(-\rho\overline{u_i' u_j'}\right) \tag{3.17}$$

Eqs. (3.16) and (3.17) above are referred to as RANS equations and have a similar general form as the instantaneous Navier-Stokes equations with the velocities and other solution parameters now denoting the ensemble-averaged or time-averaged values. Eq. (3.17) also shows some extra terms which denote turbulence effects with the need to model the Reynold stresses, $-\rho\overline{u_i' u_j'}$. ANSYS (2018) explains that for variable density flows, Eqs. (3.16) and (3.17) can be taken as Favre-averaged Navier-Stokes equations (Hinze, 1975), where the velocities now represent mass-averaged values.

3.4. Turbulence models

ANSYS Fluent has several Turbulence models as shown in Fig. 3.1 below:

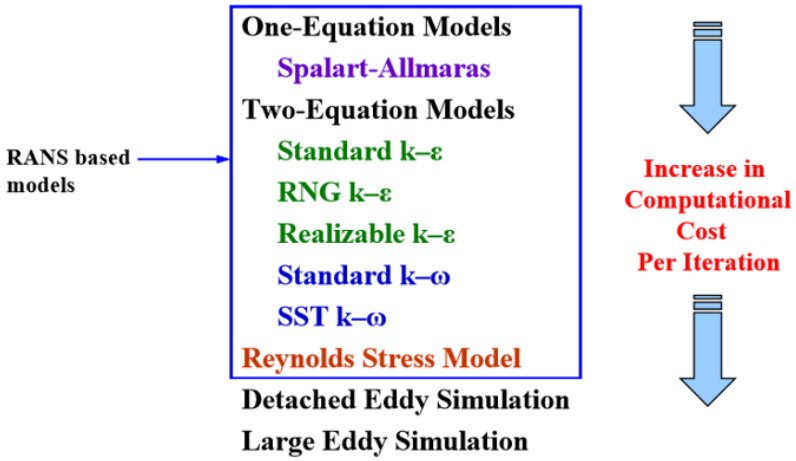

Figure 3.1: Turbulence Models Available in Fluent (ANSYS, 2018)

Fig. 3.1 represents the various turbulence models available on ANSYS Fluent with an increase in complexity and computational cost from top to bottom. This research has tried to investigate the effects of the standard k-ε, realizable k-ε, SST k-ω, and Reynolds stress on SBI thus necessitating the elaborate examination of the theories within these models.

3.4.1. The standard k-ε turbulence model

This is a two-equation turbulence models which permits the estimation of turbulent length and scale by solving two separate transport equations. It was introduced by Launder and Spalding (1972) and is characterised by stability, reduced cost, and realistic precision on a broad scale with wide applications in industrial flows and heat transfer simulations. It is also a semi-empirical model which relies on model transport equations (Launder and Spalding, 1972) for the turbulence kinetic energy, *k*, (obtained from the exact equation) and dissipation rate, ε. (derived from physical reasoning). To derive this model, it is assumed that the flow is fully turbulent, and the impacts of molecular viscosity can be ignored.

k and ε are derived from the transport equations as shown below:

$$\frac{\partial}{\partial t}(\rho k) + \frac{\partial}{\partial x_i}(\rho k u_i) = \frac{\partial}{\partial x_j}\left[\left(\mu + \frac{\mu_t}{\sigma_k}\right)\frac{\partial k}{\partial x_j}\right] + G_k + G_b - \rho\varepsilon - Y_M + S_k \tag{3.18}$$

and,

$$\frac{\partial}{\partial t}(\rho \varepsilon) + \frac{\partial}{\partial x_i}(\rho \varepsilon u_i) = \frac{\partial}{\partial x_j}\left[\left(\mu + \frac{\mu_t}{\sigma_\varepsilon}\right)\frac{\partial \varepsilon}{\partial x_j}\right] + C_{1\varepsilon}\frac{\varepsilon}{k}(G_k + C_{3\varepsilon}G_b) - C_{2\varepsilon}\rho\frac{\varepsilon^2}{k} + S_\varepsilon \tag{3.19}$$

From Eqs. (3.18) and (3.19), G_k denotes the production of turbulence kinetic energy influenced by the mean velocity gradients and computed as given below:

$$G_k = -\rho\overline{u_i' u_j'}\frac{\partial u_j}{\partial x_i} \tag{3.20}$$

G_k can also be computed in a way that is consistent with the Boussinesq hypothesis as given below:

$$G_k = \mu_t S^2 \tag{3.21}$$

where S is the modulus of the mean rate-of-strain tensor given as:

$$S \equiv \sqrt{2S_{ij}S_{ij}} \tag{3.22}$$

G_b denotes the generation of turbulence kinetic energy as a result of buoyancy computed as shown below:

$$G_b = \beta g_i \frac{\mu_t}{Pr_t}\frac{\partial T}{\partial x_i} \tag{3.23}$$

where Pr_t denotes the turbulent Prandtl number for energy (with default value = 0.85 for the standard and realizable k- ε) and g_i represents the i^{th} direction component of the gravitational vector. The thermal expansion coefficient, β is given as:

$$\beta = -\frac{1}{\rho}\left(\frac{\partial \rho}{\partial T}\right)_p \tag{3.24}$$

For ideal gases, Eq. (3.23) becomes:

$$G_b = -g_i \frac{\mu_t}{\rho Pr_t} \frac{\partial \rho}{\partial x_i} \tag{3.25}$$

Henkes et al. (1991) also expressed the degree to which the dissipation rate, ε, is impacted by the buoyancy as determined by the constant $C_{3\varepsilon}$ which is not specified on ANSYS fluent but can be computed using Eq. (3.26) below:

$$C_{3\varepsilon} = tanh \left| \frac{v}{u} \right| \tag{3.26}$$

where v and u represent the flow velocity components parallel and perpendicular to the gravitational vector. respectively ANSYS (2018) thus explains that $C_{3\varepsilon}$ will be unity for buoyant shear layers where there exists an alignment between the main flow and gravity direction but will be zero when the buoyant shear layers are perpendicular to the gravitational vector. From Eq. (3.18), Y_M denotes the fluctuating dilatation contribution (in compressible turbulence) to the total dissipation rate and expressed below:

$$Y_M = 2\rho\varepsilon M_t^2 \tag{3.27}$$

where, M_t denotes the turbulent Mach number given as:

$$M_t = \sqrt{\frac{k}{a^2}} \tag{3.28}$$

where a is the sound speed $\equiv \sqrt{\gamma RT}$

From Eq. (3.19), $C_{1\varepsilon}$, $C_{2\varepsilon}$ and $C_{3\varepsilon}$ are constants with default values 1.44, 1,92 and 0.09 respectively; while σ_k and σ_ε are turbulent Prandtl numbers for k and ε respectively and have default values 1.0 and 1.3 respectively. S_k and S_ε are user-defined source terms (Launder and Spalding, 1972). μ_t denotes the turbulent (or eddy) viscosity and calculated by combining k and ε given below:

$$\mu_t = \rho C_\mu \frac{k^2}{\varepsilon} \tag{3.30}$$

where C_μ represents a constant.

3.4.2. The realizable k-ε turbulence model

This model represents a variant or modification to the standard k-ε model to enhance its performance (Shih et al., 1995). This model is different from the standard k- ε as it comprises a different formulation for the turbulent viscosity and its modified transport equation for the dissipation rate, ε, has been obtained from an exact equation for the transport of the mean-square vorticity fluctuation. It is also called realizable as it fulfils certain mathematical constraints on the Reynolds stresses thus conforming to the physics of turbulent flows (standard k-ε and RNG k-ε models are not realizable)

The Boussinesq relationship and the eddy viscosity definition can be combined to fully understand the mathematics that drives this model which yields the normal Reynolds stress in an incompressible strained mean flow as shown below:

$$\overline{u^2} = \frac{2}{3}k - 2v_t\frac{\partial U}{\partial x} \tag{3.31}$$

From Eq. (3.31), and when $v_t \equiv \mu_t/\rho$, yields the case where the normal stress, $\overline{u^2}$, which is a positive quantity, becomes negative i.e., becomes non-realizable when the strain is substantial enough to satisfy the relation below:

$$\frac{k}{\varepsilon}\frac{\partial U}{\partial x} > \frac{1}{3C_\mu} \approx 3.7 \tag{3.32}$$

In the same way, ANSYS (2018) explains that Schwarz inequality for shear stresses ($\overline{u_\propto}\overline{u}_\beta^2 \leq \overline{u_\propto^2 u_\beta^2}$; with no summations on α and β) can be ignored when the mean strain rate is large. It continues by stating the easiest way to attain realizability, i.e., positivity of normal stresses and Schwarz inequality for shear stresses, is to vary the constant, C_μ, by sensitizing it to the mean flow i.e., mean distortion and the turbulence (k, ε). C_μ has been used extensively by many researchers (e.g., Reynolds, 1987) and has been sufficiently validated by experimental support where it is discovered to have a value of 0.09 and 0.05 for a logarithmic layer of equilibrium boundary layers and for a strong homogenous flow respectively. The realizable k-ε turbulence model is a massive upgrade on its standard k-ε counterpart for cases where the flow structures include strong streamline curvature, vortices and rotation. This model also has proven competencies for a broad range of flows (Shih et al., 1995; Kim et al., 1997) like rotating homogeneous shear flows, free flows including jets and mixing layers, channel and boundary layer flows, and separated flows with performances significantly better than the standard k- ε model. Finally, this model can calculate the spreading rate for axisymmetric jets and planar jets, i.e., possesses good resolution of the round-jet anomaly. These reasons have ensured that this turbulence model is applied in this research.

Another weakness of the standard k-ε model or other traditional k-ε turbulence models abound in the modelled equation for ε. For the standard k-ε model or other traditional k-ε turbulence models, the popular round-jet anomaly based on the discovery that the prediction of the spreading rate for axisymmetric jets is unexpectedly poor mainly attributable to the modelled dissipation equation. Thus, the realizable k-ε Turbulence Model introduced by Shih et al. (1995) was intended to address the shortcomings of the traditional k-ε Turbulence Models by incorporating; a novel eddy-viscosity formula comprising a variable C_μ originally introduced by Reynolds (1987); and a new model equation for ε dependent on the dynamic equation for the fluctuation of the mean-square vorticity. ANSYS (2018) warns that creation of non-physical turbulent viscosities in cases when the computational domain has rotating and stationary fluid zones like multiple reference frames, rotating sliding meshes etc. poses a drawback for the realizable k-ε Turbulence Model. This is because this model incorporates the impacts of mean rotation in the definition of turbulent viscosity (see Eq. (3.30) above and Eqs. (3.38) and (3.39) below).

ANSYS (2018) derived the modelled transport equations for k and ε in the realizable k-ε model as given below:

$$\frac{\partial}{\partial t}(\rho k) + \frac{\partial}{\partial x_j}(\rho k u_j) = \frac{\partial}{\partial x_j}\left[\left(\mu + \frac{\mu_t}{\sigma_k}\right)\frac{\partial k}{\partial x_j}\right] + G_k + G_b - \rho\varepsilon - Y_M + S_k \tag{3.33}$$

And,

$$\frac{\partial}{\partial t}(\rho\varepsilon) + \frac{\partial}{\partial x_i}(\rho\varepsilon u_j) = \frac{\partial}{\partial x_j}\left[\left(\mu + \frac{\mu_t}{\sigma_\varepsilon}\right)\frac{\partial \varepsilon}{\partial x_j}\right] + \rho C_1 S\varepsilon - \rho C_2\frac{\varepsilon^2}{k + \sqrt{v\varepsilon}} + C_{1\varepsilon}\frac{\varepsilon}{k}C_{3\varepsilon}G_b + S_\varepsilon \tag{3.34}$$

where:

$$C_1 = max\left[0.43, \frac{\eta}{\eta + 5}\right] \tag{3.35}$$

$$\eta = S\frac{k}{\varepsilon} \tag{3.36}$$

$$S = \sqrt{2S_{ij}S_{ij}} \tag{3.37}$$

From Eqs. (3.33) and (3.34) above, G_k, G_b and Y_M denote the same parameters (and have the same equations) as detailed in Eqs. (3.20), (3.23), and (3.27)). C_2 and $C_{1\varepsilon}$ represent constants with default values of 1.44 and 1.9 respectively and are selected to enable the model to work appropriately for particular canonical flows. σ_k and σ_ε represent the turbulent Prandtl numbers for *k* and ε respectively having default values of 1.0 and 1.2 respectively.

From Eq. (3.34), the production term in the ε equation i.e., the second term on the right-hand side, does not require the production of *k* as it does not comprise the same G_k term as seen in the standard k- ε turbulence model. This present equation structure more appropriately denotes the spectral energy transfer. Also, there exists a destruction term i.e., the third term on the right-hand side of Eq. (3.34) which has no singularity as it denominator never disappears even when *k* disappears or tends towards 0 or even gets negative. The standard *k*-ε model has a singularity due to *k* in the denominator.

The eddy viscosity for the realizable *k*-ε turbulence model is same as in the standard *k*-ε turbulence model. However, for the realizable *k*-ε turbulence model, the constant, C_μ, is calculated as shown below:

$$C_\mu = \frac{1}{A_0 + A_s\frac{kU^*}{\varepsilon}} \tag{3.38}$$

where:

$$U^* \equiv \sqrt{S_{ij}S_{ij} + \tilde{\Omega}_{ij}\tilde{\Omega}_{ij}} \tag{3.39}$$

and,

$$\tilde{\Omega}_{ij} = \Omega_{ij} - 2\varepsilon_{ijk}\omega_k \tag{3.40}$$

$$\Omega_{ij} = \overline{\Omega_{ij}} - \varepsilon_{ijk}\omega_k \tag{3.41}$$

where Ω_{ij} denotes the mean rate-of-rotation tensor viewed in a moving reference frame with the angular velocity, ω_k. A_0 and A_s which represent the model constants represented by:

$$A_0 = 4.04 \tag{3.42}$$

and,

$$A_s = \sqrt{6}cos\varphi \tag{3.43}$$

where:

$$\varphi = \frac{1}{3}cos^{-1}(\sqrt{6}W) \tag{3.44}$$

and,

$$W = \frac{S_{ij}S_{jk}S_{ki}}{\tilde{S}^3} \tag{3.45}$$

$$\tilde{S} = \sqrt{S_{ij}S_{ij}} \tag{3.46}$$

$$S_{ij} = \frac{1}{2}\left(\frac{\partial u_j}{\partial x_i} + \frac{\partial u_i}{\partial x_j}\right) \tag{3.47}$$

From Eqs. (3.30) and (3.38), it is evident that the constant, C_μ, is dependent on the mean strain and rotation rates, the angular velocity of the system rotation as well as the turbulence fields, *k* and ε. ANSYS (2018) also assigns a standard value of 0.09 for an initial sublayer in an equilibrium boundary layer to C_μ. The values for $C_\mu = 0.09$ and $A_0 = 4.04$ have been used (particularly for the realizable *k*-ε turbulence model) as they are default values recommended by ANSYS Fluent and yielded desirable results for the simulated cases.

3.4.3. Shear-stress transport (SST) k-ω model

The standard *k*- ω model is an empirical model dependent on model transport equations for the turbulence kinetic energy, *k*, and the specific dissipation rate, ω, which is synonymous to the ratio of the dissipation rate to the turbulence kinetic energy i.e., ε/k (Wilcox, 1998). The standard *k*-ω model adopts the Wilcox *k*-ω model (Wilcox, 1998) which inputs modifications for the impact of low Re, compressibility and shear flow spreading. However, the Wilcox model is limited with respect to the solutions' sensitivity to values for *k* and ω particularly outside the shear layer i.e., freestream sensitivity. The Baseline (BSL) *k*- ω model was introduced by Menter (2009) to ensure the efficient combination of the robust and precise formulation of the *k*- ω model in the wall vicinity region with the freestream independence of the k- ε model in the far field. The BSL *k*- ω model is more advanced than the standard *k*- ω model based on the three refinement processes. First, the standard *k*- ω and the transformed *k*- ε models are multiplied by a blending function after which both models are summed up. The blending function is designed to be unity in the vicinity of the wall region thus activating the standard *k*- ω model, while it is set to 0 away from the surface thus activating the transformed *k*- ε model. Secondly, the BSL model adopts a damped cross-diffusion derivative term in ω. Finally, the BSL model incorporates different modelling constants. The transport equations for the BSL *k*- ω model closely resemble the standard *k*- ω model:

$$\frac{\partial}{\partial t}(\rho k) + \frac{\partial}{\partial x_i}(\rho k u_i) = \frac{\partial}{\partial x_j}\left(\Gamma_k \frac{\partial k}{\partial x_j}\right) + G_k - Y_k + S_k \tag{3.48}$$

and,

$$\frac{\partial}{\partial t}(\rho \omega) + \frac{\partial}{\partial x_j}(\rho \omega u_j) = \frac{\partial}{\partial x_j}\left(\Gamma_\omega \frac{\partial \omega}{\partial x_j}\right) + G_\omega - Y_\omega + D_\omega + S_\omega \tag{3.49}$$

From Eq. (3.48) above, G_k denotes the production of turbulent kinetic energy and is expressed in a similar fashion as the standard $k-\omega$ and realizable $k-\varepsilon$ model. G_ω, from Eq. (3.49), denotes the production of ω and is computed using:

$$G_\omega = \frac{\alpha\alpha^*}{v_t} G_k \tag{3.50}$$

The formulation given in Eq. (3.50) above varies from the standard k- ω model with respect to the manner in which the term, α_∞, is estimated. For the standard k- ω model, α_∞ is expressed as a constant, i.e., 0.52 while for the BSL k- ω model, it is given as:

$$\alpha_\infty = F_1 \alpha_{\infty,1} + (1 - F_1)\alpha_{\infty,2} \tag{3.51}$$

where:

$$\alpha_{\infty,1} = \frac{\beta_{i,1}}{\beta^*_\infty} - \frac{\kappa^2}{\sigma_{\omega,1}\sqrt{\beta^*_\infty}} \tag{3.52}$$

$$\alpha_{\infty,2} = \frac{\beta_{i,2}}{\beta^*_\infty} - \frac{\kappa^2}{\sigma_{\omega,2}\sqrt{\beta^*_\infty}} \tag{3.53}$$

and $\kappa = 0.41$. Y_k and Y_ω denote the dissipation of k and ω as a result of turbulence. The dissipation of k is given as:

$$Y_k = \rho\beta^* f_{\beta^*} k\omega \tag{3.54}$$

where:

$$f_{\beta^*} = \begin{cases} 1, & \chi_k \le 0 \\ \frac{1+680\chi_k^2}{1+400\chi_k^2}, & \chi_k > 0 \end{cases} \tag{3.55}$$

where:

$$\chi_k \equiv \frac{1}{\omega^3}\frac{\partial k}{\partial x_j}\frac{\partial \omega}{\partial x_j} \tag{3.56}$$

and

$$\beta^* = \beta^*_i[1 + \zeta^* F(M_t)] \tag{3.57}$$

$$\beta^*_i = \beta^*_\infty \left(\frac{4/15 + \left(Re_t/R_\beta\right)^4}{1 + \left(Re_t/R_\beta\right)^4} \right) \tag{3.58}$$

where $\zeta^* = 1.5$; $R_\beta = 8$ and $\beta^*_\infty = 0.09$

and,

$$Re_t = \frac{\rho k}{\mu\omega} \tag{3.59}$$

For the BSL k- ω model, f_{β^*} is unity and thus Eq. (3.54) reduces to:

$$Y_k = \rho\beta^* k\omega \tag{3.60}$$

The dissipation of ω is given by:

$$Y_\omega = \rho\beta f_\beta \omega^2 \tag{3.61}$$

where:

$$f_\beta = \frac{1+70\chi_\omega}{1+80\chi_\omega} \tag{3.62}$$

$$\chi_\omega = \left| \Big/_{(\beta^*_\infty \omega)^3} \right| \tag{3.63}$$

$$\Omega_{ij} = \frac{1}{2}\left(\frac{\partial u_i}{\partial x_j} - \frac{\partial u_j}{\partial x_i}\right) \tag{3.64}$$

where the strain rate tensor, S_{ij}, is given below:

$$S_{ij} = \frac{1}{2}\left(\frac{\partial u_j}{\partial x_i} + \frac{\partial u_i}{\partial x_j}\right) \tag{3.65}$$

Eq. (3.65) above comprises both the rotation and strain tensors which suppresses the creation of eddy viscosity and consequently suppresses the eddy viscosity itself at locations where the measure of vorticity is greater than the strain rate. β in Eq. (3.61) is given as:

$$\beta = \beta_i\left[1 - \frac{\beta_i^*}{\beta_i}\zeta^* F(M_t)\right] \tag{3.66}$$

The compressibility function, $F(M_t)$, is given below:

$$F(M_t) = \begin{cases} 0, & M_t \le M_{to} \\ M_t^2 - M_{to}^2, & M_t > M_{to} \end{cases} \tag{3.67}$$

where:

$$M_t^2 = \frac{2k}{a^2} \tag{3.68}$$

and $M_{to} = 0.25$ while a is given as:

$$a = \sqrt{\gamma RT} \tag{3.69}$$

ANSYS (2018) explains that for the high Re scenario of the k-ω model, $\beta_i^* = \beta_\infty^*$. For the incompressible case, $\beta^* = \beta_i^*$. The standard k- ω model constants as adopted by ANSYS (2017)

are: $\alpha_\infty^* = 1$; $\alpha_\infty = 0.52$; $\alpha_0 = \frac{1}{9}$; $\beta_\infty^* = 0.09$; $\beta_i = 0.072$; $R_\beta = 8$; $R_k = 6$; $R_\omega = 2.95$; $\zeta^* = 1.5$; $M_{to} = 0.25$; $\alpha_k = \alpha_\omega = 2$.

For the standard k-ω model, β_i is described as a constant with the default value of 0.072 while Eq. (3.62) describes f_β. However, for the BSL k-ω model, f_β is unity and Eq. (3.61) is reduced to:

$$Y_\omega = \rho\beta\omega^2 \tag{3.70}$$

Also, for the BSL k-ω model, β_i, as opposed to having a constant value, is derived as:

$$\beta_i = F_1\beta_{i,1} + (1 - F_1)\beta_{i,2} \tag{3.71}$$

F_1 is described by Eq. (3.78), and the default constant value of 0.072 is still used for β_i in low Re correction for BSL to describe α_0^* as seen in Eq. (3.72) below:

$$\alpha_0^* = \frac{\beta_i}{3} \tag{3.72}$$

As the BSL k-ω model is dependent on both the standard k-ω model and the standard k-ε model (ANSYS, 2018), there is then a need to change the standard k-ε model into k and ω adopted equations to allow for the combination of these two models together. This then leads to the adoption of a cross-diffusion term, as seen as the fourth term on the right-hand-side of Eq. (3.49) shown below:

$$D_\omega = 2(1 - F_1)\rho\frac{1}{\omega\sigma_{\omega,2}}\frac{\partial k}{\partial x_j}\frac{\partial \omega}{\partial x_j} \tag{3.73}$$

From Eqs. (3.48) and (3.49), Γ_k and Γ_ω denote the effective diffusivities for the BSL *k*- ω model as derived below:

$$\Gamma_k = \mu + \frac{\mu_t}{\sigma_k} \tag{3.74}$$

$$\Gamma_\omega = \mu + \frac{\mu_t}{\sigma_\omega} \tag{3.75}$$

where σ_k and σ_ω represent the turbulent Prandtl numbers for *k* and ω respectively and are expressed as:

$$\sigma_k = \frac{1}{F_1/\sigma_{k,1} + (1 - F_1)/\sigma_{k,2}} \tag{3.76}$$

$$\sigma_\omega = \frac{1}{F_1/\sigma_{\omega,1} + (1 - F_1)/\sigma_{\omega,2}} \tag{3.77}$$

where F_1 denotes the blending function and given as:

$$F_1 = tanh(\Phi_1^4) \tag{3.78}$$

$$\Phi_1 = min\left[max\left(\frac{\sqrt{k}}{0.09\omega y}, \frac{500\mu}{\rho y^2\omega}\right), \frac{4\rho k}{\sigma_{\omega,2}D_\omega^+ y^2}\right] \tag{3.79}$$

$$D_{\omega}^{+} = max\left[2\rho\frac{1}{\sigma_{\omega,2}}\frac{1}{\omega}\frac{\partial k}{\partial x_j}\frac{\partial \omega}{\partial x_j}, 10^{-10}\right] \tag{3.80}$$

where y represents the distance to the next surface and D_{ω}^{+} denotes a positive portion of the cross-diffusion term. The turbulent viscosity, μ_t, is given by:

$$\mu_t = \alpha^* \frac{\rho k}{\omega} \tag{3.81}$$

Constants $\sigma_{k,1}$, $\sigma_{\omega,1}$, $\sigma_{k,2}$, $\sigma_{\omega,2}$, $\beta_{i,1}$ and $\beta_{i,2}$ for the BSL k-ω model have default values of 2.0, 2.0, 1.0, 1.168, 0.075 and 0.0828 respectively. Other constants like; α_{∞}^{*}; α_{∞}; α_0; β_{∞}^{*}; β_i; R_{β}; R_k; R_{ω}; ζ^*; M_{to}; α_k, and α_{ω} have equivalent default values as the standard k-ω model.

The SST *k*-ω model incorporates all the refinements of the BSL *k*-ω model, and also considers the transport of the turbulence shear stress in turbulent viscosity description thus ensuring that this model possesses more accuracy and reliability for a broader range of flows like the adverse pressure gradient flows, airfoils, transonic shock waves compared to the standard and the BSL k-ω model. The BSL model merges the merits of the Wilcox and the k-ε model but is unable to properly estimate the start and amount of flow separation from smooth surfaces. This is because both models do not consider the transport of the turbulent shear stress thus leading to an overproduction of the eddy-viscosity. The appropriate transport behaviour can be derived by using a constraint to the formulation of the eddy-viscosity as shown below:

$$\mu_t = \frac{\rho k}{\omega}\frac{1}{max\left[\frac{1}{\alpha^*}, \frac{SF_2}{a_1\omega}\right]} \tag{3.82}$$

where S is the magnitude of strain rate and the coefficient α^* is defined as:

$$\alpha^* = \alpha_{\infty}^{*}\left(\frac{\alpha_0^* + Re_t/R_k}{1 + Re_t/R_k}\right) \tag{3.83}$$

where:

$$Re_t = \frac{\rho k}{\mu\omega} \tag{3.84}$$

and: $R_k = 6$. α_0^* is as defined by Eq. (3.72). F_2 can be expressed as:

$$F_2 = tanh(\Phi_2^2) \tag{3.85}$$

$$\Phi_2 = max\left[2\frac{\sqrt{k}}{0.09\omega y}, \frac{500\mu}{\rho y^2 \omega}\right] \tag{3.86}$$

where y denotes the distance to the next surface. Constants $\sigma_{k,1}$, $\sigma_{\omega,1}$, $\sigma_{k,2}$, $\sigma_{\omega,2}$, a_1, $\beta_{i,1}$ and $\beta_{i,2}$ for the SST *k*-ω model have default values of 1.176, 2.0, 1.0, 1.168, 0.31, 0.075 and 0.0828 respectively. Other constants like; α_{∞}^{*}; α_{∞}; α_0; β_{∞}^{*}; R_{β}; R_k; R_{ω}; ζ^*; M_{to}; and $\propto_k$, have equivalent default values as the standard *k*-ω model.

3.4.4. Reynolds stress model

Yang (2014) notes that the averaging procedure presents some unknown terms such as the Reynolds stresses $\left(-\partial\left(\overline{u_\iota u_j}\right)/\partial x_j\right)$. These Reynolds stresses have been given by a turbulence model before the governing equations can be solved.

Several turbulence models have been developed till date and this research looks to utilise the most advanced turbulence models like the Reynolds stress model (RSM), which computes the Reynolds stresses utilising transport equations as opposed to approximating them adopting other techniques such as an eddy viscosity approach like the *k*-epsilon model. The Reynolds stress transport equations can be obtained from the Navier-Stokes equations and can thus be derived, ignoring body and rotation forces as follows:

$$\frac{\partial\left(\overline{u_\iota u_j}\right)}{\partial t}+\frac{\partial\left(\overline{U}_k\overline{u_\iota u_j}\right)}{\partial x_k} = -\left[\overline{u_\iota u_k}\frac{\partial\left(\overline{U}_j\right)}{\partial x_k}+\overline{u_j u_k}\frac{\partial\left(\overline{U}_j\right)}{\partial x_k}\right]+\frac{\partial}{\partial x_k}\left[\nu\frac{\partial\left(\overline{u_\iota u_j}\right)}{\partial x_k}-\overline{u_\iota u_j u_k}-\overline{\frac{p}{\rho}\left(u_\iota\delta_{jk}+u_j\delta_{\iota k}\right)}\right]+\overline{\frac{p}{\rho}\left[\frac{\partial u_\iota}{\partial x_j}+\frac{\partial u_j}{\partial x_\iota}\right]} - 2\nu\overline{\frac{\partial u_\iota}{\partial x_k}\frac{\partial u_j}{\partial x_k}} \tag{3.87}$$

The two terms on the left-hand side of Eq. (3.87) above denote the time derivative and convection term. The first term on the right-hand side of the equation denotes the generation induced by mean flow distortion; the second term denotes the diffusive transport influenced by molecular, turbulent and pressure diffusion; the third term denotes the pressure-strain term which explains the stress redistribution as a result of oscillating pressure; while the fourth term denotes the dissipation term. As several terms in this exact transport equation require modelling, the turbulent diffusive transport term is thus modelled using a simplified version of the generalised gradient diffusion model introduced by Daly and Harlow (1970) with the aim of improving stability. This is shown below:

$$D_{T,ij}=\frac{\partial}{\partial x_k}\left[\frac{\mu_t}{\sigma_k}\frac{\partial\left(\overline{u_\iota u_j}\right)}{\partial x_k}\right] \tag{3.88}$$

Gibson and Launder (1978) proposed a pressure-strain model for the pressure-strain term, which is represented by the third term on the right-hand side of Eq. (3.87) adopting the classical decomposition technique comprising of three components; the slow pressure-strain term, the rapid pressure strain term and the wall reflection term as given by:

$$\phi_{ij}=\phi_{ij,1}+\phi_{ij,2}+\phi_{ij,w} \tag{3.89}$$

$$\phi_{ij,1}=-C_1\rho\frac{\varepsilon}{k}\left[\overline{u_\iota u_j}-\frac{2}{3}\delta_{ij}k\right] \tag{3.90}$$

$$\phi_{ij,2}=-C_2\left[\left(P_{ij}+C_{ij}\right)-\frac{2}{3}\delta_{ij}(P-C)\right] \tag{3.91}$$

$$\phi_{ij,w}=C_1'\left[\overline{u_k u_m}n_k n_m\delta_{ij}-\frac{3}{2}\overline{u_k u_\iota}n_k n_j-\frac{3}{2}\overline{u_k u_j}n_k n_i\right]\frac{0.4k^{1/2}}{d}+C_2'\left[\phi_{km,2}n_k n_m\delta_{ij}-\frac{3}{2}\phi_{ik,2}n_k n_j-\frac{3}{2}\phi_{jk,2}n_k n_i\right]\frac{0.4k^{3/2}}{\varepsilon d} \tag{3.92}$$

From Eq. (3.92), $C_1 = 1.8$, $C_2 = 0.6$, $C_1' = 0.5$ and $C_2' = 0.3$, d, P_{ij} and C_{ij} represent the normal distance to the wall, production term and the convective terms respectively. Yang (2014) also presented the modelled transport equation for the dissipation rate as given by:

$$\frac{\partial(\varepsilon)}{\partial t} + \frac{\partial(\varepsilon \overline{U}_1)}{\partial x_i} = \frac{\partial}{\partial x_i}\left[\left(v + \frac{v_t}{\sigma_\varepsilon}\right)\frac{\partial \varepsilon}{\partial x_i}\right] + \frac{1}{2}C_{\varepsilon 1}P_{ii}\frac{\varepsilon}{\rho k} - C_{\varepsilon 2}\frac{\varepsilon^2}{k} \tag{3.93}$$

here, σ_ε, $C_{\varepsilon 1}$ and $C_{\varepsilon 2}$ have numerical values of 1.0, 1.44 and 1.92 respectively.

ANSYS (2018) notes that the RSM must be utilised if the investigated flow field show anisotropy In the Reynolds stresses as seen in flow cases like cyclone flows, highly swirling flows in combustors, rotating flow passages, and stress-influenced secondary flows in ducts. ANSYS (2018) also details that the exact form of the Reynold stress transport equations can be obtained by taking moments of the exact momentum equation, i.e., multiplying the exact momentum equation for the fluctuations by the fluctuating velocities and averaging. This multiplication is subsequently Reynolds-averaged. They then expressed the exact transport equations for the transport of the Reynolds stresses, i.e., $\rho\overline{u_i'u_j'}$ which are given as:

$$\underbrace{\frac{\partial}{\partial t}\left(\rho\overline{u_i'u_j'}\right)}_{\substack{local\ time\\ derivative}} + \underbrace{\frac{\partial}{\partial x_k}\left(\rho u_k\overline{u_i'u_j'}\right)}_{C_{ij}\equiv convection} = \underbrace{-\frac{\partial}{\partial x_k}\left[\rho\overline{u_i'u_j'u_k'} + \overline{p'\left(\delta_{kj}u_i' + \delta_{ik}u_j'\right)}\right]}_{D_{T,ij}\equiv turbulent\ diffusion} +$$
$$\underbrace{\frac{\partial}{\partial x_k}\left[\mu\frac{\partial}{\partial x_k}\left(\overline{u_i'u_j'}\right)\right]}_{D_{L,ij}\equiv molecular\ diffusion} \underbrace{-\rho\left(\overline{u_i'u_k'}\frac{\partial u_j}{\partial x_k} + \overline{u_j'u_k'}\frac{\partial u_i}{\partial x_k}\right)}_{P_{ij}\equiv stress\ production} \underbrace{-\rho\beta\left(g_i\overline{u_j'\theta} + g_j\overline{u_i'\theta}\right)}_{G_{ij}\equiv bouyancy\ production} + \underbrace{p'\left(\frac{\partial u_i'}{\partial x_j} + \frac{\partial u_j'}{\partial x_i}\right)}_{\varphi_{ij}\equiv pressure\ strain} -$$
$$\underbrace{2\mu\overline{\frac{\partial u_i'}{\partial x_k}\frac{\partial u_j'}{\partial x_k}}}_{\varepsilon_{ij}\equiv dissipation} \underbrace{-2\rho\Omega_k\left(\overline{u_j'u_m'}\varepsilon_{ikm} + \overline{u_i'u_m'}\varepsilon_{jkm}\right)}_{F_{ij}\equiv production\ by\ system\ rotation} + \underbrace{S_{user}}_{\substack{user-defined\\ source\ term}} \tag{3.94}$$

3.5. Simulation techniques: interface tracking methods

Among the several interface tracking techniques, the Volume-of-Fluid (VOF) technique, Level-set method and Front-tracking approach are extensively applied for gas bubble/liquid flow interaction, shock gas bubble interaction and shock liquid bubble interaction. The first two techniques, as applied in this research, are introduced in the following sections.

3.5.1. Level-set technique

This approach was originally proposed by Osher and Sethian (1988) to simulate the motion of an incompressible two-phase flow (Osher and Sethian, 1988). The level-set technique adopts a distance function to capture the gas-liquid interface on the fixed Eulerian grid. The distance function $\phi\,(x, y, t)$ describes the distance from position (x, y) to the gas-liquid interface at time t in two dimensions. The interface, denoted as Γ, represents the zero-level set of a ϕ function. This is shown below:

$$\Gamma = \left\{\left(x, y \mid \phi(x, y, t)\right) = 0\right\} \tag{3.95}$$

The level set function is considered positive in one phase and negative in the second phase. This is shown in Fig. 3.2 and is shown in Eq. (3.96).

$$\phi(x, y, t)\begin{cases} > 0, & phase\ 1 \\ = 0, & interface \\ < 0, & phase\ 2 \end{cases} \tag{3.96}$$

The development of ϕ is controlled by a transport equation shown in Eq. (3.97):

$$\frac{\partial \phi}{\partial t} + \mathbf{u}.\nabla\phi = 0 \tag{3.97}$$

Level set techniques can handle topological variations and it is mostly straightforward to derive high precision but these approaches are not conservative. Although the initial value of the level set function, ϕ_0, is set to be the distance function as shown in Fig. 3.2, the level set function may not stay as a distance function at $t > 0$ when the advection equation is solved for ϕ (Yu and Fan, 2008). Thus, a reinitialization approach is required to maintain the zero-level set as the position of the gas-liquid interface.

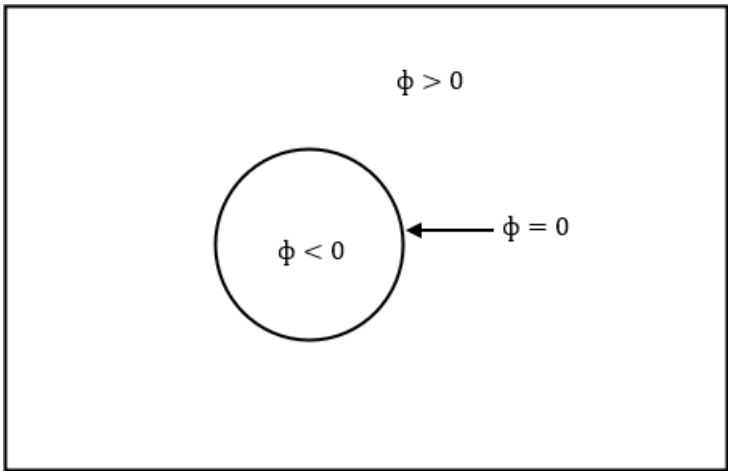

Figure 3.2: Properties of the level-set function showing that the level-set function has positive values in the continuous phase, negative values in the dispersed phase, and is equal to zero at the interface (Deshpande and Zimmerman, 2006)

The numerical studies of Deshpande and Zimmerman (2006) discovered from their 2D drop dynamics that there was still a 9% loss in the cross-sectional area of the bubble after reinitialization although this was significantly better than the 32% loss in the droplet's cross-sectional area without reinitialization (Deshpande and Zimmerman, 2006). To overcome this challenge, some researchers attempted to combine the VOF approach with the level set technique to develop a conservative scheme (Olsson and Kreiss, 2005; Olsson et al., 2007). This is discussed in further detail in Section 3.5.3. Enright et al. (2002) presented an efficient semi-Lagrangian based particle level-set technique for exact interface capturing. They explained that this technique had the potential to possess better conservation characteristics in comparison to the standalone level set approach.

3.5.2. The volume of fluid (VOF) technique

This technique has been widely applied in the simulation of two-phase flow since it was proposed by Noh and Woodward (1976). This method implicitly defines the volume fraction within every grid cell of one of the fluids. The volume fraction, γ is given as:

$$\gamma \begin{cases} = 1, & phase\ 1 \\ = 0, & phase\ 2 \\ 0 < \gamma < 1, & interface \end{cases} \tag{3.98}$$

The volume fraction is advected by the velocity field as shown in Eq. (3.99):

$$\frac{\partial \gamma}{\partial t} + \nabla.(\mathbf{u}\gamma) = 0 \tag{3.99}$$

The volume fraction is used to compute the mean density, viscosity and other characteristics in the interface grid cells. Afterwards, the gas-liquid two-phase problem is converted into a one fluid problem by solving a set of momentum equations. The surface tension can also be computed using the volume fraction within and adjacent to the grid cell (Brackbill et al., 1992). This model is a surface tracking technique adopted for a fixed Eulerian mesh. It is normally applied to cases involving two or more immiscible fluids where the interface position (between the fluids) is of particular interest. For this model, one set of momentum equations is apportioned to the fluids, and the volume fraction for every fluid in every computational cell is tracked throughout the domain. This model also has wide applications such as stratified flows, flows at free surfaces, filling, sloshing, large bubbles' motion in a liquid, liquid motion following a dam break, jet breakup estimation incorporating surface tension, and the tracking of liquid-gas interface either in the steady or transient modes (ANSYS, 2018). The VOF model formulation in ANSYS Fluent is generally utilised to calculate a time-dependent solution. This model formulation also depends on the absence of interpenetration by the two fluids. The volume fraction of a phase in the computational cell is introduced as a variable on the addition of that phase to the model. ANSYS (2018) also notes that the sum of volume fractions of all phases must equal one and the field for all variables and properties are allocated to the phases as well as denote volume-averaged values provided the volume fraction of every phase is known at every location. This then implies that the variables and properties in any particular cell are either wholly representative of one of the phases or representative of a mixture of the phases reliant on the values of the volume fraction. Following from this, if the q^{th} fluid's volume fraction in the cell is represented by γ_q, then subsequently any of the conditions listed below are possible:

- ✓ If γ_q is zero, then the cell of the q^{th} fluid is empty.
- ✓ If γ_q is one, then the cell of the q^{th} fluid is full.
- ✓ When γ_q is greater than zero but less than one, then the computational cell contains the interface between the q^{th} fluid and one or more other fluids.

γ_q is similar to γ except that γ denotes the volume fraction of any of the phases depending on its value i.e., 0, 1 or $0 < \gamma < 1$ (see Eq. 3.98) while γ_q denotes the volume fraction of the q^{th} fluid in the cell such that any of the conditions listed above are possible. ANSYS Fluent then assigns the suitable properties and variables to every control volume within the computational domain depending on the local value of γ_q.

3.5.2.1. Volume fraction equation

The tracking of interface(s) between the phases is achieved using the solution of a continuity equation for the volume fraction of one or several other faces. This equation, corresponding to the q^{th} phase, is given below:

$$\frac{1}{\rho_q}\left[\frac{\partial}{\partial t}\left(\alpha_q\rho_q\right) + \nabla\cdot\left(\alpha_q\rho_q\vec{v}_q\right) = S_{\alpha_q} + \sum_{p=1}^{n}\left(\dot{m}_{pq} - \dot{m}_{qp}\right)\right] \tag{3.100}$$

where $\dot{m}_{qp}$ denotes the mass transfer rate from phase q to phase p and $\dot{m}_{pq}$ represents the mass transfer rate from phase p to phase q. ANSYS (2018) states that the source term on the right-hand side of Eq. (3.100) = 0 by default but a constant or a user-defined mass source for every phase can be defined. The equation for the volume fraction will not be solved for the primary phase as the volume fraction of the primary phase can be calculated using the limitation below:

$$\sum_{p=1}^{n} \propto_q = 1 \tag{3.101}$$

Eq. (3.101) is solved by adopting the implicit or explicit time formulation as explained below.

3.5.2.2. The implicit formulation

The volume fraction is discretised as shown below using this formulation scheme:

$$\frac{\alpha_q^{n+1}\rho_q^{n+1} - \alpha_q^n \rho_q^n}{\Delta t} V + \sum_f \left(\rho_q^{n+1} U_f^{n+1} \alpha_{q,f}^{n+1}\right) = \left[S_{\alpha_q} + \sum_{p=1}^{n} \left(\dot{m}_{pq} - \dot{m}_{qp}\right)\right] V \tag{3.102}$$

where; $n+1$, n, α_q^{n+1}, α_q^n, $\alpha_{q,f}^{n+1}$, U_f^{n+1}, and V represent the present time step index, initial time step index, cell value of volume fraction at time step n+1, cell value of volume fraction at time step n, face value of the q^{th} volume fraction at time step n+1, volume flux through the face at time step n+1, and cell volume. As the volume fraction at the present time is dependent on other quantities at the present time step, a scalar transport equation is solved iteratively for every secondary phase volume fraction at every time step. The faces fluxes are also interpolated utilising the chosen spatial discretization scheme. This formulation scheme can be applied for both a time-dependent and steady-state simulations.

3.5.2.3. The explicit formulation

This formulation is time-dependent and the discretization of the volume fraction follows the equation below;

$$\frac{\alpha_q^{n+1}\rho_q^{n+1} - \alpha_q^n \rho_q^n}{\Delta t} V + \sum_f \left(\rho_q U_f^n \alpha_{q,f}^n\right) = \left[\sum_{p=1}^{n} \left(\dot{m}_{pq} - \dot{m}_{qp}\right) + S_{\alpha_q}\right] V \tag{3.103}$$

where n+1, n, $\propto_{q,f}$, V and U_f represent the present time step index; initial time step index, face value of the q^{th} volume fraction, volume of cell and the volume flux through the face influenced by normal velocity respectively. As the volume fraction at the present time step is directly computed depending on known quantities at the previous time step, the explicit formulation does not need an iterative solution of the transport equation at every time step. The face fluxes can then be interpolated using interface tracking or capturing schemes such as Geo-Reconstruct, CICSAM, Compressive, and Modified HRIC. ANSYS (2018) usefully points out that the software package impulsively refines the time step for the volume fraction equation integration, but the dynamism of this software also allows the user to influence the time step calculation by suitably adjusting the Courant number with options to update the volume fraction once for every time step or once for every iteration within each time step. The numerical simulations for this research have employed the explicit formulation.

3.5.2.4. Near interface interpolation

There is a need for convection and diffusion fluxes, via the control volume faces to be calculated and balanced with the source terms inside the control volume. The geometric reconstruction and donor-accepted schemes ensure that a special interpolation treatment is adopted at the cells that are close to the interface between the phases. Fig. 3.3 details the real interface shape together with the interfaces denoted by these individual techniques:

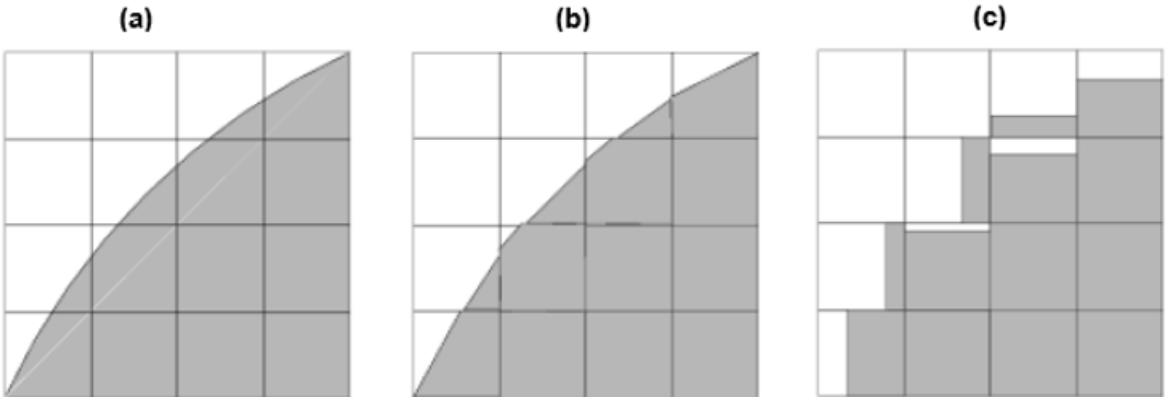

Figure 3.3: Interface computations for: (a) real interface shape; (b) Geometric reconstruction (piecewise-linear) scheme representation of the interface shape; and (c) Donor-accepted scheme for representation of the interface shape (ANSYS, 2018).

This research has used the explicit formulation scheme to handle cells that are close to the interface, between the phases, with the same interpolation as the cells that are wholly occupied with one phase or the other. The Compressive Scheme and Interface-Model-based Variants, which is a second order reconstruction scheme developed from the slope limiters, is then applied in the selected spatial discretization scheme. This scheme prevents the spurious oscillations or wiggles that would otherwise exist with high order spatial discretization schemes because of sharp alterations in the solution domain. The theory behind this scheme can be used in zonal discretization and the phase localized discretization which adopt the compressive scheme framework. This is shown as:

$$\alpha_f = \alpha_d + \beta \nabla \alpha_d \cdot \overrightarrow{dr} \tag{3.104}$$

where α_f, α_d, β, $\nabla\alpha_d$, and $\overrightarrow{dr}$ represent the face VOF value, donor cell VOF, value of slope limiter, donor cell VOF gradient value and the cell to face distance. The values for the slope limiter are within the range $0 \leq \beta \leq 2$ and for $\beta < 1$, the spatial discretization is denoted by a low-resolution scheme and for $1 \leq \beta \leq 2$, the spatial discretization is denoted by a high-resolution scheme. This is shown extensively in Table 3.1 below:

Table 3.1: Values of the slope limiter and the applicable discretization schemes.

Value of Slope Limiter, β	Appropriate Applicable Scheme
0	first order upwind
1	second order reconstruction confined by the global minimum/maximum of the volume fraction
2	compressive
$0 < \beta < 1$ and $1 < \beta < 2$	blended: where a value that lies between 0 and 1 implies blending of the first order and second order and a value that lies between 1 and 2 implies blending of the second order and the compressive scheme.

The compressive scheme is also based on the interface regime type selection as when sharp interface regime modelling is chosen, this scheme is just appropriate for modelling sharp interfaces. But when sharp/dispersed interface modelling is selected, the compressive scheme is suitable for both sharp and dispersed interface modelling.

3.5.2.5. Material properties

The material properties that exist in the VOF transport equations are defined by the presence of the component phases in every control volume. For instance, for a two-phase system, assuming both phases are denoted by subscripts 1 and 2, as well as the volume fraction of phase 2 being tracked, the density in each cell can then be expressed as:

$$\rho = \alpha_2 \rho_2 + (1 - \alpha_2)\rho_1 \tag{3.105}$$

Generally, for an n-phase system, the volume fraction averaged density can be expressed as:

$$\rho = \sum \propto_q \rho_q \tag{3.106}$$

ANSYS (2018) explained that all other properties like viscosity are calculated in a similar fashion.

3.5.2.6. Momentum equation

One momentum equation is solved across the domain, and the resulting velocity field is shared among the phases. The momentum equation, which is based on the volume fractions of every phase across the properties of ρ and viscosity, μ, is shown below:

$$\frac{\partial}{\partial t}(\rho\vec{v}) + \nabla \cdot (\rho\vec{v}\vec{v}) = -\nabla \mathrm{p} + \nabla \cdot [\mu(\nabla\vec{v} + \nabla\vec{v}^T)] + \rho\vec{g} + \vec{F} \tag{3.107}$$

3.5.2.7. Energy equation

The energy equation as shared among the phases, is expressed below:

$$\frac{\partial}{\partial t}(\rho E) + \nabla \cdot \left(\vec{v}(\rho E + p)\right) = \nabla \cdot \left(k_{eff}\nabla T - \sum_q \sum_j h_{j,q}\vec{J}_{j,q} + \left(\overline{\tau}_{eff}.\vec{v}\right) \right) + S_h \tag{3.108}$$

where k_{eff} denotes the effective conductivity and can also be expressed as $k + k_t$ (k_t represents the turbulent thermal conductivity, and is defined based on the applied turbulence model), $\vec{J}_j$ denotes the diffusion flux species j, $h_{j,q}$ represents the enthalpy of species j in phase q, and $\vec{J}_{j,q}$ denotes the diffusive flux of species j in phase q. The first three terms on the right-hand side of Eq. (3.108) denote the energy transfer due to conduction, species diffusion, and viscous dissipation respectively. S_h comprises volumetric heat sources that have been defined by the user without including the heat sources created by finite-rate volumetric or surface reactions as species formation enthalpy has already been included in the total enthalpy computation.

The VOF model handles energy, E, as a mass-averaged variable as shown below:

$$E = \frac{\sum_{q=1}^{n} \propto_q \rho_q E_q}{\sum_{q=1}^{n} \propto_q \rho_q} \tag{3.109}$$

where E_q for every phase is dependent on the specific heat of that phase as well as the shared temperature and is given below:

$$E_q = h_q - \frac{p}{p_q} + \frac{v^2}{2} \tag{3.110}$$

where h_q for the individual phases is based on the specific heat of the particular phase and the shared temperature. The density, ρ, effective thermal conductivity, k_{eff}, and effective viscosity, μ_{eff} are also shared by the phases and computed by volumetric averaging over the phases.

3.5.3. Coupled level-set and VOF scheme

The level-set approach is a well-known interface tracking approach for calculating two-phase flows with topologically complex interfaces. In the level set method (Osher and Sethian, 1988), the interface is captured and tracked by the level-set function designated as a signed distance from the interface. As the level set function is smooth and continuous, its spatial gradients can be accurately computed which will subsequently yield accurate approximations of interface curvature and surface tension force caused by this curvature. However, there is an associated deficiency with this method's ability to preserve volume conservation (Olsson et al., 2007). On the contrary, the VOF method is naturally volume-conserved as it calculates and tracks the volume fraction of a particular phase in every cell instead of the interface itself. The limitation of the VOF method rests in the computation of its spatial derivatives as the volume of fluid of a particular phase is discontinuous throughout the interface. Therefore, to conquer the deficiencies of the level-set method and the VOF method, a coupled level-set and VOF technique is provided in ANSYS Fluent. The coupled level-set and VOF scheme is mainly created for two-phase flows where no mass transfer is included as well as is adopted for just transient flow problems. The level-set function, φ, is described as a signed distance to the interface. Following from this, the interface, represented by a zero level-set, $\varphi(x,t)$, can be written as $\Gamma = \{x|\varphi(x,t) = 0\}$ in a two-phase flow system. This zero level-set is shown as:

$$\varphi(x,t) = \begin{cases} +|d|, & provided\ x \in the\ primary\ phase \\ 0, & provided\ x \in \Gamma \\ -|d|, & provided\ x \in the\ secondary\ phase \end{cases} \tag{3.111}$$

where d represents the distance to the interface.

The development of the level set function can be expressed in a comparable way as the VOF model as shown below:

$$\frac{\partial(\rho\vec{u})}{\partial t} + \nabla \cdot (\rho\vec{u}\vec{u}) = -\nabla \mathrm{p} + \nabla \cdot \mu[\nabla\vec{u} + (\nabla\vec{u})^T] - \vec{F}_{sf} + \rho\vec{g} \tag{3.112}$$

where $\vec{F}_{sf}$ is the force existing from the surface tension effects as derived below:

$$\vec{F}_{sf} = \sigma\kappa\delta(\varphi)\vec{n} \tag{3.113}$$

where σ represents the co-efficient of surface tension. $\delta(\varphi)$ is expressed as:

$$\delta(\varphi) = \begin{cases} 0, & |\varphi| \geq a \\ \dfrac{1 + cos(\pi\varphi/a)}{2a}, & |\varphi| < a \end{cases} \tag{3.114}$$

where a denotes the thickness of the interface on each side. The local interface normal, $\vec{n}$, and curvature, κ, of the interface can be expressed as:

$$\vec{n} = \frac{\nabla\varphi}{|\nabla\varphi|}\Big|_{\varphi=0} \tag{3.115}$$

$$\kappa = \nabla \cdot \frac{\nabla\varphi}{|\nabla\varphi|}\Big|_{\varphi=0} \tag{3.116}$$

The application of the default surface tension as given in Eq. (3.113) can yield spurious currents appearing in the solution. To prevent these impacts, ANSYS Fluent presents two weighting functions that redistribute the surface tension force in the direction of the heavier phase in the interface cells. These are:

1) The density correction formulation which modifies Eq. (3.113) by including a density ratio as shown below:

$$\vec{F}_{sf} = \frac{\rho}{1/2(\rho_1 + \rho_2)}\sigma\kappa\delta(\varphi)\vec{n} \tag{3.117}$$

where ρ is the volume-based density

2) The Heaviside function scaling formulation modifies Eq. (3.113) by including the Heaviside function as shown below:

$$\vec{F}_{sf} = 2H_{\varphi}\sigma\kappa\delta(\varphi)\vec{n} \tag{3.118}$$

where:

$$H_{\varphi} = \begin{cases} 0, \ \varphi < -a \ \ i.e. \ gas \ phase \\ 1, \ \varphi > a \ \ i.e. \ liquid \ phase \\ \frac{1}{2}\left[1 + \frac{\varphi}{a} + \frac{1}{\pi}sin\left(\frac{\pi\varphi}{a}\right)\right], \ |\varphi| \leq -a \end{cases} \tag{3.119}$$

3.6. Surface tension modelling

Surface tension exists due to the attractive forces between molecules in a fluid. This research has mainly investigated SBI for gas pairs and shock wave liquid interaction. For the SBI involving gas

pairs, surface tension can generally be ignored. For a liquid bubble in air i.e., shock propagating through the air and impacting the liquid bubble, surface tension effects have been considered. Within the liquid bubble, the net force on a liquid molecule due to its neighbouring liquid molecules is zero. However, at the liquid bubble surface, the net force is radially inward and the combined impacts of the radial components of force across the entire surface yields a surface contraction. This leads to a boost in pressure on the concave side of the bubble interface. Therefore, the surface tension is a force acting only at the surface and is required to maintain equilibrium for these types of interactions. It is also looks to stabilize the radially inward inter-molecular attractive force with the radially outward pressure force across the bubble surface. In areas where the two fluids i.e., air and water are separated but one of them is not in the form of spherical or cylindrical bubbles, the surface tension looks to decrease the free energy by reducing the interfacial area. The essence of the surface tension impacts is dependent on the value of two dimensionless quantities; the Re, and the capillary number, Ca; or Re and We. For Re << 1, *Ca* given below is the quantity of interest:

$$Ca = \frac{\mu U}{\sigma} \tag{3.120}$$

And for Re >>1, We given below is the quantity of interest:

$$We = \frac{\rho L U^2}{\sigma} \tag{3.121}$$

where *U* denotes the free-stream velocity. ANSYS (2018) added that it is safe to ignore the surface tension effects provided $Ca \gg 1$ or $We \gg 1$.

3.7. Spatial discretization techniques

ANSYS Fluent, by default, stores discrete values of the scalar, φ, at the cell centres, c_0 and c_1 (as seen in Fig. 3.4) but face values φ_f are needed for the convection terms in Eq. (3.122) below:

$$\frac{\partial \rho \varphi}{\partial t} V + \sum_{f}^{N_{faces}} \rho_f \vec{v}_f \varphi_f \cdot \vec{A}_f = \sum_{f}^{N_{faces}} \Gamma_\varphi \vec{\nabla} \varphi_f \cdot \vec{A}_f + S_\varphi V \tag{3.122}$$

where, $\frac{\partial \rho \varphi}{\partial t} V, N_{faces}$, φ_f, $\rho_f \vec{v}_f \cdot \vec{A}_f$, $\vec{A}_f$, $\vec{\nabla}\varphi_f$, and V represent the, temporal discretization, number of faces enclosing cell, value of φ convected via face f, mass flux via the face, area of the face $f, |A|$ $(= \left|A_x \hat{\imath} + A_y \hat{\jmath}\right|$ in 2D, gradient of φ at face f and the cell volume respectively.

Eq. (3.122) is derived from the discretization of Eq. (3.123) below:

$$\int_V \frac{\partial \rho \varphi}{\partial t} dV + \oint \rho \varphi \vec{v}. d\vec{A} = \oint \Gamma_\varphi \nabla \varphi. d\vec{A} + \int_V S_\varphi dV \tag{3.123}$$

where; $\rho, \vec{v}, \vec{A}, \Gamma_\varphi, \nabla\varphi,$ and S_φ represent the density, the velocity vector = $\hat{u}\imath + \hat{v}\jmath$ in 2D, surface area vector, diffusion coefficient for φ, gradient of $\varphi = (\partial\varphi/\partial x)\hat{\imath} + (\partial\varphi/\partial j)\hat{\jmath}$ in 2D, and source of φ per unit volume. Eq. (3.123) above is used at every control volume, or cell, in the computational domain. Eq. (3.123) also represents the discretization of the governing equations taking into account the unsteady conservation for the transport of a scalar quantity, φ, expressed in integral form for an arbitrary control volume, *V*.

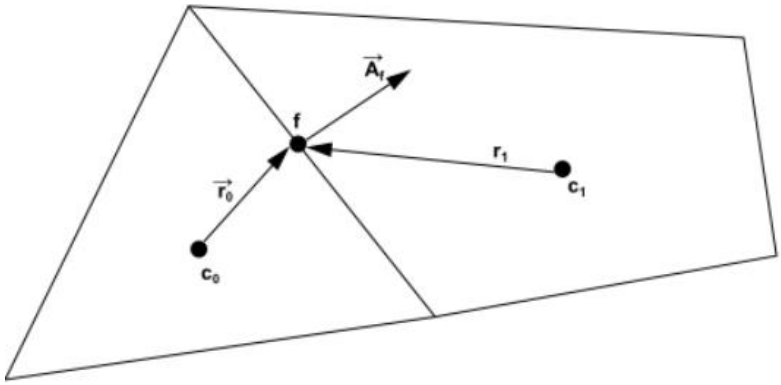

Figure 3.4: Diagrammatic representation of control volume adopted for the discretization of a Scalar Transport Equation

Thus, the face values φ_f require interpolation from the cell centre values. This is achieved utilising an upwind scheme. ANSYS (2018) defines upwinding as the process whereby the face value φ_f, is obtained from quantities in the cell upstream or upwind with respect to the direction of the normal velocity, v_n, in Eq. (3.122). The diffusive terms in Eq. (3.122) are central-differenced and possess a second-order accuracy. Several upwind schemes are available on the ANSYS Fluent package and applicable to the studied SBI scenarios. These include the; First-Order Upwind, Second-Order Upwind, Centra-Differencing, Bounded Central Differencing, Quick, and Third-Order Monotone Upstream Schemes for Conservation Laws (MUSCL), This research has adopted the Third-Order MUSCL Scheme. This scheme was introduced by Van Leer (1979) based on the original MUSCL by blending a central differencing scheme and second-order upwind scheme as shown below:

$$\varphi_f = \theta\varphi_{f,CD} + (1-\theta)\varphi_{f,SOU} \tag{3.124}$$

where $\varphi_{f,CD}$ and $\varphi_{f,SOU}$ denote the face values for a variable, φ_f, computed using the central-differencing scheme and second-order upwind scheme respectively. θ is solution-dependent variable whose values satisfies the inequality; $0 \leq \theta \leq 1$. When $\theta = 1$, φ_f yields a central differencing second-order interpolation value. If $\theta = 0$, φ_f results in a second-order upwind value.

$\varphi_{f,CD}$ can be derived using Eq. (3.125) given below:

$$\varphi_{f,CD} = \frac{1}{2}(\varphi_0 + \varphi_1) + \frac{1}{2}\left(\nabla\varphi_{r,0}\cdot\vec{r}_0 + \nabla\varphi_{r,1}\cdot\vec{r}_1\right) \tag{3.125}$$

where the indices 0 and 1 denote the cells that share face f. $\nabla\varphi_{r,0}$ and $\nabla\varphi_{r,1}$ represent the reconstructed gradients at cells 0 and 1 respectively. $\vec{r}$ represents the vector that is directed to the face centroid from the upstream cell centroid. In the derivation of $\varphi_{f,SOU}$, higher-order accuracy is achieved at cell faces via a Taylor series expansion of the cell-centered solution about the cell centroid. A multidimensional linear reconstruction technique (Barth and Jespersen, 1989) is then applied to calculate quantities at the cell faces thus ensuring that second-order accuracy is attained. $\varphi_{f,SOU}$ is computed as shown below:

$$\varphi_{f,SOU} = \varphi + \nabla\varphi.\vec{r} \tag{3.126}$$

where φ and $\nabla\varphi$ denote the cell-centered value and its gradient within the upstream cell. This gradient is determined in each cell. As opposed to the QUICK scheme, which is just suited to structured hex meshes, this scheme can be applied to arbitrary meshes. It also has the ability to enhance spatial accuracy for all categories of meshes by substantially decreasing numerical diffusion for complicated

three-dimensional flows in comparison to the second-order upwind scheme. This scheme is also available for all transport equations.

3.8. Temporal discretization techniques

The governing equations must be discretised in both space and time for transient simulations. Temporal discretization involves the integration of each term in the differential equations over a time step Δt. The integration of the transient term is simple as shown below via a generic expression for the time progression of a variable φ:

$$\frac{\partial \varphi}{\partial t} = F(\varphi) \tag{3.127}$$

where the function F includes any spatial discretization. When the time derivative is discretised adopting backward differences, the first order accurate temporal discretization is expressed as:

$$\frac{\varphi^{n+1} - \varphi^{n}}{\Delta t} = F(\varphi) \tag{3.128}$$

And the second-order discretization is expressed as:

$$\frac{3\varphi^{n+1} - 4\varphi^{n} + \varphi^{n-1}}{2\Delta t} = F(\varphi) \tag{3.129}$$

where φ, $n+1$, and n represent a scalar quantity; value at succeeding time level, $t + \Delta t$, and value at present time level, t.

This research has adopted the first order accurate temporal discretization technique because it is completely stable irrespective of the time step size. This scheme is also compatible with the explicit volume fraction scheme which has been employed in this research.

3.9. Conclusions

This chapter presented the governing laws/equations, turbulence models and numerical techniques/schemes that have been employed to solve the SBI challenge. Details of the URANS equations solved using a pressure-based finite volume method (FVM) are presented. It was demonstrated by Onwuegbu and Yang (2022) that for this kind of flow, the URANS approach could predict the flow accurately at a substantially lowered cost so that there was no requirement for two other more accurate approaches, i.e., LES or DNS. The URANS equations are developed by averaging the instantaneous Navier-Stokes equations with some additional terms called Reynolds stresses being created during the averaging process. These terms need to be approximated/modelled using a turbulence model. Three turbulence models have been examined and presented aimed at selecting the model that best matches the experimental results. The CLSVOF scheme, for interface tracking and treating complex topological interfacial changes, has also been presented and explained to predict the bubble compression dynamics and formation of vortical structures/vortices. A third order MUSCL scheme, for the spatial discretization of both momentum and the continuity equations, has also been presented. Descriptions are also provided for the compressive scheme adopted for spatial discretization of the volume fraction equations thus aiding in the avoidance of spurious oscillations or wiggles. With respect to this scheme, explanations are also offered for the different interface regime types. Finally, descriptions of the first-and second-order schemes, for the temporal discretization of the URANS equations, are provided.

4. Shock/Spherical Bubble Interaction

4.1. Introduction

The interaction between the incident shock and a spherical helium bubble was simulated using a finite volume method (FVM) to solve the governing integral equations for the conservation of mass and momentum within the commercial CFD software, ANSYS Fluent 19.0. Hence, the objective of this chapter is to accurately perform two-dimensional (2D) and three-dimensional (3D) computational fluid dynamics (CFD) simulations to investigate the complex interaction of a supersonic shock wave (Ma = 1.22) with a spherical helium bubble aimed at properly comprehending and analysing shock wave travel, bubble compression and deformation with time. To do this, the Unsteady Reynolds-Averaged Navier-Stokes (URANS) mathematical model and the coupled Level Set (LS) and Volume of Fluids (VOF) method, also referred to as the CLSVOF scheme, have been applied in the present study. Mesh refinement was executed on different 2D and 3D meshes using Adaptive Mesh Refinement (AMR) which ensured fine cells surrounded and travelled with the bubble and shock wave. The different grid configurations (from the smallest number of element sizes to the highest) were then used to simulate shock travel in air and through the bubble to determine the positions of the: upstream interface, downstream interface, and jet. The results from the different meshes were then compared to experimental measurements to determine the optimal grid configuration. This process is the mesh independence study where the best mesh is selected for the other aspects of shock bubble interaction (SBI) to be simulated.

The simulations are evaluated by comparing predicted velocities of refracted wave, transmitted wave, upstream interface, downstream interface, jet, and vortex ring with related existing experimental data. The predicted non-dimensional bubble and vortex velocities have also been compared with experimental data and other theoretical models. The experimental data of Haas and Sturtevant (1987) detailed the interaction of a weak shock wave with a spherical helium bubble and presented valuable qualitative and quantitative data related to bubble motion, bubble deformation, vortex ring formation, and air/helium mixing. The theoretical models of Rayleigh Taylor (Taylor, 1953) and Rudinger & Somers (1960) presented numerical relations for interface distortion and bubble acceleration respectively. Comprehensive flow visualization has been provided and analysed to elucidate the SBI process from the inception of bubble compression up to the creation of vortex rings as well as vorticity production and distribution. The constant reflection and refraction of the acoustic wave patterns as well as the location of the incident, refracted and transmitted waves at the bubble compression stage are also presented. To gain further understanding into the SBI flowfield, turbulence is examined to allow for the investigation of small flow structures and turbulent mixing between helium and air at the later stage of SBI. This is because to the best of our knowledge, no previous studies have addressed the generation and development of turbulence at the later stages of SBI as well as the evolution of the vortex rings from inception to the later phases. These knowledge gaps will be elucidated in the current study. Furthermore, it is demonstrated that turbulence is generated with some small flow structures formed and more intensive turbulent mixing of helium with air starts to develop at the later stage of SBI. 2D simulations of SBI have also been conducted in the present study to assess their accuracy through a direct comparison against 3D SBI simulations and previous experimental data.

4.2. Methodology

4.2.1. Governing equations and numerical methods

SBI is predominantly unsteady and turbulence is usually generated after the interaction so that the URANS approach is adopted in the present study. It was demonstrated by Onwuegbu and Yang (2022) that the URANS approach could be adopted to predict the flow accurately at a significantly lower cost compared to two other approaches, i.e., LES or DNS. These two other approaches for

simulating turbulent flows have not been selected in the present study principally because the flow consists of mainly unsteady large scale flow structures which URANS can capture very well. The URANS equations are derived by averaging the instantaneous Navier-Stokes equations and the averaging procedure leads to extra terms called Reynolds Stresses which need to be modelled using a turbulence model. There have been many turbulence models developed and the selection of a suitable turbulence model in the present study will be presented in Section 4.2.5.

It is crucial to capture the bubble deformation in SBI studies and hence an interface tracking method is needed. There are many methods available to track the interface but some of those methods could fail when handling large interface deformations such as disintegration and fusing of fronts (Shyue, 1998). It has been demonstrated that a CLSVOF scheme boosts a higher accuracy than the standalone LS or VOF method as it combines their merits and overcomes their deficiencies (Olsson and Kreiss, 2005). The CLSVOF approach has proven to be a potent tool to solve huge interface deformations and applied successfully by Niederhaus et al. (2008) to study SBI. Therefore, this approach has been employed in the present study. A third-order Monotone Upstream-centered Schemes for Conservation Laws (MUSCL) scheme was used for the spatial discretization. The scheme is selected as it has the capabilities to boost spatial accuracy for all grid types by decreasing numerical diffusion particularly for complex 3D flows (ANSYS, 2018). The compressive scheme, which is a second order reconstruction scheme, was also adopted for spatial discretization of the volume fraction equations thus aiding in the avoidance of spurious oscillations or wiggles. With respect to the compressive scheme, the sharp/dispersed interface regime was applied. The sharp method helps to resolve the air-gas bubble interface sharply while the diffuse interface methods are simpler and robust and can efficiently handle high Ma shocks, high pressure, and density gradients across the interface as well as the huge topological alterations of the interface. A first-order implicit scheme was used for the temporal discretization of the 2D and 3D URANS equations. To achieve numerical stability and accuracy, the Courant Friedrichs Lewy number was set as 0.5 and a very small-time step of 4×10^{-7} seconds was used to accurately capture detailed flow developments.

4.2.2. Computational details

The computational set-up is based on the experiment carried out by Haas and Sturtevant (1987) with the main parameters listed in Table 4.1 below.

Table 4.1: Experimental conditions

Bubble gas	Ambient gas	Ma	A
Helium	Air	1.25	-0.715

Figures 4.1(a) and (b) present the computational domains and the boundary/initial conditions for the 2D (half of the domain/axisymmetric model) and 3D cases. The flow is assumed axis-symmetrical in the 2D case with the horizontal x -axis in the direction of the shock tube axis and the y -axis in the vertical direction. The domain length in the 2D case is L_u + 0.44d (d= 45mm is the bubble diameter) where L_u is variable to ensure enough room that will allow the shocked bubble travel throughout the monitored time. The domain height is 0.99d as shown in Fig. 4.1(a). The computations are performed only on the upper half as it is a mirror image of the lower half. The lower boundary of the grid (Edge GH) represents the shock-tube axis. A no-slip wall boundary condition is applied at the upper boundary i.e., wall of shock tube (Edge EF). The computational set-ups match those in the experiment by Haas & Sturtevant (1987) with the right boundary (Edge EH) being the inlet as the incident shock propagated from right to left in the experiment. The left boundary corresponds to the outlet, which is shown as Edge FG. At inlet, density, pressure, and velocity are specified and the right boundary cells comprise of parameter values, i.e., $\rho_2, P_2, v_x =$

$V_2, v_y = 0$, which is equivalent to the area behind the supersonic planar shock. As revealed from within the computational domain, identical values are utilised as initial conditions behind the shock which are located at a few cells within the computational grid. The values of these parameters also denote the post-shock properties of the ambient gas utilised in the initialisation and are calculated from the Rankine-Hugonoit relationships (Houghton and Brock, 1993). The right boundary condition allows the smooth outflow of reflected waves created by the SBI. The left boundary condition equivalently allows the smooth outflow of any leftward-moving waves, including the distorted incident shock. Fig. 4.1(a) also reveals that the left boundary condition is achieved by sustaining a 'zero gradient' for all fluid variables, i.e., $\nabla u = 0, \nabla P = 0, \nabla \rho = 0$.

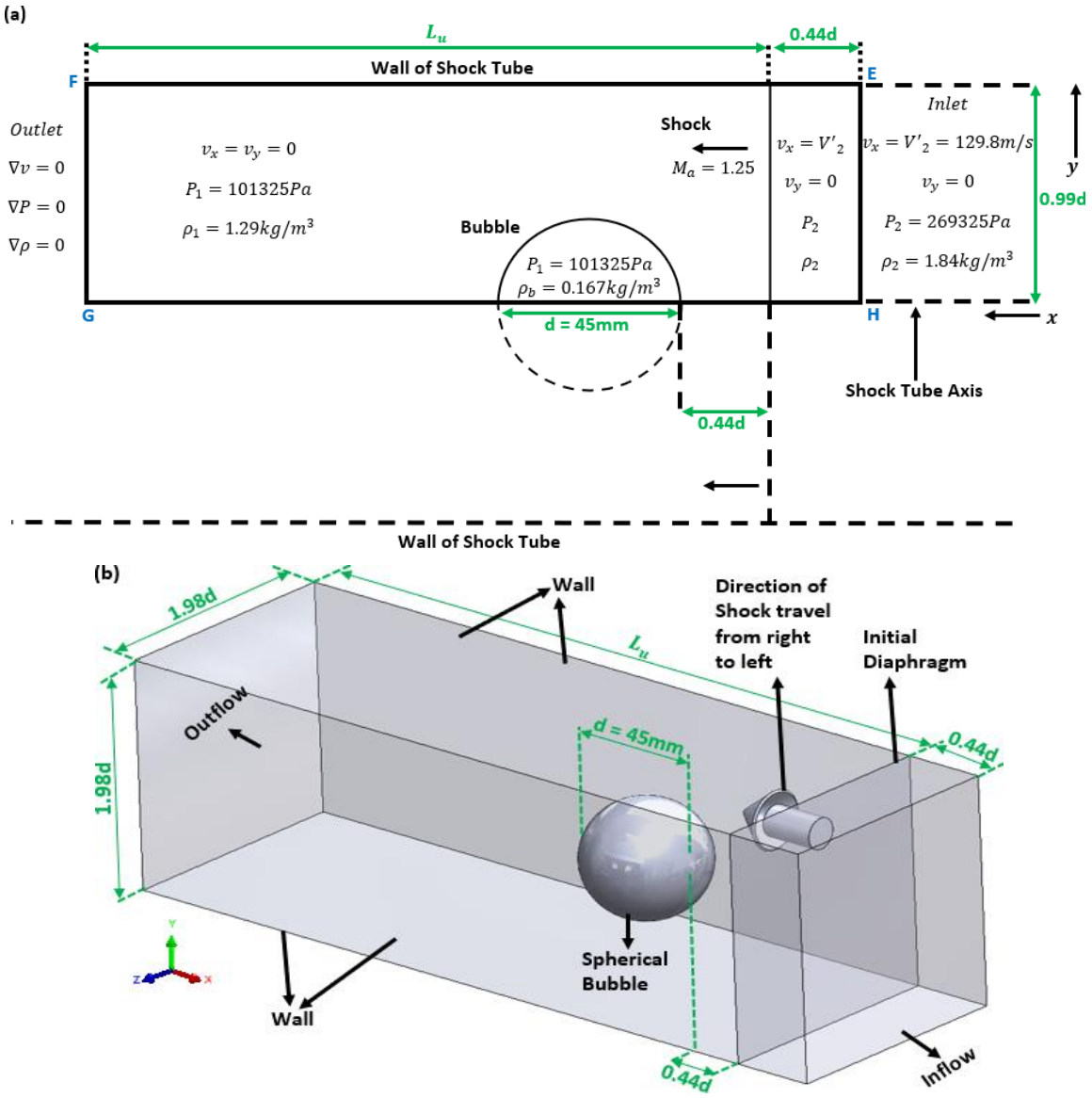

Figure 4.1: (a) Top half of the computational domain and boundary/initial conditions for the 2D case; and (b) Computational domain for the 3D case.

The computational domain length in the 3D case is the same as that in the 2D case while the domain height and width are both 1.98d as shown in Fig. 4.1(b). The same boundary conditions used in the 2D case are applied in the 3D case and a no-slip wall boundary condition is applied on the side walls. Like the 2D scenario, the 3D outflow condition has adopted a zeroth-order extrapolation to the boundary whereby the outermost data plane is transferred into the boundary such that the gradients across the boundary equate zero ($\nabla v = 0, \nabla P = 0, \nabla \rho = 0$). The 2D and 3D scenarios, as

in Quirk and Karni (1996), distanced the bubble from the incident shock in order to prevent 'start-up' errors, which reveal themselves as a couple of small-frequency waves travelling on the inert features (Quirk, 1991), from disrupting the SBI process. This 'start-up' errors are created when a shock spreads to its actual profile in the presence of an 'exact' discontinuity like the bubble as initial conditions (Hillier, 1991). As one of the major challenges to the simulation of high-order CFD procedures involving high-Reynolds number flows is mesh generation, this research has looked to produce a high-quality 2D and 3D mesh to ensure that the best predictions that match the experimental results are obtained. To this effect, an unstructured mesh (particularly in the bubble surrounding for the 2D mesh and the entire 3D mesh, see Fig. 4.2(a) – (c)) has been produced. As a justification, this research has studied the works of several authors (e.g., Jameson and Mavriplis, 1986; Mavriplis et al., 1989; Jameson, 1995; Mavriplis, 1995; 1996; 1997; 1998; Venkatakrishnan, 1996; Gerhold et al., 1997; Hasselbacher et al., 1999; Eliasson, 2001) who have explained that finite volume methods formulated on unstructured grids are extensively adopted in the treatment of complex geometries. Unstructured grids also offer the capability of adapting the grid locally to enhance the accuracy of the simulations without suffering computational difficulties associated with global refinements (Dalal et al., 2008). The 2D and 3D computational grids are shown below:

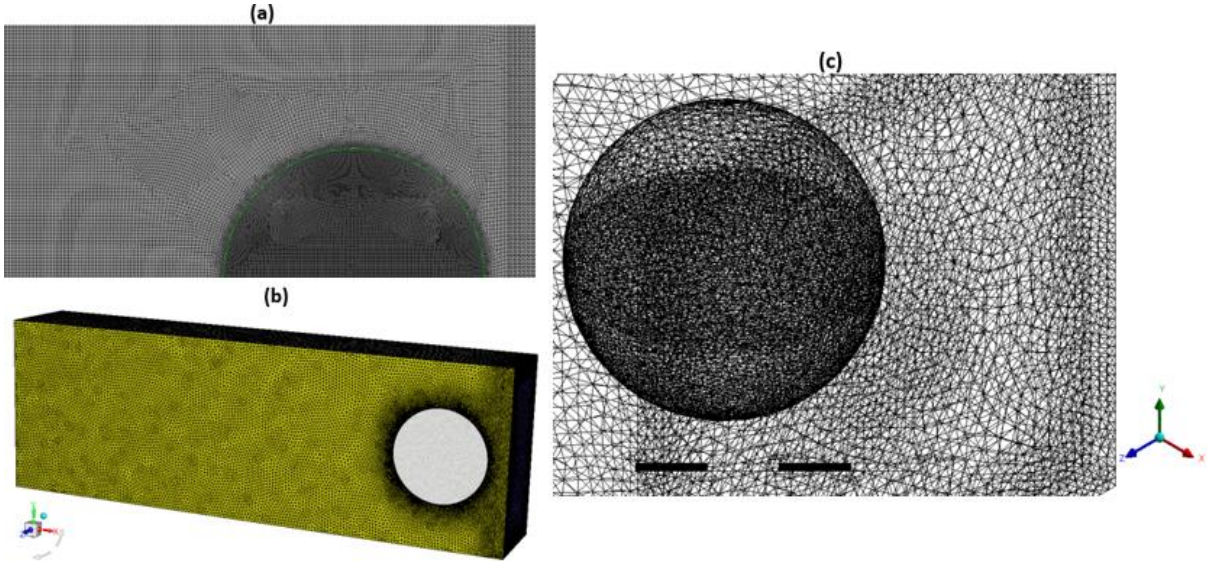

Figure 4.2: (a) Hybrid mesh for the 2D case; (b) unstructured mesh for the 3D case; and (c) Close view of fine mesh around bubble; all from Adaptive Mesh Refinement (AMR).

As seen from Fig. 4.2(a), the main flow region has been discretised into quadrilateral cells while the near bubble surrounding consists of triangular cells i.e., the mesh can then be classified as a hybrid mesh consisting of a structured uniform grid in most of the flow region and an unstructured grid in the vicinity of the bubble. The hybrid mesh was adopted to ensure an appropriate grid resolution was attained in areas close to the boundaries and the air-bubble interface as well as specify spatial discretization suitable for the current flow problem (Cameron, 2011). The triangulation method was adopted to create the grid in the bubble surroundings. This concept has been previously used by Lohner and Parikh (1988). The 3D computational grid (Figure 4.2(b) and (c)) shows an unstructured mesh consisting of a tetrahedral volume mesh in the main flow region and the gas bubble while a triangular surface mesh is applied at the air/helium bubble interface. The mesh also shows that the unstructured tetrahedral volume mesh is mainly uniform away from the bubble surroundings and has a greater element size compared to the cells within the bubble. This mesh was generated using the tetrahedralization technique as previously applied by Betro (2010) with the target of adding adaptive competences to the background grid. As unstructured meshes have irregular connectivity with each cell having varying number of neighbours, this research has employed a combination of a finite-volume discretization with pressure velocity coupling via a Coupled algorithm to allow for the co-located storage of velocity and pressure components (Jiang and Przekwas, 1994;

Thomadakis and Leschziner, 1994; Demirdzic and Muzaferija, 1995; Davidson, 1996). This research has then applied Adaptive Mesh Refinement (AMR) to superimpose finer sub-grids within the bubble and its vicinity as these regions require finer resolution. The AMR algorithm generally represents a scheme for integrating systems of hyperbolic partial differential equations and it aims to lessen the integration costs by fitting the local resolution of the generated mesh to the local requirements of the intended solution. The research findings of Berger & Oliger (1984) and Berger & Collela (1989) provided the foundation for AMR. Quirk (1991) and Quirk & Karni (1996) built on these past works to describe AMR within a hierarchical grid context. Other authors (e.g., Henderson et al., 1991; Klein et al., 1994; Bell et al., 1994; Nourgaliev et al., 2006; Nierderhaus et al., 2008) have adopted AMR in their numerical studies of SBI. For this research, AMR is built in by ANSYS Fluent and can be manipulated by the user to achieve the desired amount of extra grid cells that surround the interface and travel with the bubble and shock wave. This ensured complete control of grid resolution. In Figs 4.2(a) – (c), the adapted mesh has two levels of AMR superposed on the original grid with a refinement ratio of 2 each.

4.2.3. Initialization of the computational problem

This research initialised the helium gas within the bubble, and the unshocked surrounding fluid i.e., area between initial diaphragm and outlet at atmospheric conditions (see Fig. 4.1(a) and (b)). The initialisation assumes that the bubble and the unshocked surrounding fluid are originally in a state of rest as well as in thermal and mechanical equilibrium thus implying that any original buoyant movement of the bubble is ignored.

The JANAF data (Gordon and McBride, 1976) is used to derive the ratio of specific heats, γ, for bubble gas (helium) and surrounding gas (air) utilising the original, unshocked pressure and temperature. Both fluids retained a constant value of γ throughout the computation.

This research adopted the Rankine-Hugonoit relationships (Houghton and Brock, 1993) to calculate the post-shock characteristics of the surrounding air, as shown on the right-hand side of Fig. 4.1(a). The post-shock Ma, pressure and density are computed using the following mathematical relations respectively:

$$Ma_2{}^2 = \frac{(\gamma-1)Ma_1{}^2 + 2}{2\gamma Ma_1{}^2 - (\gamma-1)}, \tag{4.1}$$

$$\frac{P_2}{P_1} = \frac{2\gamma}{\gamma+1} Ma_1{}^2 - \frac{\gamma-1}{\gamma+1}, \tag{4.2}$$

$$\frac{\rho_2}{\rho_1} = \frac{\frac{\gamma+1}{\gamma-1}\left(\frac{P_2}{P_1}\right) - 1}{\frac{\gamma+1}{\gamma-1}\left(\frac{P_2}{P_1}\right)}, \tag{4.3}$$

where $Ma_1 = 1.25$, P_1 and ρ_1 represent the initial Mach number, pressure and density of the ambient air respectively, as shown on the left-hand side of Fig. 4.1(a).

4.2.4. Mesh independence study

Mesh refinement was executed on different 2D and 3D meshes using AMR which ensured fine cells surrounded and travelled with the bubble and shock wave. The different grid configurations (from the smallest number of element sizes to the highest), after AMR, were then used to simulate shock travel in air and through the bubble to determine the positions of the: upstream interface, downstream interface, and jet. The results from the different meshes were then compared to experimental measurements to determine the optimal grid configuration. This process is the mesh independence study where the best mesh is selected for the other aspects of shock bubble

interaction (SBI) to be simulated. A mesh independence study has been carried out with three meshes for both 2D case (0.16, 0.24 and 0.28 million cells) and 3D case (3.6, 6.2, 9.2 million cells). Fig. 4.3 presents the bubble compression and changes against time in terms of three representative points (upstream, jet and downstream locations). It can be seen that for the 2D case (Fig. 4.3(a)), the results are hardly changing when the mesh is refined from 0.24 to 0.28 million cells and hence there is need to refine the mesh further and the rest of the 2D simulations have been performed using 0.28 million cells. Similarly for the 3D case (Fig. 4.3(b)), the results obtained using the mesh with 6.2 million cells are very close to the results obtained using the mesh with 9.2 million cells and hence there is no need to refine the mesh further. The rest of the 3D simulations have been carried out using 9.2 million cells.

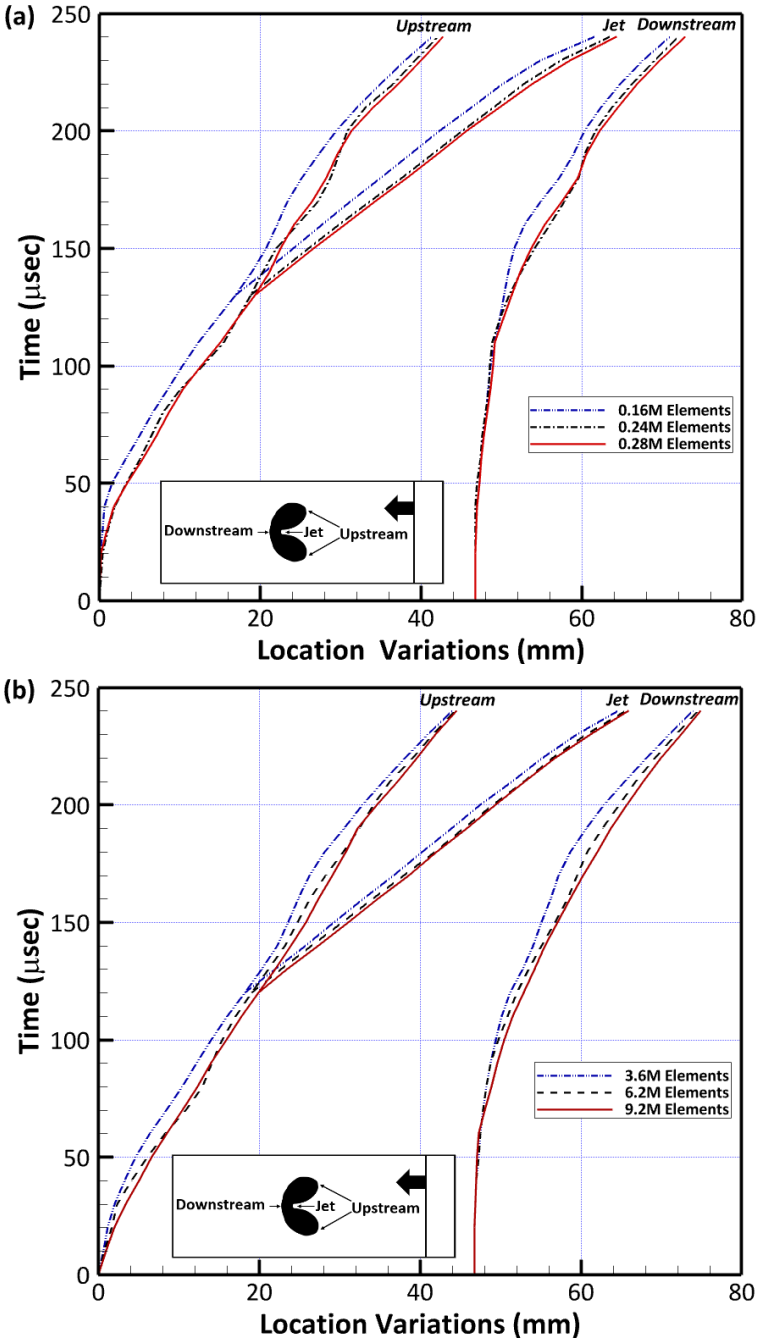

Figure 4.3: (a) Results obtained with three meshes for the 2D case; and (b) Results obtained with three meshes for the 3D case.

4.2.5. Turbulence model selection

There are many turbulence models and there is no general consensus which model is the best as their performances are very much case dependent. There is hardly any knowledge gained so far about the performance of turbulence models in the simulation of SBI. Hence in the present study, three widely used and high rated turbulence models, the realizable *k-ε*, the shear stress transport, SST *k-ω* and a Reynolds Stress Model (RSM), have been tested to assess their performance in the 3D case. Fig. 4.4 presents the comparison between the predicted three location changes of the bubble against the experimental data of Haas & Sturtevant (1987). It is evident from Fig. 4.4 that the predictions using all three turbulence models are very close to each other, but the results obtained using the realizable *k-ε* are slightly closer to the experimental data. Therefore, the realizable *k-ε* is employed in the present study.

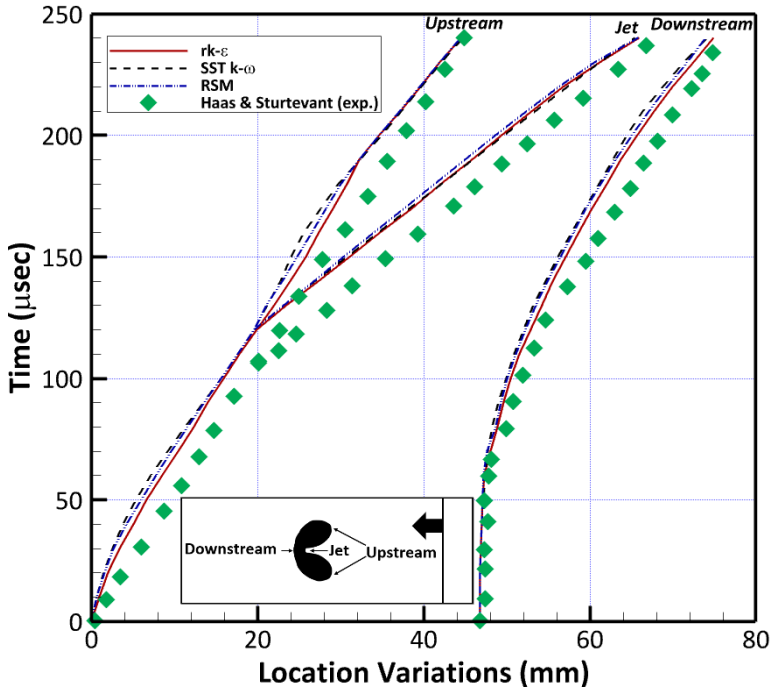

Figure 4.4: Comparison of predictions with experimental data for different turbulence models.

4.3. Results and discussion

4.3.1. Comparison between the measured and predicted velocities

Table 4.2 presents the comparison between the measured and predicted velocities of incident (v_I), refracted (v_R) and transmitted waves (v_T), initial upstream interface (v_{IU}), final upstream interface (v_{FU}), initial downstream interface (v_{ID}), air-jet head (v_{AJ}), and vortex ring (v_{VR}). The average velocities of these acoustic wave characteristics are derived by utilising minimum squares line adjustments to approximate their approximate locations at different times along the advected bubble trajectory. Generally speaking, the calculation of these velocities entails the measurement of the changes in their respective positions over 50-time steps and dividing by the elapsed duration, T, i.e., $T \geq 4\ x\ 10^{-7} x\ 50 \geq 20\mu s$. As such, the values provided in Table 4.2 have been computed by averaging over a number of such intervals.

Table 4.2: Comparison between the experimental data of Haas & Sturtevant (1987) and the predictions.

	v_I	v_R	v_T	v_{IU}	v_{FU}	v_{ID}	v_{AJ}	v_{VR}
Experimental data	420	960	365	190	125	145	335	165
Predictions (2D)	406.7	932.1	351.5	178.7	115	134.6	318.9	155.8
Predictions (3D)	416	951.4	361.3	184.7	122	142.4	331.1	161.8

As can be seen from Table 4.2, an excellent agreement between the 3D predictions and experimental data has been obtained for all velocities with the maximum error being 2.8% for the initial upstream interface velocity. The 2D predictions also agree well with the measured values with the maximum error being 8% for the final upstream interface velocity.

4.3.2. Bubble acceleration and vortex formation

Air is accelerated in the shock tube as the shock wave propagates, from a state of rest to a uniform velocity, V'_2. This V'_2 is derived as (Jacobs, 1992; 1993):

$$V'_2 = \frac{2a_0}{\gamma+1}\left(Ma_1 - \frac{1}{Ma_1}\right), \tag{4.4}$$

where γ, a_0, and Ma_1 represent the specific heats ratio, sound speed behind the shock and the Mach number of the shock respectively. As helium is less dense than air, the major flow velocity trailing the incident shock functions as a piston on the bubble thus contributing to bubble deformation and compression (Layes et al., 2003). The sphere will then be accelerated to a higher velocity than V'_2, which means that the light helium gas travels ahead of the ambient air as it is transported down the shock tube. Rudinger and Somers (1960) developed a basic two-stage model for this: in the first stage and during the early transient, the helium bubble accelerates as a solid body to velocity V'_b; in the second stage, it changes into a vortex ring with velocity V'_v based on the Taylor mechanism (Taylor, 1953). Within the first stage, the travelling undistorted bubble acts as Taylor's 'dissolved' vortex-generating disk and as such, V'_b, denotes the disk velocity. Rudinger and Somers (1960) proposed that in the first stage, the impulse per unit volume experienced by the bubble, I_b would be the same as that underwent by the ambient air i.e., product of ρ_{air} and V'_2. This is given in the following equation:

$$I_b = \rho_{air}\, x\, V'_2 = \rho_b V'_b + k\rho_{air}(V'_b - V'_2), \tag{4.5}$$

k denotes the apparent mass fraction for a sphere and is equal to 0.5 (Rudinger and Somers, 1960) and ρ_b is the gas density in the bubble. From Eq. (4.5), the initial non-dimensional velocity of the bubble is then computed as:

$$V_{ND_b} = \frac{V'_b}{V'_2} = \frac{1+k}{\sigma+k}, \tag{4.6}$$

where $\sigma = \rho_b/\rho_{air}$

The conversion of the helium bubble into a vortex indicates a drop in the relative velocity. This is shown below as:

$$V'_v - V'_2 = \beta(V'_b - V'_2), \tag{4.7}$$

β has a numerical value of 0.436 as presented by Taylor (1953) and all calculations used the same value of β. Similarly, from Eq. (4.6), the non-dimensional vortex velocity can be computed as:

$$V_{ND_v} = \frac{V'_v}{V'_2} = 1 + \beta \frac{1-\sigma}{\sigma + k}, \tag{4.8}$$

To compute V_{ND_b} and V_{ND_v}, V'_b is calculated as the average of the predicted v_{IU} and v_{ID} while V'_v is taken as v_{VR} from Table 4.2. The V_{ND_v} and V_{ND_b} as well as the predicted and measured values are presented in Table 4.3 below.

Table 4.3: Theoretical, numerical and experimental non-dimensional bubble and vortex velocities

	V_{ND_b}	V_{ND_v}
Theoretical	2.199	1.52
Experimental data	1.3	1.28
Predictions (2D)	1.177	1.181
Predictions (3D)	1.26	1.246

It can be seen from Table 4.3 that the predictions and the experimental data agree very well, especially that the 3D predictions are very close to the experimental data while the theoretical values are much larger with the non-dimensional bubble velocity being almost twice the prediction and experimental values. This strongly indicates that the two-stage model proposed by Rudinger and Somers (1960) does not quite represent the real situation of bubble acceleration and vortex formation in the process of SBI.

4.3.3. Deformation and development of the interface: prediction of upstream and jet interface velocities

In this section and Section 4.3.4, the predicted rates of deformation will be compared to the experimentally measured ones and the growth rate of small sinusoidal perturbations induced by the impulsive acceleration of a plane interface proposed by the Rayleigh-Taylor theory. This comparison will be made at three characteristic interface points, i.e., upstream, jet, and downstream interfaces. Haas and Sturtevant (1987) stated that it is informative to investigate the relationship between the shock-generated deformation of gas cylinders and the Rayleigh-Taylor instability (RTI) of plane interfaces. They used the illustration where a cylinder is taken to be representative of a sinusoidal perturbation having an amplitude of $\eta_0 = R$ (R represents the cylinder's radius) and wavelength $\lambda = 2\pi R$ (wavenumber $k = 1/R$). This then meant that the sine wave is tangential to and has identical curvature at crests and troughs as the cylinder. This further implied that the amplitude of the effective perturbation is significantly large ($k\eta_0 = 1$) and variations of the observations from linear theory may indicate the impacts of finite amplitude and non-linearity.

According to the theory of impulsive RTI, the interface is assigned a mean translational velocity, V, and a constant perturbation velocity, v, at the troughs and crests when a shock wave impacts a plane interface deformed by the small undulating perturbations of long wavelength (Markstein, 1957a; 1957b; Richtmyer, 1960). This perturbation velocity is given below:

$$v = \pm k\eta_0 VA, \tag{4.9}$$

where A denotes the Atwood number. The interface deforms at a constant rate and there is a continuance of the velocity field as there is no further acceleration after shock impingement. The crests or trough velocity normalised by the translational velocity V can be expressed as:

$$\Upsilon = 1 + v/V, \tag{4.10}$$

Employing Eq. (4.9) into Eq. (4.10) as well as equations for the wave number, $k\ (= 1/R)$, and amplitude, $\eta_0 (= R)$, yields Eq. (4.11) below:

$$\Upsilon = 1 \pm \alpha A, \tag{4.11}$$

where the plus sign relates to a shock incident on a concave interface (trough), and α = 1 for a locally cylindrical interface. Haas and Sturtevant (1987) adopted the first-order correction for non-linearity suggested by Richtmyer (1960) considering the compression of the interface shape by the incident shock by replacing the amplitude, η_0, with $\eta_0(1 - V/v_I)$. They then stated that for their experiments, the compression $(1 - V/v_I)$ varies from 0.59 to 0.9. Table 4.4 shows, with respect to the upstream and jet interface, the normalised perturbation velocity estimated from the RTI theory as well as the translational velocity, dimensionless upstream and jet interface velocities measured from the experiments and predicted from our simulations (both 2D and 3D). The dimensionless upstream interface velocity, Υ_{IU}, is computed by normalising v_{IU} with V, i.e., $\Upsilon_{IU} = v_{IU}/V$. Similarly, the dimensionless jet velocity, Υ_{AJ}, has been obtained by normalising v_{AJ} with V, i.e., $\Upsilon_{AJ} = v_{AJ}/V$. Haas and Sturtevant (1987) computed the values of V from one-dimensional theory. V, used in the current study, has been computed adopting the same method applied in the derivation of the various wave velocities and characteristic interface point velocities (see Section 4.3.1).

Table 4.4: Dimensionless upstream interface and jet interface velocities from CFD simulations compared to the Rayleigh-Taylor theory and experiments. U is in m/s.

V	Theory	Experimental		CFD Predictions (2D)			CFD Predictions (3D)		
	Υ	Υ_{IU}	Υ_{AJ}	V	Υ_{IU}	Υ_{AJ}	V	Υ_{IU}	Υ_{AJ}
177	1.432	1.07	1.89	171.16	1.04	1.82	175.50	1.05	1.89

Table 4.4 compares the predicted Υ_{IU} and Υ_{AJ} with both experiments and theory. The predicted initial rate of deformation at the upstream interface, Υ_{IU}, is significantly lower than the estimation, Υ, of RTI theory but is in close agreement with the experimentally measured Υ_{IU}, particularly in the 3D predictions. The predicted Υ_{AJ}, on the other hand, is higher than the predicted Υ_{IU}, and there is little disparity between the predicted Υ_{AJ} (2D and 3D) and both; Υ (estimated from RTI theory) and the experimentally measured Υ_{AJ}. This is indicative of the fact that our numerical model is sufficiently reliable and accurate. Again, the 3D predictions are more accurate than the 2D predictions.

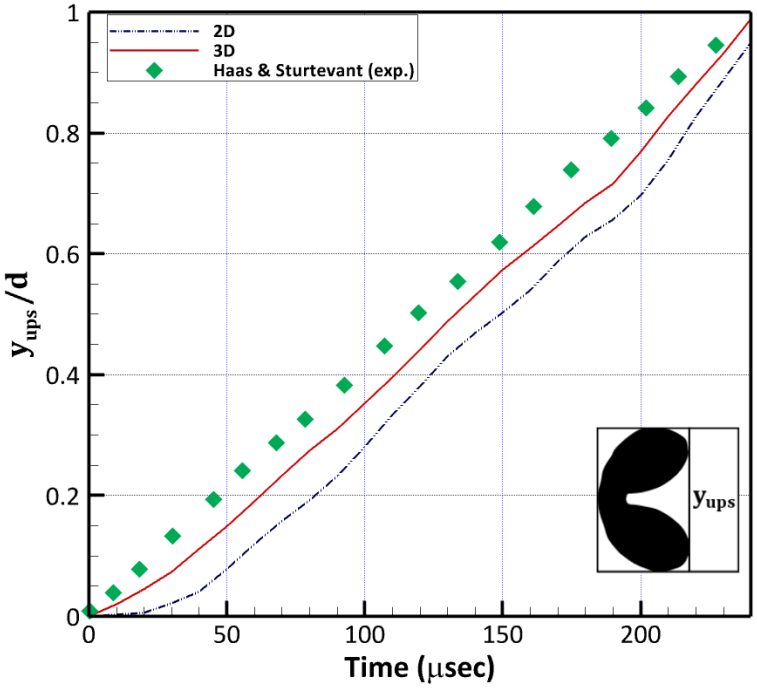

Figure 4.5: Comparison between numerical and experimental dimensionless displacements of the upstream edge against time.

As shown in Fig. 4.5, the characteristic upstream interface displacement, y_{ups}, is normalised by the bubble diameter (d) to allow an efficient comparison of our predicted results to other experimental findings. Fig. 5.5 presents the comparison between the predicted dimensionless displacement of the upstream interface (y_{ups}/d) and the experiments of Haas and Sturtevant (1987). It can be seen clearly that a very good agreement between the present 3D predictions and the experimental data has been obtained. It is also shown in Fig. 4.5 that the 3D predictions are much closer to the experimental data than the 2D predictions, confirming that 3D simulation is needed when a shock wave interacts with a spherical bubble in order to capture such interaction accurately.

4.3.4. Deformation and development of the interface: prediction of downstream interface velocities

Following from the analysis provided in Section 4.3.3, Table 4.5 has been provided, with respect to the downstream interface, and shows the normalised perturbation velocity estimated from the RTI theory as well as the translational velocity, dimensionless downstream interface velocities measured from experiments and predicted from our simulations (both 2D and 3D). The dimensionless downstream interface velocity, Υ_{ID}, is computed by normalising v_{ID} with V, i.e., $\Upsilon_{ID} = v_{ID}/V$. Similarly, V, used in the experiments of Haas and Sturtevant (1987) have been computed from one-dimensional theory. V, used in the current study, has been computed adopting the same method applied in the derivation of the various wave velocities and characteristic interface point velocities (see Section 4.3.1).

Table 4.5: Downstream interface velocities from CFD simulations compared to the Rayleigh-Taylor theory and experiments.

V	Theory	Experimental	CFD Predictions (2D)		CFD Predictions (3D)	
	Υ	Υ_{ID}	V	Υ_{ID}	V	Υ_{ID}
110.9	1.869	1.31	104	1.29	108.33	1.31

During SBI, the downstream interface is initially disrupted by the shock that has previously impinged on and distorted the upstream interface. This is evident from the development of small-scale undulations on the downstream interface. Table 4.5 compares the predicted Υ_{ID} with both experiments and theory. The predicted Υ_{ID} is considerably lower than the estimation, Υ, of RTI theory but is in close agreement with the experimentally measured Υ_{ID}. This again confirms the reliability and precision of our numerical model. There is also a small difference between the 2D and 3D results with the 3D predictions showing better concordance.

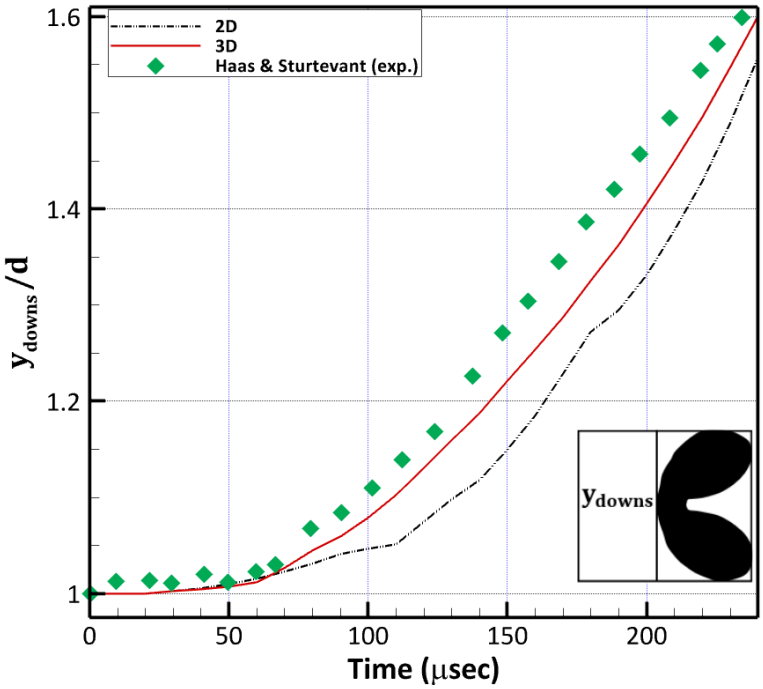

Figure 4.6: Dimensionless numerical and experimental measurements of the characteristic scales against time.

As shown in Fig. 4.6, the characteristic downstream interface displacement, y_{downs}, is normalised by bubble diameter (d). It is evident that the 3D predictions agree very well with the experimental data (Haas and Sturtevant, 1987). Furthermore, it can be seen clearly from Fig. 4.6 that 2D predictions are not as accurate as the 3D predictions, which is consistent with the above discussion that 3D simulations are needed to capture the shock bubble interaction accurately.

Further comparison of the 2D and 3D predictions against the experimental data is shown in Fig. 4.7 which presents the predicted and measured three location changes of the bubble against time. It can be clearly seen that the predictions agree well with the experimental data and as expected better agreement has been obtained between the 3D predictions and the experimental data. It is clear from the previously discussed quantitative comparisons between the predictions and experimental data that the present numerical simulations, particularly the 3D simulations, have depicted the complicated process of SBI excellently. As a result, subsequent analysis will follow the 3D results. The CPU times per 50 iterations are 144 seconds and 4,032 seconds for the performed 2D and 3D simulations respectively using the best 2D and 3D grids as detailed in Section 4.2.4.

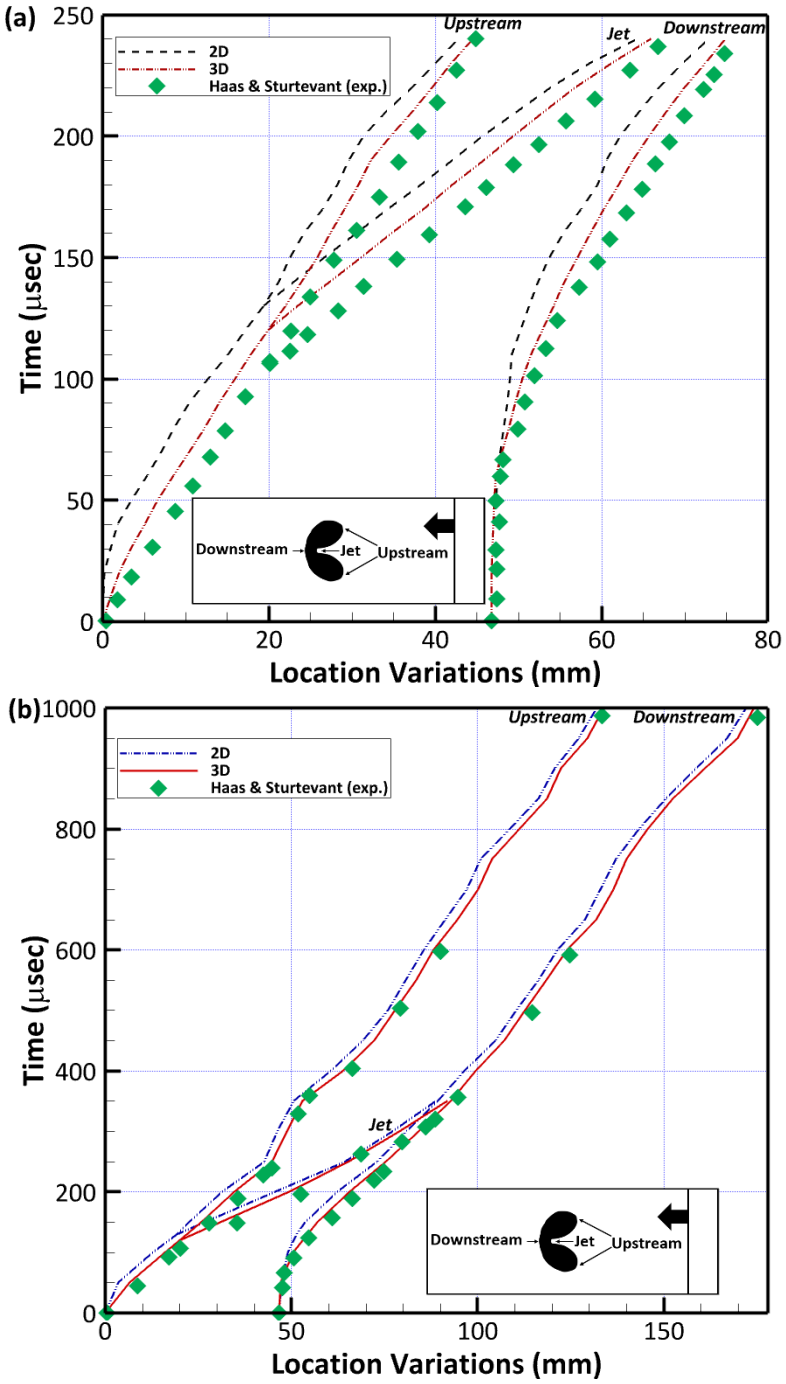

Figure 4.7: Comparison of the 2D and 3D predictions against the experimental data at: (a) small time; and (b) large time.

4.3.5. Quantitative evolution of the bubble length and width

There are various ways a spherical bubble subjected to a shock wave can deform based on the direction of shock wave travel across the density gradient. This has been experimentally proven by Haas & Sturtevant (1987), Layes at al. (2003) and Levy et al. (2003). Two directions are important for the distortion of the bubble post shock wave propagation. These two directions are parallel and perpendicular to the direction of shock wave travel. Layes et al. (2005) clarified that there is not one orientation of distortion perpendicular to the flow but an entire plane orthogonal to the shock wave travel. They then assumed that the distortions which occurred in this plane are radial i.e., an axisymmetric flow, provided the size of the bubble was not too large in comparison to the square

cross section of the shock tube. They then referred to the length and height of the bubble as the horizontal and vertical size of the bubble respectively. Fig. 4.8 shows a representation of side and front view of the original inhomogeneities (before shock wave impact) and the deformed bubbles (after shock impingement).

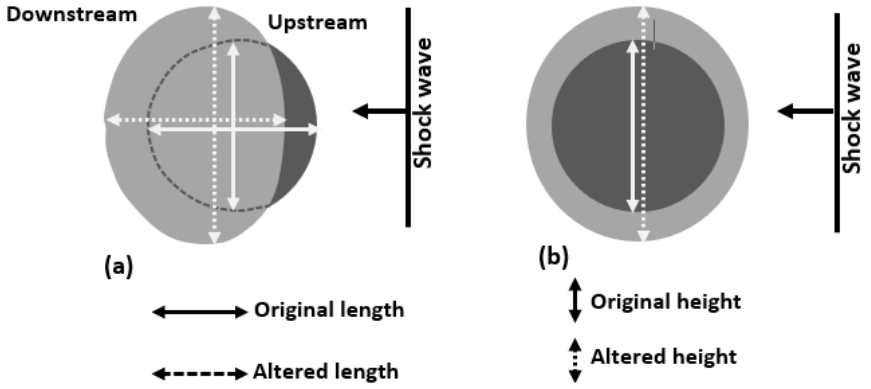

Figure 4.8: Representation of (a) the side views of the initial length and height of the original bubble as well as that of the altered length and height of the deformed bubble; and (b) front views of the initial height of the original bubble as well as that of the altered height of the deformed bubble.

All results presented here and in Section 4.3.6 are compared to the experimental work of Layes et al. (2005). The evolution of the deforming bubble length is shown in Fig. 4.9 (a) which shows a reduction of the bubble length after the shock wave propagates through it. This reduction in length corresponds to the compression phase of the bubble and continues up to 250 μs. This stage is followed by an increase in the bubble length and corresponds to the period when the air-jet impinges on the downstream interface of the bubble. The air-jet effect on the downstream interface of the bubble leads to a stretching of the deforming bubble which results in an increase in the length of the bubble. Fig. 4.9 (a) also shows the rise in the bubble length after 250 μs, albeit at varying incremental rates, up to 1000 μs. From Fig. 4.9(a), it is clear that the current prediction of the evolution of bubble length compares well with experimental measurements.

The evolution of the deforming bubble height is shown in Fig. 4.9(b). Fig. 4.9(b) also presents the prediction of the downstream ring height starting from when this downstream ring emerges from the downstream interface of the bubble after shock impingement. The description of both heights for the upstream and downstream rings is presented within Fig. 4.9(b). Due to bubble compression, the bubble expands vertically which leads to a small initial increase in its height. This increase continues up to 250 μs (rapidly from SBI inception to 100 μs; less steeply from 100 μs to 200 μs, and gradually from 200 μs to 250 μs) followed by the observation of an almost uniform height up till 450 μs (the height is actually increasing from 250 μs to 450 μs but at a very slow rate) before the height of the deformed bubble starts to drop slowly up to 900 μs. The height then tends towards a steady value from 900 μs to 1000 μs. Very interestingly, the period when the bubble height rises very slowly corresponds to when the air-jet starts piercing through the downstream interface and the subsequent formation of the downstream ring. This is consistent with Fig. 4.9(b) which also shows predictions for the evolution of the downstream ring height starting from approximately 250 μs. All the heights predicted before the downstream ring emerges are representative of the evolution of the height of the upstream ring. The height of the downstream ring increases rapidly till 300 μs followed by a less swift rise in the height up to 400 μs. From 400 μs, the height increases gradually with varying degrees of increments up to 850 μs. From 850 μs, the downstream height starts to approach a constant value. As will be explained in Section 4.3.9, the height of the downstream ring increases from inception up to 850 μs because the downstream ring continues to grow attributable to the amount of vorticity contained within it. Similarly, the upstream ring height reduces from approximately 450 μs up till 1000 μs as the upstream ring reduces in size owing to a reduction in

the amount of vorticity contained within it compared to the downstream ring. Finally, Fig. 4.9(b) shows that the predicted upstream/downstream ring heights compare well with the experimentally measured ones.

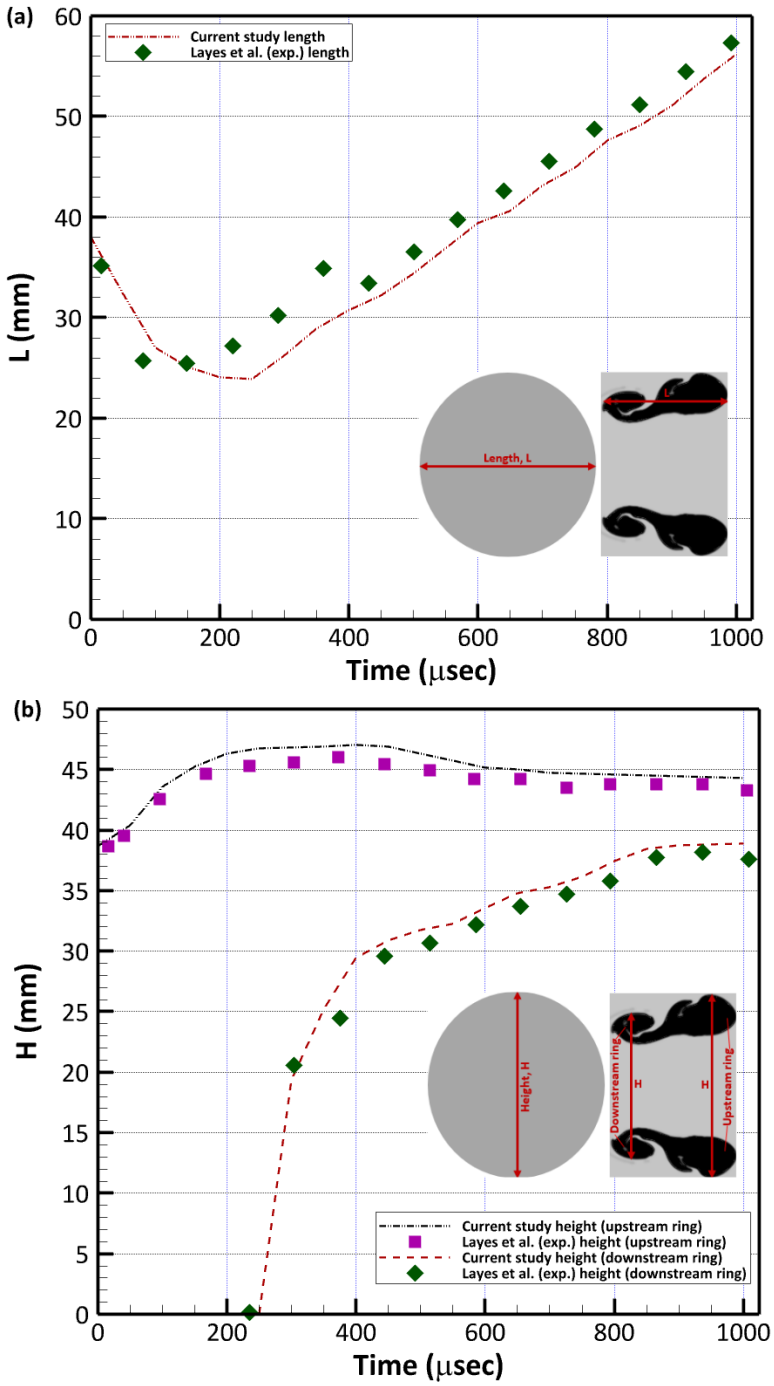

Figure 4.9: (a) Comparison of the predicted to the measured bubble length; and (b) Comparison of the predicted to the measured upstream/downstream ring height.

4.3.6. Quantitative evolution of the vortex ring size and vortex pair spacing

Vorticity develops from the non-collinearity between the pressure and density gradients. The vorticity is responsible for the creation, emergence, and development of a vortex ring. The ring shape of produced vortices arises from the original spherical geometry (Layes et al., 2005). As already established in Section 4.3.5, two rings emerge after the shock pierces through the

downstream interface of the deformed bubble. Fig. 4.10(a) below shows the evolution of the vortex ring size

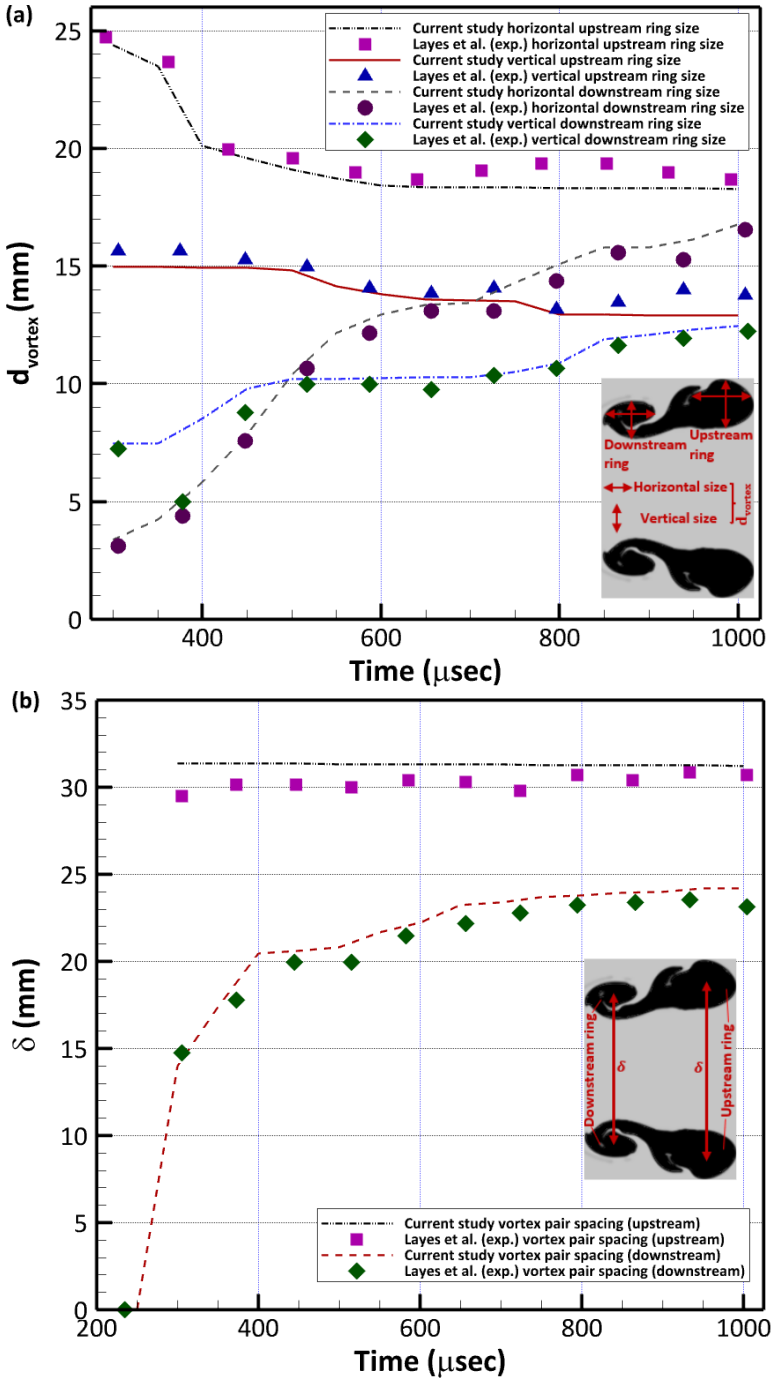

Figure 4.10: (a) Comparison of the predicted to measured vortex ring sizes; and (b) Comparison of the predicted to measured vortex pair spacing.

From Fig. 4.10(a), it is shown that the upstream ring sizes (both in the horizontal and vertical directions) reduce while the downstream components rise. This leads to the downstream ring becoming larger than the upstream ring attributable to increased concentration of the generated vorticity in the downstream ring. Layes et al. (2005) links this increased size of the downstream ring in comparison to the upstream ring to the transfer of mass between this pair of rings. The downstream ring contains most of the produced vorticity as the turbulent mixing of helium and air intensifies within this ring (see Section 4.3.13). Fig. 4.10(a) also shows that the main difference between the decrease in the horizontal and vertical upstream vortex ring sizes is that the former

revealed a steeper rate of reduction from 300 μs to 500 μs compared to the latter. However, the reduction trend of the vertical upstream ring size showed a steeper rate of reduction from about 600 μs to 800 μs compared to that of the horizontal upstream ring size with both upstream sizes showing similar reduction patterns between 500 μs and 600 μs. Both horizontal and vertical upstream ring sizes look to approach a constant value from 800 μs to 1000 μs. With respect to the increase in the downstream ring size, the evolution of the horizontal downstream ring size showed a steeper rise compared to that of the vertical downstream ring size. Again, as in the previously presented comparisons, Fig. 4.10(a) shows an excellent concordance between the predicted and measured evolution of the vortex ring in both the horizontal and vertical directions.

The progression of the spacing between the vortex pair is presented in Fig. 4.10(b). Fig. 4.10(b) details the evolution of the distance between the centers of the two opposite upstream vortex rings and that of the two opposite downstream vortex rings. It also shows a steady progression of the vortex spacing between the centers of the two opposite upstream vortex rings i.e., the change in the upstream vortex pair spacing between successive time steps is almost constant shown by the small reductions in this parameter from 300 μs to 1000 μs as this parameter approaches a constant value. On the other hand, the spacing between the downstream pair rises very rapidly from 250 μs to 300 μs and less swiftly from 300 μs to 400 μs. This is followed by a gradual rise in the downstream vortex pair spacing up till 800 μs after which this parameter approaches an almost constant value up till 1000 μs. Similar to the increase in the downstream height, the downstream vortex pair spacing shows a rising profile because the downstream ring continues to grow attributable to the amount of vorticity contained within it. Similarly, the upstream vortex pair spacing drops very slowly from 300 μs to 1000 μs and approaches a constant value as the upstream ring reduces in size. This is attributable to a reduction in the amount of vorticity contained within the upstream ring compared to that held in the downstream ring. Finally, the predicted upstream/downstream vortex pair spacing compare well with the experimentally measured ones as shown by Fig. 4.10(b).

4.3.7. Vortex generator representation for the spherical helium bubble

This section predicts the vortex strength produced by the penetration of spherical helium bubble by the air-jet stimulated by the RTI. Haas and Sturtevant (1987) treated the jet head as a solid piston with the piston velocity (V_p) given below:

$$V_p = v_{AJ} - V'_b, \tag{4.12}$$

The distance travelled by the piston can be represented with D_p. The works of Maxworthy (1977) and Didden (1979) investigated the production of vortex rings by an impulsive motion of a piston which expels a cylindrical fluid volume from a short compartment into the ambient environment. Haas and Sturtevant (1987) adapted these works to compute the circulation related to the motion of the piston and the vortex circulation. Their comparison of these two circulation values helped estimate the 'efficiency' of the effective piston generator. They then derived the circulation related to the piston given as:

$$\Gamma_p = \frac{1}{2} V_p D_p, \tag{4.13}$$

The Reynolds number (Re) related to the piston is given as:

$$Re = \frac{\Gamma_p}{\vartheta}, \tag{4.14}$$

where ϑ represents the kinematic viscosity of air. The Kelvin formula for the velocity of a vortex ring of Radius, (R_v) and core radius (r_c) can be used to estimate the circulation in the vicinity of the vortex, Γ_v. The velocity of a vortex ring ($V_{v,kel}$) as computed from the Kelvin formula is given below:

$$V_{v,kel} = \frac{\Gamma_v}{4\pi R_v}\left[ln\left(\frac{8R_v}{r_c}\right) - \frac{1}{4}\right], \tag{4.15}$$

Haas and Sturtevant (1987) explained that r_c is small in comparison to R_v which is similar to what this research predicted as presented in Table 4.6.

Table 4.6: Parameters for the piston and vortex ring.

	V_p	D_p	$V_{v,kel}$	R_v	r_c	Γ_p	Γ_v	Γ_v/Γ_p	Re
Haas & Sturtevant (Exp.)	167	30	37	15	4	2.51	2.21	0.88	1.75 x 10^5
Current Study	167.55	25.92	32.11	14.96	3.38	2.17	1.82	0.84	1.4 x 10^5

From Table 4.6, V_p, D_p, R_v, and r_c are estimated from this research's numerical findings i.e., 3D schlieren images while $V_{v,kel}$ can be estimated using some previously derived velocities as presented below:

$$V_{v,kel} = V'_v - V'_2, \tag{4.16}$$

Table 4.6 also shows a good agreement between the predicted and measured Γ_p, Γ_v and Re. Both numerical predictions and experimental measurements also show a remarkably huge percentage of the jet/piston related circulation transmitted to the vortex i.e., 84% for this numerical study and 88% for experimental analysis of Haas and Sturtevant (1987). Lastly, the Re which is of the order of 10^5 prove that the generated vortex rings are turbulent.

4.3.8. Visualization of the shock bubble interaction process

The elaborate and important processes involved in bubble distortion, vorticity production, air-jet development, and the entire late-time development of the SBI process will be further analysed in this section. This section was not presented first as this research intended to quantitatively validate the obtained numerical predictions as shown from Section 4.3.1 to Section 4.3.7 before the presentation of the qualitative comparisons. Fig. 4.11 presents six snapshots of the simulated images (left) and shadow-photographs (right) taken in the experiment. Time, t, is normalized using the shock velocity and the diameter of the bubble. Hence t is non-dimensional.

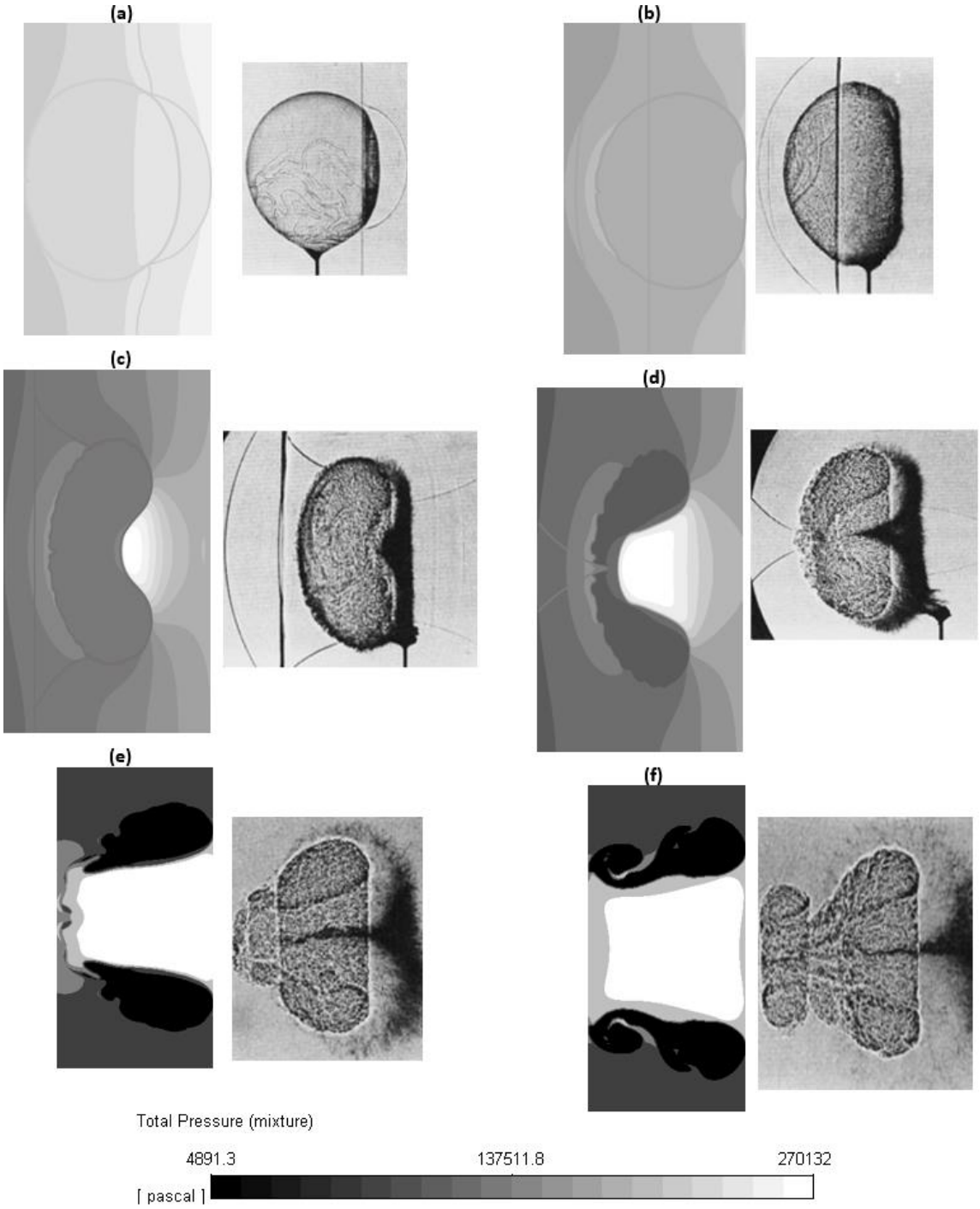

Figure 4.11: Snapshots of simulated images (left) on the central x-y plane and shadow-photographs (right) at: (a) t=0.27; (b) t=0.84; (c) t=1.33; (d) t=2.09; (e) t=3.73; and (f) t=5.76.

Overall, the predictions capture the SBI process, especially the key features, very well as the simulated images are quite similar to the shadow-photographs at all those six times. The simulation results are symmetrical because of the applied boundary conditions. Fig. 4.11(a) shows the incident shock wave shortly after its collision with the helium bubble and the refracted wave, travelling ahead of the incident shock, can be clearly seen from the simulated image while it is barely observable from the shadow-photograph. The shadow-photograph in Fig. 4.11(b) reveals the spherical transmitted shock wave at the left trailed by a flat front which represents the torus-shaped secondary transmitted wave's projection. All these features are well captured in the simulation as shown in the simulated image (left side of Fig. 4.11(b)). Fig. 4.11(b) also shows that the bubble is flattened in the

direction of shock travel. As time progresses, a developing air jet has started to penetrate the upstream interface of the helium volume, which appears to be sinking inwards as seen from Fig. 4.11(c), thus making the distorted bubble appear kidney shaped due to the re-entrant jet's formation at the upstream end. The re-entrant jet is formed due the impact of the ambient air on the upstream interface driven by the generated vorticity (Zhu et al., 2019) and pierces much further into the bubble as shown in Fig. 4.11(d), accompanied by back-scattered waves to the right which are more clearly observable in the simulated images. In the meantime, diffracted waves are observed in both the simulated images and shadow-photographs, more obvious in the shadow-photographs. During bubble deformation and the formation of the air-jet, which is shaped as a convergence nozzle, clearly shown in Fig. 4.11(f), and also observed in the study by Yoo and Sung (2018), there is a gradual rise in the velocity magnitude arriving at the bubble centre. Due to the interfacial density mismatch, the pressure preceding the upstream region of the bubble increases with the air-jet causing the lighter helium gas with the bubble to move to the right and the heavier air to move to the left. These movements are responsible for the bubble hollowing from the upstream interface and through the centre. Similarly, as can be seen from Figs. 4.11(a) to 4.11(d), the pressure upstream of the helium volume is considerably higher than that on the downstream region and this pressure differential means that the heavier air accelerates the lighter helium thus subjecting the deformed bubble to the Richtmyer–Meshkov (RM) instability (shock-induced Rayleigh-Taylor instability). It is understood that vortex rings in the post-shock are formed due to the RM instability at the bubble interface. The simulated images in Figs. 4.11(e) and 4.11(f) in the present study show a visible appearance and formation of such vortex rings, demonstrating the existence of the RM instability. Both the simulated images and shadow-photographs in Figs. 4.11(e) and 4.11(f) also show that the air jet impinges on the downstream air-helium interface and eventually passes through the bubble.

4.3.9. Visualization of vorticity

Vorticity production and transport possibly denotes the most essential component of SBI, and Fig. 4.12 presents the predicted contours of vorticity at various phases of the SBI process. Vorticity is so important in SBI as it, together with the aerodynamic forces, predominantly controls the bubble's motion and shape (Layes et al., 2003) so that the visualization of vorticity can help to understand the SBI process. It is generally accepted that vorticity is generated due to a misalignment of the local pressure and density gradients, which is then deposited and transported in the flow when the shock waves (incident, refracted, diffracted, and focused waves) travel through the bubble. It is interesting to note that even at the early stage, vorticity is generated as shown in Fig. 4.12(a) around the air-helium interface (bubble surface) where pressure and density gradient are located. The vorticity produced by the baroclinic mechanism initiates the deformation of the upstream surface and leads to the caving in/inversion of the upstream bubble surface towards the downstream bubble surface as shown in Figs. 4.12(b) to (d), ensuring that the related rotational fluid motion creates an air-jet which pierces the downstream bubble interface as shown in Fig. 4.12(e). The magnitude of the deposited vorticity is determined by the non-collinearity of the local pressure and density gradients. As the maximum misalignment is located at the diametral plane, the maximum vorticity is thus accumulated at this location thus a justification for the formation of a pair of vortex rings close to the diametral plane. During the process of shock wave interaction with the helium bubble, the RM instability causes the bubble collapse and deformation after which the fluids i.e., helium and air, rotate and continue to develop to form the vortical structures as shown in both Fig. 4.11(f) and Fig. 4.12(f). As these perturbations develop, vortices produced at the interface rolls up and drags helium into a distinctive downstream (primary) vortex ring. Figure 4.12(f) also shows that most of the generated vorticity is situated in the downstream vortex ring.

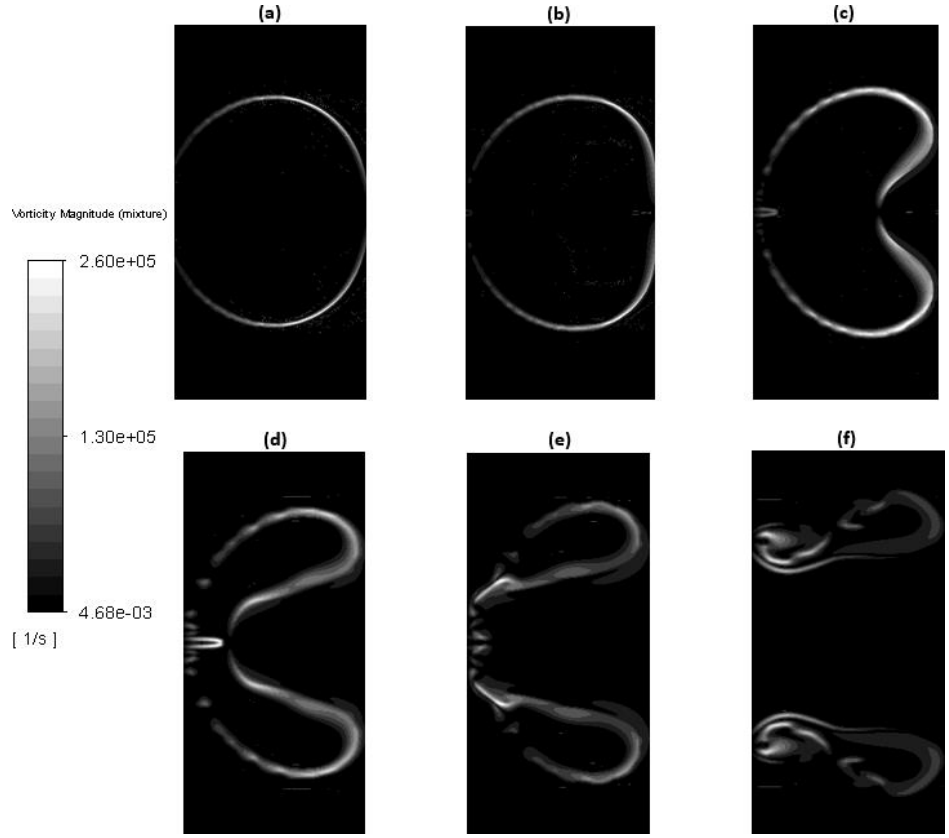

Figure 4.12: Snapshots of vorticity contours on the central x-y plane at: (a) t=0.27; (b) t=0.84; (c) t=1.33; (d) t=2.09; (e) t=3.73; and (f) t=5.76.

4.3.10. 3D flow visualization

3D flow visualization will be presented in this section to further illustrate the SBI process. The notations used in the analysis are defined in the schematic below (Fig. 4.13).

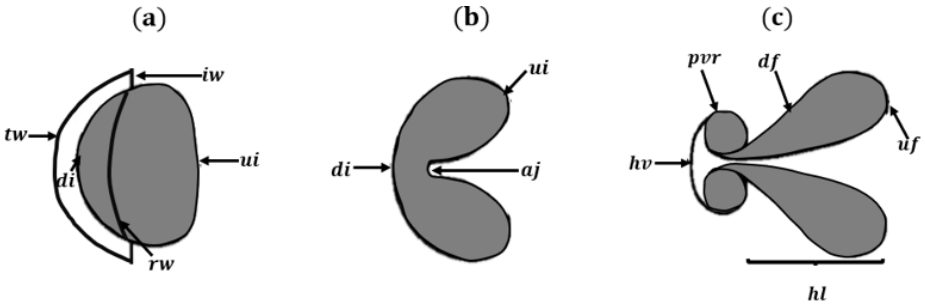

Figure 4.13: Schematic of the SBI process: (a) upstream/downstream interfaces; (b) air-jet; and (c) primary vortex ring and helium lobe (adopted from Haas and Sturtevant (1987))

Snapshots of the predicted pressure iso-surfaces showing a quarter bubble (better suited to show certain feature) are presented below to elucidate the change in position of the helium bubble, generation of the various wave patterns as well as the formation of the vortical structures. There are two points, a point on the upstream edge of the bubble – point C and the highest point of the bubble – point D as shown in Fig. 4.14(a), which are very relevant in understanding how the shocked bubble travel as well as the formation of the vortical structures.

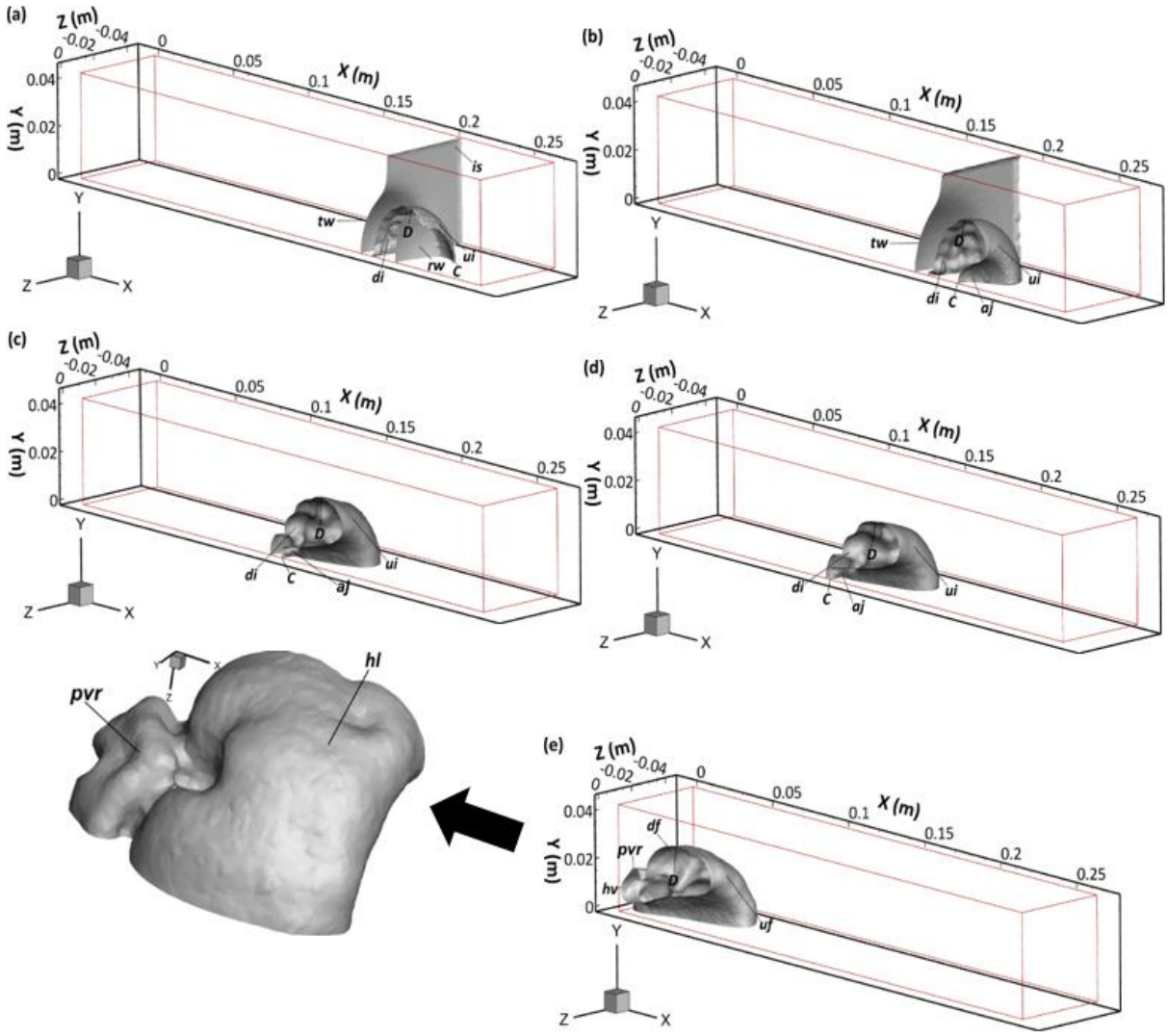

Figure 4.14: Pressure iso-surfaces at: (a) t=0.84; (b) t=1.33; (c) t=2.09; (d) t=3.73; and (e) t=5.76.

At early stage as shown in Fig. 4.14(a), the planar incident shock has collided with the bubble face, generating a refracted shock inside the bubble. The shocked bubble is subsequently deformed and at t=0.84, the incident shock has propagated more than half the length of the bubble and lagged the refracted shock as shown in Fig. 4.14(a). At t=1.33, the incident shock travels past the entire bubble length as shown in Fig. 4.14(b) and lags the transmitted shock culminating from the encroachment of the refracted shock on the downstream bubble edge. At this stage, points C and D have moved a considerable distance from their original positions. As previously discussed, the resulting baroclinic vorticity generation from shock motion across the bubble ensures that the associated rotational motion pulls a jet of surrounding air through the bubble centre. This air-jet is first detected t=1.33 as shown in Fig. 4.14(b), which also shows how far the transmitted wave has travelled ahead of the shocked bubble with the generated vorticity causing the upstream surface to continuously cave-in in the direction of the impinging air-jet and towards the downstream surface. This air-jet that penetrates the helium volume and pierces through the downstream edge of the bubble is analogous to the so-called spike of the RM instability at a perturbed gaseous air-helium interface. This caving-in/inversion continues as shown in Figs. 4.14(c) and (d) until point C is no longer visible in Fig. 4.14(e). At the later stage (t=3.73 and t=5.76), the inverted part of the upstream surface has impinged on the downstream surface with vorticity spinning up and dragging the bubble fluid (helium) into a characteristic vortex ring at the downstream bubble end.

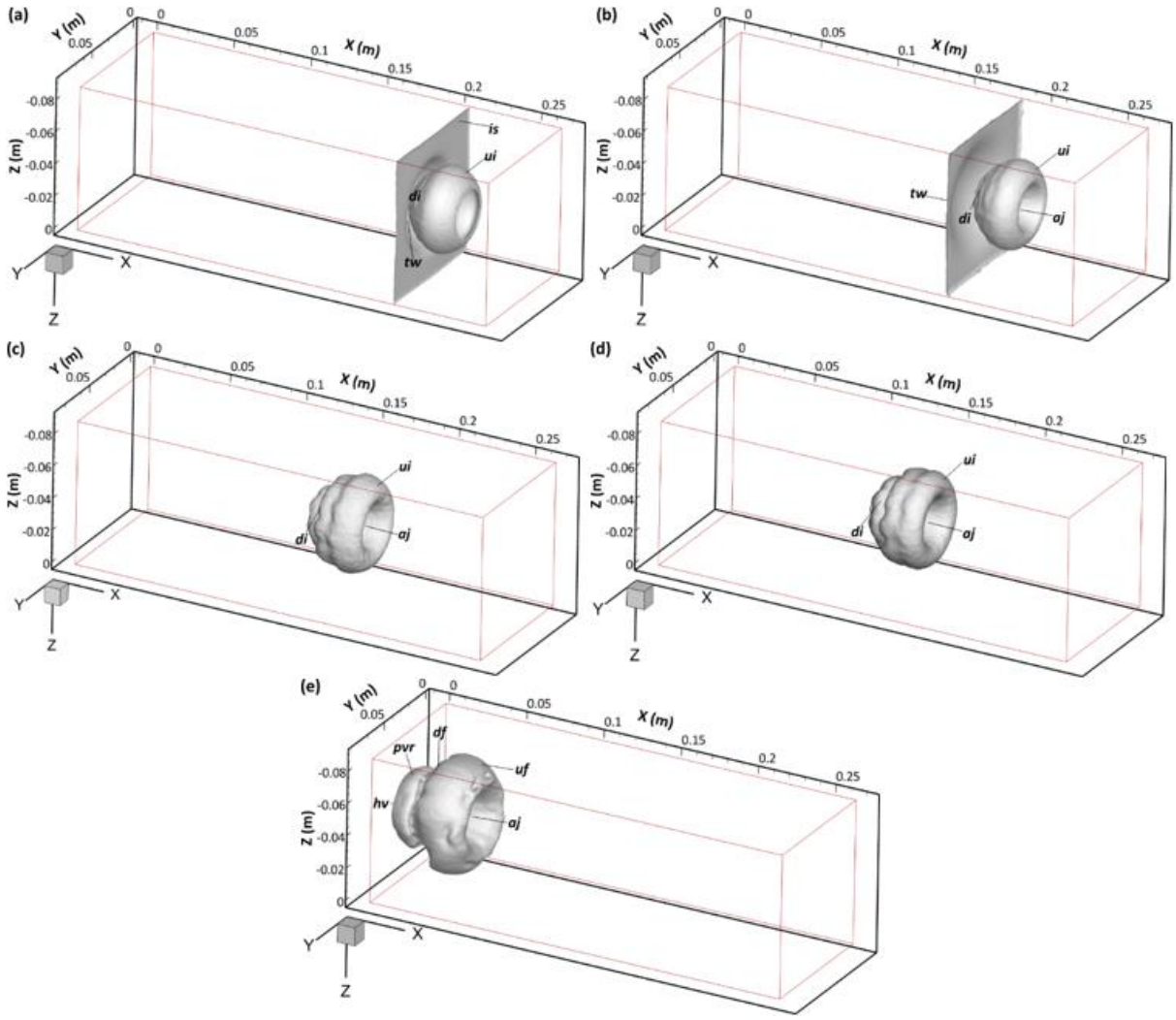

Figure 4.15: Pressure iso-surfaces at: (a) t=0.84; (b) t=1.33; (c) t=2.09; (d) t=3.73; and (e) t=5.76.

Fig. 4.15 presents snapshots of the predicted pressure iso-surfaces showing more clearly certain features of the full bubble compression process and shock propagation. It can be seen from Fig. 4.15(a) that at t=0.84 the transmitted wave is already behind the bubble while the incident shock is still propagating through the bubble. Distortion and movement of the spherical inhomogeneity has already taken place. The upstream region of the bubble has gradually become flat. The transmitted wave travels further behind the bubble and significant distortion of the bubble is observable in Fig. 4.15(b). The air-jet has become evident as shown in Fig. 4.15(b) and the piercing effects of the air-jet are pronounced in Figs. 4.15(c) and (d) where the upstream interface approaches the downstream interface. This is then followed by the formation of a well-defined vortex ring as shown in Fig. 4.15(e).

4.3.11. Vortex ring evolution

The primary vortex ring (pvr) involves highly complex, distorted rotational motion and mixing which have formed from the non-linear coupling of shock compression and acceleration, nonlinear acoustic impacts as well as generation and transport of vorticity (Layes et al., 2005; Ranjan et al., 2007; Ranjan et al., 2008; Ranjan et al., 2011). Hence the development of pvr at the later stage of the SBI with respect to its formation and evolution will be further explained through flow visualization in this section. It can be seen from Fig. 4.16a(i) and Fig. 4.16b(i) that the initial spherical bubble has evolved into three distinct volumes at t=3.73, with the smallest volume at the downstream end. This

smallest volume increases in size with time as shown in Figs. 4.16a(ii – iii) and Figs. 4.16b(ii – iii). As time goes by, helium is drawn in and rolled up by the generated vorticity induced by shock propagation within this smallest volume. The apparent onset of the pvr's formation is observed in Fig. 4.16a(iii) and Fig. 4.16b(iii) at t=4.69. This process continues and at t=5.28, a distinctive pvr has been formed, which is clearly observable in Fig. 4.16a(iv) and Fig. 4.16b(iv). This pvr becomes more and more distinctive as shown in Figs. 4.16a(v – viii) and Figs. 4.16b(v – viii). These figures also clearly show that the hl extends from the upstream edge to where the pvr exists and carries more than 60% of the helium volume, i.e., the hl is much larger than the pvr in volume.

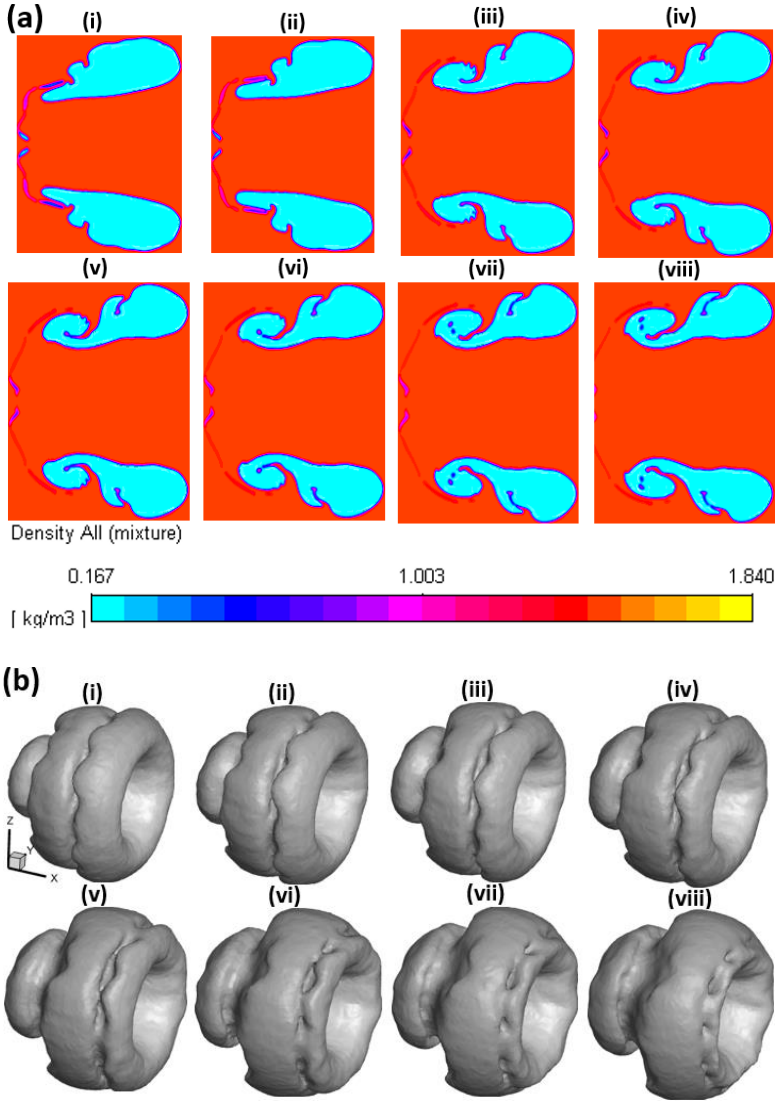

Figure 4.16: (a) contours of density on the central x-y plane at: (i) t=3.73; (ii) t=4.02; (iii) t=4.69; (iv) t=5.28; (v) t=5.38; (vi) t=5.48; (vii) t=5.67; (viii) t=5.76. (b) iso-surfaces of density at: (i) t=3.73; (ii) t=4.02; (iii) t=4.69; (iv) t=5.28; (v) t=5.38; (vi) t=5.48; (vii) t=5.67; (viii) t=5.76.

To the best of our knowledge, very little information is available regarding the rotation direction of the hl and the pvr as SBI progresses. This is especially the case with respect to the evolution of the pvr and its increase in size as revealed above. Similarly, the rotation of the pvr is also linked to the deposition of vorticity in it as SBI increases. This leads to a subsequent reduction in the hl as pvr increases in size throughout the SBI process. From Fig. 4.17, the top hl rolls up in a counterclockwise direction while the top pvr develops and rolls up in the clockwise direction. On the flip side, Figs. 4.17(a) and (c) show that the bottom hl rotates in the clockwise direction while

the bottom pvr evolves and rolls up in the anticlockwise direction. Fig. 4.17(b) is provided as it shows the streamlines on the sides of the hl and pvr which are clearer and more traceable.

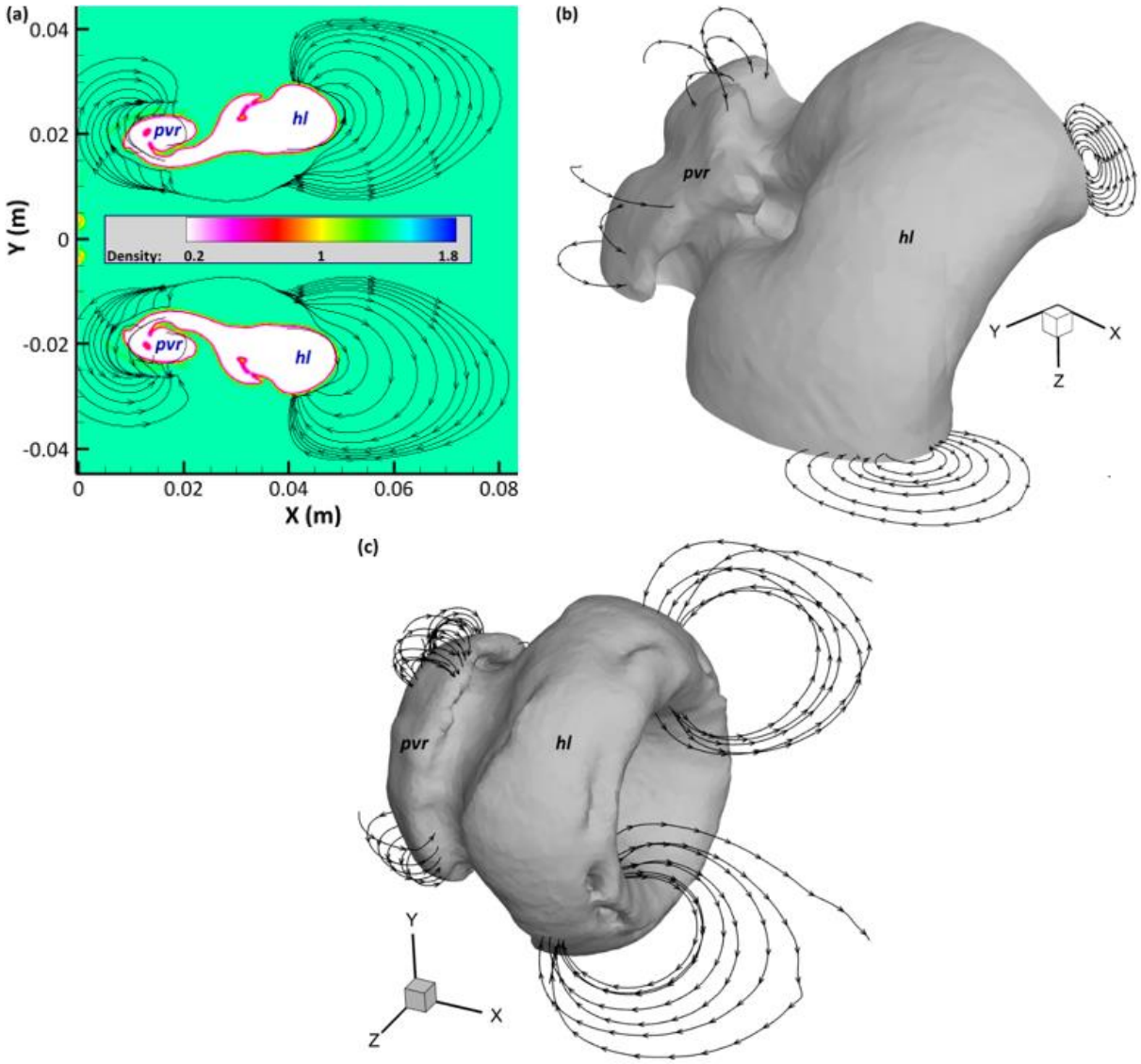

Figure 4.17: Rotation direction of hl and vf revealed by (a) density contours on the central x-y plane; (b) deformed quarter spherical bubble; and (c) distorted full spherical bubble. All images are at t=5.76.

4.3.12. Onset and development of turbulent mixing

The RM instability, which appears when the shock wave accelerates the perturbed interface separating the heavier air and the lighter helium, initially starts with perturbations which develop linearly followed by a non-linear stage where these perturbations grow into complex structures shaped as a converging spike as seen previously in Figs. 4.11(c) and (d). As time progresses, the downstream end of the helium bubble is ruptured by the impinging air-jet as shown in Figs. 4.11(e) and (f). Subsequently, more intensive mixing of helium with air occurs with some small flow structures formed as shown in Fig. 4.18 below, indicating that turbulent mixing starts to develop at the later stage of the SBI in the present study. It can be seen from Fig. 4.18 that the mixing is mainly concentrated inside the pvr, the bridge region which connects the hl to the pvr as well as the outer interface of these areas. This is concordant with the findings of Tomkins et al. (2008) who observed three main regions of mixing i.e., the vortex core, the outer boundary, and the bridge area joining

the two major vortices. Furthermore, it is evident from Fig. 4.18 that large-scale entrainment occurs around the pvr, leading to the increase of pvr and reduction of hl as time passes by. The density contours from t=0.84 to t=5.76 were not displayed in Fig. 4.18 as they did not show any notable signs of turbulent mixing between air and helium.

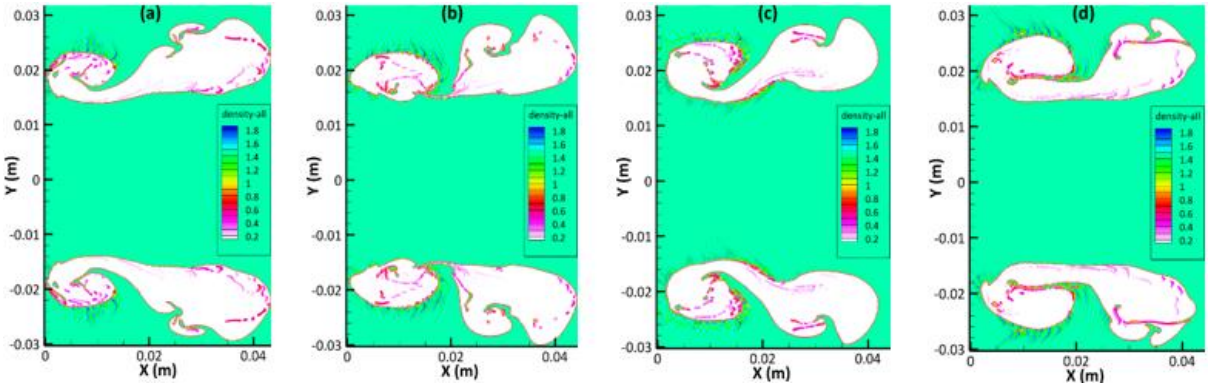

Figure 4.18: Density contours on the central x-y plane revealing the development of turbulent mixing, (a) t=6.15, (b) t=7.16, (c) t=8.31, (d) t=9.90.

4.3.13. Turbulence generation and development

This section focuses on the turbulence generation and development of the SBI process. Fig. 4.19 presents contours of turbulence intensity which has been used to characterise freestream turbulence. Turbulence intensity (represented by turb-intensity in Fig. 4.19) has been computed by ANSYS Fluent using the empirical correlation shown below (ANSYS, 2018):

$$\text{turb-intensity} = \frac{100}{U}\sqrt{\frac{2}{3}k} \tag{4.17}$$

where U and k represent the streamwise velocity and turbulent energy respectively.

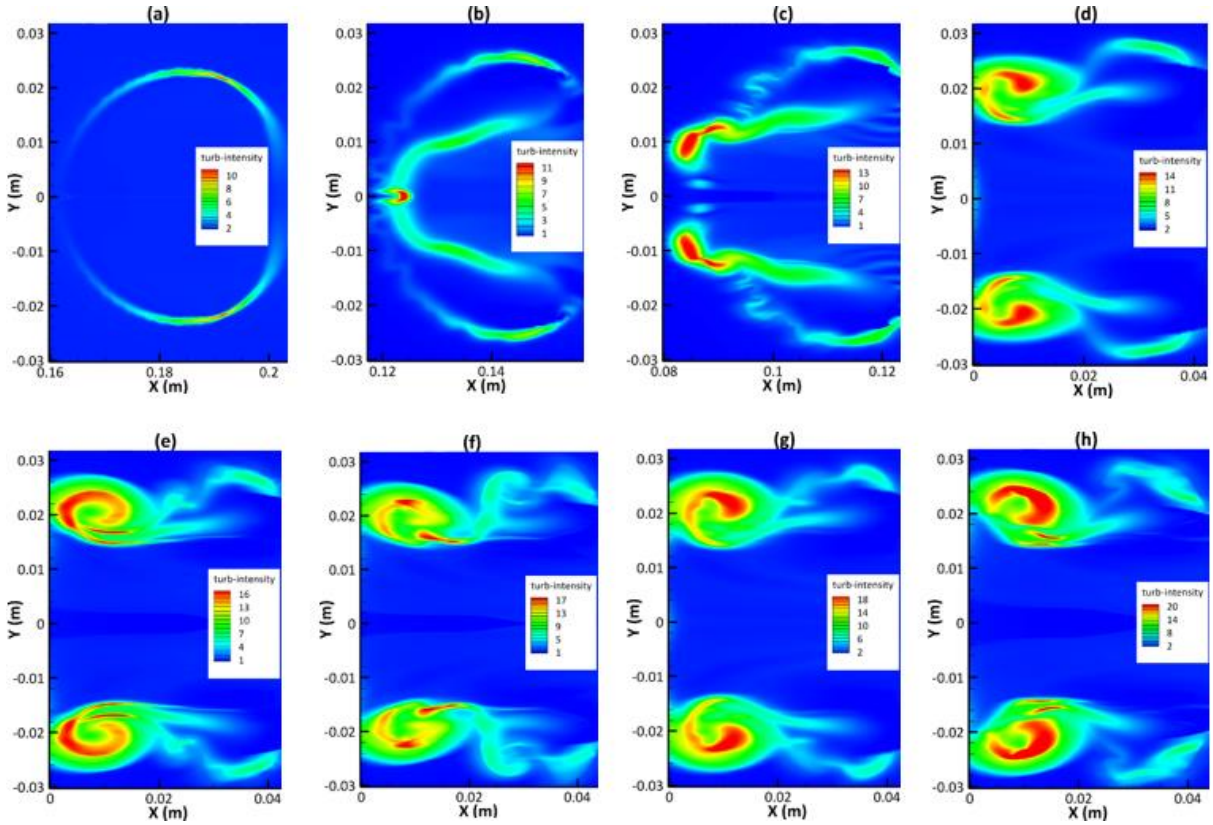

Figure 4.19: Contours of turbulence intensity on the central x-y plane at: (a) t=0.84, (b) t=2.09, (c) t=3.73, (d) t=5.76, (e) t=6.15, (f) t=7.16, (g) t=8.31, (h) t=9.90.

It is well known that SBI involves a broad range of complicated features, from shock wave refraction and reflection, generation, and transport of vorticity, to the onset of turbulent mixing but hardly any previous experimental and numerical studies have addressed one very important feature – turbulence generation and development. It can be seen from Fig. 4.19(a) that turbulence starts to be generated initially around the bubble interface at early stage when t=0.84. As times passes by, the bubble interface is severely distorted, and more turbulence is generated around the tip of the air-jet as shown in Fig. 4.19(b) with the maximum turbulence intensity reaching about 11%. After the air-jet pierces through the downstream bubble interface, turbulence is mainly generated around the pvr region and maximum turbulence intensity level increases gradually to about 14% when a distinctive pvr has already been formed at t=5.76 as shown in Fig. 4.19(d). Afterwards the turbulence field looks similar and turbulence level increases gradually as shown in Figs. 4.19(e-g) to a maximum turbulence intensity of about 20% at t=9.9 as shown in Fig. 4.19(h).

4.4. Conclusions

The mechanism of a spherical bubble deformation and compression from the interaction with an incident shock at Ma = 1.25 has been examined through a numerical study. The URANS mathematical model is employed with a CLSVOF scheme to capture the helium bubble and air interface accurately. Both 2D and 3D simulations have been carried out and it is demonstrated that the 3D predictions are much closer to the measured values, with a very good agreement between the predicted velocities of refracted wave, transmitted wave, upstream interface, downstream interface, jet, vortex ring and the corresponding measured values. Also, a comparison of the 2D and 3D predicted non-dimensional bubble and vortex velocities to the experimentally measured ones show a very good agreement, but the 3D predictions showed better concordance. This suggests that 3D simulations are necessary for accurate predictions of SBI which is inherently 3D, especially at the later stage of SBI. The predicted

dimensionless upstream, downstream, and jet interface velocities were also compared to both the Rayleigh Taylor Theory, for estimating the growth rate of small sinusoidal perturbations, and past experimental results. Our 2D and 3D results show a good agreement with the theoretical predictions and experiments. As in the previous comparisons, the 3D predictions are much closer to the theoretical estimations and experimental measurements.

Another quantitative assessment that was conducted involved comparing the predicted temporal variations of the bubble length and width as well as the produced vortex sizes and vortex pair spacing to that measured in past experimental works. There was a good agreement between the predictions of the current study and the experimental data. This research noticed that the bubble length initially decreased due to bubble compression before increasing due to an increase in the bubble length in the lateral direction after the air-jet pierces the downstream interface and the downstream ring emerges. The upstream ring height initially increased corresponding to the bubble compression which resulted in bubble elongation in the vertical direction. This was followed by a very gradual rise in this parameter after which it dropped in connection to the increasing height of the downstream ring. The height of the downstream ring continuously increased albeit at different incremental rates. Finally, these sets of comparisons revealed that the upstream ring height, downstream ring height, horizontal upstream ring size, vertical upstream ring size, upstream vortex pair spacing and downstream vortex pair spacing tended towards a constant value. The final quantitative assessment conducted involved comparing the predicted piston and vortex ring circulations to the experimentally measured ones. This research's estimations showed a very good agreement with the experimental measurements with the order of the computed Reynolds number i.e., 10^5, proving that the generated vortex rings are turbulent.

Flow visualization shows that the predictions have captured many salient flow features observed experimentally very well as the simulated images generally conform to the experimental shadowgraphs. The simulated images have clearly shown the initial distortion and flattening of the upstream edge of helium-filled spherical bubble, followed by the formation of an air-jet that grows towards and impinges on the downstream bubble edge. The evolution of wave patterns involved in the SBI, i.e., incident wave, transmitted wave and refracted wave, is also clearly illustrated. As the SBI progresses at the air-helium interface which has already been deformed by little undulating perturbations of long wavelengths that grew linearly, the formation of the primary vortex ring induced by the RM instability is observed. The detailed evolution process of the primary vortex ring from its onset to its development to a full distinctive vortex ring has been revealed via the flow visualization. In particular, the present study shows clearly that turbulence is generated at relatively early stage of the SBI before the formation of primary vortex ring (pvr). After the formation of this distinctive pvr, turbulence is mainly generated around the pvr region with the maximum turbulence intensity reaching around 20%. To our best knowledge, turbulence generation and development has not been presented/discussed in any of the previous relevant studies.

5. Shock/Cylindrical Bubble Interaction

5.1. Introduction

The objective of this chapter is to accurately perform two-dimensional (2D) and three-dimensional (3D) computational fluid dynamics (CFD) simulations to investigate the complex interaction of a supersonic shock wave (Ma = 1.22) with a cylindrical helium bubble. To do this, the Unsteady Reynolds-Averaged Navier-Stokes (URANS) mathematical model and the coupled Level Set (LS) and Volume of Fluids (VOF) method, also referred to as the CLSVOF scheme, within the commercial CFD code, FLUENT, have been applied in the present study. The simulations are evaluated by comparing predicted velocities of refracted wave, transmitted wave, upstream interface, downstream interface, jet and vortex filament with related existing experimental data. The predicted non-dimensional bubble and vortex velocities have also been compared with experimental data and a simple model of shock-induced Rayleigh-Taylor (RT) instability (i.e., Richtmyer–Meshkov instability) and other theoretical models. Comprehensive flow visualization has been used to explain the shock-bubble interaction (SBI) process from the onset of bubble compression up to the formation of the vortex filaments as well as the production and distribution of vorticity. Comparisons are also shown between the predicted bubble length/width and the experimentally measured results to elucidate changes in the shape and size of the 2D and 3D bubbles. To gain further understanding into the SBI flowfield, turbulence is examined to allow for the investigation of small flow structures and turbulent mixing between helium and air at the later stage of SBI. This is because, to the best of our knowledge, no previous studies have addressed the generation and development of turbulence at the SBI later stages as well as the evolution of vortex filaments from inception to the later phases. These knowledge gaps will be elucidated in the current study. 2D simulations are also performed as most numerical studies are 2D primarily due to its computational efficiency but there is always a question mark on the precision of 2D simulations. Hence, the 2D SBI simulations are directly compared against 3D SBI numerical simulations and previous experimental data to evaluate their accuracy.

5.2. Methodology

5.2.1. Governing equations and numerical methods

The interaction between supersonic air and a cylindrical helium bubble at the air-helium interface as well as the subsequent shock wave travel and bubble deformation were simulated using a pressure-based FVM to solve the governing integral equations for the conservation of mass and momentum i.e., URANS equations. This ensured that the present understanding of the complex SBI process is advanced. SBI is predominantly unsteady, and turbulence is generated at the later stage of SBI with usually large-scale unsteady flow structures. It was demonstrated by Onwuegbu and Yang (2022) that for this kind of flow, the URANS approach could predict the flow accurately at a significantly reduced cost so that there was no need using two other more accurate approaches, i.e., LES or DNS. The URANS equations are derived by averaging the instantaneous Navier-Stokes equations with some extra terms called Reynolds stresses being generated during the averaging process. These terms need to be approximated/modelled using a turbulence model. There are many turbulence models available and the selection of an appropriate turbulence model for this research will be presented in Section 5.2.5. As this kind of computational problem involves mixing the incident shock wave and the bubble gas at the air-gas interface which leads to the creation of complex turbulent structures in the supersonic flow, it is expedient to efficiently capture the bubble deformation. As such, an accurate interface tracking technique is required to capture the bubble deformation properly. Several methods are available to track the interface but most of them often fail to sustain pressure equilibrium for grid cells nearby the interfaces where two or more fluid components are mixed. They also struggle to handle large interface distortions, i.e., disintegration and fronts fusing (Shyue, 1998). From a numerical investigation of SBI viewpoint, various

researchers (e.g., Niederhaus et al., 2008; Taniguchi et al. 2014) had investigated the subject using VOF with varied success. 2D and 3D CLSVOF schemes were then adopted to track the air/helium interface, predict the bubble compression dynamics and formation of vortex filaments as well as treat topological changes at the interface. A third order MUSCL scheme was employed to discretize both momentum and the continuity equations spatially. The compressive scheme, which is a second order reconstruction scheme, was also adopted for spatial discretization of the volume fraction equations. With respect to the compressive scheme, the sharp/dispersed interface regime was applied. A first-order implicit scheme was used for the temporal discretization of the 2D and 3D URANS equations. To achieve numerical stability and accuracy, the Courant Friedrichs Lewy number was set as 0.5 and a very small-time step of 4×10^{-7} seconds was used to accurately capture detailed flow developments. These equations, models and schemes have been elaborately discussed in Chapter 3.

5.2.2. Computational details

The computational set-up replicates the experiment carried out by Haas and Sturtevant (1987) with the key parameters, which are shown in Table 5.1.

Table 5.1: Experimental conditions.

Bubble gas	Ambient gas	Ma	A
Helium	Air	1.22	-0.715

Fig. 5.1(a) shows the 2D representation of the computational domain (half of the domain) detailing the initial conditions within the domain and boundary conditions for the computations. This research simulated this 2D cross-section using cartesian coordinates where the x-axis is horizontal, and the y-axis is vertical. The dimensions of the 2D computational domain $(d \times (L_a + 0.4d)$ are provided as a function of the bubble diameter, d (= 50 mm as in the experimental demonstrations of Haas and Sturtevant, 1987) while L_x varies and is selected to provide enough room to hold the shocked bubble travel throughout the monitored time. The computations are performed only on the upper half as it is a mirror image of the lower half. The lower boundary of the grid (Edge CD) represents the shock-tube axis while the upper boundary of the computational grid (Edge AB) is treated as a solid wall with the no-slip wall boundary condition applied. The right boundary is the inlet, which is shown as Edge AC, while the left boundary corresponds to the outlet, which is shown as Edge BD. The incident shock propagates from right to left and the right boundary cells comprise of parameter values, i.e., $\rho_2, P_2, u_x = U_2, u_y = 0$, which is equivalent to the area behind the supersonic planar shock. As revealed from within the computational domain, identical values are utilised as initial conditions behind the shock which are located at a few cells within the computational grid. The values of these parameters also denote the post-shock properties of the ambient gas utilised in the initialisation and are calculated from the Rankine-Hugonoit relationships (Houghton and Brock, 1993). The right boundary condition allows the smooth outflow of reflected waves created by the SBI. The left boundary condition equivalently allows the smooth outflow of any leftward-moving waves, including the distorted incident shock. Fig. 5.1(a) also reveals that the left boundary condition is achieved by sustaining a 'zero gradient' for all fluid variables, i.e., $\nabla u = 0, \nabla P = 0, \nabla \rho = 0$. For both 2D and 3D cases, the upstream end of the bubble is kept at some distance from the incident shock. This is because a shock has an expected tendency to spread to its usual profile given an 'exact discontinuity' as initial conditions (Hillier, 1991) which could lead to errors that adversely delay the SBI process.

For the 3D simulations (see Fig. 5.1(b)), the *x*-axis is coincident with the shock-tube long axis in the direction of shock-wave travel. The *y*-axis and *z*-axis are along the traverse directions. The incident shock wave and the free stream flow propagate in the *x* direction. The computational geometry represents a physical region (shown as a cuboid) with dimensions $2d \times (L_x + 0.4d) \times 2d$, where *d* is the bubble diameter and L_x has been selected to enable complete propagation of the shocked bubble for the required times. Similar boundary conditions as in the 2D case are applied for the 3D case and a no-slip boundary condition is employed on the top, bottom, and side walls e.g., the inflow and outflow boundary conditions for the 3D case are as specified for the 2D inlet and outlet boundary conditions as shown in Fig. 5.1(a). As in the 2D case, the 3D outflow condition has adopted a zeroth-order extrapolation to the boundary whereby the outermost data plane is transferred into the boundary such that the gradients across the boundary equate zero ($\nabla v = 0, \nabla P = 0, \nabla \rho = 0$).

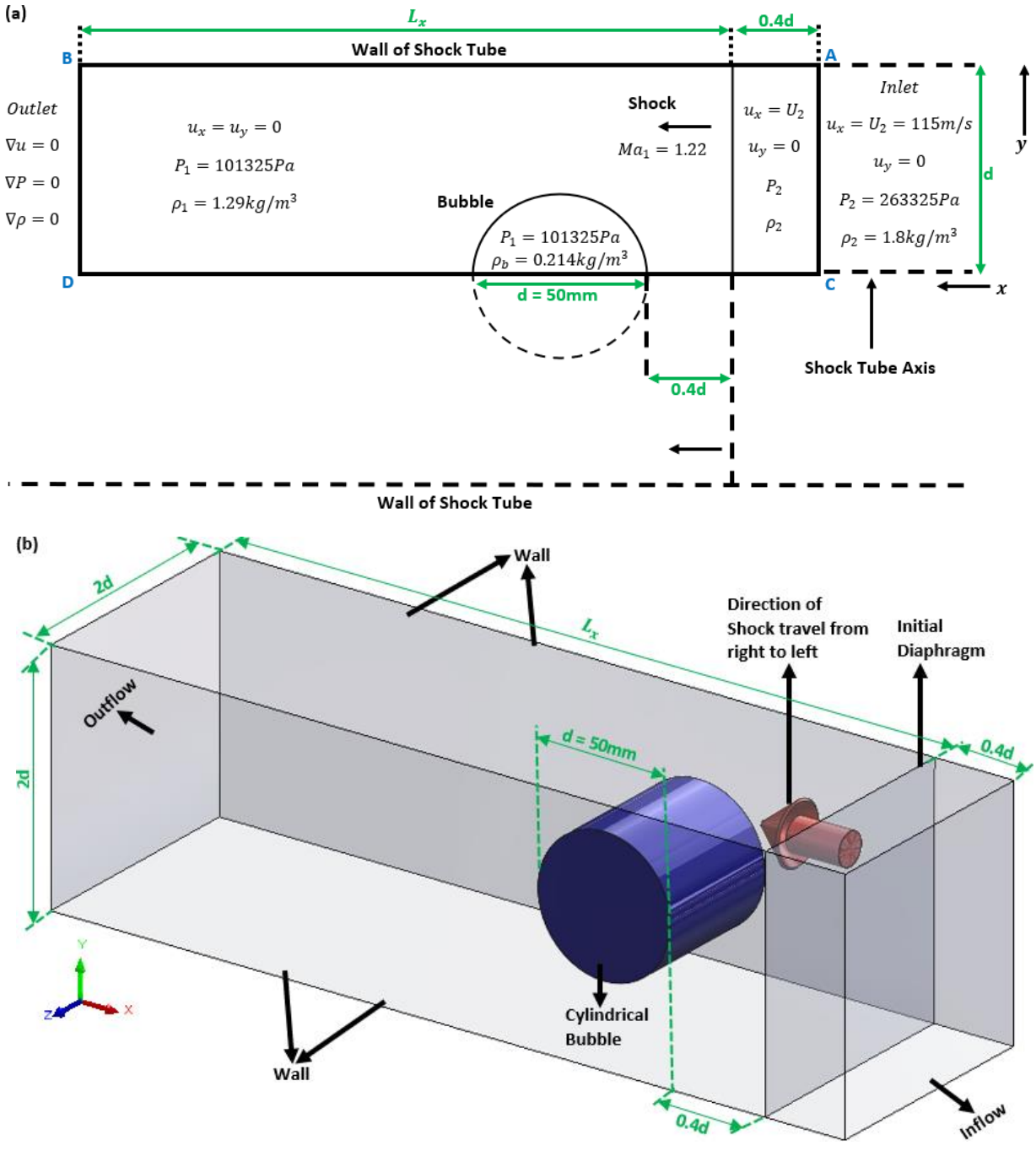

Figure 5.1: (a) The upper half of the shock tube revealed by the surrounding heavy black line and boundary/initial conditions for the 2D case; and (b) Computational domain for the 3D case.

The 2D cylindrical challenge (set-up and boundary conditions) is similar to the 2D spherical problem as both scenarios have replicated the experimental conditions of Haas and Sturtevant (1987). Their experiments showed that they used a similar set-up for both experiments performed on either a single cylindrical or spherical bubble. As in the experiments, this research has only varied the flow Mach number (1.25 for the spherical case and 1.22 for the cylindrical case) and bubble dimensions (45mm diameter for spherical case and 50mm diameter for cylindrical case).

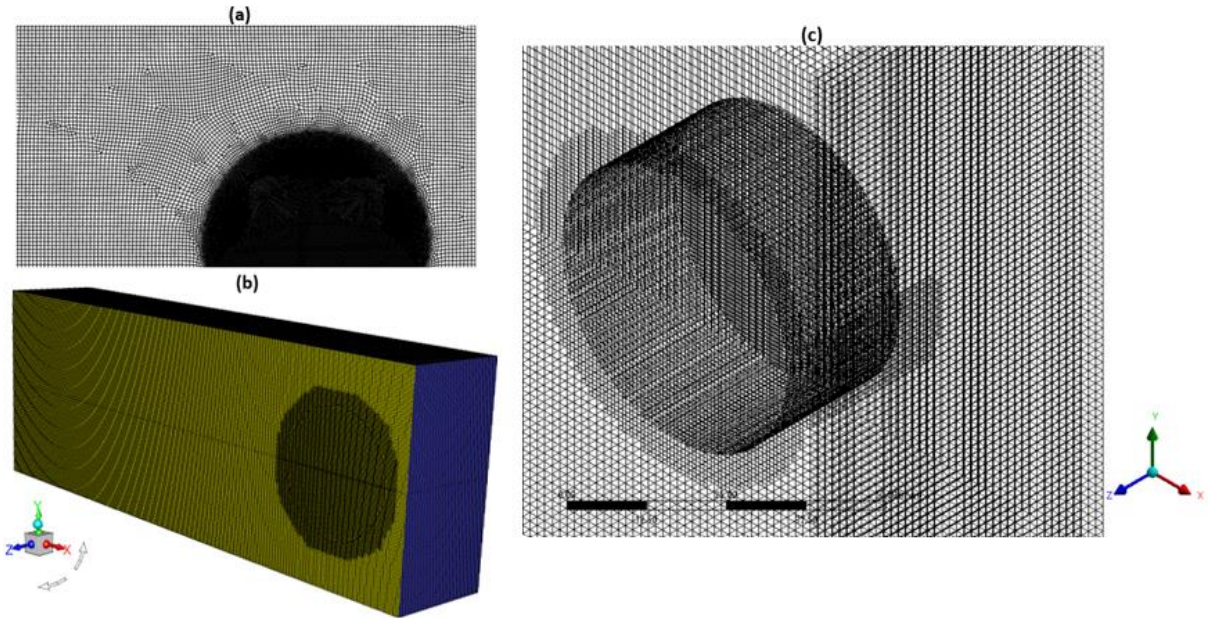

Figure 5.2: (a) 2D hybrid mesh; (b) 3D unstructured mesh; and (c) Close view of fine mesh around bubble from Adaptive Mesh Refinement (AMR).

The 2D (Fig. 5.2(a)) and 3D computational grids (Figs. 5.2(b) and (c)) consist mainly of structured meshes in the main flow region while the region in the vicinity of the bubble (both inside and outside) has been discretised into unstructured grids, i.e., both hybrid grids. The unstructured cells used in the bubble vicinity for both 2D and 3D cases enable the local alignment of the grid orientation to the dominant flow direction due to their flexible nature thus lessening numerical diffusion (Holleman et al., 2013) and have been validated by the works of previous researchers (e.g., Holleman et al., 2013; Zubair et al., 2013). These unstructured grids make it easy to dynamically adapt the grid to the local structures of interest. As seen from Figs. 5.2(b) and (c), the 3D mesh is a hybrid grid consisting of uniform hexahedral meshes in most of the main flow region and smaller uniform hexahedral meshes within the bubble while the bubble vicinity (just outside and inside) is discretised into ‘smaller-cell’ unstructured triangular prisms. The cartesian cut-cell method, previously applied by Ingram *et al*. (2013), Berger *et al*. (2012), and Johnson (2013), has been used to generate this mesh. This method proves very useful to preserve the decoupling between the volume hexahedral mesh resolution and the surface triangulation in the bubble vicinity whilst focusing on resolution requirements close to the boundaries and reducing mesh irregularities in the cut cells (Berger *et al*., 2012).

Prior to the application of AMR, the cells inside the bubble and in its vicinity were made to be finer than the cells in the main flow region and the wall. AMR helps to generate a more robust high-resolution grid capable of reproducing a sharp representation of discontinuities as well as can sufficiently resolve the various flow structures to be investigated. With respect to AMR, several authors (Berger and Oliger, 1984; Henderson et al., 1991; Bell et al., 1994; Klein et al., 1994; Quirk and Karni, 1996; Nourgaliev et al., 2006; Nierderhaus et al., 2008, etc.) had extensively applied it to SBI computations. The AMR settings are selected to ensure maximum refinements in all areas

having a non-zero bubble fluid volume fraction and close to any strong density gradients (Nierderhaus et al., 2008). AMR thus ensured that the mesh is refined inside the bubble and its vicinity (including the primary shock wave) guaranteeing that the fine cells surround and travel with the bubble to provide for the strong interaction between the incident shock waves and the bubble. For this research, AMR is built in by ANSYS Fluent and can be manipulated by the user to achieve the desired amount of extra grid cells that surround the interface and travel with the bubble and shock wave. This procedure gave us complete control of grid resolution. In Figs 5.2(a) – (c), the adapted mesh has two levels of AMR superposed on the original grid with a refinement ratio of 2 each.

5.2.3. Initialization of the computational problem

This research initialised the helium gas within the bubble and the unshocked surrounding fluid, i.e., area between initial diaphragm and outlet at atmospheric conditions. The initialisation assumes that the bubble and the unshocked surrounding fluid are originally in a state of rest as well as in thermal and mechanical equilibrium thus implying that any original buoyant movement of the bubble is ignored.

The JANAF data (Gordon and McBride, 1976) is used to derive the ratio of specific heats, γ, for bubble gas (helium) and surrounding gas (air) utilising the original, unshocked pressure and temperature. Both fluids retained a constant value of γ throughout the computation.

This research adopted the Rankine-Hugonoit relationships (Houghton and Brock, 1993) to calculate the post-shock characteristics of the surrounding air, as shown on the right-hand side of Fig. 5.1(a). The post-shock Ma, pressure and density are computed using the following mathematical relations respectively:

$$Ma_2{}^2 = \frac{(\gamma-1)Ma_1{}^2 + 2}{2\gamma Ma_1{}^2 - (\gamma-1)}, \tag{5.1}$$

$$\frac{P_2}{P_1} = \frac{2\gamma}{\gamma+1} Ma_1{}^2 - \frac{\gamma-1}{\gamma+1}, \tag{5.2}$$

$$\frac{\rho_2}{\rho_1} = \frac{\frac{\gamma+1}{\gamma-1}\left(\frac{P_2}{P_1}\right) - 1}{\frac{\gamma+1}{\gamma-1}\left(\frac{P_2}{P_1}\right)}, \tag{5.3}$$

where $Ma_1 = 1.22$, P_1 and ρ_1 represent the initial Mach number, pressure and density of the ambient air respectively, as shown on the left-hand side of Fig. 5.1(a).

5.2.4. Mesh independence study

A mesh independence study has been performed with three mesh qualities for both 2D case (0.14, 0.20, and 0.29 x 10^6 cells) and 3D case (4.5, 5.8, and 9.5 x 10^6 cells) to determine the best grid resolution that will yield the most optimal computational results in comparison to the experimental works of Haas and Sturtevant (1987). Figs. 5.3(a) and (b) show the changes in bubble compression and jet formation with respect to three representative positions, i.e., upstream, jet, and downstream locations as specified in the respective figures. For the 2D case represented by Fig. 5.3(a), the results show little disparity when the mesh is refined from 0.20 to 0.29 x 10^6 cells, and hence there is no need to refine the mesh further. As such, the remaining 2D simulations are carried out using 0.29 x 10^6 cells. Similarly, for the 3D case represented by Fig. 5.3(b), the derived results from the mesh with 5.8 x 10^6 cells show little variation from the results obtained from the mesh with 9.5 x 10^6 cells and hence there is no need to further refine the mesh. Following this analysis, all 3D computations are performed using 9.5 x 10^6 cells.

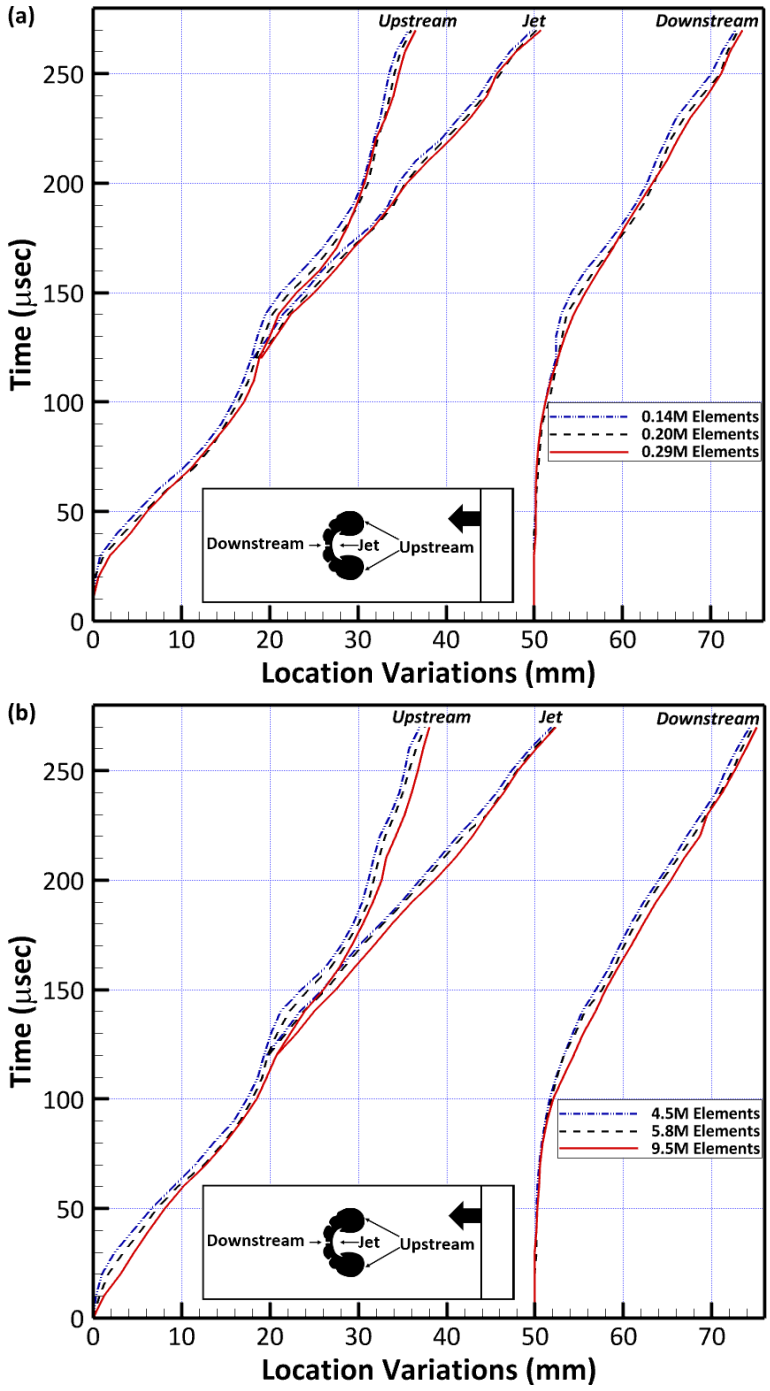

Figure 5.3: (a) Coarse, fine and finer meshes in 2D case; and (b) Coarse, fine and finer meshes in 3D case.

5.2.5. Turbulence model selection

Lawson and Barakos (2011) explained that the associated flow fields for a SBI will be characterised by the strong acoustic effects, unsteadiness, and turbulence. This means that the mixing process between the supersonic shock wave and the bubble will yield more complex turbulent features. Also, SBI shows structures that are preliminarily turbulent (Haas and Sturtevant, 1987) and there is a fundamental variation in the behaviour of 2D and 3D turbulence which is due to the lack of the

vortex-stretching mechanism in 2D (Pope, 2000). Furthermore, Klein *et al*. (2003) experimentally investigated the presence of non-axisymmetric perturbations in the original bubble geometry which they observed to trigger azimuthal vortex-ring instabilities like the type described by Widnall *et al*. (1974). Several authors (e.g., Quirk and Karni, 1996; Grasso and Pirozzoli, 1999; Nierderhaus et al., 2008; Ding at el., 2018; Georgievskiy et al, 2018; Lei and Li, 2018; Fan et al., 2019; Ray et al., 2019; Zhai et al., 2019; Liang et al., 2020; Li et al., 2021) had numerically investigated SBI using the compressible Euler equations which govern the adiabatic and inviscid flows (Toro, 2009). But if the late-stage RMI involving small-scale structures and even turbulent mixing are to be discussed (as in the current study), physical viscosity should be considered (Ding et al., 2018). This then necessitates the use of turbulence models to effectively study the SBI phenomenon as there is hardly any knowledge acquired till date concerning the performance of turbulence models for SBI simulations. This research thus stands as a new research dimension to studying SBI. There are several turbulence models and there is no general agreement which model is most superior as their individual performance is very case dependent. Based on this, this research has adopted three extensively applied and highly rated turbulence models: the realizable *k-ε*, the shear stress transport (SST) *k-ω*, and a Reynolds stress model (RSM). These three turbulence models have been examined to evaluate their performance for the 3D case. Fig. 5.4 shows the comparison between the predicted three location variations of the bubble using these three turbulence models versus the experimental data of Haas and Sturtevant (1987). It is clearly seen in Fig. 5.4 that the predictions using all three turbulence models show little disparity but the results from the realizable *k-ε* are slightly closer to the experimental data. Therefore, realizable *k-ε* turbulence model is adopted in this research.

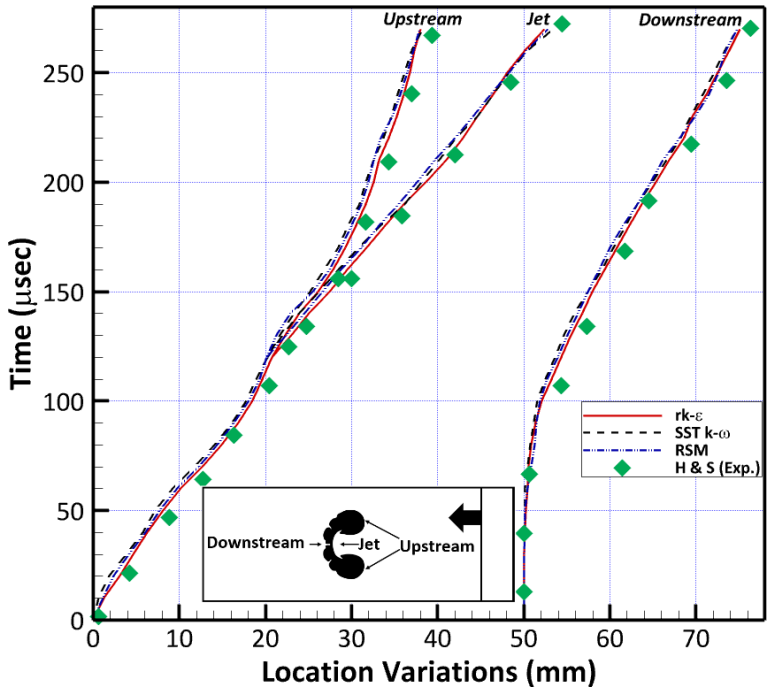

Figure 5.4: Comparison of numerical results between different turbulence models and experimental data.

5.3. Results and discussion

5.3.1. Comparison of measured to predicted velocities

Table 5.2 below shows the comparison between the measured (experimental) and predicted (numerical) velocities of incident (u_I), refracted (u_R) and transmitted waves (u_T), as well as the different characteristic interface points, i.e., initial upstream interface (u_{IU}), final upstream interface

(u_{FU}), initial downstream interface (u_{ID}), air-jet head (u_{AJ}), and vortex filament (u_f). The average velocities of these acoustic wave characteristics are obtained by using minimum squares line adjustments to estimate their approximate locations at different times along the advected bubble trajectory. Generally speaking, the computation of these velocities involves the measurement of the changes in their respective positions over 50-time steps and dividing by the elapsed duration, T, i.e., $T \geq 4\,x\,10^{-7} x\,50 \geq 20\mu s$. Therefore, the values provided in Table 5.2 have been calculated by averaging over a number of such intervals.

As seen from Table 5.2, there is an excellent agreement between the 3D predictions and the experimental data for all the derived velocities with the maximum error being 2.65% for the final upstream interface velocity. There is also a good concordance between the 2D predictions and the measured experimental values with the maximum error being 11.68% for the final upstream interface velocity clearly demonstrating that the 3D simulations produce more accurate results.

Table 5.2: Comparison between the experimental data of Haas & Sturtevant (1987) and the numerical predictions. All velocities provided are in *m/s*.

	u_I	u_R	u_T	u_{IU}	u_{FU}	u_{ID}	u_{AJ}	u_f
Experimental data	410	900	393	170	113	145	230	128
CFD Predictions (2D)	397.5	882.7	378.1	153.6	99.8	130.4	217.3	115.9
CFD Predictions (3D)	403.3	894.6	388.8	166.5	110	141.3	226.7	122.2

5.3.2. Air displacement, bubble acceleration and vortex formation

This section looks to compare the predicted rates of deformation with the experimentally measured values and a model of bubble acceleration/vortex generation put forward by Rudinger and Somers (1960). Ding *et al*. (2017) explained that the pressure oscillations occurring around the evolving air/helium interface, to an extent, control the movement of the interface at early SBI phases. Air is accelerated in the shock tube during shock wave propagation, from a state of rest to a uniform velocity, U_2, derived as (Jacobs, 1992; 1993):

$$U_2 = \frac{2a_0}{\gamma + 1}\left(Ma_1 - \frac{1}{Ma_1}\right), \tag{5.4}$$

As helium is less dense than air, the cylinder will be accelerated to a larger velocity than U_2 and the principal flow velocity behind the incident shock acts as a piston on the bubble thus leading to the bubble deformation and compression. This then means that the light helium gas travels ahead of the ambient air as it is propagated down the shock tube following the incident shock wave. Even though helium bubble initially translates as a solid cylinder, it eventually yields to the forces induced by the propagation of the ambient air. This is what leads to the formation of the vortex filament pair.

Rudinger and Somers (1960) presented a simple two-phase model of SBI in which throughout the early transients, the bubble accelerates as a solid body to a velocity of U_b and is transformed into a vortex ring with a velocity of U_v in the final evolution phase following Taylor's mechanism (1953). The travelling, undistorted bubble during the first phase functions as Taylor's 'undissolved' vortex-generating disk such that U_b represents the disk velocity. Rudinger and Somers (1960) proposed that the impulse per unit volume undergone by the bubble, I_b, would equal that underwent by the ambient air, i.e., $\rho_{air} \times U_2$, where ρ_{air} denotes the ambient gas density. This is shown below:

$$I_b = \rho_{air}\,x\,U_2 = \rho_b U_b + k\rho_{air}(U_b - U_2), \tag{5.5}$$

where ρ_b denotes the bubble gas density. k represents the apparent mass fraction for a cylinder, which is equal to 1.0 (Rudinger and Somers, 1960). Rudinger and Somers (1960) used 1.0 for k in

their calculations because it allowed the initial non-dimensional bubble velocity, U_{ND_b}, to be calculated from Eq. (5.5) as the ratio of the disk velocity to the uniform air velocity after shock propagation. From their calculations, they derived U_{ND_b} as:

$$U_{ND_b} = \frac{U_b}{U_2} = \frac{1+k}{\sigma+k}, \tag{5.6}$$

where $\sigma = \rho_b/\rho_{air}$.

The conversion of the bubble into a vortex implies a drop in the relative velocity, as shown below:

$$U_v - U_2 = \beta(U_b - U_2), \tag{5.7}$$

in which β has a numerical value of 0.203 for the cylinder as computed by Rudinger and Somer (1960).

From Eq. (5.7), the non-dimensional vortex velocity can be calculated as:

$$U_{ND_v} = \frac{U_v}{U_2} = 1 + \beta\frac{1-\sigma}{\sigma+k}, \tag{5.8}$$

The predicted, theoretical, and measured values for these two non-dimensional velocities are presented in Table 5.3.

Table 5.3: Theoretical, numerical and experimental non-dimensional bubble and vortex velocities.

	U_{ND_b}	U_{ND_v}
Theoretical	1.692	1.140
Experimental data	1.37	1.12
CFD Predictions (2D)	1.240	1.012
CFD Predictions (3D)	1.345	1.068

It can be seen from Table 5.3 that the predicted initial bubble velocity in the 3D case agrees very well with the experimental data while the theoretical value is far too large. Nevertheless, for the vortex velocity, the theoretical value is slightly closer to the experimental data than the 3D prediction, indicating that the theoretical model could capture the vortex formation reasonably well but not the bubble acceleration. It is demonstrated again that the 3D predictions are more accurate than the 2D predictions and the complete process of bubble acceleration and vortex formation can be well captured by the 3D simulations.

5.3.3. Distortion and evolution of the interface: prediction of upstream and jet interface velocities

In this section and Section 5.3.4, this research will compare the predicted rates of deformation to experimentally measured ones and the growth rate of small sinusoidal perturbations induced by the impulsive acceleration of a plane interface proposed by the Rayleigh-Taylor theory. This comparison will be made at three characteristic interface points, i.e., upstream, downstream, and interfaces. Haas and Sturtevant (1987) stated that it is informative to investigate the relationship between the shock-generated deformation of gas cylinders and the Rayleigh-Taylor instability (RTI) of plane interfaces. They used the illustration where a cylinder is taken to be representative of a sinusoidal perturbation having an amplitude of $\eta_0 = R$ (R represents the cylinder's radius) and wavelength $\lambda = 2\pi R$ (wavenumber $k = 1/R$). This then meant that the sine wave is tangential to and has identical curvature at crests and troughs as the cylinder. This further implied that the amplitude of the effective perturbation is significantly large ($k\eta_0 = 1$) and variations of the observations from linear theory may indicate the impacts of finite amplitude and non-linearity.

According to the theory of impulsive RTI, the interface is assigned a mean translational velocity, U, and a constant perturbation velocity, u, at the troughs and crests when a shock wave impacts a plane interface deformed by the small undulating perturbations of long wavelength (Markstein, 1957a; 1957b; Richtmyer, 1960). This perturbation velocity is given below:

$$u = \pm k\eta_0 UA, \tag{5.9}$$

where A denotes the Atwood number. The interface deforms at a constant rate and there is a continuance of the velocity field as there is no further acceleration after shock impingement. Changing to laboratory coordinate system, the crests or trough velocity normalised by the translational velocity U is shown below:

$$\Upsilon = 1 + u/U, \tag{5.10}$$

The laboratory coordinate system represents a Cartesian-coordinate system where the x and y axes are in the horizontal plane while the z axis is in the vertical plane (Atkins and Escudier, 2013). It is frequently employed to reference experimental observations. Substituting Eq. (5.9) into Eq. (5.10) as well as equations for the wave number, $k\ (= 1/R)$, and amplitude, $\eta_0 (= R)$, yields Eq. (5.11) below:

$$\Upsilon = 1 \pm \alpha A, \tag{5.11}$$

where the plus sign relates to a shock incident on a concave interface (trough), and α = 1 for a locally cylindrical interface. Haas and Sturtevant (1987) adopted the first-order correction for non-linearity suggested by Richtmyer (1960) considering the compression of the interface shape by the incident shock by replacing the amplitude, η_0, with $\eta_0(1 - U/u_I)$ and stated that for their experiments, the compression $(1 - U/u_I)$ varies from 0.59 to 0.9. Table 5.4 shows, with respect to the upstream and jet interface, the normalised perturbation velocity estimated from the RTI theory as well as the translational velocity, dimensionless upstream and jet interface velocities measured from the experiments and predicted from our simulations (both 2D and 3D). The dimensionless upstream interface velocity, Υ_{IU}, is computed by normalising u_{IU} with U, i.e., $\Upsilon_{IU} = u_{IU}/U$. Similarly, the dimensionless jet velocity, Υ_{AJ}, has been obtained by normalising u_{AJ} with U, i.e., $\Upsilon_{AJ} = u_{AJ}/U$. Haas and Sturtevant (1987) had computed the values of U from one-dimensional (1D) theory. U, used in the current study, has been computed adopting the same method applied in the derivation of the various wave velocities and characteristic interface point velocities (see Section 5.3.1).

Table 5.4: Dimensionless upstream interface and jet interface velocities from CFD simulations compared to the Rayleigh-Taylor theory and experiments. U is in *m/s*.

U	Theory	Experimental		CFD Predictions (2D)			CFD Predictions (3D)		
	Υ	Υ_{IU}	Υ_{AJ}	U	Υ_{IU}	Υ_{AJ}	U	Υ_{IU}	Υ_{AJ}
158	1.432	1.08	1.46	152.6	1.01	1.42	157.7	1.06	1.44

Table 5.4 compares the predicted Υ_{IU} and Υ_{AJ} with both experiments and theory. The predicted initial rate of deformation at the upstream interface, Υ_{IU}, is significantly lower than the estimation, Υ, of RTI theory but is in close agreement with the experimentally measured Υ_{IU}, particularly in the 3D predictions. The predicted Υ_{AJ}, on the other hand, is higher than the predicted Υ_{IU}, and there is little disparity between the predicted Υ_{AJ} (2D and 3D) and both; Υ (estimated from RTI theory) and the experimentally measured Υ_{AJ}. This is indicative of the fact that our numerical model is sufficiently reliable and accurate. Again, the 3D predictions are more accurate than the 2D predictions

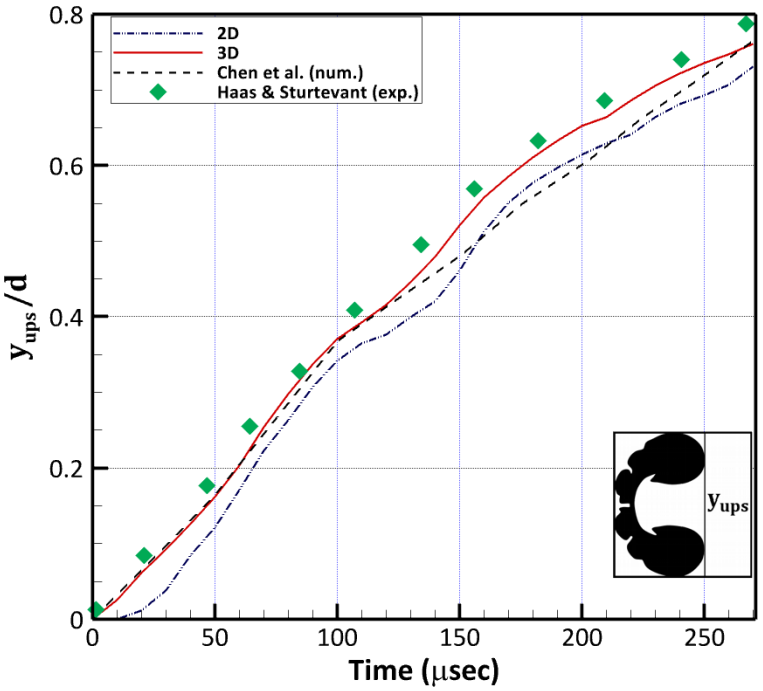

Figure 5.5: Comparison between numerical and experimental dimensionless displacements of the upstream edge against time.

As shown in Fig. 5.5, the characteristic upstream interface displacement, y_{ups}, is normalised by the bubble diameter (d) to allow an efficient comparison of our predicted results to other experimental and numerical findings. Fig. 5.5 presents the comparison between the predicted dimensionless displacement of the upstream interface (y_{ups}/d) and the experiments of Haas and Sturtevant (1987), including the previous numerical results by Chen *et al*. (2021). It can be seen clearly that a very good agreement between the present 3D predictions and the experimental data has been obtained while the numerical results by Chen et al. (2021) are extremely close to the present 3D predictions at the early stage of the shock bubble interaction (first 125 μs). Nevertheless, after the first 125 μs, the predictions by Chen et al. (2021) starts to divert away from both experimental data and the current 3D predictions. It is also shown in Fig. 5.5 that the 3D predictions are much closer to the experimental data than the 2D predictions, confirming that 3D simulation is needed when a shock wave interacts with a cylindrical bubble in order to capture such interaction more accurately.

5.3.4. Distortion and evolution of the interface: prediction of downstream interface velocity

Table 5.5 has been provided, with respect to the downstream interface, and shows the normalised perturbation velocity estimated from the RTI theory. It also shows the translational velocity, dimensionless upstream and jet interface velocities measured from experiments and predicted from our simulations (both 2D and 3D). The dimensionless downstream interface velocity, Υ_{ID}, is computed by normalising u_{ID} with U, i.e., $\Upsilon_{ID} = u_{ID}/U$. Similarly, U, used in the experiments of Haas and Sturtevant (1987) have been computed from one-dimensional theory. U, used in the current study, has been computed adopting the same method applied in the derivation of the various wave velocities and characteristic interface point velocities (see Section 5.3.1).

Table 5.5: Downstream interface velocities from CFD simulations compared to the Rayleigh-Taylor theory and experiments.

U	Theory	Experimental	CFD Predictions (2D)		CFD Predictions (3D)	
	Υ	Υ_{ID}	U	Υ_{ID}	U	Υ_{ID}
98.8	1.622	1.47	92.3	1.41	97.5	1.45

During SBI, the downstream interface is initially disrupted by the shock that has previously impinged on and distorted the upstream interface. This is evident from the development of small-scale undulations on the downstream interface. This will be extensively discussed in Section 5.3.6. Table 5.5 compares the predicted Υ_{ID} with both experiments and theory. The predicted Υ_{ID} is considerably lower than the estimation, Υ, of RTI theory but is in close agreement with the experimentally measured Υ_{ID}. There is also a slight variation between the 2D and 3D results. This again shows the reliability and precision of our numerical model.

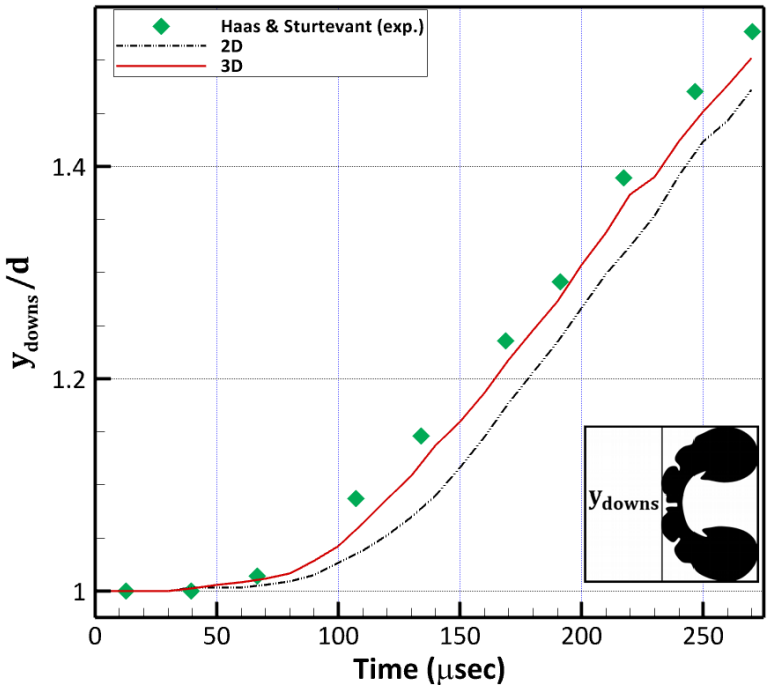

Figure 5.6: Comparison between numerical and experimental dimensionless displacements of the downstream edge against time.

As shown in Fig. 5.6, the characteristic downstream interface displacement, y_{downs}, is normalised by bubble diameter (d). It is evident that the 3D predictions agree very well with the experimental data (Haas and Sturtevant, 1987). Furthermore, it can be seen clearly from Fig. 5.6 that 2D predictions are not as accurate as the 3D predictions, which is consistent with the above discussion that 3D simulations are needed in order to capture the shock bubble interaction accurately.

5.3.5. Numerical measurements of the temporal changes of the interfacial characteristic scales

Temporal changes in the length and width of the developing interface are plotted in Fig. 5.7. These measurements have been made using the series of images derived from the numerical simulations. The description of these interfacial characteristic scales is enclosed in Fig. 5.7. As in Sections 5.3.3 and 5.3.4, the length and width of the evolving interface have been normalised using the diameter of the cylinder.

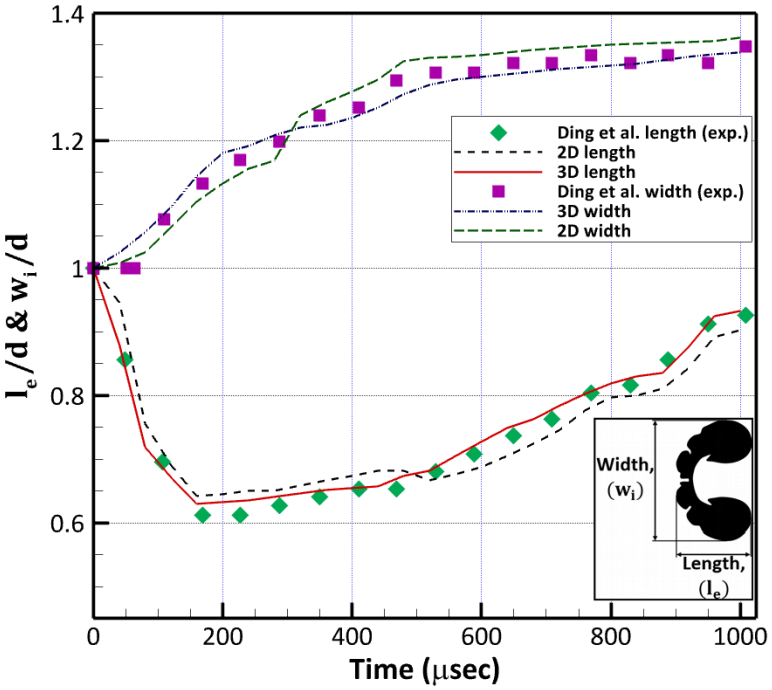

Figure 5.7: Dimensionless numerical and experimental measurements of the characteristic scales against time.

As seen from Fig. 5.7, the length of the developing interface decreases rapidly after the incident wave impinges the upstream interface, i.e., early shock compression quickly shortens the evolving interface's length. This is also obvious from the deformation and compression of the upstream interface. For the 2D and 3D cases, the length attains a minimum value at about 160 μs. At this stage, the helium bubble has been flattened at the upstream interface. After this phase, the length gradually increases up to 470 μs for the 2D case and up to 440 μs for the 3D case. This phase is characterised by the formation of the air-jet, upstream interface's inversion and roll-up as well as the formation inception of the downstream vortex filament due to the acceleration of the vorticity induced air/helium interface by the shock wave This is followed by a gradual decrease in the 2D length between 470 μsec and 520 μs and a slightly steeper increase in the 3D length between 440 μsec and 520 μs. Up to 480 μs, where the 3D interface lengths are lower than the 2D lengths, it can be inferred that the 3D case is more representative of the early shock acceleration and bubble deformation compared to the 2D case as the 3D movement of the evolving interface dominates the flow field. This is because observations of the 2D and 3D lengths at any time in Fig. 5.7, up to 480 μs, show that the 3D case produces a comparatively shorter length which indicates a greater bubble compression. The period up to 480 μs covers and extends beyond early stage SBI as the air jet has almost reached the downstream interface and vortex filaments have appeared. A turning point exists at about 500 μsec after which the 3D length becomes greater than the 2D length. The stage after the turning point up to when the 2D lengths start to increase again is characterised by a steep decline in 2D length and a gradual increase in the 3D length between 500 μs and 520 μs. The physical meaning of the turning point is indicative of the steep rise in the 3D length over the 2D length. The greater 3D length showed that the 3D bubble has started to become stretched in the flow direction influenced by the formation of the distinctive vortex filaments. After the turning point, 3D stretching is more pronounced than 2D stretching. This is also indicative that the 3D vortex filaments are more developed than the 2D vortex filaments. This again shows that the 3D case is more representative of bubble deformation and evolution of vortical structures compared to the 2D case. After 520 μs, the 2D and 3D lengths continue to increase up to 880 μs with varying growth rates. Subsequently, a steep increase in the 2D and 3D lengths is observed up to 960 μs followed

by a gradual increase in the 2D and 3D lengths up till the end of the simulation. From 480 μs till the end of the simulation, the 3D lengths remain greater than the 2D lengths.

The width of the perturbed interface for the 2D and 3D case initially keeps rising with a decreasing velocity (attributable to the greater change in the SBI time compared to the change in the bubble width as SBI progresses). This growth in the width is very fast up to approximately 200 μs before an ensuing decrease in the growth rate of the width up to about 300 μs for the 3D case and approximately 280 μs for the 2D case. The period between 280 μs and 300 μs for the 2D case is characterised by a steep increase in the width. Up till this point, the 3D widths are greater than the 2D widths i.e., up till 300 μs, the greater 3D widths show that the deformed 3D bubble has been stretched more laterally compared to the deformed 2D bubble. The period up to 300 μs when the 3D width is greater than 2D width is also consistent with the observations for the 2D and 3D length comparisons. A greater compression for the 3D case, due to the 3D lengths being smaller than the 2D lengths, will lead to a higher 3D bubble width compared to the 2D bubble width. Thus, the temporal variations of the interfacial characteristic scales for the 3D setup shows a more compressed and vertically stretched/elongated bubble compared to the 2D setup, which is indicative that the 3D case is more representative of shock acceleration, bubble deformation and compression. Another turning point exists at about 300 μsec after which the 2D width becomes greater than the 3D width. The physical meaning of the turning point is indicative of the steep rise in the 2D width over the 3D width. Shortly after this stage, the 2D width increases faster than the 3D width, which has now been further subjected to a reduced growth rate, i.e., at SBI times greater than 300 μs, a greater width is observed for the 2D case in comparison to the 3D case. This stage is also characterised by a steep rise in 2D width and a gradual rise in the 3D width (between 300 μs and 320 μs). Ding *et al*. (2017) explained that this reduced 3D width compared to the 2D width at late stages shows that the 3D cylinder's width is greatly hindered by the 3D effects, i.e., gradients of pressure and vorticity generation, irrespective of its direction of principal curvature. Subsequently, the 2D width continues to increase at a swift rate up to about 480 μs (steeper growth rate observed between 300 μs and 320 μs followed by a comparatively reduced growth rate up to 480 μs) while the 3D width continues to increase at a steady rate but still below the higher 2D width. After 480 μs, the 2D and 3D widths continue to increase but at a lower rate compared to the previous phase. This persists up to approximately 720 μs for the 2D case and about 680 μs for the 3D case after which both widths tend towards an almost constant value. This lasts for about 80 μs, i.e., from 720 μs to 800 μs for the 2D case and from 680 μs to 760 μs for the 3D case. This stage coincides with when the air has encroached the downstream interface and the vortex filaments have significantly evolved. Afterwards, the 2D width slowly increases with time and remains higher than the 3D width. At this stage, the rate of change of the 3D width is steeper than that of the 2D width, as seen from the slope of both lines in this period. The fluctuating changes in the widths of the evolving interface from 480 μs is indicative of the formation, evolution and deformation of the vortex filaments. Generally, the 3D case is more representative of an ideal SBI scenario as the interfacial characteristic scales suffer from 3D effects with respect to pressure/density gradient mismatch as well as vorticity generation, deposition and transport.

Fig. 5.8 below presents the predicted and measured bubble evolution using three representative positions, i.e., upstream, jet, and downstream locations. It can be seen clearly again that the 3D predictions match the experimental data of Haas and Sturtevant (1987) extremely well while the 2D predictions are a bit further away from the experimental data. It is evident from this comparison and the above quantitative comparisons between the predictions and experimental data that the 3D simulation has captured the complex shock bubble interaction accurately and all the following analysis will be based on the 3D results. The CPU times per 50 iterations are 127 seconds and 3,558 seconds for the performed 2D and 3D simulations respectively using the best 2D and 3D grids as detailed in Section 5.2.4.

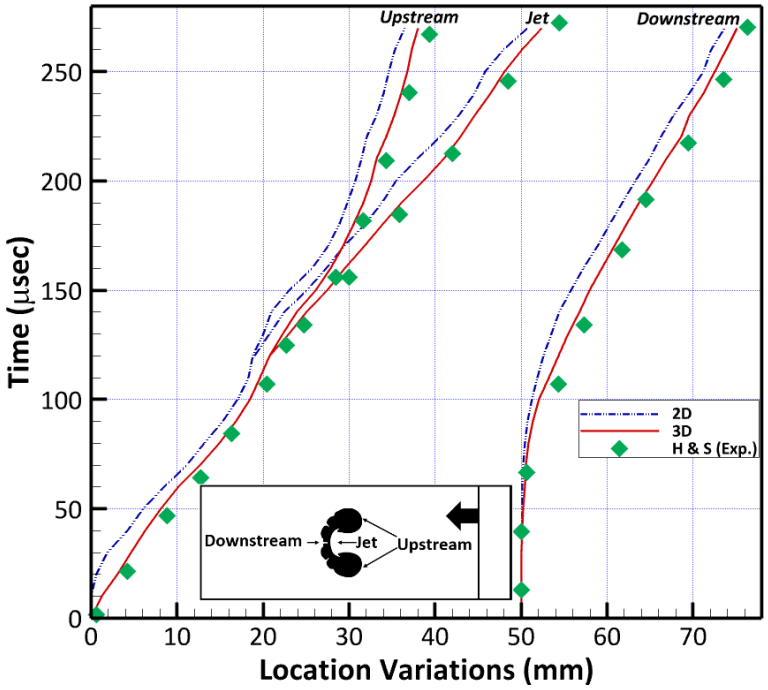

Figure 5.8: Comparison of the 2D and 3D predictions against the experimental data.

5.3.6. Visualization of shock-bubble interaction morphology

The intricate and crucial processes involved in bubble deformation, generation of vorticity, growth of air-jet and the overall late-time development of the SBI process will be further investigated in this section. Fig. 5.9 presents eight (8) snapshots of the simulated images (right) and shadow-photographs (left) captured in the experiment. Time, *t*, is normalised by the shock velocity and the diameter of the bubble. The dimensionless time, *t = 0* corresponds to the instant when the incidence shock impinges the upstream end of the bubble. The predictions captured the SBI process excellently, particularly the major characteristics, as the simulated images are considerably like the shadow-photographs at all 8 times. The notations used in the analysis are defined in Fig. 5.9. ue, de, and aj represent the upstream interface, downstream interface, and air-jet. hbs, and vf denote the helium bridge structure and vortex filament. Fig. 5.9(a) shows the helium cylindrical bubble at t=0.34 following the incident shock wave (iw) impingement on the upstream side of the helium volume from the right-hand-side. The iw is seen as two straight branches connected at the top and bottom of the bubble interface to the curved refracted wave (rs) on the left side of Fig. 5.9(a) (travelling inside the bubble) and to the reflected wave (rfw) on the right side of Fig. 5.9(a) (travelling outside the bubble). Fig. 5.9(a) is also indicative of regular refraction as the rs and the iw intersect the interface at the same point (Ranjan et al., 2011). Fig. 5.9(b) (t=0.51) reveals the rs travelling further forward and faster than the iw (because the sound velocity of the helium bubble is greater than that of air). The rs is connected to the two branches of the primary transmitted wave, pts, (at the top and bottom of the bubble). The top and bottom pts intersect the two branches of the iw before tangentially meeting the rfw. The pts, on crossing the iw, forms a precursor to it. Fig. 5.9(b) is also indicative of an irregular shock refraction pattern as the pts transmits downstream in front of the exterior iw (Henderson, 1966; Henderson, 1989; Niederhaus, 2007). There is a slight flattening of the upstream interface of the bubble during this period as observed from Fig. 5.9(b). At t=0.6, there is a complete emergence of the pts from the downstream end of the bubble, i.e., left-hand interface coupled with the appearance of the converging internal reflected wave (irw) seen with two cusps, as shown in Fig. 5.9(c). The simulated image in Fig. 5.9(d) at t=0.85 shows that the irw has developed into a diverging wave (not very visible from experiments) after propagating

across its caustic. Outside the bubble, the two branches of the sts intersect each other around the centre of the bubble and connected to the ends of the irw at the interface. The continuous compression of the upstream interface means the cylinder distortion persists and at t=2.11, the deformed helium cylinder has attained a kidney shape, as seen in Fig. 5.9(e). From t=2.11 to t=8.44 (see Figs. 5.9(e – h)), the re-entrant aj/spike forms and develops through the bubble centre. This aj is shaped as a convergence nozzle (Yoo and Sung, 2018) (see Figs. 5.9 (f), (g) and (h)) and the magnitude of the velocity arriving at bubble centre becomes progressively greater. Due to the interfacial density mismatch, the pressure on the upstream end of the bubble increases with the aj, which makes the lighter helium to push against the heavier air causing the top and bottom ends of the upstream interface to move up (to the right) and the middle end of the upstream interface (area through which aj pushes through) to move down (to the left in the direction of shock propagation). This movement leads to a caving of the upstream interface through the centre. As seen from Figs. 5.9(a-j), the pressure upstream of the helium volume is significantly greater than that on the downstream area. This pressure difference means the heavier air accelerates the lighter helium thus subjecting the distorted bubble to the Richtmyer-Meshkov instability, RMI (shock-induced Rayleigh-Taylor Instability, RTI) (Sharp, 1984). During the evolution of the shock induced RTI and after the development of small amplitude perturbations, which grow linearly with time on the bubble interface, a nonlinear regime follows. This non-linear regime is characterised by the appearance of a mushroom-shaped spike (MSS) formed when the heavier air penetrates the lighter helium. The simulated image in Fig. 5.9(g) clearly shows the MSS (the area highlighted with blue markers). When the top of the aj impinges the downstream air/helium interface, the downstream interface spreads out horizontally ultimately producing a pair of vf. The simulated images in Figs. 5.9(g) and (h) for the current study reveal a visible presence and formation of such vf pair demonstrating the existence of the RMI. Generally, it is recognised that the MSS and the vf pair in the post shock are formed because of the RMI (shock induced RTI) at the bubble interface.

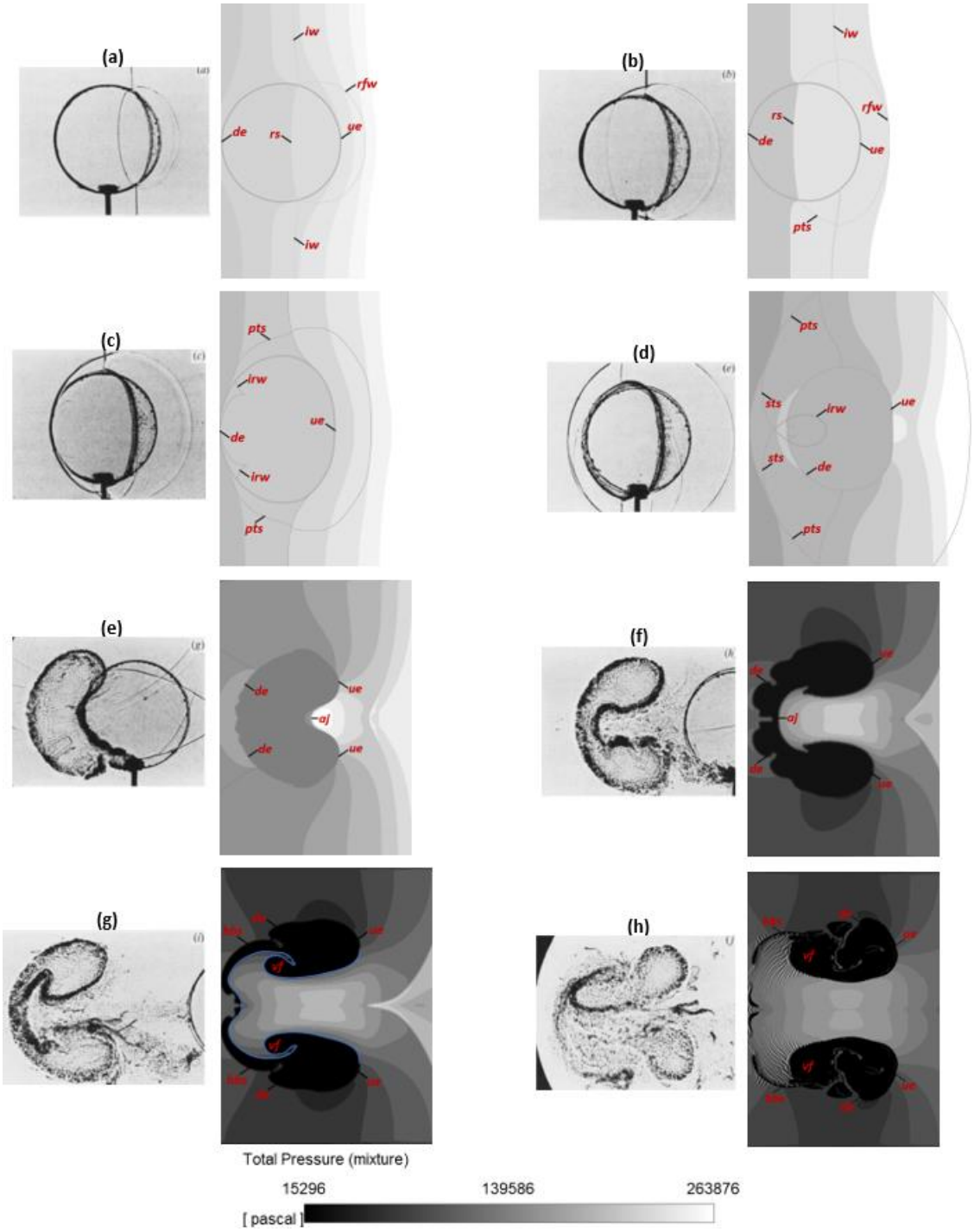

Figure 5.9: Snapshots of experimental shadow-photographs (left) and simulated images (right) on the central x-y plane at: (a) t=0.34; (b) t=0.51; (c) t=0.6; (d) t=0.85; (e) t=2.11; (f) t=3.88; (g) t=5.74; and (h) t=8.44.

5.3.7. Vorticity generation dynamics

One of the most essential phases of SBI is the vorticity generation and deposition due to the disparity between pressure and density gradients. As the shock waves (incident, refracted, diffracted, and focused waves) propagate through the bubble, vorticity is generated and transported in the flow. Vorticity is so essential in SBI as it, together with aerodynamic forces, principally influences the motion and structure of the bubble (Layes et al., 2003).

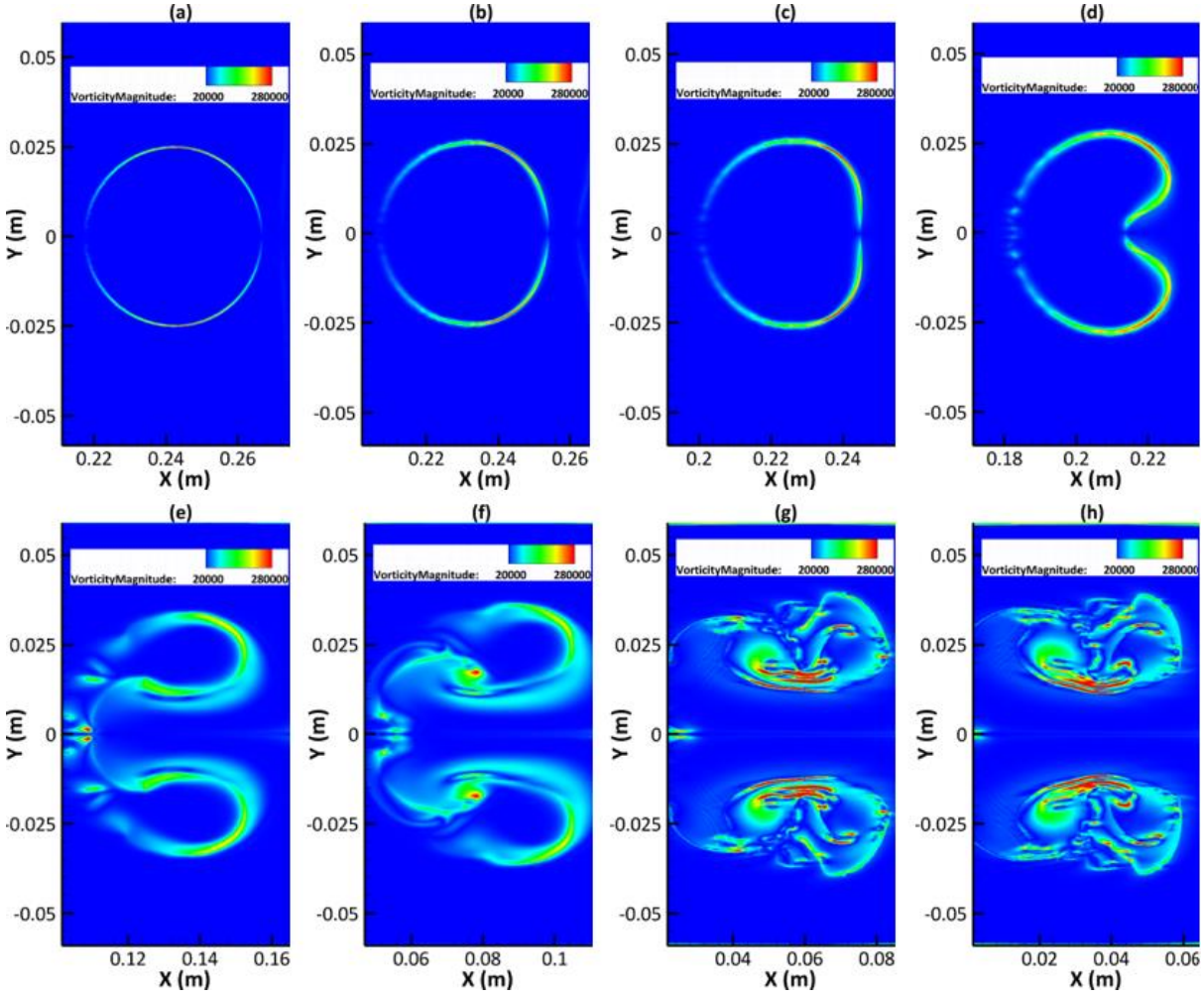

Figure 5.10: Snapshots of vorticity contours on the central x-y plane at: (a) t=0.51; (b) t=0.68; (c) t=1.02; (d) t=2.11; (e) t=3.88; (f) t=5.74; (g) t=6.92; and (h) t=8.44.

Fig. 5.10 shows contours of the vorticity magnitude at different stages of SBI process. At the early stage as shown in Figs. 5.10(a-d), vorticity is produced around the air/helium interface (bubble surface) as a result of flow baroclinity, i.e., due to the misalignment between the local pressure gradient and the density gradient. The air-jet formation can be clearly seen in Fig. 5.10(d). In Fig. 5.10(e), at t=3.88, the air-jet is about to reach the downstream interface and the upstream interface is severely distorted with more vorticity generated around the interface region. At t=5.74, the air-jet reaches the downstream interface, as shown in Fig. 5.10(f), and a pair of vortex filaments (vf) is clearly observed with high vorticity concentrated in the vortex filament region. As time passes by, more vorticity is generated around the vf region and the surrounding regions, as shown in Figs. 5.10(g) and (h), and small flow structures can be observed too at the later stage of SBI process. This strongly suggests that vorticity, generated by baroclinic mechanism, plays a very important role in the SBI process. It initiates the deformation of the upstream surface and afterwards, strong rotational motion pulls a jet of ambient air through the centre of the bubble. Subsequently, the jet

deforms the bubble until it pierces the downstream bubble interface, and vortices at the bubble surface roll up and drag helium into a distinctive downstream vf pair, as shown in Figs. 5.10(f-h).

5.3.8. Visualisation of 3D flow

Fig. 5.9 shows the shock-bubble interaction process on a cross section, and the 3D morphology of the deformed cylindrical bubble is shown in Figs. 5.11(a-h), corresponding to the simulated schlieren images shown in Fig. 5.9 at the same instants. Fig. 5.11 presents a more realistic perspective to bubble compression and distortion as it reveals: a gradual flattening of the upstream interface after the iw impingement; the air-jet penetration of the bubble; as well as the formation, roll-up, and evolution of the vf pair.

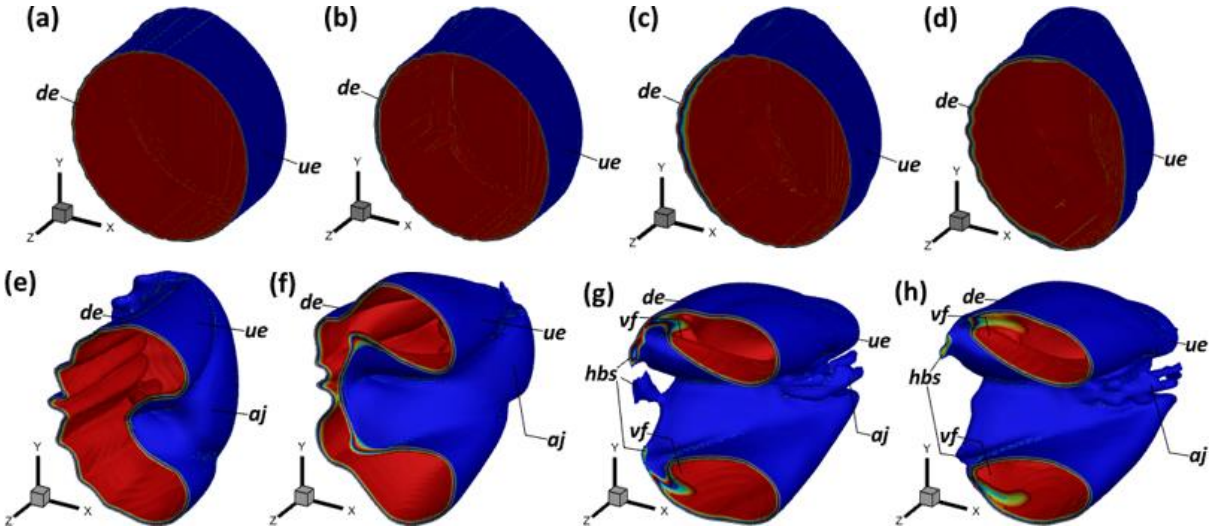

Figure 5.11: Three-dimensional (3D) morphology of the deformed cylindrical bubble at: (a) t=0.34; (b) t=0.51; (c) t=0.6; (d) t=0.85; (e) t=2.11; (f) t=3.88; (g) t=5.74; and (h) t=8.44.

The 3D flow visualisation presented in Fig. 5.12 will help to further demonstrate the SBI process, particularly with respect to the observation of various wave patterns, wave propagation, positional changes of the cylindrical helium bubble, bubble deformation and vf development.

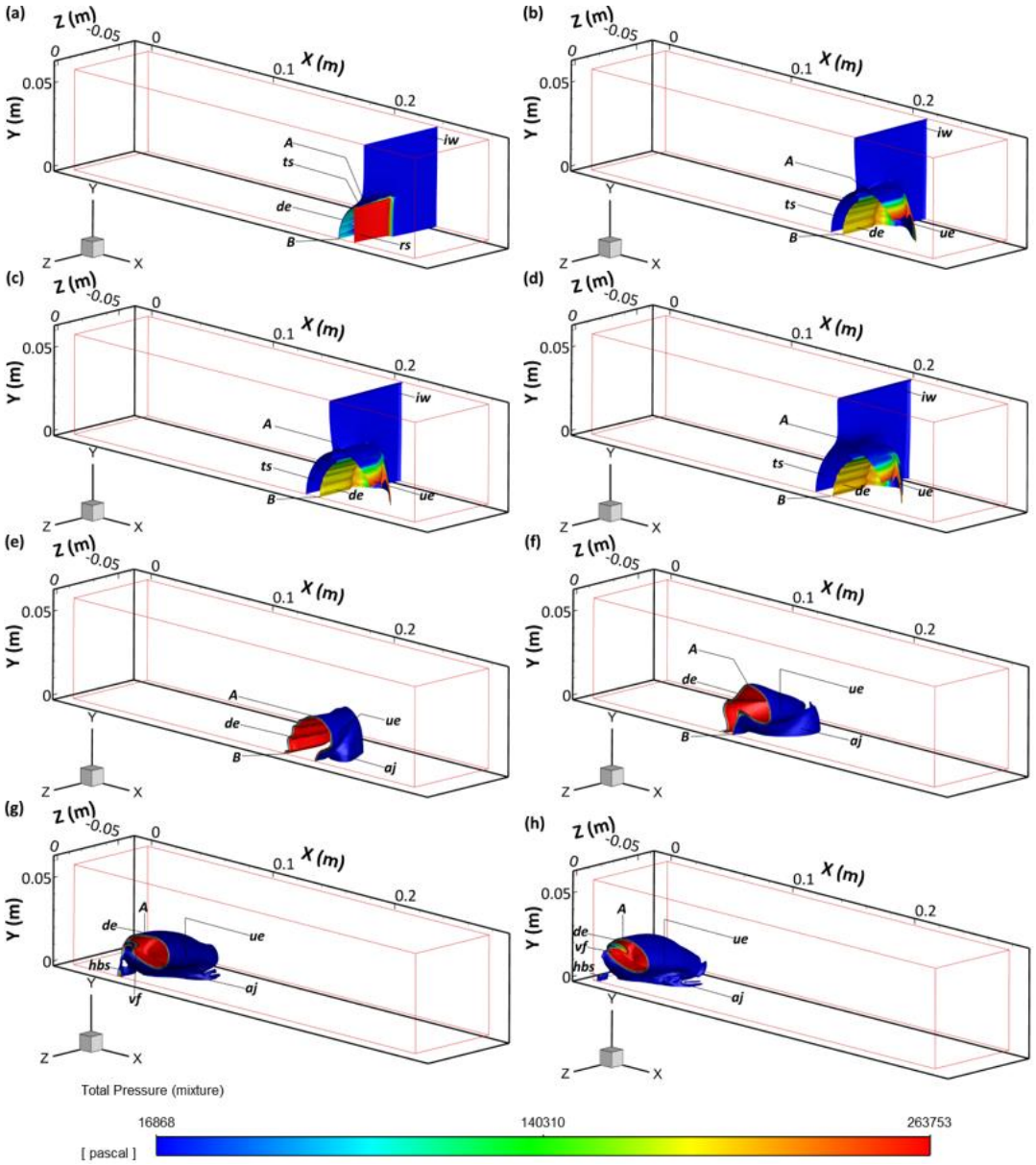

Figure 5.12: Pressure iso-surfaces at: (a) t=0.51; (b) t=0.68; (c) t=0.85; (d) t=1.02; (e) t=2.11; (f) t=3.88; (g) t=5.74; and (h) t=8.44.

Snapshots of the predicted pressure iso-surfaces presenting a quarter bubble (better suited to reveal certain features and changes in the helium bubble location) are shown in Fig. 5.12. With respect to explaining the change in bubble position with time, this research has labelled two points, A (on the upstream edge of the bubble) and B (farthest point of the bubble located on the downstream edge), as shown in Fig. 12(a). The two points are very important in understanding how the shocked and deformed bubble travels as well as the formation of the vf. At an early phase as shown in Fig. 5.12(a), the planar iw has impacted the bubble's upstream interface generating a rs inside the bubble that travels faster than the iw because the speed of sound in the bubble gas, i.e., helium, is greater than the speed of sound in the surrounding gas, i.e., air. This then means that the rs is slowly invading the downstream end at t=0.51, as shown in Fig. 5.12(a). This rs, which is travelling far ahead of the iw, is connected at the air/helium interface to the pts, which in turn intersects the iw. Fig. 5.12(a) does not show the deforming upstream end of the bubble, which is gradually becoming flatter (see Fig. 5.11(b)), so that the location of the rs in comparison to the iw can be clearly revealed particularly as the rs approaches the downstream interface. As the upstream interface continues to deform and compress at t=0.68, the transmitted shock (ts) has

emerged from the downstream end and has travelled a small distance away from the downstream interface, as shown in Fig. 5.12(b). The iw has travelled about half of the bubble length and lags the ts, as shown in Fig. 5.12(b). Points A and B have moved a small distance compared to their initial positions in Fig. 5.12(a). This shows that the shocked bubble has travelled a small distance from its initial location. Fig. 5.12(c) (t=0.85) shows that the ts has travelled a large distance away from the downstream interface with the iw still trailing but has itself propagated more than half of the length of the helium bubble. Similarly, points A and B have moved more distance compared to their positions in Fig. 5.12(b). At t=1.02, the iw is still travelling past the bubble length but has almost propagated the entire bubble length, as shown in Fig. 5.12(d), and still lags the ts which has travelled ahead of the shocked bubble. In this phase, points A and B have moved a considerable distance from their original locations and considerable motion of the helium volume has already taken place. The bubble is also almost completely flattened at the upstream interface, as shown in Fig. 5.12(d), as it has suffered considerable deformation and compression. Vorticity production, deposition and distribution across the air/helium interface produced by the baroclinic effect during shock impingement on the upstream end of the bubble and the subsequent shock propagation across the bubble ensures that the associated rotational motion pulls a jet of ambient air through the centre of the bubble. This aj is first noticed at t=2.11, as shown in Fig. 5.12(e), with produced vorticity leading to the continuous inversion of the upstream surface in the direction of the penetrating aj and towards the downstream end. This aj which pierces through the helium bubble volume and impinges on the downstream edge is analogous to the so-called RMI spike at a perturbed gaseous air/helium interface. This caving-in/inversion continues as seen in Fig. 5.12(f) at t=3.88 until point B is no longer visible in Figs. 5.12(g) and (h). Point A in Fig. 5.12(f) has also moved a significantly further distance compared to its original position. At the later phase (t=5.74 and t=8.44), the inverted part of the upstream interface, i.e., through the centre of the bubble, has impinged on the downstream bubble end with vorticity rolling up and dragging helium into a characteristic vf pair at the downstream side of the deformed helium volume. The final position of point A which is almost at the end of the shock tube is indicative of the significant distance travelled by the distorted bubble from SBI inception to late times.

Fig. 5.13 shows the snapshots of the predicted pressure iso-surfaces revealing more clearly specific characteristics of the full bubble compression process and shock travel, particularly with respect to the observation of various wave patterns, wave propagation, bubble deformation and the air-jet formation. Fig. 5.13 also reveals the development of the air-jet, induced by vorticity, which leads to the formation of a pair of vf at the later phase of the shock-bubble interaction process.

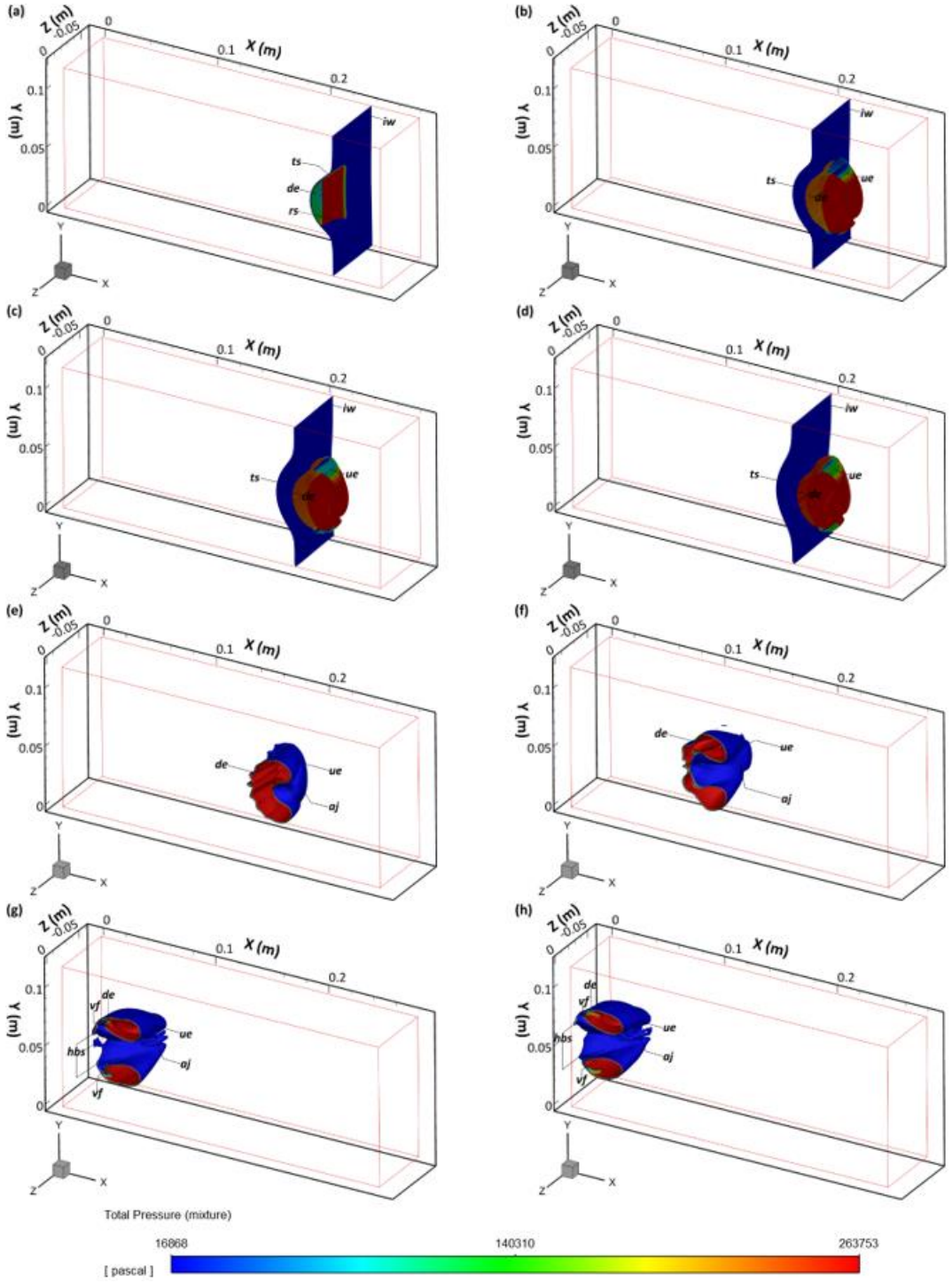

Figure 5.13: Pressure iso-surfaces at: (a) t=0.51; (b) t=0.68; (c) t=0.85; (d) t=1.02; (e) t=2.11; (f) t=3.88; (g) t=5.74; and (h) t=8.44.

Once the planar incident wave (iw) impacts the bubble's upstream edge, a refracted wave (rs) is generated inside the bubble and the rs travels faster than the iw because the speed of sound in the bubble gas, i.e., helium is greater than the speed of sound in the surrounding gas, i.e., air. As shown in Fig 5.13(a) at t=0.51, the rs travels quickly towards the downstream bubble interface. The curved rs is connected at the top and bottom of the bubble surface to two curved branches of the pts. The two branches of the ts (at the top and bottom of the shocked bubble) intersect the two branches of the iw. At t=0.68 and as the distortion and compression of the upstream interface persists, the ts has emerged from the downstream end and has propagated a slight distance away from the

downstream interface, as shown in Fig. 5.13(b). The iw has travelled about half of the bubble length and lags the ts, as shown in Fig. 5.13(b). Fig. 5.13(c) (t=0.85) shows that the ts has propagated more distance away from the downstream interface with the iw still trailing but has itself travelled more than half of the length of the helium bubble. Deformation and movement of the cylindrical inhomogeneity has already occurred at this stage in comparison to the original shape and position of the helium bubble. At t=1.02, the iw is still travelling past the bubble length but has almost travelled the entire bubble length, as shown in Fig. 5.13(d), but still lags the ts which has propagated way ahead of the shocked bubble. The bubble is also nearly entirely flattened at the upstream interface, as shown in Fig. 5.13(d). This is because the shocked bubble has been perturbed by continuous wave accelerations thus subjecting it to considerable compression and distortion. At t=2.11 and as the iw propagates across the bubble, baroclinic vorticity is generated, deposited, and transported locally at the bubble surface which acts as the discontinuity between the helium gas and the surrounding air. Subsequently, the first clear appearance of the aj, which penetrates the bubble through its centre at the upstream end, is observed. As shown in Fig. 5.13(e), the bubble has deformed considerably and is now 'kidney-shaped'. At t=3.88, the aj is more well-defined and clearly visible (see Fig. 5.13 (f)) as vorticity has intensified significantly. Fig. 5.13(g) shows the bubble stretching horizontally and forming the vf pair as the head of the aj impinges on the downstream interface at t=5.74. Fig. 5.13(g) shows the fully developed vf which are separated by the hbs at t=8.44. Interestingly, Figs. 5.13(e-g) reveal how the aj forms. This represents an area of SBI that has not been clearly detailed and communicated in past literature, particularly with respect to shock cylindrical bubble interaction.

5.3.9. Evolution of vortex filament

The distortion of the bubble at late timescales shows that the shock interaction with the helium bubble having a lower density than its surrounding air leads to the formation of vf pair. These pairs of vortices stay close to each other and propagate faster than the surrounding air. During the development of the RMI and after the emergence of small-scale amplitude perturbations, which originally develop linearly with time at the bubble surface, a non-linear regime ensues where the flow is soon dominated by a pair of counter-rotating vf, i.e., the top vf rolling up in the clockwise direction and the bottom vf rolling up in the anti-clockwise direction. Both vortex filaments evolve from opposite-sign vorticity (suggestive of the filaments' direction of rotation) that is baroclinically deposited along the top and bottom edges of the downstream bubble interface. Tomkins *et al*. (2003) explained that it is vorticity that leads to the non-linear growth of the bubble interface and the subsequent curling into two vortices such that the flow is swiftly controlled by a pair of counter-rotating vortex. Fig. 5.14(a) shows the emergence and development of the vortex filament from t=3.88 to t=8.44. Figs. 5.14(a, i-viii) also show some undulation on the bubble surface. Tomkins *et al*. (2003; 2008) clarified that these undulations can be construed as an indication of a secondary instability, probably connected with the Kelvin-Helmholtz shear instability or probably baroclinic in nature. Fig. 5.14 also shows that the volume and intensity of the curled vortices increase significantly as SBI progresses from Fig. 5.14(a) to Fig. 5.14(h), and these vortices are noticeable at the air/helium interface (visible from the small-scale undulations on the bubble surface) because of the baroclinic deposition and accumulation of vorticity as time progresses. This also explains the increase in the size of vf as SBI progresses, as seen in Fig. 5.14, where the distorted and evolved helium bubble in Figs. 5.14(a, viii) and (b, viii) have the largest vf pair compared to the deformed bubbles at the previous timescales. When the aj pierces through the evolving interface, the vf pair evolve progressively with an almost constant distance between them. Hence, the shape and size of the resultant vf pair change with time attributable to the wave pattern evolution and baroclinic vorticity with respect to the original 3D interface. With respect to size, Figs. 5.14(a) and (b) show that as the vf pair increases in size, the trailing helium lobe decreases in size as SBI progresses.

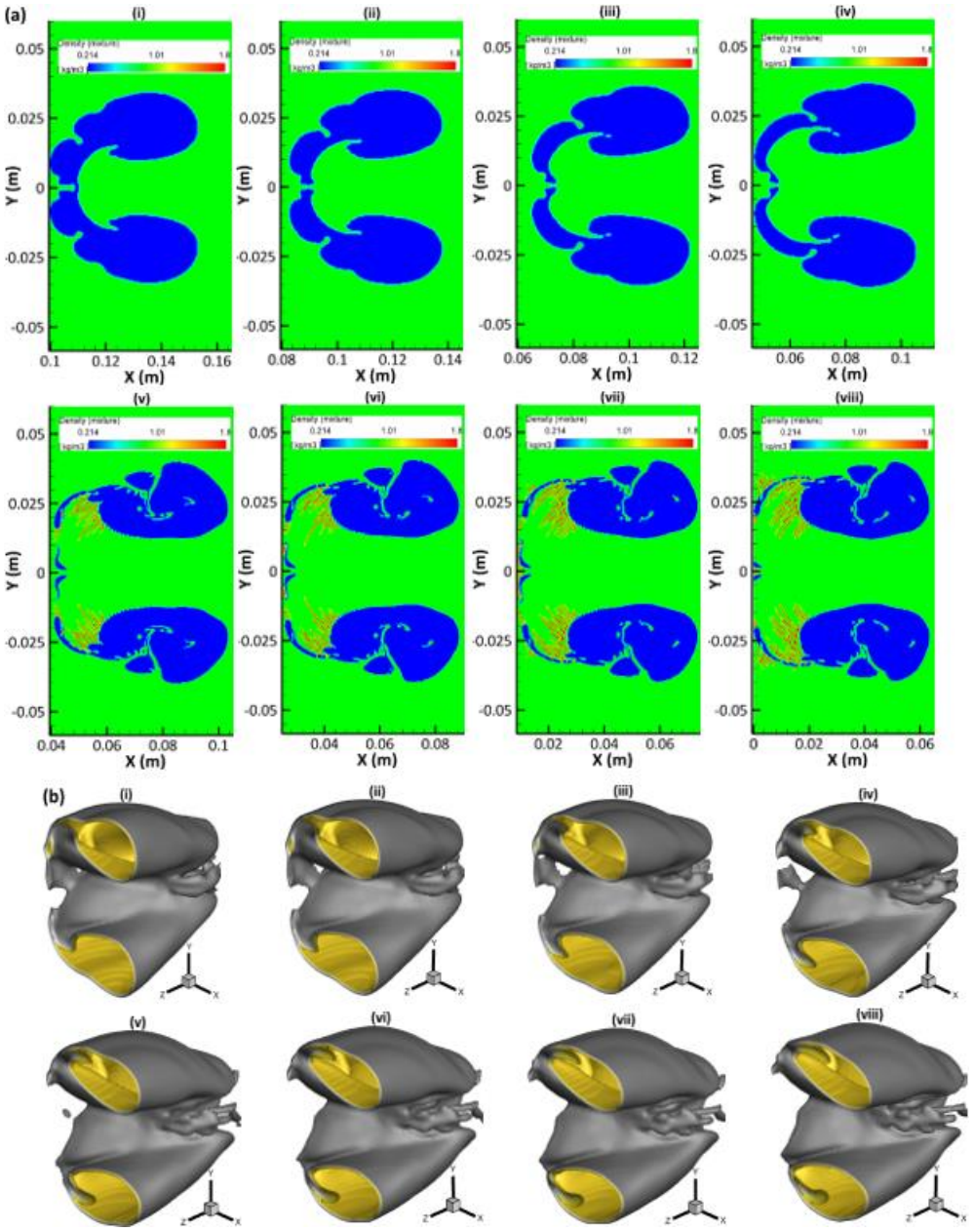

Figure 5.14: (a) Contours of density on the central x-y plane at: (i) t=3.88; (ii) t=4.56; (iii) t=5.15; (iv) t=5.74; (v) t=6.16; (vi) t=6.92; (vii) t=7.68; and (viii) t=8.44. (b) Iso-surfaces of density at: (i) t=3.88; (ii) t=4.56; (iii) t=5.15; (iv) t=5.74; (v) t=6.16; (vi) t=6.92; (vii) t=7.68; and (viii) t=8.44.

Fig. 5.14(b) shows the evolution of the aj. To the best of our knowledge, jet formation and development has not been accurately visualised in the past. The aj can be best explained by observing the RMI driven MSS highlighted in Fig. 5.9(i) and easily detectable from Figs. 5.14(a, iii and iv). Figs. 5.14(b, i-viii) reveal the emergence of small and large-scale turbulent structures on the air-jet as it evolves and as SBI progresses. A look at the flow dynamics involved in Figs. 5.14(a, i-viii; b, i-viii) with respect to the evolution of the vf pair, aj and hbs show that there is a transition from the development of the RMI (which begin as small amplitude perturbations at the bubble surface) (see Fig. 5.14(a, i)) to the development of a non-linear turbulent regime characterised by a MSS and the emergence of a vf pair from vorticity induced fluid roll-up (see Figs. 5.14(a, i-viii; b, i-viii)). Summarily, the flow at t=3.88 shows the encroachment of the downstream bubble interface by aj while it shows a fully developed vf pair and fully stretched and almost non-existent hbs at t=8.44.

To the best of our knowledge, very little information is available regarding the roll-up direction of the hl and the vf as SBI progresses. This is especially the case with respect to the evolution of the vf and its increase in size as revealed above. Similarly, the roll-up of the vf is also linked to the deposition of vorticity in the vf as SBI increases. This leads to a subsequent reduction in the hl as vf increases in size throughout the SBI process. From Fig. 5.15, the top hl rolls up in a counterclockwise direction while the top vf develops and rolls up in the clockwise direction. On the flip side, Figs. 5.15(a) and (c) show that the bottom hl rotates in the clockwise direction while the bottom vf evolves and rolls up in the anticlockwise direction. Fig. 5.15(b) is provided as it shows the streamlines on the inside of the deformed bubble which are more traceable and clearer.

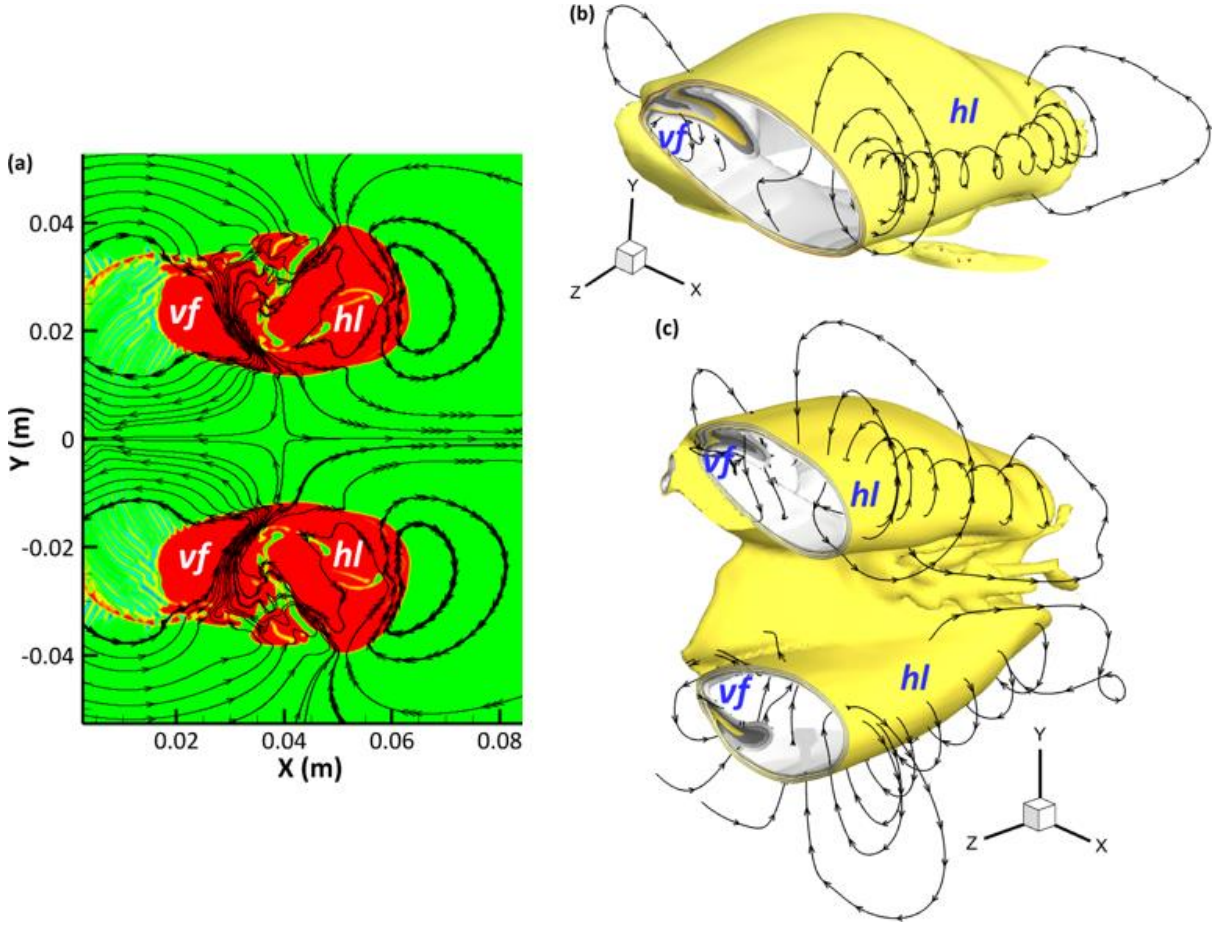

Figure 5.15: Roll-up direction of helium lobe (hl) and vf revealed by (a) density contours on the central x-y plane; (b) density iso-surfaces of deformed quarter cylindrical bubble; and (c) density iso-surfaces of distorted whole cylindrical bubble. All images are at t=8.44.

5.3.10. Inception and progression of turbulent mixing

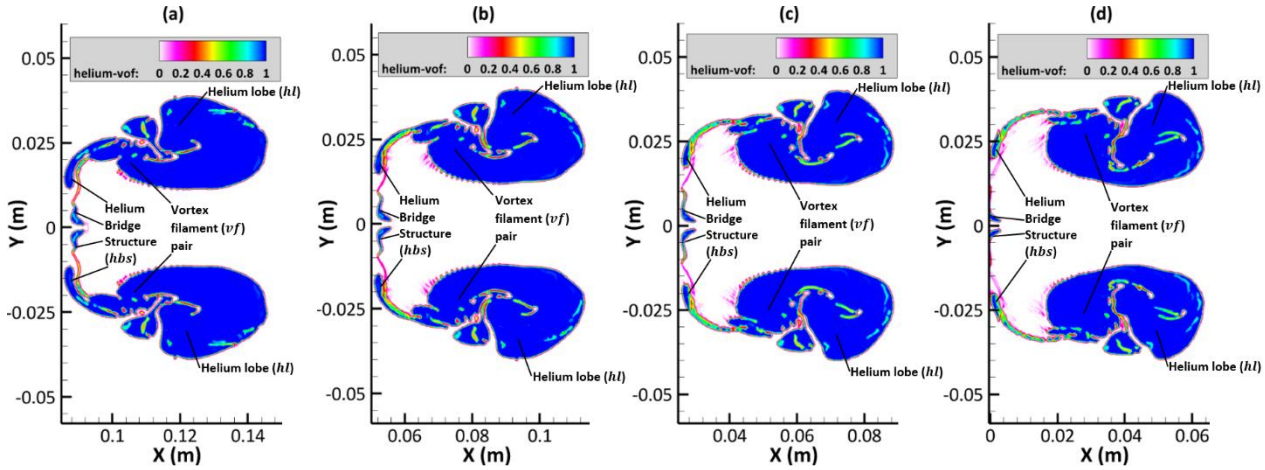

Figure 5.16: Density contours on the central x-y plane revealing the development of turbulent mixing at: (a) t=4.56; (b) t=5.74; (c) t=6.92; and (d) t=8.44.

Chen *et al*. (2021) explained that the vorticity production and distribution has an essential influence on bubble interface distortion after which turbulent mixing of the two-phase gas is accelerated. Singh *et al*. (2021) similarly clarified that the mixing of the surrounding air with the deformed cylindrical bubble is driven by the generated vortices from SBI. Turbulent mixing between the air and helium is thus strengthened by the gradual diffusion of the vortices. Tomkins *et al*. (2008) discovered three mixing regions for a SBI flow. These regions include the bridge connecting the vf pair, the vortex cores, and the Kelvin-Helmholtz (KH) region. For the bridge, mixing is linked with gradient intensification as a result of the straining velocity field. Mixing in the KH regions and the vortex cores is driven by the large-scale strain fields at early times even though the induced movements caused by vorticity generate both gradient intensification and an increase in surface area from growing spirals. The KH region in Fig. 5.16 is represented by the outer surfaces or air/helium interface bounding the hl and the vf. It is characterised by the appearance of small perturbations/undulations which grow in high shear regions as SBI progresses. The vortex cores (vf pair) and the bridge (hbs) connecting the vf pair are shown in Fig. 5.16. At late timescales, mixing is predominantly linked with the elongation and collapsing of concentration fields due to an induced motion stimulated by the secondary instability (Tomkins et al., 2008). These three regions are well observed in the current study and are thoroughly explained in the following paragraphs.

Fig. 5.16 shows contours of the helium bubble volume fraction. The scale shows that the maximum volume fraction, i.e., 1 (blue) signifies helium filled area. Figs. 5.16(a-d) reveal a drop in the volume fraction of helium; at the bubble interface, within the vf pair, within the hl ahead of and connected to the vf, as well as along the hbs. These regions reveal areas of mixing between the air and helium at the respective timescales. This is shown by the small-scale vortices generated on the vf pair, helium lobe, and hbs due to the baroclinic vorticity production. This goes to show that bubble distortion is linked to the production, distribution, and deposition of vortices, which have the capacity of accelerating the turbulent mixing between air and helium. Chen *et al*. (2021) also provided an interesting background to the turbulent mixing acceleration by deposited vortices when they stated that vortices play a key role in accelerating the interaction between the internal flow and external flow in the bubble, i.e., the baroclinic mechanism induced by a mismatch between pressure and density gradients. There is pronounced mixing at the bubble surface, as shown by the helium volume fraction scale. This is attributable to the rapid steepening of gradients along the air/helium interface associated with the generated vorticity, which has been deposited across the interface after impact by propagating the shock wave.

Fig. 5.16(a) (at t=4.56) shows that the most intense mixing in the flow is contributed by the hbs. Significant level of instantaneous mixing takes place in the hbs, as shown in Fig. 5.16(a). This is because large-scale strain field produced by vortices linked to the primary instability swiftly elongates the air/helium interface, regularly steepening the concentration gradients such that considerable mixing is noticed in the hbs. However, after t=5.74, there is a reduction in mixing along the hbs. This drop at late times was reported by Tomkins *et al*. (2008) and attributable to the advection of material away from the mask lower boundaries, i.e., diminishing material supply held within the bridge. A look at the helium volume fraction scales also reveals a similar scenario from t=6.92 to t=8.44 (see Figs. 5.16(b-d)), which show that the air entrained within the hbs becomes dissipated leading to a reduced total mixing. Another reason could be that the hbs is no longer adequately supplied with the fresh (unmixed) air on which any small-scale gradients can function. Also, even though vorticity deposited by shock propagation significantly boosts mixing, the total mixing rate is not at its highest, i.e., areas where the fine-scale velocity gradients are expected are spatially separated from the regions of purest air.

The well mixed state of the vf pair and the trailing helium lobe at late times, i.e., t=6.92 and t=8.44 (see Figs. 5.16(c-d)), shows that the unstable small-scale structures are efficient mixers as a close examination of Figs. 5.16(a-d) shows that these structures are in constant motion, and in Fig. 5.16(d), a certain combination of two such structures is observed in the hbs and trailing hl. These small-scale movements observed in the flow field deform the air/helium interface and augment the diffusive mixing of air and helium. These small-scale structures, which have various sizes as seen in Figs. 5.16(a-d), are indeed trapped islands of air. As the evolving aj interacts with the growing vf pair, these islands of air are trapped within the filaments. As SBI progresses, the vf no longer comprises of pure helium but mostly well mixed regions of helium and air. The vortices linked to the primary instability accelerate mixing in these regions by stretching the interface (Tomkins et al., 2008). This stretching leads to further entrainment of air and increased air/helium mixing such that as more air mass is infused into the mixing region via SBI, the entrained fluid, i.e., air, becomes homogenised with the helium by turbulent mixing via the intermingling of the two fluids. Thus, the volume fraction of helium within the vf pair and the helium lobe reduces while that of air increases within the same areas. Figs. 5.16(a-d) reveal smaller ‘satellite’ vortices outside the vortex filament pair, which again according to the helium volume fraction scale represent the small-isolated pockets of air.

5.3.11. Generation and development of turbulence

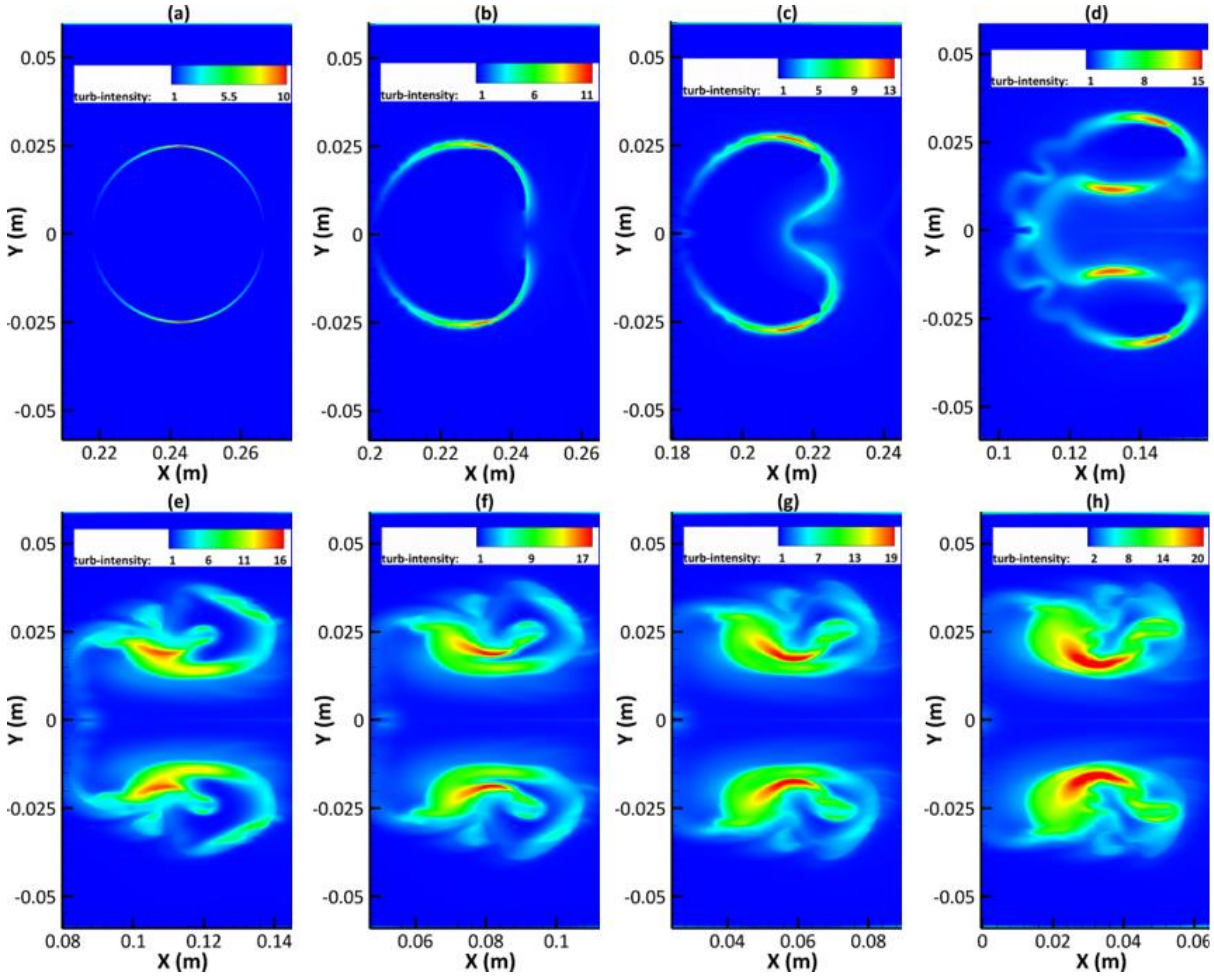

Figure 5.17: Contours of turbulence intensity on the central x-y plane at: (a) t=0.51; (b) t=1.02; (c) t=2.11; (d) t=3.88; (e) t=4.56; (f) t=5.74; (g) t=6.92; and (h) t=8.44.

The RMI happens when the material interfaces are impulsively accelerated which leads to the misalignment between the density and pressure gradients (Richtmyer, 1960; Meshkov, 1969). This misalignment causes a baroclinic deposition of the vorticity which deforms the bubble surface resulting in air/helium mixing and transition to turbulence at late times. Following clarifications provided by Tomkins *et al*. (2003) regarding the manifestation of a secondary instability, i.e., the KH instability, they also explained that these instabilities could combine to evolve the flow into a state of turbulence. It has been shown above that the shock bubble interaction process entails a wide range of complicated characteristics, from shock wave refraction and reflection, generation and transport of vorticity, to the air-jet (aj) penetrating through the severely distorted bubble and the formation of vortex filament. Nevertheless, to the best knowledge of this research, there are rarely any previous experimental and numerical studies that have addressed one very important aspect of the shock cylindrical bubble interaction process – turbulence generation and development. Fig. 5.17 shows contours of turbulence intensity, and it can be seen from Fig. 5.17(a) that turbulence starts to be generated initially in a small region at the bubble interface at a quite early stage (t=0.51). As time progresses, the bubble interface is deformed, as shown in Figs. 5.17(b) and (c) at t=1.02 and t=2.11 respectively. The upstream edge has caved in through the middle under the influence and penetration of the aj, but turbulence is still concentrated in a narrow region around the bubble interface with the maximum turbulence intensity reaching about 15% at t=3.88, as shown in Fig. 5.17(d). Afterwards, the turbulence region starts to expand as the aj has pierced the bubble and a

pair of vf has formed, leading to an increase of the maximum turbulence level to about 16% around the vf pair regions, as shown in Fig. 5.17(e) at t=4.56. These vortical filaments are transported downstream leading to an increased region of high turbulence intensity. Subsequently, it can be seen from Figs. 5.17(f-h) that the turbulence region continues to expand gradually with the turbulence level increasing steadily up to the maximum turbulence intensity (around 20%) as shown in Fig. 5.17(h) at t=8.44. Figs. 5.17(e-h) also show that the highest turbulence intensity areas are within the vf.

5.4. Conclusions

The mechanism of bubble distortion and compression from an interaction with a supersonic (Ma = 1.22) incident shock has been investigated via a numerical study. The URANS computational approach is adopted with a coupled level set and VOF method to capture the helium bubble and air interface accurately. 2D and 3D simulations have been performed and this research proved that the 3D predictions are much closer to the experimentally measured data, with an excellent concordance observed between the predicted velocities of the incident wave, refracted wave, transmitted wave, upstream interface, downstream interface, jet, vortex filament and the corresponding measured values. The predicted dimensionless upstream interface and jet velocities were also compared to both the Rayleigh Taylor (R-T) Theory, for estimating the growth rate of small sinusoidal perturbations, and past experimental results as presented in Section 5.3.3. Similarly, the predicted dimensionless downstream interface velocity was also compared to both the R-T Theory and past experimental results as presented in Section 5.3.4. Our 2D and 3D results show a good agreement with the theoretical predictions and experiments. As in the previous comparisons, the 3D predictions are much closer to the theoretical estimations and experimental measurements. The final quantitative assessment that was conducted involved comparing the predicted temporal variations of the interfacial characteristic scales, i.e., the length and width of the evolving interface to that measured in past experimental works. There was a good agreement between the 2D/3D predictions and the experimental data, but the 3D estimations were more representative of the early shock acceleration and bubble distortion as they showed shorter lengths (hence more compression) during the early SBI phases. A similar trend is noticed for the width of the developing interface where the 3D widths were predicted to be greater than 2D widths at early SBI times which proved that an increased compression would cause the deforming bubble to become vertically elongated hence the greater 3D widths compared to the 2D predictions.

The flow visualisation revealed several salient flow characteristics that have been experimentally observed, i.e., the simulated images generally agree with the experimental shadowgraphs. The simulated images have evidently illustrated the early deformation and compression of the upstream edge of the helium filled cylinder. This is then followed by the air-jet formation that evolves and encroaches the downstream bubble end. Wave pattern evolution, i.e., incident, transmitted wave, refracted wave, internally reflected wave, etc., is also clearly shown. From a fundamental standpoint, baroclinicity is the only source for generation of vorticity as the SBI flow field evolves. During flow field evolution, vorticity is deposited and transported while the planar incident wave impulsively accelerates the air/helium interface. As the shock wave propagates through the cylindrical bubble (acting as a divergent acoustic lens), the RMI is induced evident as small undulating perturbations that grow linearly with time. This is followed by the evolution of a nonlinear regime where a mushroom-shaped spike appears. Excellent results are also obtained as regards air/helium turbulent mixing and vortex filament evolution with a comprehensive development of the vortex filaments from formation to a full distinctive structure illustrated using flow visualisation. The current study clearly reveals that turbulence is generated at the early phase of the shock cylindrical bubble interaction process in the bubble upstream interface region, well before the formation of vortex filaments and even before the air-jet is formed. After a pair of distinctive vortex filaments is formed, turbulence is mainly generated around the vortex filament regions with the maximum turbulence intensity reaching around 20%. To

our best knowledge, turbulence generation and development has not been presented/discussed in any of the previous relevant studies.

6. Shock/Liquid Bubble Interaction

6.1. Introduction

The unsteady interaction of liquid bubbles with high-speed gas flows results in their disintegration. In this research, the breakup pattern of a water bubble subjected to shock wave loading is investigated under conditions that are typical of the stripping-type bubble disintegration. This breakup mechanism, which takes place for Weber numbers (We) in the mathematical range, $100 \leq We \leq 20{,}000$, was reported by Wierzba and Takayama (1987). As the computed We for this research falls within this range, the objective of this chapter is to accurately perform two-dimensional (2D) and three-dimensional (3D) computational fluid dynamics (CFD) simulations to investigate the stripping-type breakup model involving the complex interaction of a supersonic shock wave (Ma = 1.47) with a cylindrical water bubble. To do this, a finite volume method (FVM) is used to solve the governing integral equations for the conservation of mass and momentum i.e., the Unsteady Reynolds-Averaged Navier-Stokes (URANS) mathematical model. This mathematical model combined with the coupled Level Set (LS) and Volume of Fluids (VOF) method, also referred to as the CLSVOF scheme, have been applied within the commercial CFD code, ANSYS FLUENT, to advance the current understanding of the complex SBI process.

The simulations are evaluated by comparing the: displacement/drift of the bubble with time, acceleration of the bubble with time, drag coefficient of the bubble, and variation of bubble area due to bubble distortion with related existing experimental data. Comparisons are also shown between the predicted bubble length/width and the experimentally measured results to elucidate changes in the shape and size of the 2D and 3D bubbles. Comprehensive flow visualization has been used to explain the shock-bubble interaction (SBI) process i.e., the onset of bubble compression, formation of the vortices, production and distribution of vorticity, separation point (SP) and boundary layer stripping point (BLSP) as well as the merging of these points. The generation and development of turbulence at the later stages of SBI as well as late-stage circulation of vortices have not been previously investigated. Therefore, turbulence was investigated to elucidate the appearance of small flow structures as well as the production and circulation of the vortices. Also, 2D SBI simulations are directly compared against 3D SBI numerical simulations and previous experimental data to evaluate their accuracy. Generally, this research has captured and discussed a wide range of complex interface dynamics across the range of physical conditions investigated.

6.2. Methodology

6.2.1. Governing equations and numerical methods

The interaction between supersonic air and a cylindrical water bubble at the air-water interface as well as the subsequent shock wave travel and bubble deformation were simulated using a pressure-based FVM to solve the URANS equations. SBI is predominantly unsteady, and turbulence is generated at the later stage of SBI with usually large-scale unsteady flow structures. It was demonstrated by Onwuegbu and Yang (2022) that for this kind of flow, the URANS approach could predict the flow accurately at a significantly reduced cost so that there was no need using two other more accurate approaches, i.e., LES or DNS. The URANS equations are derived by averaging the instantaneous Navier-Stokes equations with some extra terms called Reynolds stresses being generated during the averaging process. These terms need to be approximated/modelled using a turbulence model. There are many turbulence models available and the selection of an appropriate turbulence model for this research will be presented in Section 6.2.5. As this kind of computational problem involves the generation of vortices and stripping of materials at the bubble interface, it is important to efficiently capture the bubble deformation. As such, an accurate interface tracking

technique is required to capture the bubble deformation properly. There are different techniques that are available to track the interface but most of them often fail to achieve pressure equilibrium for grid cells close to the interface. They also struggle to handle large interface distortions, i.e., disintegration and fronts fusing (Shyue, 1998). From a numerical investigation of SBI viewpoint, various researchers (e.g., Niederhaus et al., 2008; Taniguchi et al. 2014) had investigated the subject using VOF with varied success. Due to the high-density variation between air and water, it is expedient that an appropriate scheme which can describe the air-water interface without smearing the density jump across the interface is selected. To achieve this, the CLSVOF scheme was applied. A third order MUSCL scheme was employed to discretize both the momentum and continuity equations spatially. This scheme is built into ANSYS FLUENT under spatial discretization schemes. The compressive scheme, which is a second order reconstruction scheme, was also adopted for spatial discretization of the volume fraction equations. With respect to the compressive scheme, the sharp/dispersed interface regime was applied. A first-order implicit scheme was used for the temporal discretization of the 2D and 3D URANS equations. To achieve numerical stability and accuracy, the Courant Friedrichs Lewy number was set as 0.5 and a very small-time step of 4×10^{-7} seconds was used to accurately capture detailed flow developments. These equations, models and schemes have been elaborately discussed in Chapter 3.

6.2.2. Physical model

During aerodynamic bubble disintegration, the breakup pattern is controlled by inertial, viscous, and capillary forces. Inertial forces lead to bubble distortion, finally resulting in fragmentation. Viscous forces delay bubble distortion while capillary forces ensure that the bubble maintains its original shape (Kaiser et al., 2020). With respect to the process of bubble breakup, two non-dimensional numbers describe bubble disintegration. These numbers are the We and the Ohnesorge number (On). We denotes the ratio of the inertial (aerodynamic) force to the capillary (surface tension) force while On represents the ratio of the liquid viscous force to the surface tension force. We is shown below:

$$We = \frac{\rho_{g,2} {U_{g,2}}^2 \mathrm{d}}{\sigma_l} \tag{6.1}$$

where $\rho_{g,2}$, $U_{g,2}$, d, and σ_l denote the post-shock gas (air) density, post-shock gas (air) velocity, initial liquid bubble diameter, and surface tension coefficient of the liquid respectively.

$$On = \frac{\mu_l}{(\rho_l \mathrm{d} \sigma_l)^{1/2}} \tag{6.2}$$

where μ_l and ρ_l denote the liquid dynamic viscosity and density respectively.

The Reynolds number (Re) represents another non-dimensional number utilized to quantify secondary atomization and is very essential for liquid-droplet breakup (Chen, 2008; Kaiser et al., 2020). Re, which represents the ratio of the inertial force to viscous force, is given below:

$$Re = \frac{\rho_{g,2} U_{g,2} \mathrm{d}}{\mu_g} \tag{6.3}$$

where μ_g denotes the gas (air) dynamic viscosity.

Re describes the ambient flow field, shock Ma which initiates the bubble disintegration process and the ratio of ρ_l to $\rho_{g,2}$, denoted by ε.

The calculations for We and Re for an incident shock Ma = 1.47 are presented in Table 6.1 following the experiments conducted by Igra & Takayama (2001) and Igra et al. (2002). These values are obtained using the corresponding fluid characteristics and original bubble diameter (=4.8mm).

Table 6.1: Comparison of Experimental and numerical We and Re for Ma = 1.47.

Condition	Bubble Fluid	Ambient Gas	Ma	We	Re
Experimental	Water	Air	1.47	$6.9\ x\ 10^3$	$1.12\ x\ 10^5$
Numerical	Water	Air	1.47	$7.3\ x\ 10^3$	$1.30\ x\ 10^5$

From Table 6.1, it is shown that the computed non-dimensional parameters are close to the corresponding parameters derived from past experimental studies. The computed values show that surface tension is negligible as both dimensionless parameters have relatively high values. This proves that the inertial forces control the flow above the surface tension and viscous forces. Similarly, this research computed On, which represents the ratio of the viscous force to the surface tension force, as 0.00169. This further proves that surface tension and viscous forces are negligible compared to the inertial force. It may therefore be justified to neglect the effects of surface tension and viscosity as seen in past numerical works (e.g., Chen, 2008; Terashima and Tryggvason, 2009; Igra and Sun, 2010; Shukla, 2010; Terashima and Tryggvason, 2010; Meng and Colonius, 2015; Nonomura et al., 2014; Shukla, 2014; Sembian et al., 2016; Xiang and Wang, 2017; Meng and Colonius, 2018) because the physical mechanisms of breakup are predominantly driven by inertia. This research has then made a reasonable first approximation to neglect surface tension effects. This research has highlighted two justifications for doing this in addition to the analysis previously provided. Firstly, Garrick et al. (2017) explained that neglecting surface tension and boosting grid resolution results in the growth of interfacial instabilities which develop with time. These instabilities are not captured with surface tension as it provides a restoring force that resists high interface curvature. Secondly, Garrick et al. (2019) pointed out that accounting for surface tension and particularly interface sharpening decreases the amount of liquid material stripped from the interface where the distorted liquid column would have otherwise been characterized by an extremely chaotic wake area thus limiting the contribution to unsteady liquid acceleration estimations. As this research intends to effectively capture the: flow instabilities, process of material stripping from the liquid bubble peripheries, and evolution of turbulence from onset of SBI to its late stages, surface tension effects have been ignored while the influence of viscosity has been taken into consideration. Viscosity effects are particularly important at late-times when the flow becomes very unstable and turbulent. It is then understandable that the previously highlighted numerical publications, which involved the compressible simulations of droplet disintegration, investigated just the early stages of the shock liquid bubble interaction and distortion for a cylindrical water column.

6.2.3. Computational details

The computational set-up replicates the experiments carried out by Igra & Takayama (2001) and Igra et al. (2002). This research has adopted a 2D and 3D cylindrical bubble configuration because both Igra & Takayama (2001) and Igra et al. (2002) used cylindrical bubbles in their experiments. Fig. 6.1(a) shows the 2D representation of the computational domain (half of the domain) detailing the initial conditions within the domain and boundary conditions for the computations. This research simulated this 2D cross-section using cartesian coordinates where the x-axis is horizontal, and the y-axis is vertical. The dimensions of the 2D computational domain $(2.75d \times (L_x + 1.27d)$ are provided as a function of the bubble diameter, d (= 4.8mm or 22mm as in the experimental demonstrations of Igra & Takayama (2001)/Igra et al. (2002) or Sembian et al. (2016) respectively) while L_x varies and is selected to provide enough room to hold the shocked bubble propagation throughout the monitored time. The smaller diameter i.e., 4.8mm was used to allow direct comparison to the experimental findings of Igra & Takayama (2001)/Igra et al. (2002) while the larger diameter i.e., 22mm was selected in reference to the experimental procedures of Sembian et al. (2016) who pointed out that a greater diameter was essential for comprehensive studies of wave motions within the water bubble. The computations are performed only on the upper half as it is a

mirror image of the lower half. The lower boundary of the grid (Edge RS) represents the shock-tube axis while the upper boundary of the computational grid (Edge PQ) is treated as a solid wall with the no-slip wall boundary condition applied. The left boundary is the inlet, which is shown as Edge PR, while the right boundary corresponds to the outlet, which is shown as Edge QS. The incident shock propagates from left to right and the left boundary cells comprise of parameter values, i.e., $\rho_2, P_2, v_x = V_2, v_y = 0$, which is equivalent to the area behind the supersonic planar shock. As revealed from within the computational domain, identical values are utilised as initial conditions behind the shock which are located at a few cells within the computational grid. The values of these parameters also denote the post-shock properties of the ambient gas utilised in the initialisation and are calculated from the Rankine-Hugonoit relationships (Houghton and Brock, 1993). The left boundary condition allows the smooth outflow of reflected waves created by the SBI. The right boundary condition equivalently allows the smooth outflow of any rightward-moving waves, including the distorted incident shock. Fig. 6.1(a) also reveals that the right boundary condition is achieved by sustaining a 'zero gradient' for all fluid variables, i.e., $\nabla u = 0, \nabla P = 0, \nabla \rho = 0$. Fig. 6.1(a) also shows the equator which will be used to explain material stripping from the deforming bubble. For both 2D and 3D cases, the upstream end (shown as the windward edge on Fig. 6.1(a)) of the bubble is kept at some distance from the incident shock. This is because a shock has an expected tendency to spread to its usual profile given an 'exact discontinuity' as initial conditions (Hillier, 1991) which could lead to errors that adversely delay the SBI process. Similarly, the downstream end is shown as leeward edge in Fig. 6.1(a).

For the 3D simulations (see Fig. 6.1(b)), a coordinate system is described, where the *x*-axis is coincident with the shock-tube long axis in the direction of shock-wave travel. The *y*-axis and *z*-axis are along the traverse directions. The incident shock wave and the free stream flow propagate in the *x* direction. The computational geometry represents a physical region (shown as a cuboid) with dimensions $5.5d \times (L_x + 1.27d) \times 5.5d$, where d is the bubble diameter and L_x is flexible and just as in the 2D case, has been selected to enable complete propagation of the shocked bubble for the required times. Similar boundary conditions as in the 2D case are applied for the 3D case and a no-slip boundary condition is employed on the top, bottom, and side walls. As in the 2D case, the outlet condition has adopted a zeroth-order extrapolation to the boundary whereby the outermost data plane is transferred into the boundary such that the gradients across the boundary equate zero ($\nabla v = 0, \nabla P = 0, \nabla \rho = 0$). This technique ensures that the shock reflections are then significantly reduced even though they are not totally eradicated for strong shock waves.

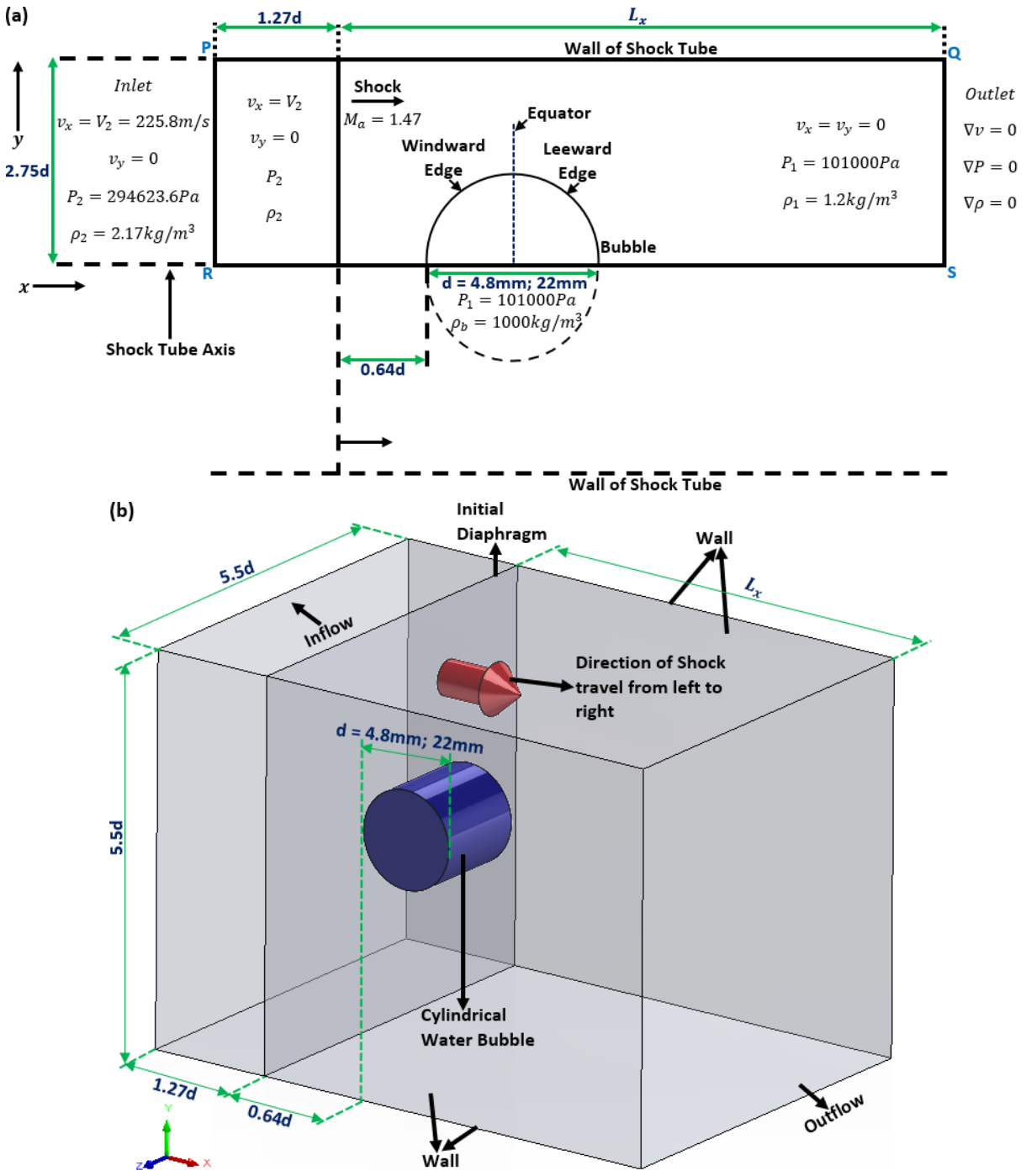

Figure 6.1: (a) The upper half of the shock tube revealed by the surrounding heavy black line and boundary/initial conditions for the 2D case; and (b) Computational domain for the 3D case.

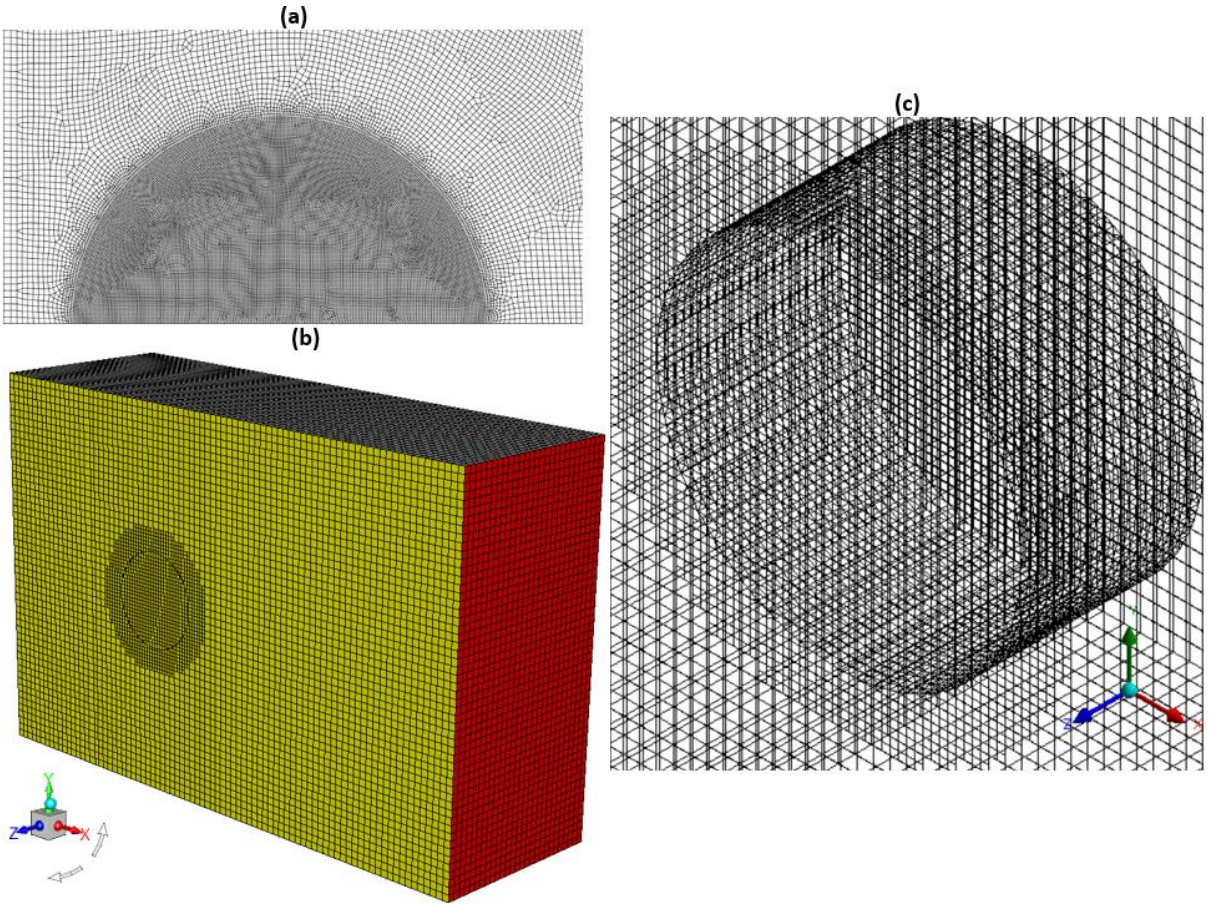

Figure 6.2: (a) 2D hybrid mesh; (b) 3D unstructured mesh; and (c) Close view of fine mesh around bubble from Adaptive Mesh Refinement (AMR).

The 2D (Fig. 6.2(a)) and 3D computational grids (Figs. 6.2(b) and (c)) consist mainly of structured meshes in the main flow region while the region in the vicinity of the bubble (both inside and outside) has been discretised into unstructured grids, i.e., both hybrid grids. The unstructured cells used in the bubble vicinity for both 2D and 3D cases enable the local alignment of the grid orientation to the dominant flow direction due to their flexible nature thus lessening numerical diffusion (Holleman et al., 2013) and have been validated by the works of previous researchers (e.g., Holleman et al., 2013; Zubair et al., 2013). These unstructured grids make it easy to dynamically adapt the grid to the local structures of interest. As seen from Figs. 6.2(b) and (c), the 3D mesh is a hybrid grid consisting of uniform hexahedral meshes in most of the main flow region and smaller uniform hexahedral meshes within the bubble while the bubble vicinity (just outside and inside) is discretised into 'smaller-cell' unstructured triangular prisms. The cartesian cut-cell method, previously applied by Ingram *et al*. (2013), Berger *et al*. (2012), and Johnson (2013), has been used to generate this mesh. This method proved very useful to preserve the decoupling between the volume hexahedral mesh resolution and the surface triangulation in the bubble vicinity whilst focusing on resolution requirements close to the boundaries and reducing mesh irregularities in the cut cells (Berger *et al*., 2012).

Prior to the application of AMR, the cells inside the bubble and in its vicinity were made to be finer than the cells in the main flow region and the wall. AMR helps to generate a more robust high-resolution grid capable of reproducing a sharp representation of discontinuities as well as can sufficiently resolve the various flow structures to be investigated. With respect to AMR, several authors (Berger and Oliger, 1984; Henderson et al., 1991; Bell et al., 1994; Klein et al., 1994; Quirk and Karni, 1996; Nourgaliev et al., 2006; Nierderhaus et al., 2008, etc.) had extensively applied it

to SBI computations. The AMR settings are selected to ensure the maximum refinements in all areas having a non-zero bubble fluid volume fraction and close to any regions with strong density gradients (Nierderhaus et al., 2008). AMR thus ensures that the mesh is refined inside the bubble and its vicinity (including the primary shock wave) guaranteeing that the fine cells surround and travel with the bubble to provide for the strong interaction between the incident shock waves and the bubble.

6.2.4. Initialization of the computational problem

This research initialised the water within the bubble and the unshocked surrounding air i.e., area between initial diaphragm and outlet at atmospheric conditions. The initialisation assumed that the bubble and the unshocked surrounding air are originally in a state of rest as well as in thermal and mechanical equilibrium thus implying that any original buoyant movement of the bubble is ignored.

The JANAF data (Gordon and McBride, 1976) is used to derive the ratio of specific heats, γ, for air utilising the original, unshocked pressure and temperature with this value kept constant throughout the computation.

This research adopted the Rankine-Hugonoit relationships (Houghton and Brock, 1993) to calculate the post-shock characteristics of the surrounding air, as shown on the left-hand side of Fig. 6.1(a). The post-shock Ma, pressure and density are computed using the following mathematical relations respectively:

$$Ma_2{}^2 = \frac{(\gamma-1)Ma_1{}^2 + 2}{2\gamma Ma_1{}^2 - (\gamma-1)}, \tag{6.4}$$

$$\frac{P_2}{P_1} = \frac{2\gamma}{\gamma+1} Ma_1{}^2 - \frac{\gamma-1}{\gamma+1}, \tag{6.5}$$

$$\frac{\rho_2}{\rho_1} = \frac{\frac{\gamma+1}{\gamma-1}\left(\frac{P_2}{P_1}\right) - 1}{\frac{\gamma+1}{\gamma-1}\left(\frac{P_2}{P_1}\right)}, \tag{6.6}$$

where $Ma_1 = 1.47$, P_1 and ρ_1 represent the initial Mach number, pressure and density of the ambient air respectively, as shown on the right-hand side of Fig. 6.1(a).

6.2.5. Mesh independence study

A mesh independence study has been performed with three mesh qualities for both 2D case (0.24, 0.40, and 0.50 x 10^6 cells) and 3D case (6.9, 10.8, and 13.6 x 10^6 cells) to determine the best grid resolution that will yield the most optimal computational results in comparison to the experimental works of Igra and Takayama (2001)/Igra et al. (2002). Figs. 6.3(a) and (b) show the changes in the distorted bubble drift, Δx_L with time. The bubble drift provides a clear history of the bubble motion as it is deformed. The bubble leading edge (x_L) is essential in determining the bubble drift. As such, Δx_L is derived as the distance between the current position of x_L and its previous location. From the descriptions provided within Fig. 6.3(a) and (b), x_L is shown as the location of the middle of the windward end of the deforming water bubble. At the onset of shock liquid bubble interaction, x_L, is represented by the first position (at the centre of the upstream end) that comes in contact with the incident shock wave. The descriptions also reveal the dimensionless times, τ, when these drifts are estimated and the shape of the distorted bubbles corresponding to τ. τ represents a normalisation of simulation time, T, using $\rho_{g,2}$, $U_{g,2}$ and ε. For emphasis, $x_{L,\tau=0.79}$, $x_{L,\tau=1.30}$, and $x_{L,\tau=1.54}$ represent the leading-edge position of the distorted bubble at $\tau = 0.79$, $\tau = 1.30$, and $\tau = 1.54$ respectively. Panchal et al. (2023) usefully pointed out that quantitative estimations for shock liquid bubble

interaction are calculated from the simulation flow-fields utilising a threshold volume fraction $\alpha_T^{(2)}$ as long as $\alpha^{(2)} > \alpha_T^{(2)}$ denotes the bubble shape whose geometrical parameters have to be established. As a result, they stated that due to the ambiguity in the experimental measurements, it was uncertain what value for $\alpha_T^{(2)}$ could be used to attain the best concordance with experimental data. They explained that this uncertainty mainly stemmed from the fact that gas/liquid interface may look diffused due to the tiny, stripped particles in the vicinity of the 'parent' bubble surface, depending on the measurement method, even though it should stay sharp realistically. Chen (2008) similarly explained that there is an associated difficulty with defining the 'exact' profile of the distorted water bubble. Therefore, this research has defined the shape of the distorted bubble by $\alpha_w = 0.9$ as in the numerical investigations of Chen (2008) and Panchal et al. (2023).

For the 2D case represented by Fig. 6.3(a), the results show little disparity when the mesh is refined from 0.40 to 0.50 x 10^6 cells, and hence there is no need to refine the mesh further. As such, the remaining 2D simulations are carried out using 0.50 x 10^6 cells. Similarly, for the 3D case represented by Fig. 6.3(b), the derived results from the mesh with 10.8 x 10^6 cells show little variation from the results obtained from the mesh with 13.6 x 10^6 cells and hence there is no need to further refine the mesh. Following this analysis, all 3D computations are performed using 13.6 x 10^6 cells.

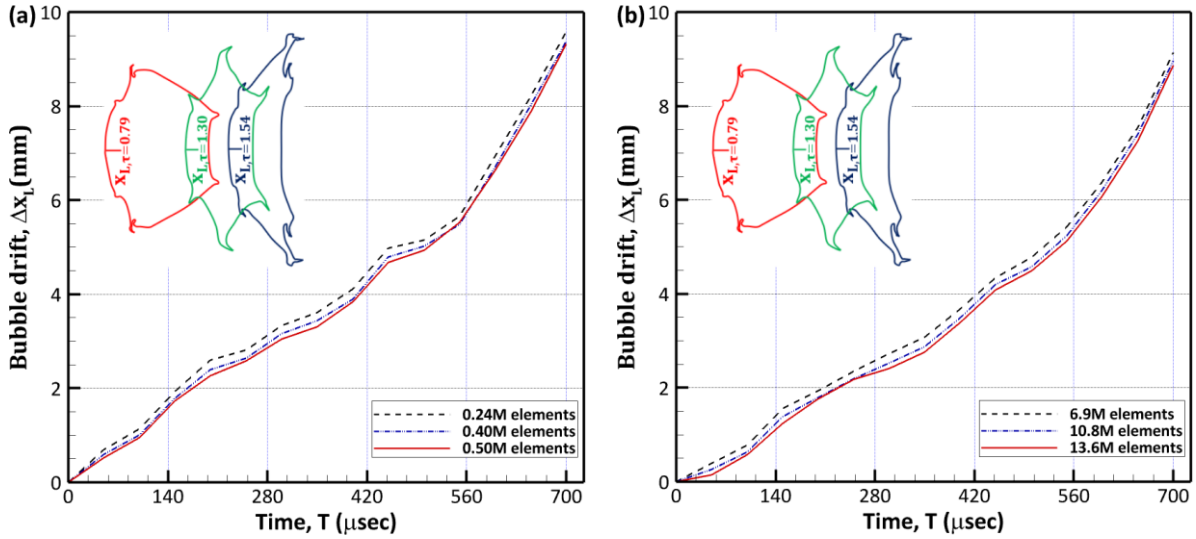

Figure 6.3: (a) Coarse, fine, and finer meshes in 2D case; and (b) Coarse, fine and finer meshes in 3D case

6.2.6. Turbulence model selection

Lawson and Barakos (2011) explained that the associated flow fields for a SBI will be characterised by the strong acoustic effects, unsteadiness, and turbulence. This means that the SBI process between the supersonic shock wave and the bubble will yield more complex turbulent features. Also, SBI shows structures that are preliminarily turbulent (Haas and Sturtevant, 1987) and there is a fundamental variation in the behaviour of 2D and 3D turbulence which is due to the lack of the vortex-stretching mechanism in 2D (Pope, 2000). Several authors (e.g., Chen, 2008; Terashima and Tryggvason, 2009; Igra and Sun, 2010; Shukla, 2010; Terashima and Tryggvason, 2010; Nonomura et al., 2014; Shukla, 2014; Meng and Colonius, 2015; Sembian et al., 2016; Xiang and Wang, 2017; Meng and Colonius, 2018) had numerically investigated SBI using the compressible Euler equations which govern the adiabatic and inviscid flows (Toro, 2009). But if the late-stage turbulence involving small-scale structures and full bubble disintegration are to be discussed, physical viscosity should be considered. This then necessitates the use of turbulence models to

effectively study the SBI phenomenon as there is hardly any knowledge acquired till date concerning the performance of turbulence models for shock liquid bubble interaction simulations. This research thus stands as a new research dimension to studying SBI. There are several turbulence models and there is no general agreement which model is most superior as their individual performance is very case dependent. Based on this, this research has adopted three extensively applied and highly rated turbulence models: the realizable *k*-*ε*, the shear stress transport (SST) *k*-*ω*, and a Reynolds stress model (RSM). These three turbulence models have been examined to evaluate their performance for the 3D case. Fig. 6.4 shows the comparison between the predicted bubble drift with time versus the experimental measurements for the three turbulence models. It is clearly seen in Fig. 6.4 that the predictions using all three turbulence models show little disparity but the results from the RSM are slightly closer to the experimental data. Therefore, RSM is adopted in this research.

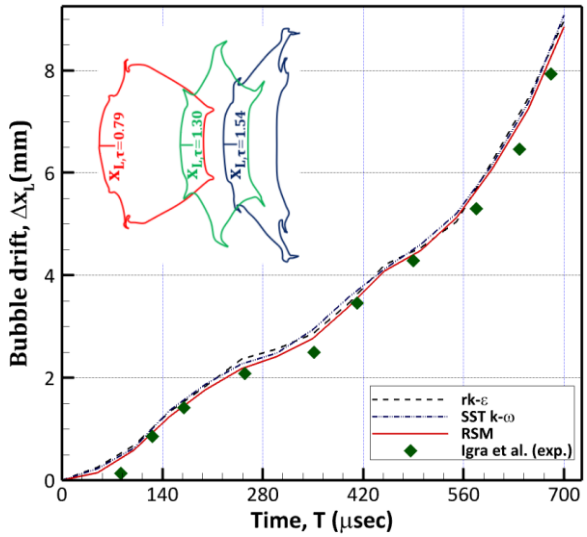

Figure 6.4: Comparison of numerical results between different turbulence models and experimental data.

Fig. 6.5 presents the predicted (2D and 3D) and experimentally measured bubble drift with time. It can be seen clearly that the 3D predictions match the experimental data of Igra et al. (2002) extremely well in comparison to the 2D predictions. It is evident from this comparison that the 3D simulations have captured the complex shock liquid bubble interaction more accurately and all the following analysis will be based on the 3D results as there was no need to present the 2D results. The CPU times per 50 iterations are 308 seconds and 5,184 seconds for the performed 2D and 3D simulations respectively using the best 2D and 3D grids as detailed in Section 6.2.5.

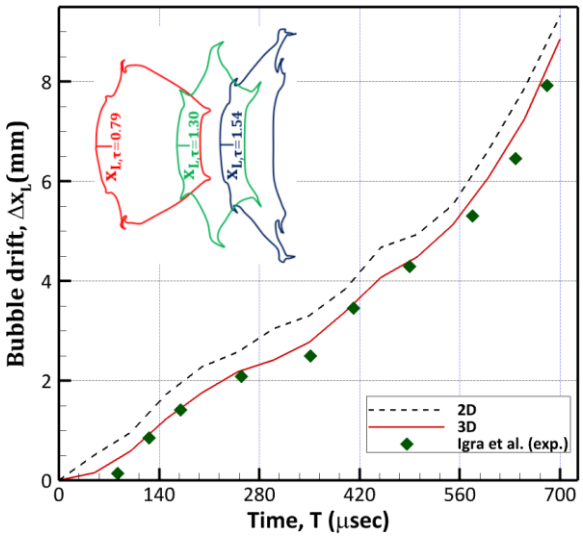

Figure 6.5: Comparison of the 2D and 3D predictions against the experimental data.

6.3. Results and discussion

6.3.1. Trajectory of the water bubble

The dimensionless drift, Δx_L^* against dimensionless time, t, for the deforming water bubble is shown in Fig. 6.6. The dimensionless drift, Δx_L^* against dimensionless time, t, for the deforming water bubble served as the most fundamental method to compare the numerical predictions of this research to past experimental measurements. It is similar to Figs. 4.3 & 4.7 (spherical helium bubble case) and 5.3 & 5.8 (cylindrical helium bubble case) which show the changes in the bubble location with respect to the positions of the jet, upstream and downstream interface. Hence, there was no need to introduce Δx_L^* against t in previous examples and Chapters (4 & 5).

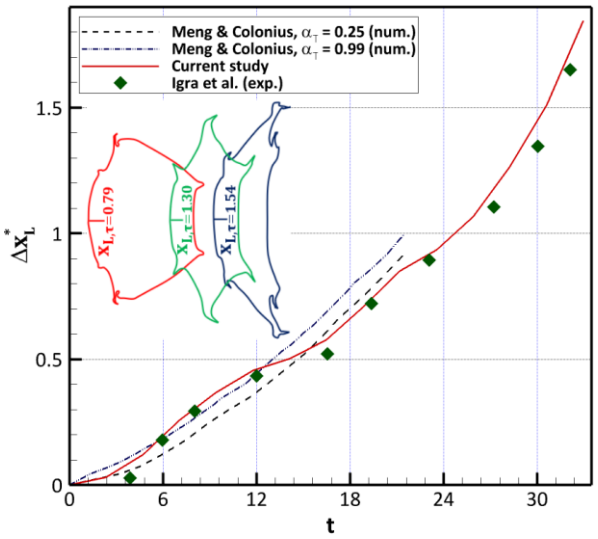

Figure 6.6: Comparison between numerical and experimental dimensionless displacements of the bubble against time.

Δx_L^* is given as:

$$\Delta x_L^* = \frac{\Delta x_L}{d} \tag{6.7}$$

while t is given as:

$$t = \frac{T U_{g,2}}{d} \tag{6.8}$$

For this research, the position of the water bubble is defined based on the upstream end of the bubble This is illustrated by the lines positioned at the middle of front edge of the deforming bubble provided in the descriptions within Fig. 6.6. The experimental measurements of Igra et al. (2002) are also presented in Fig. 6.6. The trend of our current study is congruent with the experimental data and fits a similar curve. This is because our estimations are close to and show a good concordance with the experimental measurements. It is also worth stating that our estimated drifts are higher than those provided by the experimental measurements. This research attributes this difference to the influence of drag force existent between the side walls of the shock tube and the boundaries of the water bubble in the conducted experiments of Igra et al. (2002) but such drag force is lower from our numerical estimations as revealed in Section 6.3.3. This lower drag force results in a greater velocity behind the shock wave. Fig. 6.6 also presents the comparison of our work to the numerical study of Meng and Colonius (2014). They selected a threshold liquid volume fraction, α_T, to constrain the cylindrical bubble such that any computational cell having a liquid volume fraction, α_l, and satisfies the mathematical relation, $\alpha_l \geq \alpha_T$ can be considered a component of the deforming cylinder. They did this to deal with the uncertainty inherent in the experimental measurements which has already been discussed in Section 6.2.5. They then chose a range ($0.25 \leq \alpha_T \leq 0.99$) but for the sake of comparison, we have just selected the upper and lower limits of that range. From Fig. 6.6, it is seen that their numerical predictions for $\alpha_T = 0.99$ agree with both the experimental data and our current estimations from the onset of SBI up to $t \approx 13.2$ after which it starts deviating away. The reverse is noticed for their estimations at $\alpha_T = 0.25$ which starts deviating from the onset of SBI away from both our current predictions and the experimental measurements up till $t \approx 15.6$ and $t \approx 19.2$ respectively after which it starts getting closer.

6.3.2. Acceleration of water bubble

Fig. 6.7 shows the acceleration history of the water bubble as material stripping and bubble disintegration progresses.

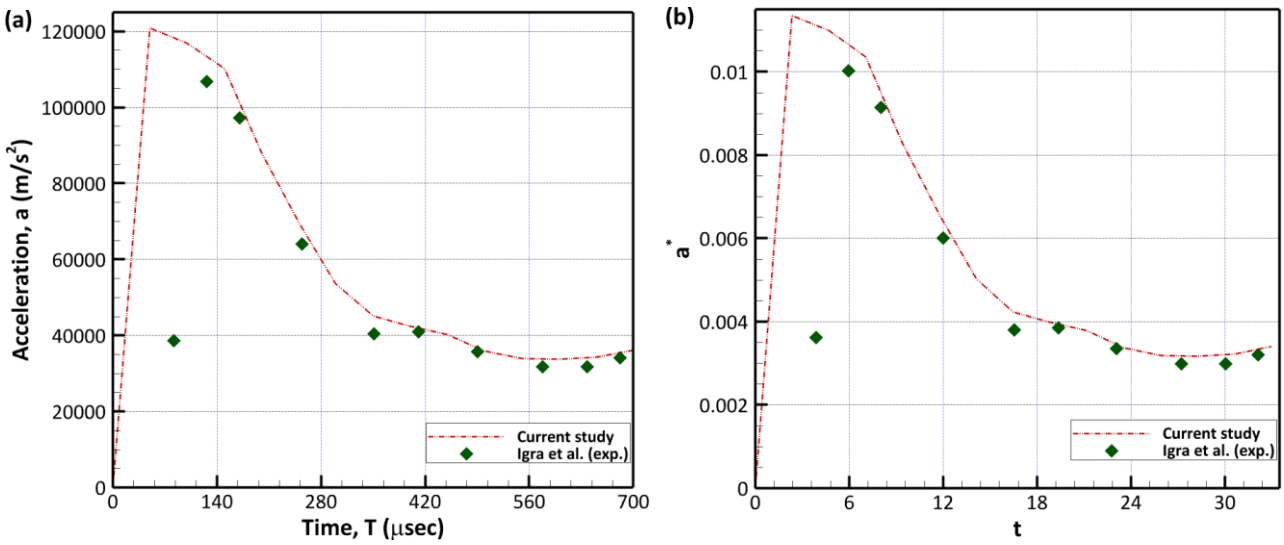

Figure 6.7: (a) Acceleration history of deforming water bubble in dimensional form (b) Acceleration history of deforming water bubble in non-dimensional form.

Acceleration is very important as it is serves as a 'driver' for bubble deformation and disintegration. (Theofanous et al., 2012). From Fig. 6.7(a), it is shown that the trend of the current numerical study mostly matches the experimental measurements except at the early stages when acceleration is

not constant. Similarly, in the dimensionless form, Fig. 6.7 (b) shows that our numerical estimations mostly coincide well with experimental data except in early phases of SBI when material stripping has not developed significantly and a complex, chaotic wake has not formed from unsteady vortex shedding. Material stripping involves the continuous removal of liquid sheets and microdrops from the surface of the bubble until the parent bubble is completely compressed (Ranger and Nicholls, 1969; Wierzba and Takayama, 1988; Chou et al., 1997; Xu et al., 2022). From Fig. 6.7 (b), a^*, is given as:

$$a^* = \frac{ad}{{U_{g,2}}^2} \tag{6.9}$$

where a stands for the acceleration in m/s^2. From Fig. 6.7(a) and (b), a and a^* rise with time from the onset of SBI up to T $\approx 56\mu sec$ and t ≈ 2.4 respectively before dipping swiftly up to T $\approx 154\mu sec$ and t ≈ 7.2 respectively. This is followed by a steeper drop in a and a^* up to T $\approx 294\mu sec$ and t ≈ 13.8 respectively. Both a and a^* continue to decrease but at a rate that is less steep compared to the previous period. This continues up till T $\approx 350\mu sec$ and t ≈ 16.2 respectively. Afterwards, there is an oscillating decrease in a and a^* up to T $\approx 490\mu sec$ and t ≈ 22.8. It is safe to assume that between T $\approx 490\mu sec$ and t ≈ 22.8 up till T $\approx 700\mu sec$ and t ≈ 33 respectively, a and a^* are fairly constant as shown from Fig. 6.7(a) and (b). Generally, it can be concluded that Fig. 6.7(a) and (b) show that higher acceleration is induced at the early stage of bubble breakup before a decrease to an almost constant value. Following from this, Igra et al. (2002) explained that an empirical curve-fit for later times yields a constant acceleration shown in dimensional and non-dimensional forms by Eq. (6.10) and Eq. (6.11) respectively.

$$\Delta x_L = \frac{1}{2} a T^2 \tag{6.10}$$

$$\Delta x_L^* = \frac{1}{2} a^* t^2 \tag{6.11}$$

Using values for Δx_L, T, Δx_L^* and t to plot Eq. (6.10) and Eq. (6.11) yield Fig. 6.8(a) and Fig. 6.8(b) respectively.

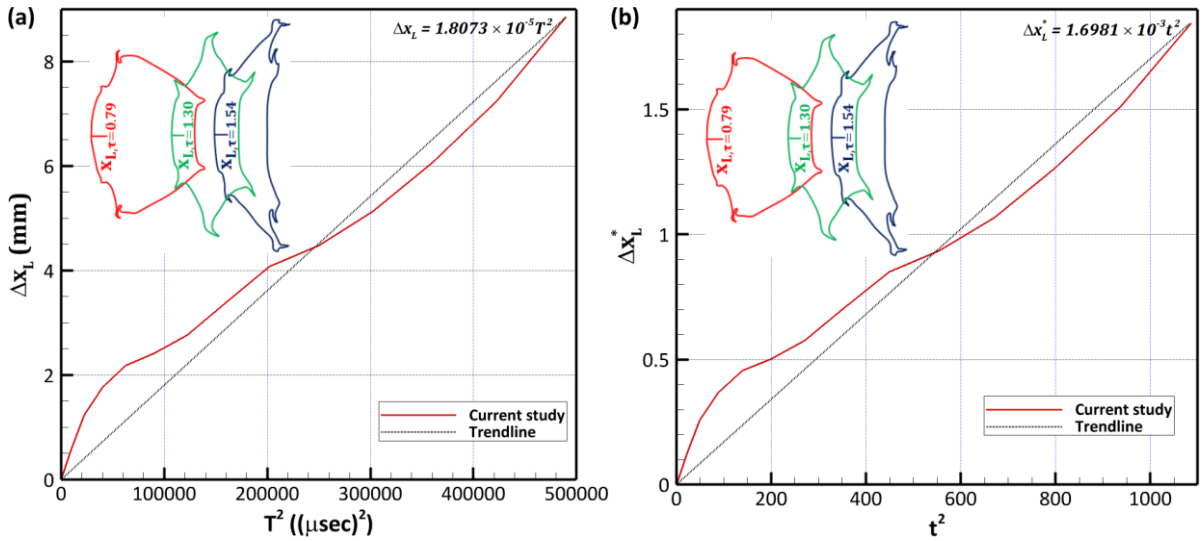

Figure 6.8: (a) Dimensional acceleration approximation (b) Non-dimensional acceleration approximation.

Eq. (6.10) resembles the equation of a straight line i.e., $y = mx + c$, where m and c denote the gradient and intercept of the straight line respectively. Δx_L is then plotted on the y-axis and T^2 plotted

on the x-axis. This is shown in Fig. 6.8(a). As Eq. (6.10) has no intercept i.e., $c = 0$, the drawn trendline that defines the curve in Fig. 6.8(a), will pass through the origin with a gradient equivalent to $\mathrm{a}/2$. Similarly, Eq. (6.11) resembles the equation of a straight line i.e., $y = mx + c$, with $\Delta \mathrm{x}_\mathrm{L}^*$ plotted on the y-axis and t^2 plotted on the x-axis. This is shown in Fig. 6.8(b). Similarly, as Eq. (6.11) has no intercept, the drawn trendline in Fig. 6.8(b) will pass through the origin with a gradient of $\mathrm{a}^*/2$. Following from this, the drawn trendline that defines the curve in Fig. 6.8(a) has the equation; $\Delta \mathrm{x}_\mathrm{L} = 1.8073\ x\ 10^{-5}\mathrm{T}^2$ and the gradient is $1.8073\ x\ 10^{-5}\mathrm{mm/(\mu sec)^2}$. The unit is converted to $\mathrm{m/s^2}$ by multiplying the gradient by 10^9. The gradient then becomes $1.8073\ x\ 10^4\ \mathrm{m/s^2} = 18{,}073\ \mathrm{m/s^2}$. Equating this gradient to the gradient of Eq. (6.10) (i.e., $\mathrm{a}/2$) gives a = $36{,}146\ \mathrm{m/s^2}$. Following the same procedure, a trendline with equation $\Delta \mathrm{x}_\mathrm{L}^* = 1.6981\ x\ 10^{-3}\mathrm{t}^2$ and gradient of $1.6981\ x\ 10^{-3}$ can be drawn for the curve in Fig. 6.8(b). Equating this gradient to the gradient of Eq. (6.11) (i.e., $\mathrm{a}^*/2$) yields $\mathrm{a}^* = 3.3962\ x\ 10^{-3}$. The deformed water bubble dimensional and non-dimensional acceleration are compared with experimental measurements as shown in Table 6.2.

Table 6.2: Comparison of dimensional and non-dimensional numerical acceleration to experimental measurements

Condition	Water bubble diameter (mm)	Ma	$\mathrm{a\ (m/s^2)}$	a^*
Experimental	4.8	1.47	$3.4035\ x\ 10^4$	$3.3754\ x\ 10^{-3}$
Numerical	4.8	1.47	$3.6146\ x\ 10^4$	$3.3962\ x\ 10^{-3}$

From Table 6.2, we see that the numerical predictions for a and a^* are very close to the experimental measurements. As previously pointed out in Section 6.3.1, the difference is caused by the experimental drag force generated by the contact which the side walls of the shock tube make with the water bubble. This drag force offers resistance to the force induced by the high-speed air behind the shock wave.

6.3.3. Approximations for the drag coefficient of the water bubble

The drag coefficient (C_D) plays an essential role in bubble disintegration. The magnitude of C_D is dependent on the velocity and acceleration of the bubble. For this research, C_D plays an important role in controlling the penetration of the deformed bubble, which has been impacted by the shock, into the ambient air. Ranger & Nicholls (1969) and Pilch & Erdman (1987) suggested a simplistic approach to determine the drag coefficient of a bubble. Ranger and Nicholls (1969) assumed that the bubble shape, mass and acceleration do not change and derived the equation of motion provided in Eq. (6.12).

$$\frac{1}{2} C_D \rho_{g,2} {U_{g,2}}^2 S = m_l \mathrm{a} \tag{6.12}$$

where C_D, S, and m_l denote the drag coefficient, frontal area and bubble mass. Fig. 6.1(a) shows that S (represented by the bubble surface area which is first impacted by the incident shock wave) takes the shape of a square bounded, on a pair of opposite sides, by the diameter of the circular portion of the cylinder. The other pair of opposite sides is bounded by the height of the cylinder which is equal to the diameter of the circular portion of the cylinder. We can then express S as d^2. m_l can be expressed as a product of ρ_l and volume of the liquid bubble, V_l. The volume of a cylinder, V, is given as:

$$\mathrm{V} = \pi r^2 h = \pi ({}^{d}/_{2})^2 h = \pi\, {}^{d^2}/_{4}\, h \tag{6.13}$$

where r, d, and h represent the cylinder's radius, diameter and height respectively. In our case, since the cylindrical liquid bubble's height is the same as the diameter. We can then adopt Eq. (6.13) and express V_l as:

$$V_l = \pi \, \mathrm{d}^3/_4 \tag{6.14}$$

m_l can then be expressed as:

$$m_l = \rho_l . \pi \, \mathrm{d}^3/_4 \tag{6.15}$$

Placing Eq. (6.15) and $S = \mathrm{d}^2$ into Eq. (6.12) and making a the subject of the equation yields:

$$\mathrm{a} = \frac{2}{\pi} \frac{C_D}{\mathrm{d}} \frac{\rho_{g,2}}{\rho_l} {U_{g,2}}^2 \tag{6.16}$$

Rewriting Eq. (6.10) using Eq (6.16) yields

$$\Delta \mathrm{x_L} = \frac{C_D}{\pi} \frac{\rho_{g,2}}{\rho_l} \frac{{U_{g,2}}^2}{\mathrm{d}} . \mathrm{T}^2 \tag{6.17}$$

If we divide both sides of Eq (6.17) by d yields

$$\frac{\Delta \mathrm{x_L}}{\mathrm{d}} = \frac{C_D}{\pi} \frac{\rho_{g,2}}{\rho_l} \frac{{U_{g,2}}^2}{\mathrm{d}^2} . \mathrm{T}^2 \tag{6.18}$$

The left-hand side of Eq. (6.18) is equal to Eq. (6.7) We can then rewrite Eq. (6.18) as

$$\Delta \mathrm{x_L^*} = \frac{C_D}{\pi} \tau^2 \tag{6.19}$$

where τ^2 represents:

$$\tau^2 = \frac{\rho_{g,2}}{\rho_l} \frac{{U_{g,2}}^2}{\mathrm{d}^2} . \mathrm{T}^2 \tag{6.20}$$

τ represents another dimensionless time which takes into consideration $\rho_{g,2}$ and ρ_l. It is defined as:

$$\tau = \frac{\mathrm{T} . U_{g,2}}{\mathrm{d}} \sqrt{\frac{\rho_{g,2}}{\rho_l}} \tag{6.21}$$

Fig. 6.9(a) shows the water trajectory using τ while Fig. 6.9(b) estimates the drag coefficient using Eq. (6.19).

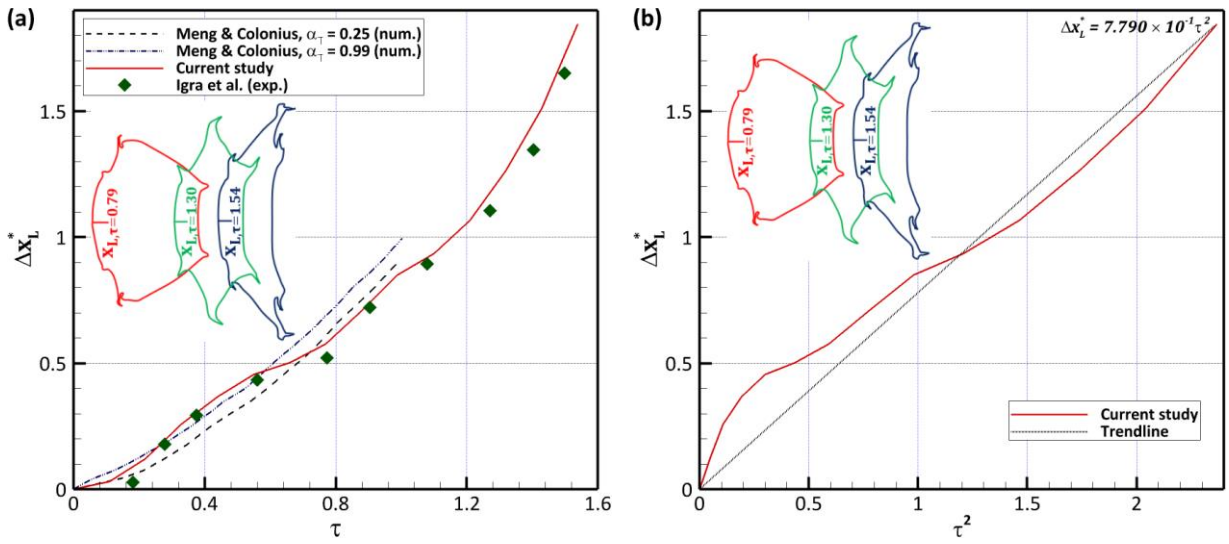

Figure 6.9: (a) Comparison between numerical and experimental dimensionless bubble drift against time (b) Non-dimensional drag coefficient approximation.

Fig. 6.9(a) compared the current study to the numerical analysis of Meng & Colonius (2014) and the experimental measurements of Igra et al. (2002). The trend of our current study is congruent with the experimental data and fits a similar curve. This is because our estimations are close to and show a good concordance with the experimental measurements. From Fig. 6.9(a), it is seen that their numerical predictions for $\alpha_T = 0.99$ agree with both the experimental data and our current estimations from the onset of SBI up to $\tau \approx 0.6$ after which it starts diverging away. The reverse is noticed for their estimations at $\alpha_T = 0.25$ which starts diverging from the onset of SBI away from both our current predictions and the experimental measurements up till $\tau \approx 0.68$ and $\tau \approx 0.88$ respectively after which it starts getting closer.

As demonstrated in Section 6.3.2, Eq. (6.19) resembles the equation of a straight line i.e., $y = mx + c$, where m and c denote the gradient and intercept of the straight line respectively. Δx_L^* is plotted on the y-axis and τ^2 is plotted on the x-axis. This is shown in Fig. 6.9(b). As Eq. (6.19) has no intercept, i.e., $c = 0$, the drawn trendline that defines the curve in Fig. 6.9(b) will pass through the origin with a gradient equivalent to C_D/π. Following from this, the trendline on Fig. 6.8(a) has the equation; $\Delta x_L^* = 7.790\, x\, 10^{-1}\tau^2$. From this equation, it is seen that the gradient is $7.790\, x\, 10^{-1}$. Equating this gradient to the gradient of Eq. (6.19) (i.e., C_D/π) and solving for C_D yields $C_D = 2.4473$. The drag coefficient of the bubble as estimated from Eq. (6.19) is compared to that obtained from the experimental measurements of Igra et al. (2002) as shown in Table 6.3.

Table 6.3: Comparison of numerical prediction of drag coefficient to experimental data

Condition	Water bubble diameter (mm)	Ma	C_D
Experimental	4.8	1.47	2.9140
Numerical	4.8	1.47	2.4473

From Table 6.3, our predicted C_D is close to the experimental C_D but the difference owes to the drag force induced by the contact between the water column and the shock tube in the experiments which can impede the force generated by the high-speed airflow. Table 6.3 shows that C_D for the current study and experiments are assumed as constants. This is valid because such an assumption could be made by recognizing that C_D computations should consider the altering spanwise diameter such that C_D can be recomputed utilizing the deformed diameter. C_D, as predicted from this research, has been done using the trajectory of the deforming bubble and has

incorporated its changing spanwise diameter. This ensured that the predicted C_D is physically more accurate than that based on just the bubble's original diameter and could help simplify the modeling of bubble dynamics. This approximation is consistent with the works of Meng and Colonius (2014) who explained that unsteady C_D can be estimated as a constant over the early times of bubble disintegration.

6.3.4. Numerical measurements of the temporal changes of the interfacial characteristic scales

Temporal changes in the centerline width (w) and spanwise height (h) of the deforming cylindrical bubble are plotted in Figs. 6.10(a) & (b) and Figs. 6.11(a) & (b) respectively. These measurements were made using the series of images derived from the numerical simulations. w is derived by measuring the width of the deforming cylindrical bubble in the x-direction while h is obtained by measuring its height in the y-direction. The description of these interfacial characteristic scales is enclosed in Figs. 6.10(a) & (b) and Figs. 6.11(a) & (b). w and h of the evolving interface have been normalised using d i.e., $\mathrm{w}^* = \mathrm{w}/\mathrm{d}$ and $\mathrm{h}^* = \mathrm{h}/\mathrm{d}$ respectively. This section also investigates changes in the area (A) of the deforming bubble as it is moved by the highspeed airstream and as material stripping takes place along its peripheries (Figs. 6.12(a) & (b)). A has also been normalised using the original area of the cylindrical water bubble ($\mathrm{A_o}$) before it is impacted by the incident shock wave i.e., $\mathrm{A}^* = \mathrm{A}/\mathrm{A_o}$. Figs. 6.10(a) and (b) show the changes in bubble width with time.

Figs. 6.10(a) and (b) show that the bubble width reduces with time as SBI progresses. This is attributable to bubble compression and material stripping from the bubble peripheries. The predicted temporal changes in bubble width (with respect to value and trend) matches well against the experimental measurements. The numerical findings of Meng and Colonius (2014) are also shown in Figs. 6.10(a) and (b). Their predictions for $\alpha_T = 0.25$ are congruent with both current numerical predictions and experimental measurements while those for $\alpha_T = 0.99$ are noticed to deviate from onset of SBI to the end of considered timeframe i.e., their values for $\alpha_T = 0.99$ are slightly underpredicted but still capture the same trend as both the current predictions and experimental data.

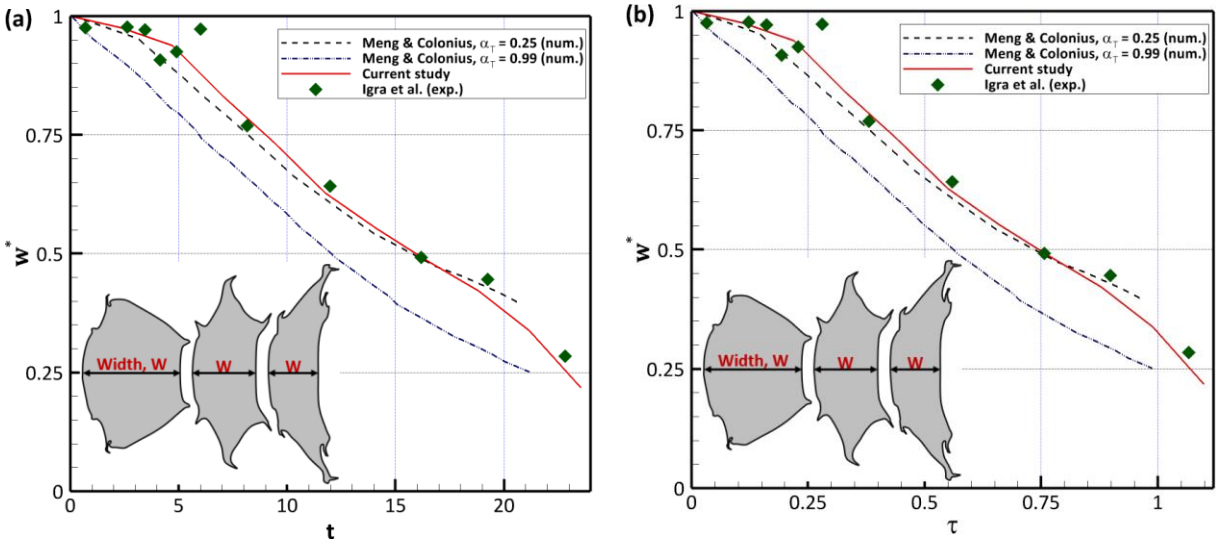

Figure 6.10: (a) Deformation of the water bubble in the x-direction against dimensionless time, t (b) Deformation of the water bubble in the x-direction against dimensionless time, τ.

Figs. 6.11(a) and (b) show the time variation of bubble distortion in the y-direction i.e., changes in bubble height with time

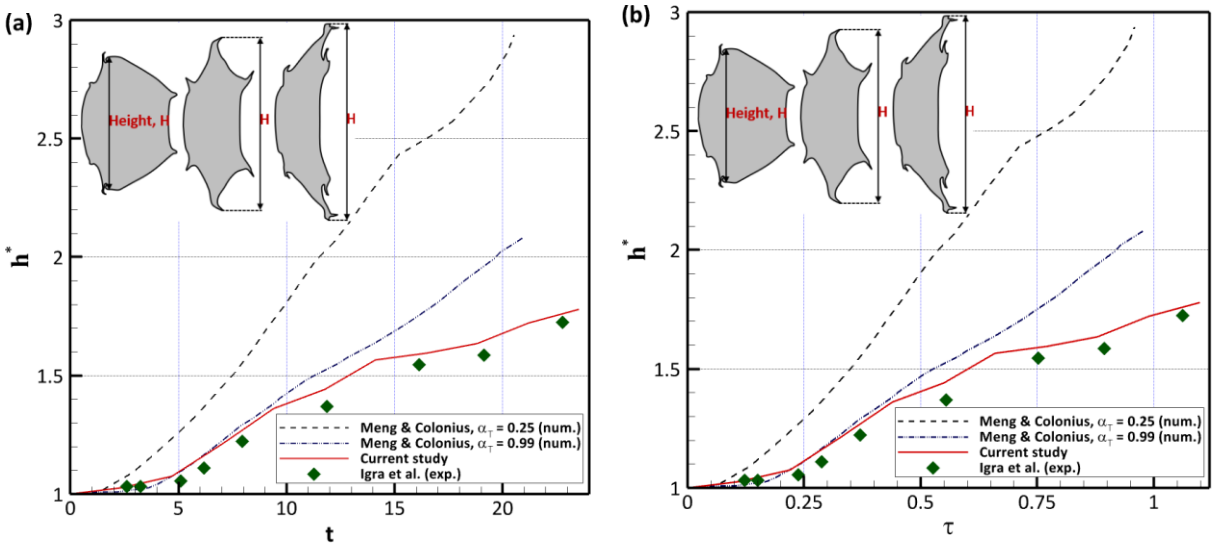

Figure 6.11: (a) Deformation of the water bubble in the y-direction against dimensionless time, t (b) Deformation of the water bubble in the y-direction against dimensionless time, τ.

Figs. 6.11(a) and (b) show that the bubble height increases with time as SBI progresses. This is consistent with the lateral stretching of the deforming bubble from its top and bottom ends (the equator) as its centerline width decreases due to bubble compression and material stripping. The predicted temporal changes in bubble height (with respect to value and trend) conforms well with the experimental measurements. The numerical findings of Meng and Colonius (2014) are also shown in Figs. 6.11(a) and (b). Their predictions for $\alpha_T = 0.99$ are comparable to both current numerical predictions and experimental measurements up to $t \approx 9$ or $\tau \approx 0.45$ after which they start to slightly deviate. This slight deviation continues till $t \approx 15$ or $\tau \approx 0.75$. Afterwards, they become overpredicted up till the end of the studied timeframe. For $\alpha_T = 0.25$, their estimations are significantly overpredicted from onset of SBI to the end of the investigated timeframe. α_T is as defined in Section 6.3.1.

Figs. 6.12 shows the time variation of the cross-sectional area of the deforming cylindrical water bubble.

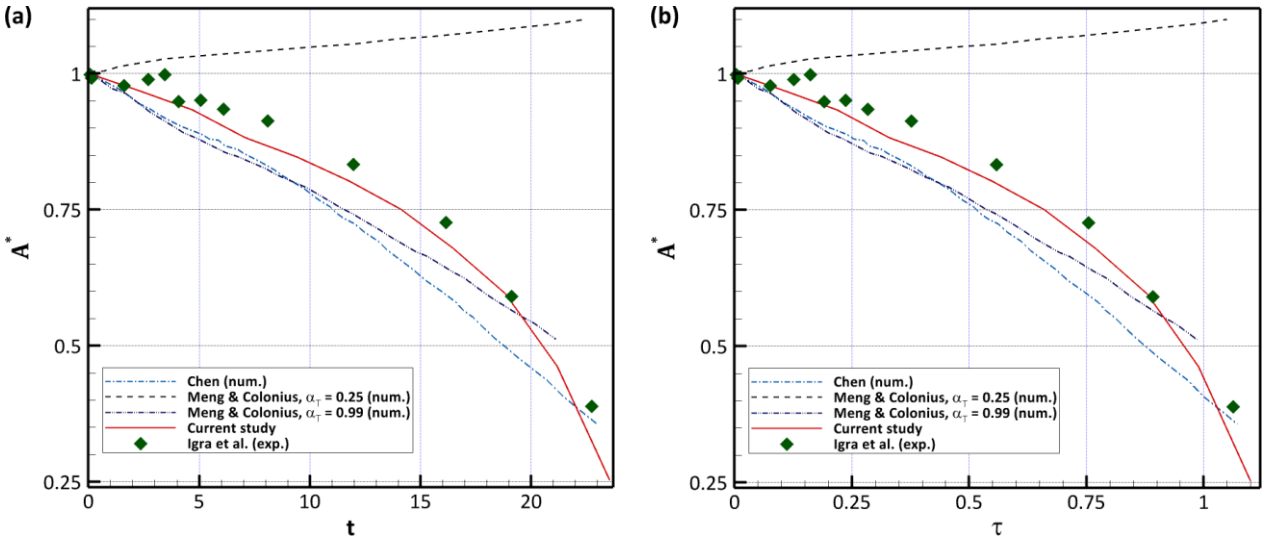

Figure 6.12: (a) Evolution of the bubble area against dimensionless time, t (b) Evolution of the bubble area against dimensionless time, τ.

Figs. 6.12(a) and (b) show the: predictions from the current study, predictions from Chen (2008), predictions from Meng and Colonius (2014) for $\alpha_T = 0.25$ and $\alpha_T = 0.99$ as well as experimental measurements. Figs. 6.12 (a) and (b) also prove that the bubble area should decrease with time as SBI progresses because of the stripping of small-sized fragments. The only exception from Figs. 6.12(a) and (b) is the case of $\alpha_T = 0.25$ (Meng and Colonius, 2014) where the estimated values are significantly overpredicted and do not follow the trends of the current predictions, Chen (2008), Meng and Colonius (2014; at $\alpha_T = 0.99$) and the experimental measurements. The predicted temporal changes in bubble area (with respect to value and trend) for this research are in good agreement with the experimental data. The predictions of Meng and Colonius (2014) at $\alpha_T = 0.99$ differ to both current numerical predictions and experimental measurements until $t \approx 19$ ($\tau \approx 0.9$) after which their estimated values become closer and converge. Similarly for Chen (2008), their predictions are underpredicted compared to our current study and the experimental data until $t \approx 22$ ($\tau \approx 1.025$) after which their estimated values become closer and converge. Figs. 6.11(a) & (b) and 6.12(a) & (b) show that the current numerical solutions are much better than those of Meng & Colonius (2014) and Chen (2008). This is because they both used Euler equations for a 2D inviscid flow while the current study has incorporated the effects of viscosity using a turbulence model to approximate the Reynold Stresses generated during the averaging of the fundamental 3D governing equations.

Figs. 6.10(a) & (b), 6.11(a) & (b) and 6.12(a) & (b) usefully point out that the slopes of our profiles vary. Chen (2008) attributes this slope variation to the more intense nature of the stripping breakup at later periods compared to the early phase of SBI. This slope variation and the wavy nature of our predicted curves is also indicative of the change in shape of the water bubble as SBI and stripping progresses. Generally, after the incident shock wave impinges on and passes through the windward end of the cylindrically water column, the bubble's distortion is typified by flattening in the streamwise direction. This is measured as a rise in the lateral bubble height and a drop in the centerline width. As material and tiny fragments of bubble masses are stripped off the deforming cylinder's periphery due to the high-speed flow behind the incident shock wave, the area of the cylinder is continuously reduced. Finally, the quantitative validations provided from Section 6.3.1 to Section 6.3.4 show that our numerical model is sufficiently reliable and accurate.

6.3.5. Visualization of shock/liquid bubble interaction morphology

The intricate and crucial processes involved in liquid bubble deformation, generation and evolution of vortices, growth of air-jet, material stripping from the bubble peripheries and the overall late-time development of the SBI process will be further investigated in this section. A direct qualitative comparison of our numerical study to the experimental works of Igra & Takayama (2001) and Igra et al. (2002) is shown in Figure 6.13.

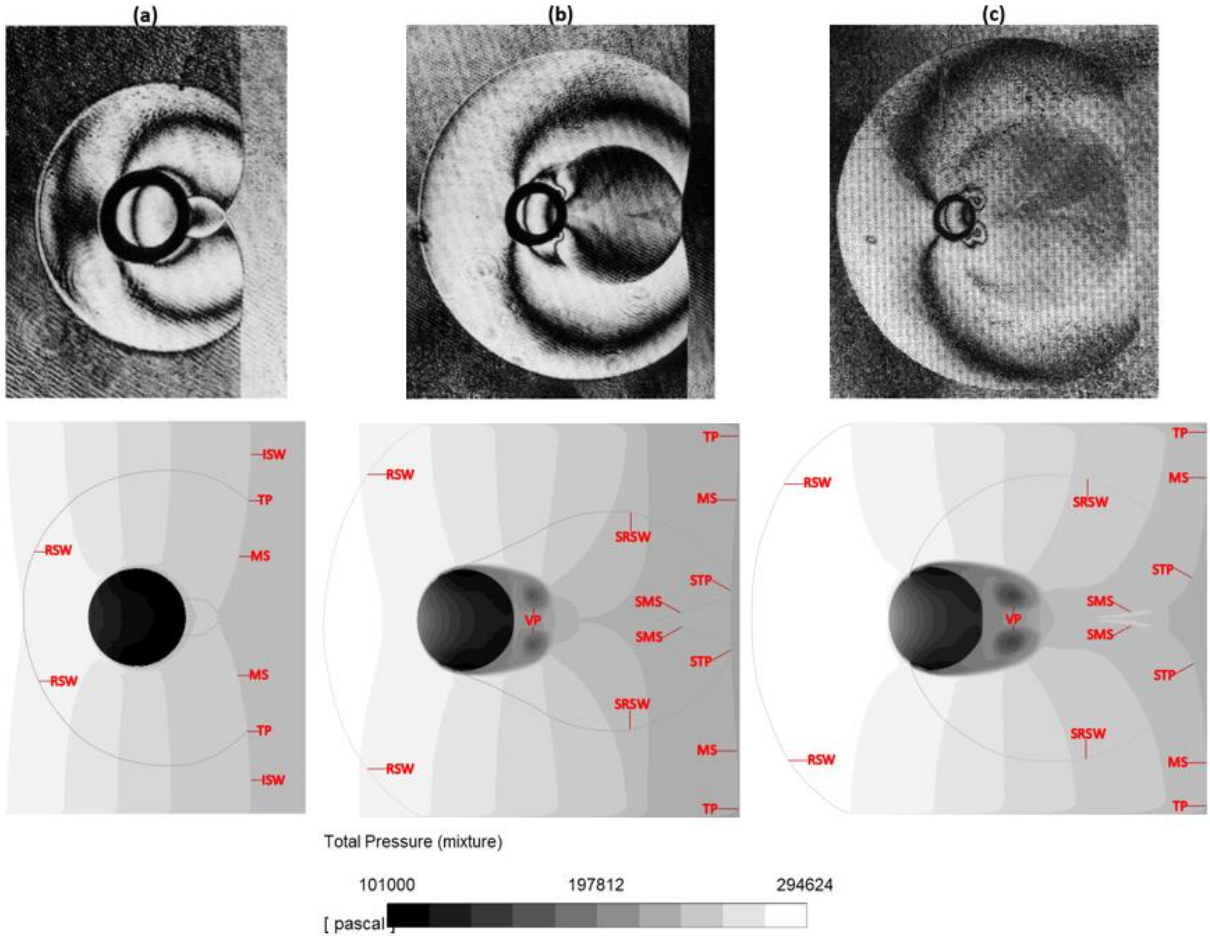

Figure 6.13: Snapshots of simulated images (bottom) on the central x-y plane and experimental shadow-photographs (top) at: (a) $\tau = 0.07$; (b) $\tau = 0.18$; and (c) $\tau = 0.26$. The pressure scale is provided for the current numerical prediction to reveal the: pressure variation within the bubble; effects of the high-pressure zone on bubble compression; and pressure in the region where entrainment occurs.

Fig. 6.13 presents three (3) snapshots of the numerically simulated images (bottom), represented by the pressure contours, and shadow-photographs (top) captured in the experiments of Igra & Takayama (2001) and Igra et al. (2002). The pressure contours clearly show all the wave patterns observed in the experimental shadow-photographs. Thus, both the numerical pressure contours and the experimental shadow-photographs are comparable. $\tau = 0$ corresponds to the instant when the incidence shock impinges the windward end of the bubble. At this stage, the liquid cylinder is not affected by the shock propagation. Aalburg et al. (2003) explained that this is because the shock travel time is significantly smaller than the bubble's relaxation time. The predictions captured the SBI process excellently, particularly the major characteristics, as the simulated images are considerably like the shadow-photographs at all three times. The notations used in the analysis are defined in the numerically simulated images. ISW, RSW, SRSW, TP, STP, MS, SMS and VP

represent the incident shock wave, reflected shock wave, secondary reflected shock wave, triple point, secondary triple point, Mach stem, secondary Mach stem and vortex pair respectively. Fig. 6.13(a) shows that at $\tau = 0.07$, ISW has propagated across the bubble (on the leeward side of the bubble) and RSW travelled in the opposite direction (on the windward side of the bubble). Prior to the formation of MS and Mach reflection (MR), ISW intersects the water bubble forming a regular reflection where the angle of attack of the ISW on the bubble is greater than a critical transition angle. It is this reflection pattern that is transmitted to MR. Igra and Takayama (2001) explained that the RSW is transformed into a MR when the angle between the ISW and the air-water interface surpasses a critical value. This takes place after the ISW has been partially reflected at the windward edge of the cylinder. The two curved MS and the RSW are thus formed by the diffraction of the ISW coupled with the MR. The TP is also shown in Fig. 6.13(a) which serves as the junction when the ISW, RSW and the MS intersect. Within the numerically simulated bubble, there are curved wavy lines which are indicative of a density variation as shock waves propagate through the cylindrical water column. There also exists a pressure variation within the numerically simulated water bubble (see pressure scale in Fig. 6.13) as the pressure at the air/water interface is 'locally continuous'. This is shown by the interaction of the shock wave with the water column as it propagates through air. Fig. 6.13(b) shows that at $\tau = 0.18$, ISW and RSW have travelled further away from the bubble in opposite directions. As the two MS are about to meet each other, they form two STP. Each STP has a SMS. Each STP serves as the confluence point where the MS meets both the SRSW and SMS. The presence of the secondary MR produces higher pressures on the downstream side which eventually leads to the compression and flattening of the numerically simulated deforming water bubble (see pressure scale in Fig. 6.13). Fig 6.13(b) also shows transmitted waves within the bubble linked with wave movements within air. These transmitted waves contribute to the flattening of the water column. Fig. 6.13(b) also shows the appearance of the VP on the leeward edge of the distorting bubble. From Fig. 6.13(c) and at $\tau = 0.26$, the VP has grown. Fig. 6.13(c) also shows that the RSW and SRSW have moved further distances on the upstream side of the bubble with the ISW also propagating well away from the downstream end of the bubble. From Fig. 6.13(c), the numerically simulated bubble shows that the SMS has a higher pressure compared to its surrounding (see pressure scale in Fig. 6.13). Figs. 6.13(b) and 6.13(c) are characterised by small fluid mists dragged from the leeward side of the deforming bubble. This entrainment is not very clear in the experimental shadowgraphs. Very interestingly, Figs. 6.13(b) and 6.13(c) show that the pressure in the zone where the liquid entrainment takes place is reduced (in comparison to the surrounding regions) with the formation and evolution of VP (see pressure scale in Fig. 6.13). This leads to the emergence of the BLSP. Generally, when the two MS intersect after the ISW has travelled across the bubble, a secondary wave structure (STP, SMS and SRSW) is created as shown from the numerically simulated images of Figs. 6.13(b) and (c). This secondary wave system travels upstream along the cylinder's surface leading to the compression and flattening of the cylindrical bubble.

For further investigation of the air-water interface distortion as well as elucidating certain flow features at late times of SBI, this research has compared the disintegration of the deforming cylindrical bubble to the 3D liquid column experiments of Theofanous et al. (2012). This is shown in Figs. 6.14(a), (b) and (c).

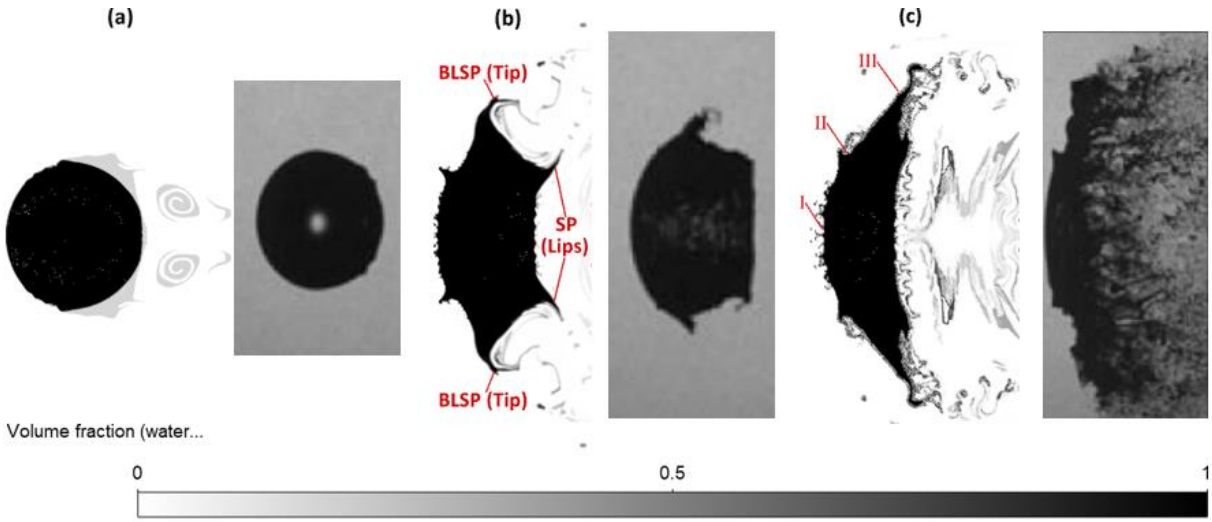

Figure 6.14: Qualitative comparison of the air-water interface distortion and water bubble breakup between this numerical study (left) using volume fraction contours on the central x-y plane and experiments (right) at: (a) $\tau = 0.40$; (b) $\tau = 1.21$; and (c) $\tau = 1.54$.

From Fig. 6.14, the representative interface distortion patterns are in good qualitative concordance. Fig. 6.14(a) shows that at $\tau = 0.40$, the leeward side of the bubble is flat due to the varying distribution of pressure along the interface. Fig. 6.14(a) also shows the developing VP on the leeward side of the bubble. Engel (1958) usefully explained that this VP slowly degrade the leeward air-water interface and fairly influence the production of fluid mist as seen in both Figs 6.14(b) and (c) (shown in both the current study and experiments). This VP interact with the air-water interface resulting in the stripping of a tiny amount of liquid from the downstream surface of the bubble. Two small tips are also noticed at the top and bottom of the deforming bubble close to the equator. These tips serve as the initiation points for the BLSP. At $\tau = 1.21$ (Fig. 6.14(b)), these two tips have developed and grown longer. It is also seen that material is dragged from the BLSP at these locations. As time progresses, these two tips are dragged into thin filaments which eventually break downstream. Fig. 6.14(b) also shows the emergence and evolution of two SP on the downstream end of the bubble. These SP also serve as locations where material is stripped and dragged from the water bubble. Two smaller lips have also developed on the leeward end of the deformed bubble at the two SP (this is not visible in the experiments). Fig. 6.14(b) is also characterised by the interface waves and disturbances which in Fig. 6.14(c) are further developed to form the hat-like structure and the liquid sheet ($\tau = 1.54$). The downstream end of the bubble has caved in as shown in Fig. 6.14(c) and the SP has merged with the BLSP. As the VP continuously interact with the air-water interface, more fluid masses are stripped from the bubble surface. These fluid masses coalesce into various small and fine particles which continuously travel downstream. These fine particles are clearly visible in the current study images and the experimental shadowgraphs (Fig. 6.14(c)). Fig. 6.14(c) also shows three important structures and phenomena which are characteristic of the stripping breakup mode.

- I represents the hat-like upstream structure bounded by two cusps;
- II denotes the transition area between the hat-like structure and the liquid sheet while;
- III represents the region depicting the sheet deformation in the vicinity of the deformed bubble's wake. It is interesting that our simulations have detected these three structures as

they have only been reported in the experimental investigations of Theofanous et al. (2012) and the numerical study of Kaiser et al. (2020). This shows the efficacy and accuracy of our numerical model.

6.3.6. Main phases of liquid droplet disintegration

Theofanous et al. (2004), Theofanous & Li (2008), Theofanous (2011), Theofanous et al. (2012) explained, through their experiments, that there are two competing regimes in the breakup of a liquid column subjected to a shock wave. These regimes are the Rayleigh Taylor piercing (RTP) and the Shear Induced Entrainment (SIE). The RTP represents a bubble disintegration regime controlled by the Rayleigh-Taylor instability after which the flattened bubble is penetrated by one or more unstable waves (Theofanous, 2011). This regime dominates low-speed flows i.e., low We. The SIE represents a bubble disintegration regime that involves a shedding effect resulting from a mixture of several Kelvin-Helmholtz (KH) instabilities. The SIE controls high-speed flows (high We) and is mainly due to viscous shearing as well as local disintegrations of films and filaments driven by surface tension (Theofanous, 2011). Liu et al. (2018) reported that for $On < 0.1$, the SIE has a critical We of 100. Following from this and the details provided in Section 6.2.2, the disintegration of the water bubble in this research is like the SIE regime. This is because the flow conditions are characterised by high Re, high We and low On. The disintegration of the water bubble as it is impacted by the propagating shock wave can be consolidated into three phases as observed in this research and previous experimental measurements i.e., Theofanous et al. (2004), Theofanous & Li (2008), Theofanous (2011), Theofanous et al. (2012). These three phases are: (a) instability of the bubble surface, (b) compression of the leeward side of the deforming water bubble, and (c) intense entrainment of small masses from liquid sheet as well as the formation of the bowl-shaped sheet.

Going forward, this research has used $\mathrm{d} = 22mm$ to allow for a detailed investigation of wave motions outside and within the bubble (see Sembian et al., 2016). The first phase which is typified by the beginning and appearance of small-scale instabilities on the bubble surface (upstream and downstream) of the cylindrical bubble is shown in Fig. 6.15. It is useful to point out that these small-scale instabilities are more pronounced on the upstream side of the bubble.

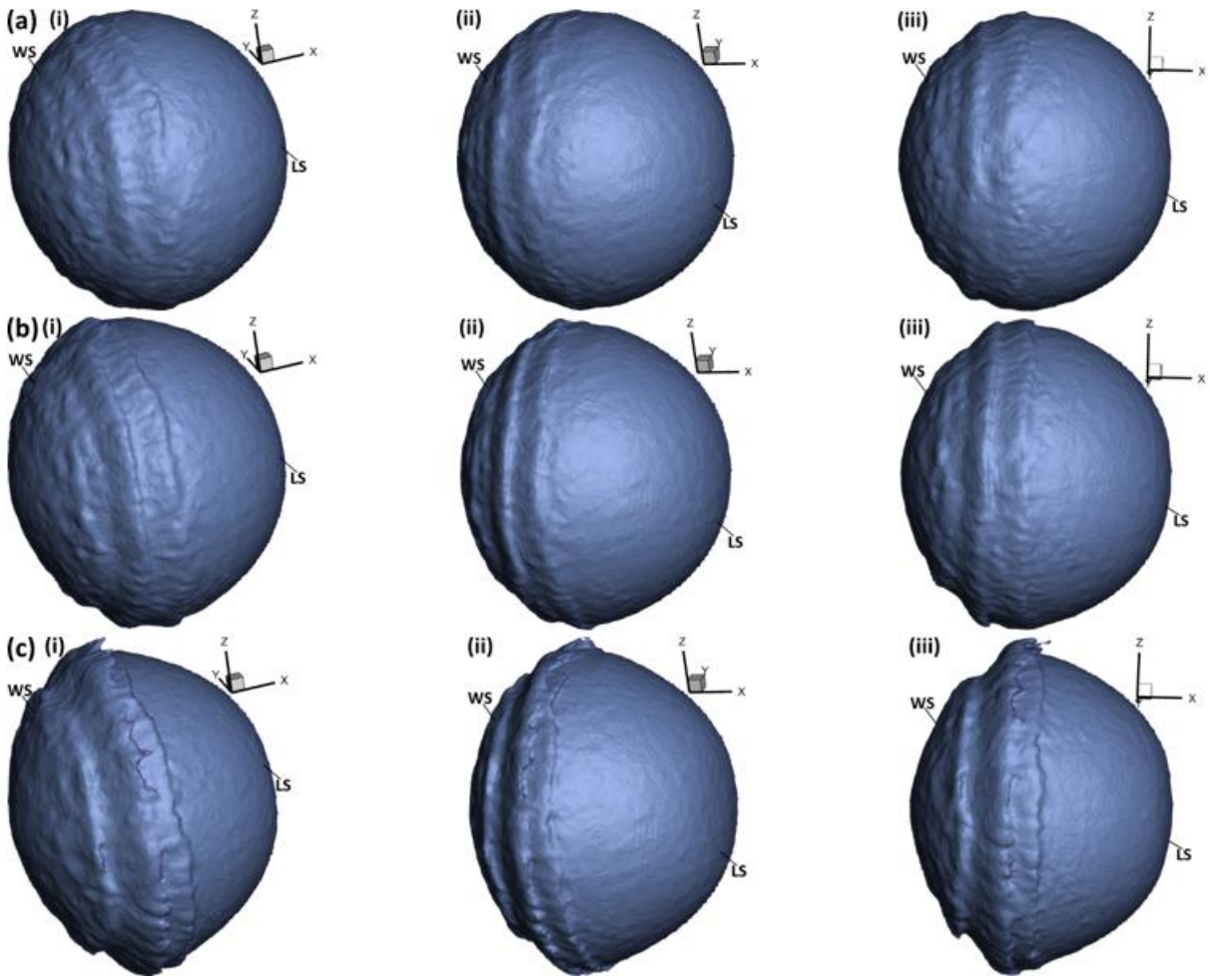

Figure 6.15: Three-dimensional (3D) representation of the first phase of the water disintegration process at: (a) $\tau = 0.12$; (b) $\tau = 0.17$; and (c) $\tau = 0.22$.

WS and LS, as used in the images, refer to windward side and leeward side respectively. Figs. 6.15(a), (b) and (c) show that the WS of the bubble is subjected to strong shear with this shear increasing from Fig. 6.15(a) to Fig. 6.15(c). This viscous shearing also induces mass loss which accompanies bubble deformation. As in the experimental works of Theofanous et al. (2012), the regions surrounding the LS stagnation point remain fairly smooth. We can then infer that the most clearly detectable unstable waves are close to the strongest shear points on the WS which is indicative that the instabilities have originated from shearing. The experimental works of Theofanous et al. (2012) and Jalaal & Mehravaran (2014) explained that the WS of the impacted bubble is under the influence of KH instability which is consistent with the findings of this research. This KH instability is also induced by the velocity difference between the airstream and the water bubble separated at the air-water interface (Theofanous, 2011). Figs. 6.15(b) and (c) show the appearance of an elevated unstable structure on the WS of the water bubble. Jalaal and Mehravaran (2014) added that the Rayleigh-Taylor (RT) instability in the radial direction has an effect on the formation and evolution of this elevated unstable structure. The 'small-scale' movements of this elevated unstable structure result in the lateral expansion (or stretching in the z-direction) of the deforming water bubble coupled with the stripping of tiny materials from the equator. As it is a well-known argument that both the RT (Taylor, 1950) and KH (Kelvin, 1871) instabilities are essential to solving the liquid bubble disintegration challenge, this research intends to use mathematical justification to show which instability has a more dominant effect. Acceleration, a, is very important parameter particularly with respect to understanding the RT instability within the framework of shock liquid bubble interaction. This is because this research involves the impulsive

acceleration of the heavy fluid i.e., water, by the light fluid i.e., air, which will automatically result in the RT instability. Meng and Colonius (2018) support this claim by explaining that the WS of the bubble should be subject to RT instability waves produced from the acceleration of the less dense gas into the heavier liquid. To elucidate the contributory importance of the RT instability, we use the Bond number, Bo, which represents the ratio of the body force to the surface tension force ratio and is given as:

$$\mathrm{Bo} = \frac{a\rho_l \mathrm{d}^2}{4\sigma_l} \tag{6.22}$$

From Eq. (6.22) we obtain a $Bo = 2860$. For this value of Bo, which falls in the range: $10^2 < Bo < 10^5$, Harper et al. (1972) described the bubble as quasi-stable. Harper et al. (1972) defined the quasi-stable mode as a regime where the distortion of the bubble is aerodynamically induced, and the impacts of shock wave acceleration on the water bubble are revealed as waves on the WS (Fig. 6.15(a) – (c)). Similarly, Simpkins and Bales (1972) described the quasi-stable mode as a regime in which the bubble deformation takes place in the presence of unsteady and long-wavelength surface waves. We can then infer that the RT instability does not play a more significant role than the KH instability and is not the principal reason for bubble fragmentation in our case. This is supported by Theofanous et al. (2012), who claimed from their investigation of the viscous KH instability, that wave numbers and growth factors of KH instability are constantly more significant than those of the RT instability by more than one magnitude order. This KH instability, which occurs when there is enough velocity variance across the air-water interface, is responsible for the vortex shedding. Unstable vortex shedding leads to varying forces acting on the surface of the water bubble. This subsequently results in bubble oscillation and stripping. This further proves that the quasi-stable bubble is deformed by mass removal which contributes significantly to bubble breakup. Eventually, as smaller droplets are shed from the deformed bubble and are subjected to sudden acceleration as they are ejected into the bubble wake, the bubble behaviour becomes acceleration dominated and unstable Taylor waves pierce through the bubble such that the Rayleigh-Taylor instability becomes the dominant effect (ANSYS, 2018).

As time progresses, the instability on the downstream side increases due to the interaction of the generated vortices with the bubble LS. This then leads to the compression (flattening) of the LS of the deforming bubble and is shown in Fig. 6.16. From Figs. 6.13(a) – (c), we see that there is a high-pressure area on the upstream side of the bubble while a low-pressure area exists on the downstream side. This pressure difference causes stripped materials that have been dragged downstream from the bubble periphery to be pulled into a jet that travels upstream to compress and flatten the LS of the deforming bubble. This compression as well as flattening increases as SBI progresses and is clearly detectable in Figs. 6.16(a)(iii), (b)(iii), (c)(iii), and (d)(iii). This flattening causes the caving in or hollowing of the LS of the deforming bubble with this effect increasing from Fig 6.16(a)(iii) to Fig 6.16(d)(iii) such that Fig 6.16(d)(iii) now looks like a sheet. The impact of flattening is clearer and more pronounced than material entrainment from the bubble edges. In this phase of bubble disintegration, the small-scale structures which were highlighted in the first stage accumulate at the equator as the instability of the LS of the deformed bubble is diminished because of flattening. The small-scale structures at the equator create a BLSP at the top and bottom of the bubble as shown in Figs 6.16(a)(i ii, & iii), (b)(I, ii & iii), (c)(i, ii & iii), and (d)(i, ii & iii). Similarly, as flattening intensifies on the LS of the deforming bubble, two lips (SP) bound the top and bottom of the hollow region. These lips are also clearly shown in Fig. 6.14(b)(iii), 6.14(c)(iii) and Fig. 6.14(d)(iii). As breakup continues, material is mainly stripped from these two locations i.e., SP and BLSP. Fig. 6.16(d)(ii & iii) show that these two locations are almost aligned on the same plane in the y-direction. Fig. 6.16(d)(i) also shows that more fluid has been dragged off the edges of the bubble at the BLSP close to the equator obvious from its rough edges.

The third stage coincides with an intense entrainment of materials from the edges of the deformed bubble after its downstream end has been completely flattened. This is shown in Fig. 6.17(i), (ii)

and (iii). In this stage, the LS of the bubble and SP are no longer visible as they have been pushed further inwards by the air-jet such that the center of the deformed bubble is extremely hollow. The bowl shape of the compressed liquid sheet is also a result of the high-speed gas flow. At this stage, the deformed bubble resembles a bowl. In comparison to the first stage, the surface instabilities are not obvious. This is because the influence of shear on the WS of the bubble and the impact of generated vortices on the LS of the bubble has become fairly subdued. As in Fig. 6.16(d)(i), Figs. 6.17(i), (ii) and (iii) show that a substantial amount of material has been dragged off the edges of the bubble at the BL, clearly seen from its rough edges.

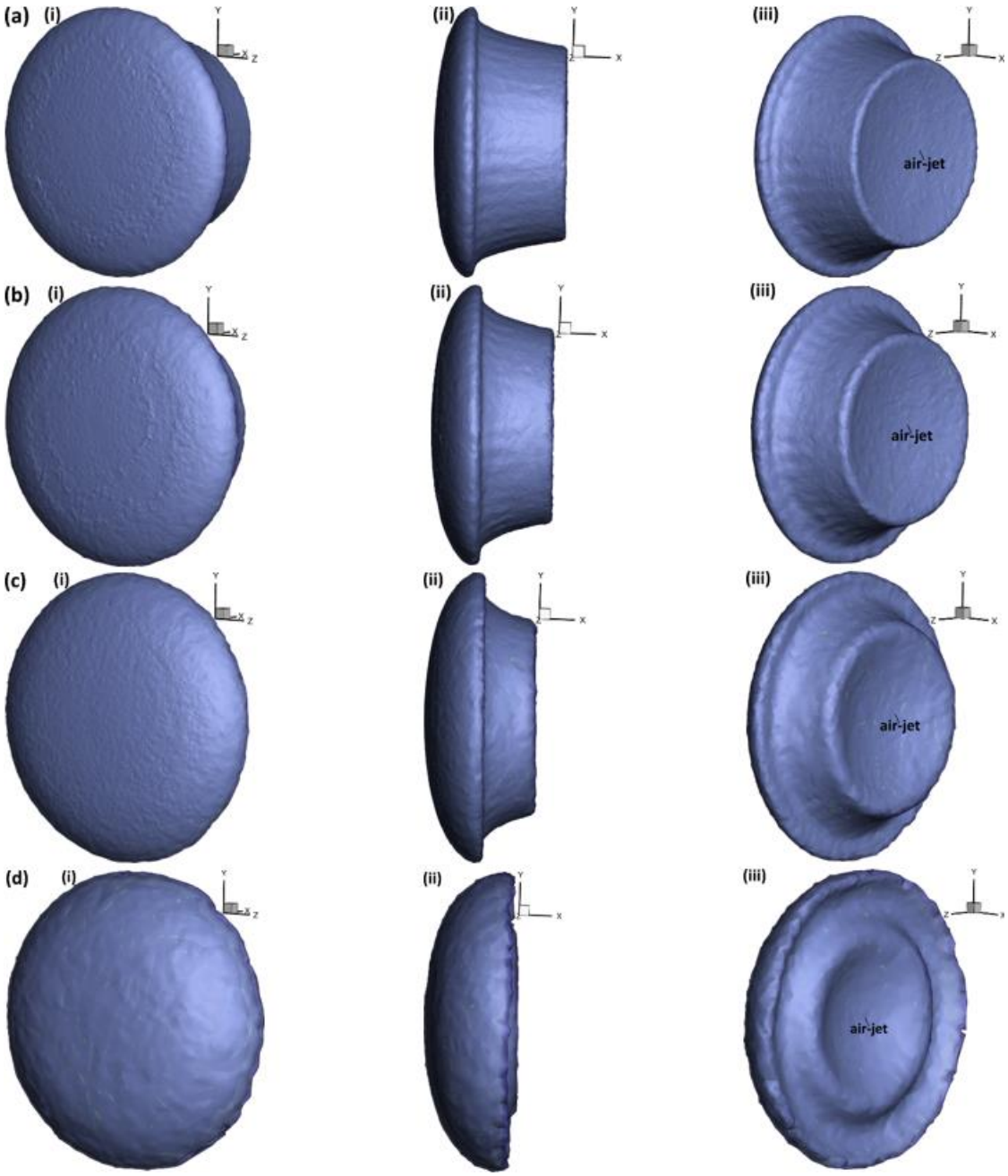

Figure 6.16: Three-dimensional (3D) representation of the second phase of the water disintegration process at: (a) $\tau = 0.30$; (b) $\tau = 0.34$; (b) $\tau = 0.41$; and (d) $\tau = 0.47$. This research recognises that the jet which impinges on the LS of the bubble is a collection of coalesced downstream fluid materials but has been termed 'air-jet' because it travels in air.

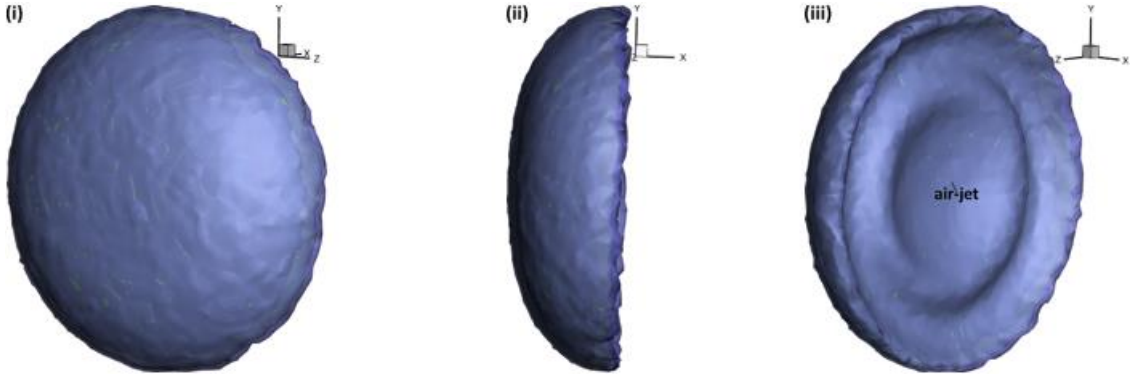

Figure 6.17: Three-dimensional (3D) representation of the third phase of the water disintegration process at $\tau = 0.51$.

6.3.7. Visualization of stripping from the BLSP and the SP

Figs. 6.18(a)(v) to (d)(v) show how small particles (microdrops) are stripped from the BL and how a curved, stretched fluid sheet (FS) is entrained from the SP. Figs. 6.18(a)(i - iii) to (d)(i - iii) are the corresponding 3D density iso-surfaces at different orientations. Fig. 6.18(a)(v) shows the two lips on the LS of the bubble situated at the SP. Strong inertial forces from the ambient flow drag a FS from the SP. The developing air-jet is also shown as a collection of small downstream fluid particles that have been coalesced together by the generated vortices like the primary vortex (PV). These coalesced particles are transported upstream and impact the LS of the deforming bubble. This leads to compression and hollowing of the region between the two lips at the SP. The density iso-surfaces shown in Fig. 6.18(a)(iii) reveal the compression and hollowing of the LS of the deformed bubble due to the effects of the air-jet. The irregular structure of the distorted bubble edges on the WS and LS as shown in Fig. 6.18(a)(ii) prove that material particles have been drawn from the BLSP and SP respectively while the rough nature of the deformed bubble periphery on the WS as shown in Fig. 6.18(a)(i) is indicative of fluid entrainment at the BLSP. This process continues in Fig. 6.18(b)(iv) where the microdrops dragged from the BLSP are transported further downstream. However, the FS is accelerated and stretched further in the flow direction and eventually disintegrates into smaller sheets (likened to ligaments by Meng and Colonius (2018)). It is also observed that the coalesced fluid particles bounding the air-jet have spread out more laterally perhaps indicative of the greater impact on the LS of the distorted bubble. This then leads to a greater hollowing (compared to Fig. 6.18(a)(iii) and Fig. 6.18(a)(iv)) of the region bounded by the two lips at the SP. This is clearly observable in Fig. 6.18(b)(iii). However, the larger FS drawn from the SP as shown in Fig. 6.18(b)(iv) appear to have shrunk as smaller particles have been stripped from it. The surface roughness of the deformed bubble edges on the WS and LS in Fig. 6.18(b)(ii) has also increased further compared to Fig. 6.18(a)(ii). This shows that more fluid particles are drawn from the BLSP and SP. Similarly, the deformed bubble boundaries appear more corrugated in Fig. 6.18(b)(i) compared to Fig. 6.18(a)(i) indicative of the greater amounts of fluid particles that are dragged from the BLSP and transported downstream. Fig. 6.18(c)(iv) is characterised by the continuous stripping of the smaller FS. The region bounded by the two lips at the SP has deepened more as shown in Fig. 6.18(c)(iii) because the air-jet has expanded more laterally compared to what was observed in Fig. 6.18(b)(iv). The surfaces of the deformed bubble at the LS (Figs. 6.18(c)(ii) & (iii)) and WS (Figs. 6.18(c)(i) & (ii)) also appear to be significantly corrugated. Finally, Fig. 6.18(d)(iv) shows that the stripping at the BLSP and SP has intensified as the microdrops and smaller FS travel downstream occupying a substantial area in the deformed bubble's wake. The region bounded by the two lips at the SP (Fig. 6.18(d)(iii)) appear to be at its deepest compared to the previous set of images because the air-jet has expanded more laterally compared to what was observed in the previous set of images. The surfaces of the deformed bubble at the LS (Figs. 6.18(d)(ii) & (iii)) and WS (Figs. 6.18(d)(i) & (ii)) also appear to be substantially jagged compared to the previous set of images.

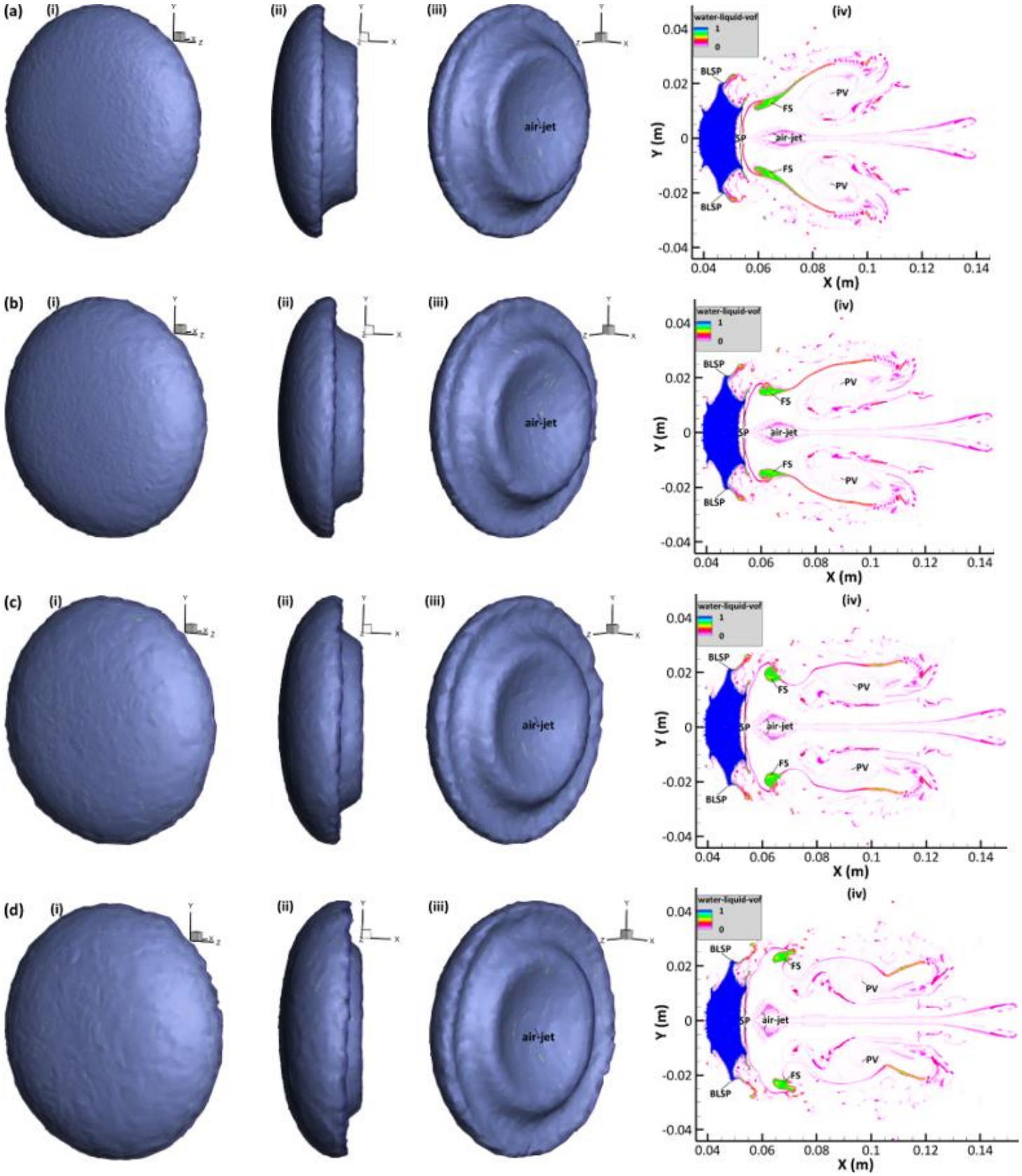

Figure 6.18: (i) – (iii) density iso-surface illustrating BLSP and SP stripping at (a) $\tau = 0.42$; (b) $\tau = 0.43$; (c) $\tau = 0.44$; and (d) $\tau = 0.45$; (iv) volume fraction contours on the central x-y plane revealing BLSP and SP stripping at (a) $\tau = 0.42$; (b) $\tau = 0.43$; (c) $\tau = 0.44$; and (d) $\tau = 0.45$.

Fig. 6.18(a)(iv) show how the two tips close to the equator and two lips bounding the LS, at the top and bottom of the deformed bubble, are entrained downstream into thin filaments. This entrainment continues through Figs. 6.18(b)(iv) and Figs. 6.18(c)(iv) until the filaments appear to be broken in Figs. 6.18(d)(iv). The disintegration of the water bubble via stripping from the onset of SBI is shown in Fig. 6.19.

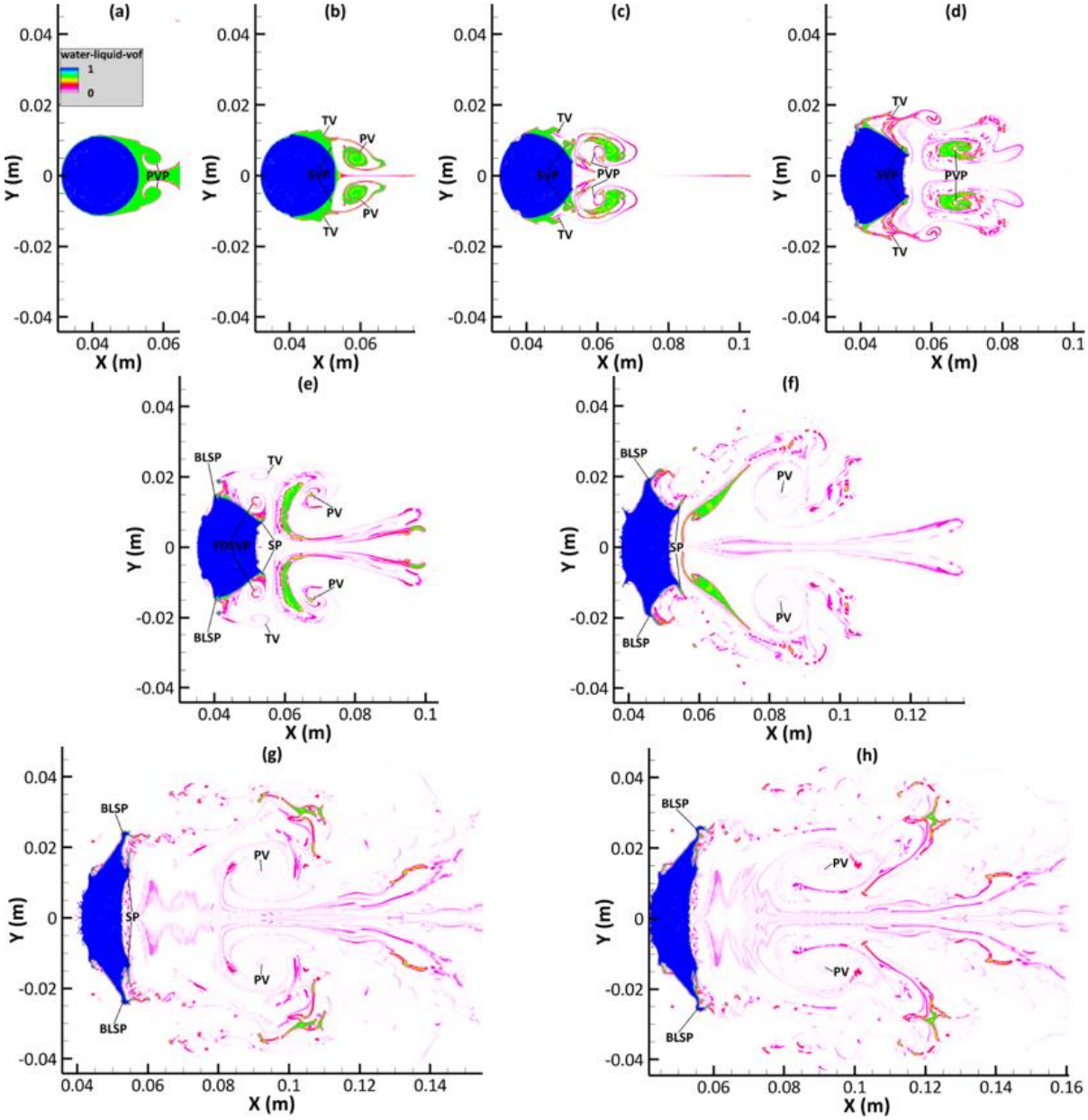

Figure 6.19: Snapshots of volume fraction contours on the central x-y plane at: (a) $\tau = 0.12$; (b) $\tau = 0.17$; (c) $\tau = 0.22$; (d) $\tau = 0.30$; (e) $\tau = 0.34$; (f) $\tau = 0.41$; (g) $\tau = 0.47$; and (h) $\tau = 0.51$.

Fig. 6.19(a) ($\tau = 0.12$) shows the formation of the PVP which are clearly visible at the LS. This PVP are induced by the separation at the BLSP. More fluid materials are stripped from the LS close to the equator to form the TV while the SVP is also seen emerging slightly above the LS stagnation point as seen in Fig. 6.19(b) ($\tau = 0.17$). Fig. 6.19(c) ($\tau = 0.22$) shows the continuous growth and rotation of these three vortices (PV and TV rotate in the same direction while SV rotates in the reverse direction, see Section 6.3.8). The LS is already flat at this stage. Fig. 6.19(d) ($\tau = 0.30$) shows the appearance of two lips on the SP. The PV is now enclosed by a FS which has been stripped from the SP. The region between the two lips on the LS already appears hollow. The FS continues to rotate in Fig. 6.19(e) ($\tau = 0.34$) and in Fig. 6.19(f) ($\tau = 0.41$). The FS in Fig. 6.19(f)

looks slenderer in comparison to that in Fig. 6.19(d) and Fig. 6.19(e) as more fluid particles have been drawn from it. A link can then be made between Fig. 6.19(f) and Fig. 6.18(d)(iv) where the FS in Fig. 6.18(d)(iv) appears smaller compared to Fig. 6.19(f) as a substantial amount of fluid material has been entrained from it. Fig. 6.19(g) and (h) ($\tau = 0.47$ & $\tau = 0.51$ respectively) show that the FS in Fig. 6.18(d)(iv) has further broken up and fragmented into a smaller FS and several microdrops which keep travelling downstream. The SP has also merged with the BLSP in Fig. 6.19(h) with most of the stripping occurring at the BL where microdrops can be seen to be drawn away.

6.3.8. Dynamics of vorticity generation

One of the most essential phases of SBI is the vorticity generation and deposition due to the disparity between pressure and density gradients i.e., baroclinity. As the shock waves propagate through the bubble, vorticity is generated and transported in the flow. Vorticity is so essential in SBI as it, together with aerodynamic forces, principally influences the motion and structure of the bubble (Layes et al., 2003). The vorticity contours are shown in Fig. 6.20.

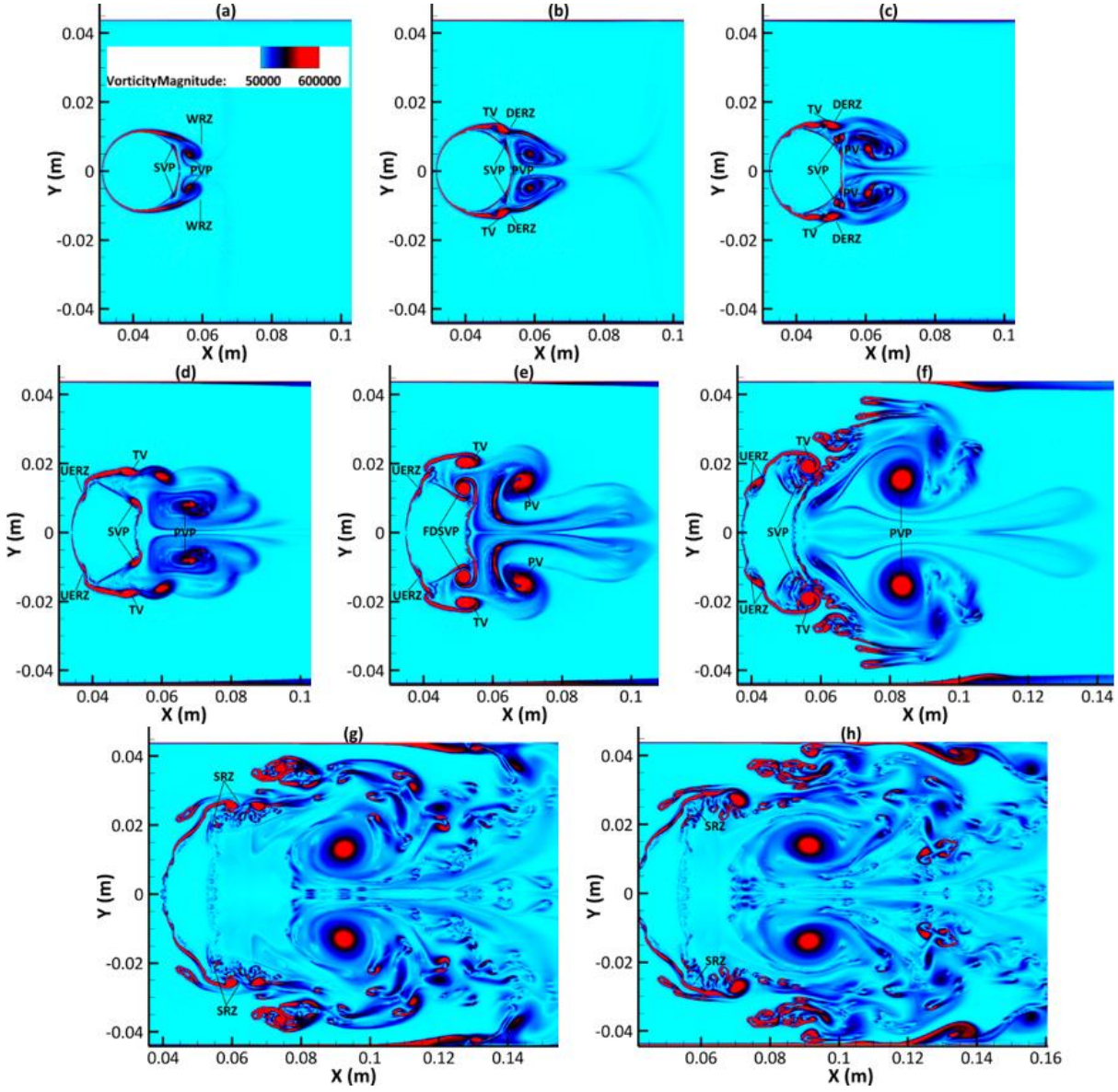

Figure 6.20: Snapshots of vorticity contours on the central x-y plane at: (a) $\tau = 0.12$; (b) $\tau = 0.17$; (c) $\tau = 0.22$; (d) $\tau = 0.30$; (e) $\tau = 0.34$; (f) $\tau = 0.41$; (g) $\tau = 0.47$; and (h) $\tau = 0.51$.

Within Fig. 6.20, the notations SVP, PVP, TV, FDSVP, WRZ, DERZ, UERZ and SRZ denote, secondary vortex pair, primary vortex pair, third vortex, fully developed secondary vortex pair, wake recirculation zone, downstream equatorial recirculation zone, upstream equatorial recirculation zone and sheet recirculation zone respectively. Fig. 6.20 (a) – (h) show the presence of several recirculation zones around the air/water interface mainly concentrated in the wake and equator of the deforming bubble. These zones perform a significant function during the bubble deformation and sheet-stripping process. They are driven by the unsteady vortex shedding at the equator of the deforming bubble. The baroclinic mechanism is responsible for the production of the two vortices (PVP) which are rotating in different directions shown in Fig. 6.20(a). Fig. 6.20(a) ($\tau = 0.12$) also shows the SVP with each SV rotating in the reverse direction to the opposite PV. This unsteady vortex pair (PVP), which has been shed after shock propagation, lead to the formation of the WRZ. Fig. 6.20(b) shows the appearance of TV which rotates in the same direction as PV and has emerged from the equator. As the PV was shed first, it keeps travelling until it is redirected at the LS stagnation point to travel back upstream thus initiating an interaction with another vorticity stream in the vicinity of the equator i.e., TV. This leads to the formation of the DERZ shown in Figs. 6.20(b) and (c) ($\tau = 0.17$ and $\tau = 0.22$). In Figs. 6.20(d), (e) and (f) ($\tau = 0.30,\ \tau = 0.34$, and $\tau = 0.41$), the UERZ is detected at the top and bottom of WS close to the equator. This is due to the local unsteady vortex shedding at the WS which has now been substantially deformed. This deformation of the WS has already been discussed in Section 6.3.6 and the unsteady vortex shedding is linked to the strong shear which is a source of the KH instability. As a result, we can infer that the UERZ formed on the upstream end of bubble in the vicinity of the equator (at $\tau = 0.30,\ \tau = 0.34$, and $\tau = 0.41$) is a result of the interface perturbations on the WS of the deforming bubble. The UERZ can also be seen between the hat-like structure on the WS of the bubble and the evolving liquid sheet at these three times. Figs. 6.20(d), (e) and (f) also show that the position of the UERZ coincide with high vorticity values. As SBI progresses, more vortices are shed leading to the chaotic outlook of the wake as shown in Figs. 6.20(g) and (h). Figs. 6.20(g) and (h) ($\tau = 0.47$ and $\tau = 0.51$) also reveal the emergence of a SRZ at the tip of the water sheet. This recirculation zone is formed from the interaction of the several shed vortices in this region which then causes the tip of the water sheet to flap in the wake of the deformed bubble. The difference between this Section and Section 6.3.11 is that the latter describes the generation and development of turbulence: around the air/water interface, within the evolving vortices; and in the chaotic wake region while this Section presents the emergence and evolution of the produced vortices and recirculation zones.

To understand the direction of rotation of the identified vortices, Fig. 6.21 is presented. The arrows in Fig. 6.21 have been used to indicate the direction of rotation for the generated vortices. Fig. 6.21(a) shows the PVP with the top PV rotating in the clockwise direction while the bottom one rotates in the reverse direction. Fig. 6.21(a) ($\tau = 0.12$) also shows the SVP with the top SV rotating anticlockwise while the bottom one rotates in the clockwise direction. Fig. 6.21(b) ($\tau = 0.17$) shows the emergence of the TV which rotates in the same direction as the PV. As such, we deduced that the SV has a direction of rotation different from that of the PV and TV. As previously stated, detached flow from the interface in the vicinity of the equator, due to the high-speed air flow on the bubble's WS, develops into PV and TV. SV evolves from the re-circulated flow that has been detached from the LS of the deforming water bubble. The complex interaction between the PVP or between the PV and the other vortices (TV and SV) leads to the formation of different re-circulation zones which have been previously discussed. All three different vortices maintain their direction of rotation as seen in Figs. 6.21(c), (d), (e) and (f) (at $\tau = 0.22,\ \tau = 0.30, \tau = 0.34$, and $\tau = 0.41$). Figs. 6.21(g) and (h) ($\tau = 0.47$ and $\tau = 0.51$) show more vortices have been shed. These newly shed vortices are created when the SV and TV collide thus contributing to the chaotic vortex structure in the wake of the deformed liquid sheet. The Figs. 6.21(g) and (h) show the PV, SV and TV which have been transported further downstream. At the end of the frames for both Figs 6.21(g) and (h), two small vortices (at the top and bottom), which have been produced from further stripping at the BLSP, are observed.

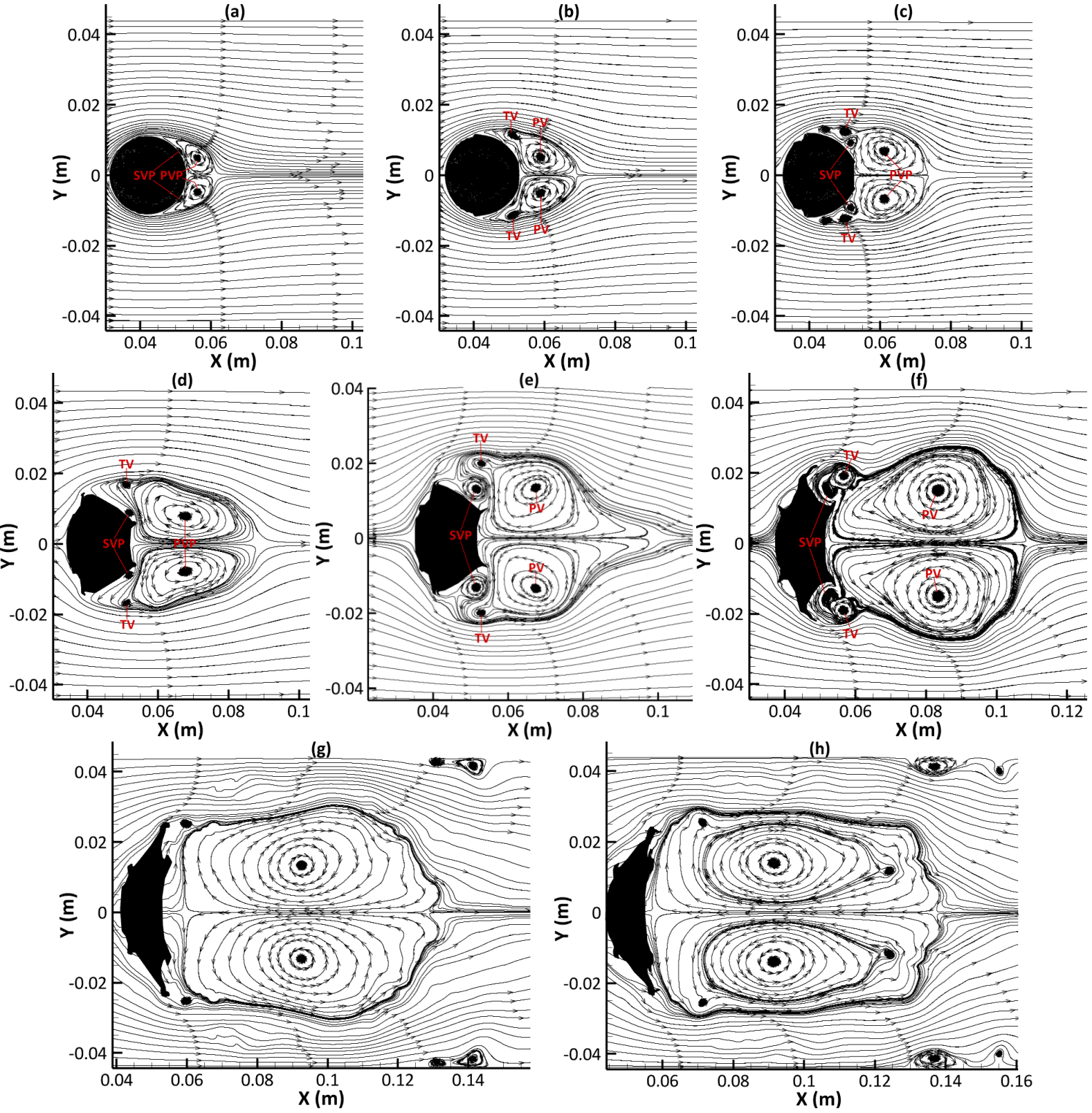

Figure 6.21: Representation of the three principal vortices on the central x-y plane using streamlines at: (a) $\tau = 0.12$; (b) $\tau = 0.17$; (c) $\tau = 0.22$; (d) $\tau = 0.30$; (e) $\tau = 0.34$; (f) $\tau = 0.41$; (g) $\tau = 0.47$; and (h) $\tau = 0.51$.

6.3.9. Pressure distribution within and outside the bubble

A shock wave induced flowfield surrounds the bubble after it is impacted by the ISW. This leads to a disturbance of the water bubble surface. Fig. 6.22 shows the unsteady pressure distribution in the vicinity of the bubble.

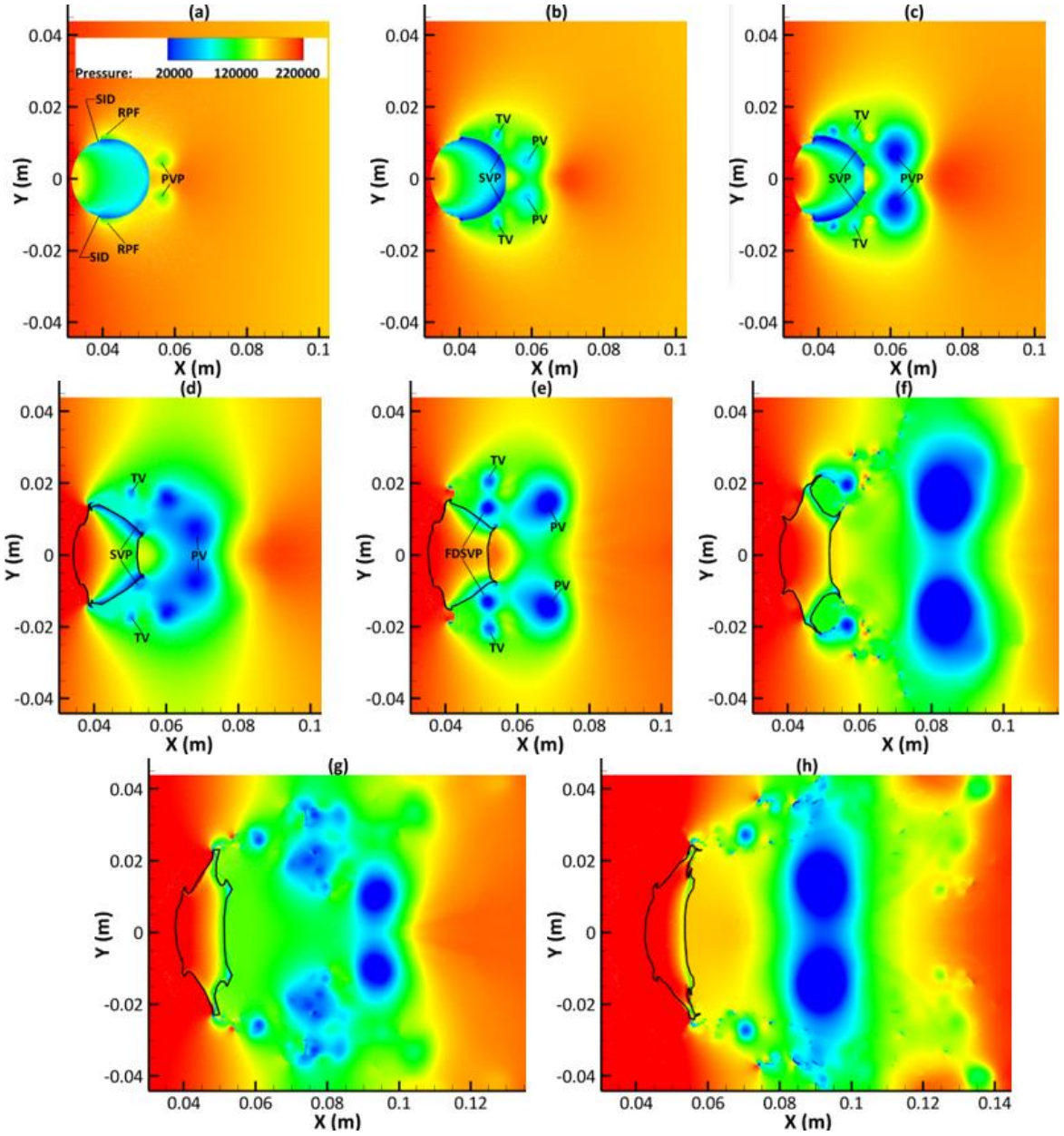

Figure 6.22: Snapshots of pressure contours on the central x-y plane at: (a) $\tau = 0.12$; (b) $\tau = 0.17$; (c) $\tau = 0.22$; (d) $\tau = 0.30$; (e) $\tau = 0.34$; (f) $\tau = 0.41$; (g) $\tau = 0.47$; and (h) $\tau = 0.51$.

SID and RPF as seen on the images represent start of interface perturbation and region of pressure fluctuation respectively. The black isolines seen in Figs. 6.22(d), (e), (f), (g), and (h) surround the region where $\alpha_w \geq 0.9$. These isolines have not been used in Figs. 6.22(a), (b) and (c) because the shape of the distorted bubble is already clearly described in these images. Fig. 6.22(a) ($\tau = 0.12$) shows that the distortion of the water bubble is initiated by the unsteady pressure distribution within and around the bubble. Fig. 6.22(b) shows that the LS of the distorted bubble has started to flatten at $\tau = 0.17$. Similar interface flattening is noticed in Fig. 6.22(c) at $\tau = 0.22$ caused by the non-unform pressure field across the air-water interface. A look at Fig. 6.22(a) also reveals that wavy

interface perturbations emerge and develop on the WS of the bubble close to the equator. This marks the inception of the SID as shown in Fig. 6.22(a) surrounded by the RPF also shown in Fig. 6.22(a). These perturbations are linked to the pressure fluctuations at the air-water interface which are seen close to the equator on the WS. As described in Section 6.3.6, the WS of the deforming bubble represents the region where the interface instabilities develop and as such, can be inferred that the pressure fluctuations match the period during which the interface waves emerge. These interface waves or disturbances are thus initiated by the interaction of the pressure waves (from shock propagation) with the density gradient at the air-water interface. This pressure fluctuations outside and within the bubble continues from when the region between the two SP becomes hollow (Fig. 6.22(d), (e), (f) and (g) at $\tau = 0.30$, $\tau = 0.34$, $\tau = 0.41$ and $\tau = 0.47$ respectively) up to when the water sheet is formed (Fig. 6.22(h) at $\tau = 0.51$). The stagnation pressure contours are also displayed in Fig. 6.23.

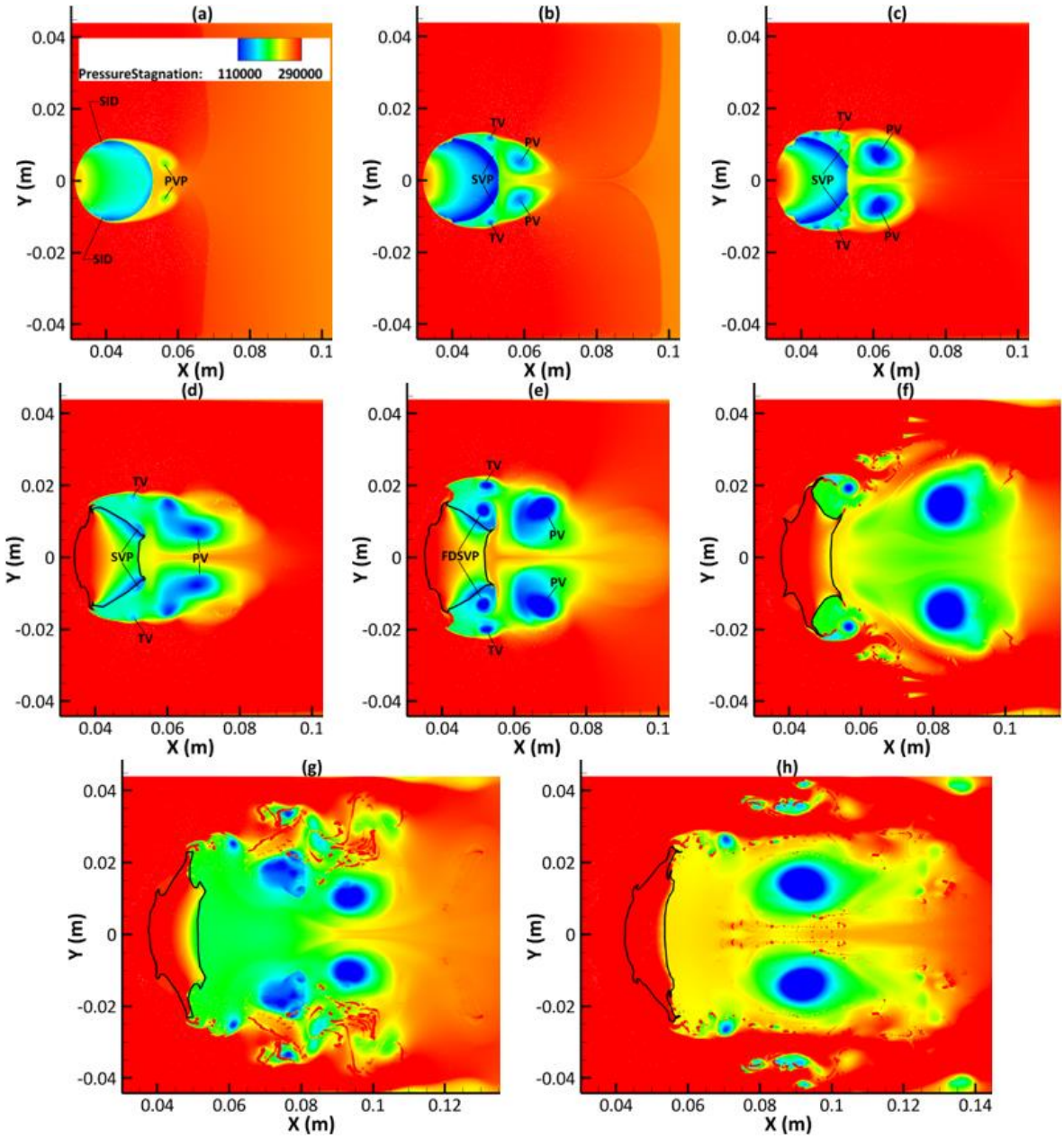

Figure 6.23: Snapshots of stagnation pressure contours on the central x-y plane at: (a) $\tau = 0.12$; (b) $\tau = 0.17$; (c) $\tau = 0.22$; (d) $\tau = 0.30$; (e) $\tau = 0.34$; (f) $\tau = 0.41$; (g) $\tau = 0.47$; and (h) $\tau = 0.51$.

The pressure fluctuations, within and outside the bubble, observed for the contours of static pressure are also seen for the stagnation pressure contours. Similarly, SID is also shown in Fig. 6.23(a) ($\tau = 0.12$). The stagnation pressure contours also show the pressure distribution around the air-jet observable in Figs. 6.23(c), (d), (e), and (f). This is linked to the convergence of the Mach stems in the LS of the cylinder resulting in the formation of the secondary wave system (already discussed in Section 6.3.5). This secondary wave system then produces high pressures. These pressures are continuous along the symmetry of the bubble and acts at the downstream stagnation point leading to bubble flattening. This bubble flattening is noticed in Figs. 6.23(b) and (c) (at $\tau = 0.17$ and $\tau = 0.22$) before the deepening of the region between the two SP (Fig. 6.23(d), (e), (f) and (g) at $\tau = 0.30$, $\tau = 0.34$, $\tau = 0.41$ and $\tau = 0.47$ respectively). The water sheet is then formed as seen in Fig. 6.22(h) ($\tau = 0.51$). Fig. 6.22 and Fig. 6.23 show that for all the displayed images, the high-pressure regions are at the upstream area and far downstream area of the deformed bubble's wake. This far downstream area also represents the zone after the shed vortices. The high-pressure regions are responsible for the compression and flattening of the bubble in the flow direction. The low-pressure regions are situated only slightly above and below the top and bottom of the deformed bubble respectively and close to the equator (see Figs. 6.22(a), (b), (c), (d), and (e) and Figs. 6.23(a), (b), (c), (d), and (e)). These low-pressure regions are responsible for the elongation of the bubble in the lateral direction hence the increase in the bubble height as SBI progresses. However, at $\tau = 0.41$, $\tau = 0.47$ and $\tau = 0.51$, corresponding to Figs. 6.22(f), (g), & (h) and Figs. 6.23(f), (g), & (h) respectively, the pressure just outside the top and bottom of the deformed bubble has increased thus impeding the rate at which the bubble elongates. This is confirmed by Fig. 6.11 where the incremental rate of bubble height begins to decline towards the end of the revealed SBI timeframe.

6.3.10. Velocity distribution within and outside the bubble

The conservation of momentum demands that the tangential viscous stresses be equal in the interface between two immiscible fluids (Meng and Colonius, 2018). This results in the continuity of velocity (Meng and Colonius, 2018). As our study has included the influence of viscosity, the velocity is continuous. This continuous velocity results in the shearing of WS of the bubble as well as the emergence of interfacial instabilities on the same surface. The velocity distribution during the SBI is shown in Fig. 6.24. As explained in Section 6.3.9, the black isolines seen in Figs. 6.24(d), (e), (f), (g), and (h) surround the region where $\alpha_w \geq 0.9$. These isolines have not been used in Figs. 6.24(a), (b) and (c) because the shape of the distorted bubble is already clearly described in these images. As seen from Figs. 6.24(a) to (h), the high-speed regions are mainly at the top and bottom of the deformed bubble. Fig. 6.24(a), at $\tau = 0.12$, show that the low-speed regions are seen on the left and right of the bubble as well as within the bubble. However, from Figs. 6.24(b) to (h) (from $\tau = 0.17$ to $\tau = 0.51$), there are high-speed zones which are situated between the bubble (including its immediate low-speed environs on the LS) and the far flowfield region i.e., towards the end of the wake region. This middle high-speed region grows in both lateral and streamwise extent as SBI continues. The high-speed regions, at the top and bottom of the deformed bubble, travel downstream as SBI progresses as shown by how the red zones spread from Figs. 6.24(a) to (h) (from $\tau = 0.12$ to $\tau = 0.51$). The high-speed regions at the top and bottom of the bubble are responsible for the lateral stretching of the bubble from Figs. 6.24(a) to (h). Figs. 6.24(d) to (h) (from $\tau = 0.30$ to $\tau = 0.51$) show that the fluid particles that are entrained downstream and jet back upstream to impact on the LS of the bubble travel at a low speed compared to the velocity at the top and bottom of the deformed water bubble.

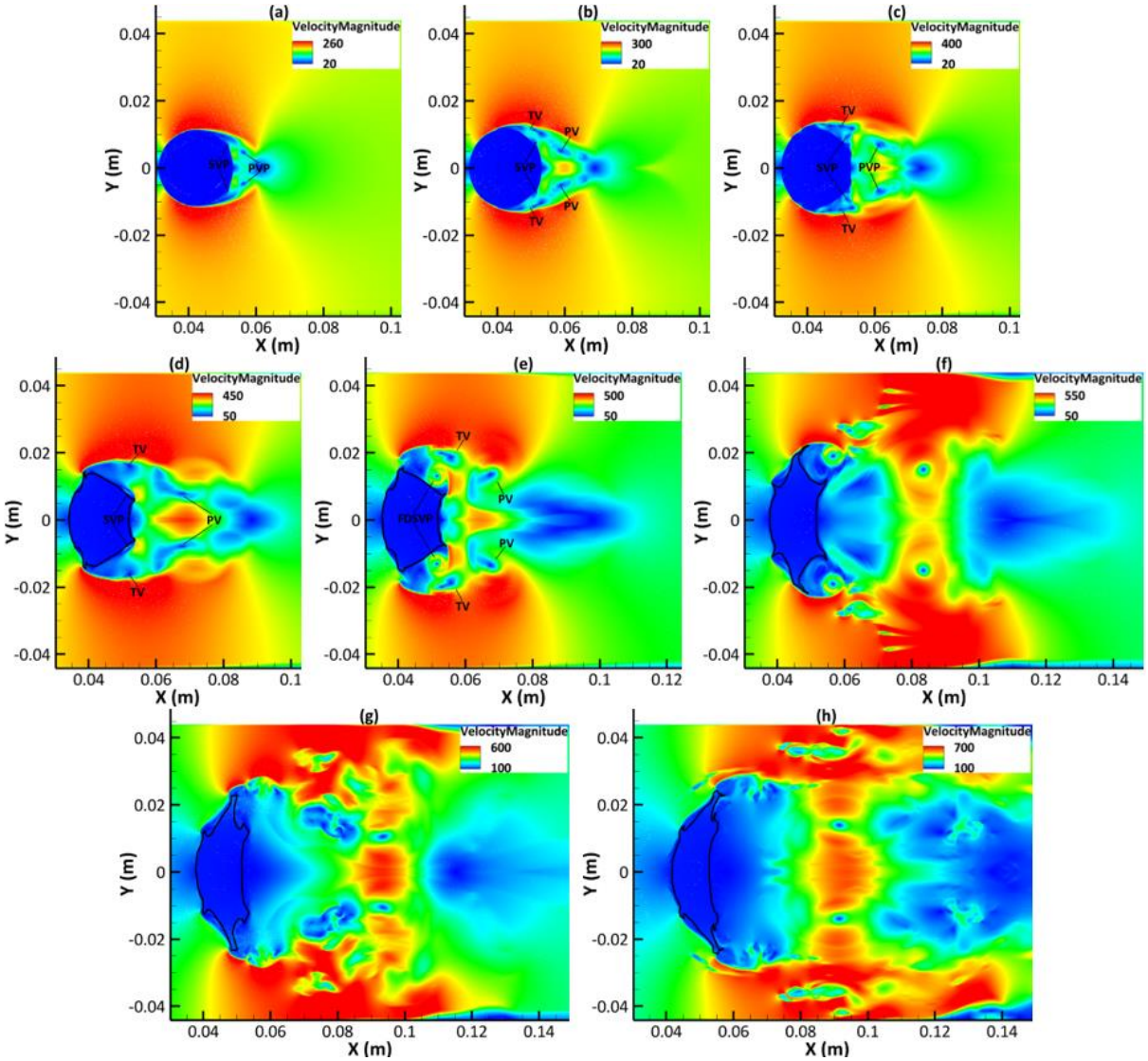

Figure 6.24: Velocity contours on the central x-y plane at: (a) $\tau = 0.12$; (b) $\tau = 0.17$; (c) $\tau = 0.22$; (d) $\tau = 0.30$; (e) $\tau = 0.34$; (f) $\tau = 0.41$; (g) $\tau = 0.47$; and (h) $\tau = 0.51$.

6.3.11. Generation and development of turbulence

Tomkins *et al*. (2003) explained that the KH instabilities could combine to evolve the flow into a state of turbulence. It has been shown that the shock bubble interaction process entails a wide range of complicated characteristics, from transition of regular reflection to Mach reflection, generation and transport of vortices, to the air-jet impacting the LS and the subsequent formation of the water sheet. Nevertheless, to the best knowledge of this research, there are rarely any previous experimental and numerical studies that have addressed one very important aspect of the shock liquid bubble interaction process – turbulence generation and development. Fig. 6.25 shows contours of turbulence intensity. It can be seen from Fig. 6.25(a) that turbulence starts to be generated initially in a small region in the LS extending from the equator to the location of the PV at a quite early stage ($\tau = 0.12$) with the maximum turbulence intensity starting at 13%. As time progresses, the bubble interface is deformed, as shown in Figs. 6.25(b) and (c) at $\tau = 0.17$ and $\tau = 0.22$ respectively. At both times, interfacial instabilities are observable on the WS while the LS is gradually becoming flat due to the interaction between the produced vortices. The maximum turbulence intensity values that match these two figures are 14% and 16% respectively and are observed around the SVP, TV and DERZ. Fig. 6.25(d) shows the region bounded by two lips (at the

SP). This region caves in as seen in Figs. 6.25(d), (e) and (f) due to the impact of the air-jet. The maximum values of turbulence intensity corresponding to these three times (i.e., $\tau = 0.30$, $\tau = 0.34$, and $\tau = 0.41$) are 17%, 18% and 19% respectively and are situated around the UERZ, TVP, FDSVP, SVP and wake region. Figs. 6.25(b),(c) and (d) show that turbulence is concentrated along the path of fluid stripped from the BLSP close to the equator. Figs. 6.25(e) and (f) ($\tau = 0.34$, and $\tau = 0.41$) also show that turbulence is also concentrated in the path of fluid mass (FS) entrained from the SP. This persists till high turbulence areas continue to travel downstream along the path of entrained fluid materials from the BLSP and SP. This is shown in Fig. 6.25(g) ($\tau = 0.47$) where the maximum intensity reaches 20% around the SRZ and wake region. Fig. 6.25(h), which takes place at $\tau = 0.51$, shows that the SP has merged with the BLSP with maximum turbulence regions travelling along the path of entrained particles from the BLSP. The maximum turbulence is 22% around the SRZ, wake region and diametral plane. Figs. 6.25(f), (g) and (h) also show high turbulence areas along the diametral plane indicative of the entrained downstream fluid that have been jet back upstream.

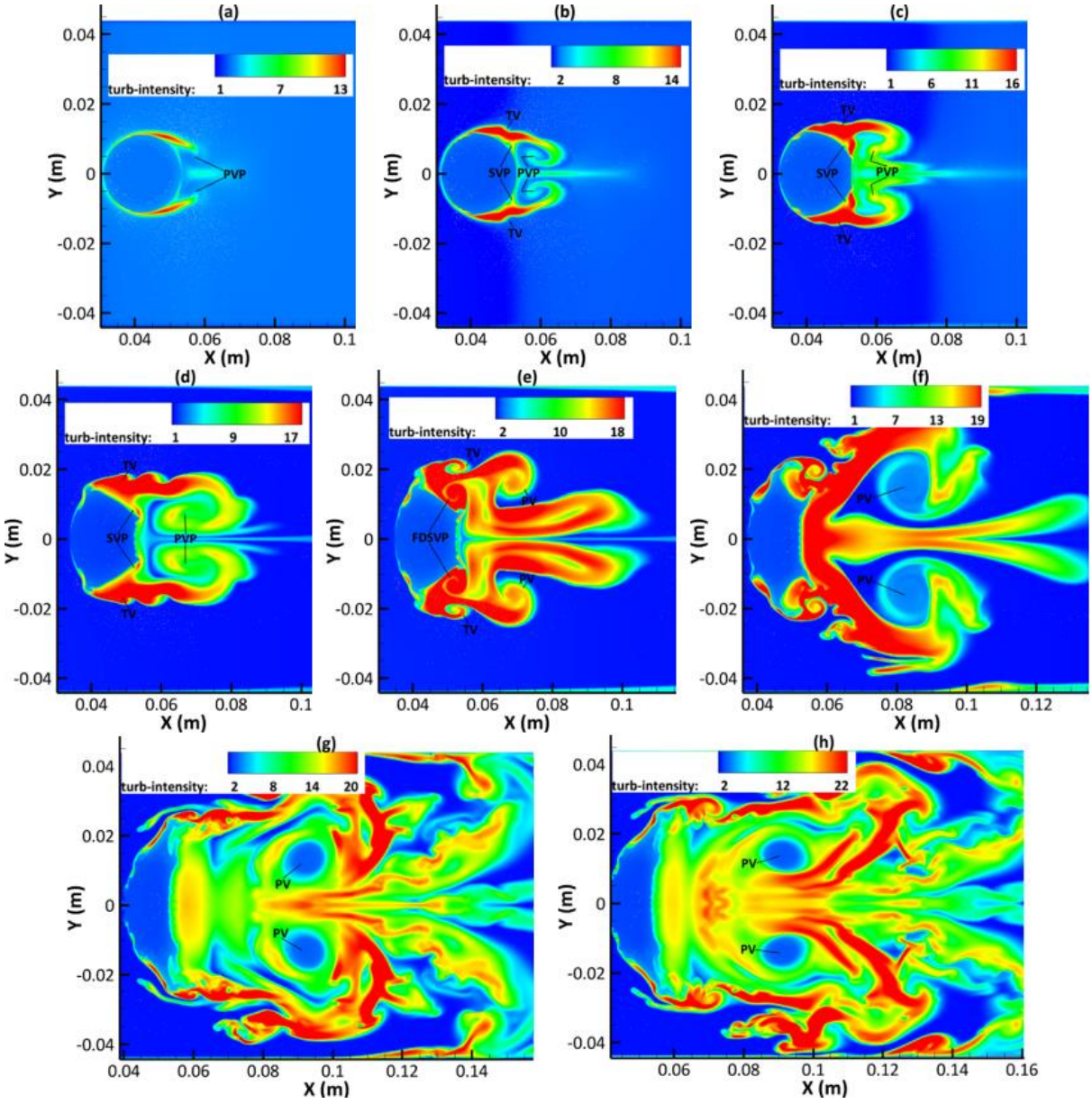

Figure 6.25: Contours of turbulence intensity on the central x-y plane at: (a) $\tau = 0.12$; (b) $\tau = 0.17$; (c) $\tau = 0.22$; (d) $\tau = 0.30$; (e) $\tau = 0.34$; (f) $\tau = 0.41$; (g) $\tau = 0.47$; and (h) $\tau = 0.51$.

This research also observed that the turbulence intensity values within the PV, for Figs. 6.25(f) (g) and (h), was lower compared to the turbulence intensity values in the other vortices at previous times. This observation was explained using the contours of volume fraction in Fig. 6.19. At the earlier times i.e., $\tau = 0.12, 0.17, 0.22, 0.30$ and 0.34, the turbulence intensity values of PV, SV and TV are close to the maximum turbulent values in the respective frames because $\alpha_w \geq 0.5$ (which means that microdrops of water exist within these vortices. However, within the PV at $\tau = 0.41, 0.47,$ and 0.51, $\alpha_w \approx 0$, which means little or no microdrops of water exist in the vicinity of PV hence the smaller turbulence intensity values. For these times, the microdrops of water are entrained from the BLSP (Figs. 6.25(f) (g) & (h)) and SP (Figs. 6.25(f) & (g)). The difference between this Section and Section 6.3.8 is that the latter details the inception and evolution of the produced vortices and recirculation zones while this Section presents the generation and development of turbulence: around the air/water interface, within the evolving vortices; and in the chaotic wake region.

With respect to the development of the air-jet, Figs. 6.26(a) & (b) (i), (ii), (iii), (iv) and (v) reveal the position of the air-jet using contours of vorticity, turbulence intensity, stagnation pressure, velocity, and the density iso-surfaces at $\tau = 0.38$ and 0.39 respectively. Figs. 6.26(a) (i), (ii), (iii) and (iv) show that after the PV, SV and TV have been shed, this vortical setup draws downstream fluid particles into a jet which is redirected upstream so that it impacts the LS of the deformed bubble. Fig. 6.26(a)(v) show the caved in region bounded by the SP after it is impinged by the air-jet. A similar level of detail is shown in Figs. 6.26(b) (i), (ii), (iii) and (iv) with Fig. 6.26(b)(v) showing a greater level of compression compared to Fig. 6.26(a)(v).

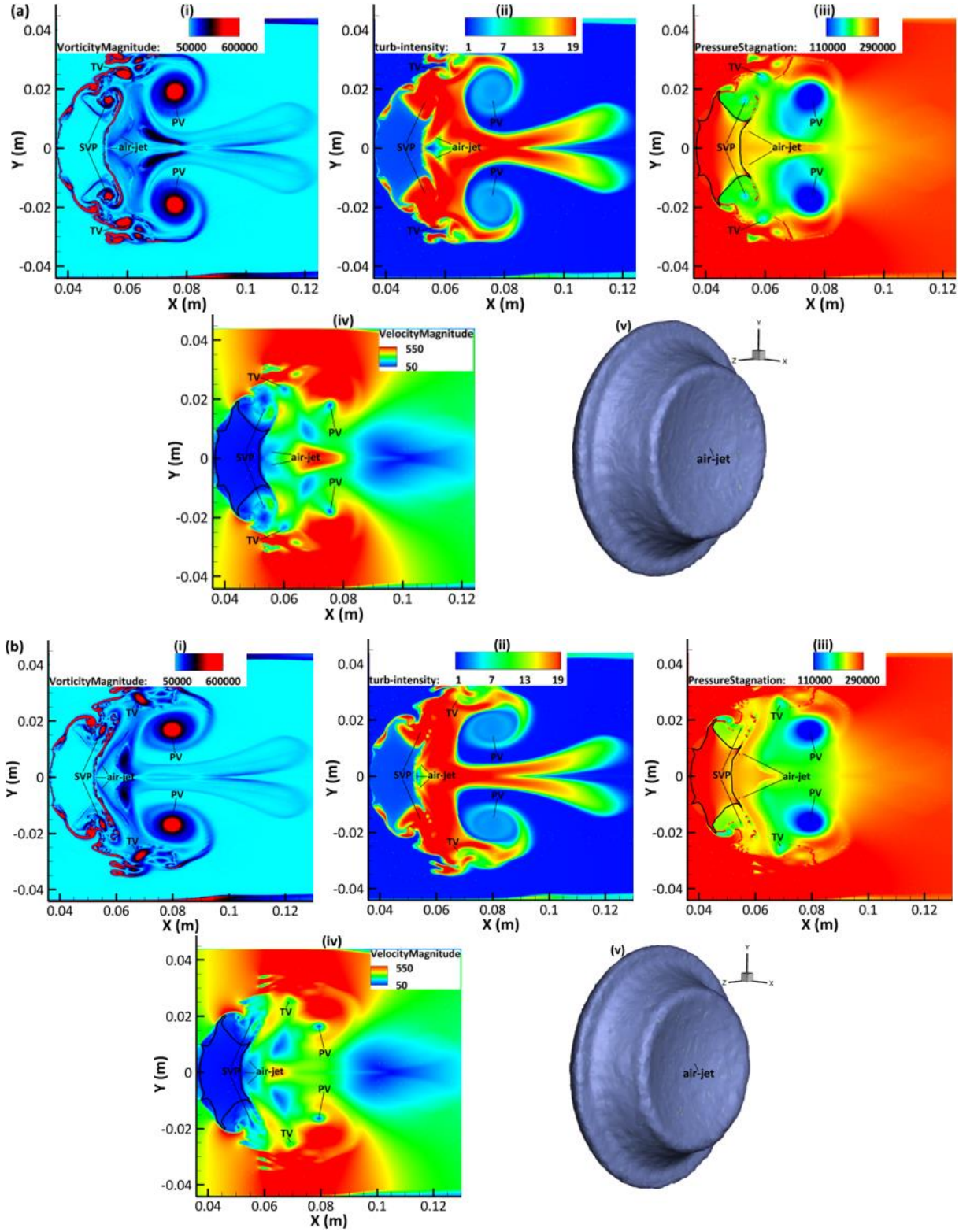

Figure 6.26: (a) Air-jet visualisation using: (i) contours of vorticity; (ii) turbulence intensity; (iii) stagnation pressure; (iv) velocity; and (v) density iso-surfaces at $\tau = 0.38$; (b) Air-jet visualisation using: (i) contours of vorticity; (ii) turbulence intensity; (iii) stagnation pressure; (iv) velocity; and (v) density iso-surfaces at $\tau = 0.39$. Figs. 6.26 (a)(i)-(iv) and (b)(i)-(iv) have been plotted on the central x-y plane.

6.3.12. Late-time stripping at the BLSP

Fishburn (1974) and Wierzba & Takayama (1988) used the term 'boundary-layer separation' or boundary layer stripping' to describe the entrainment of materials or microdrops from the BLSP on the WS of the deformed bubble close to the equator. Fig. 6.27 show how fluid materials are continuously stripped from the boundary layer which has now flapped.

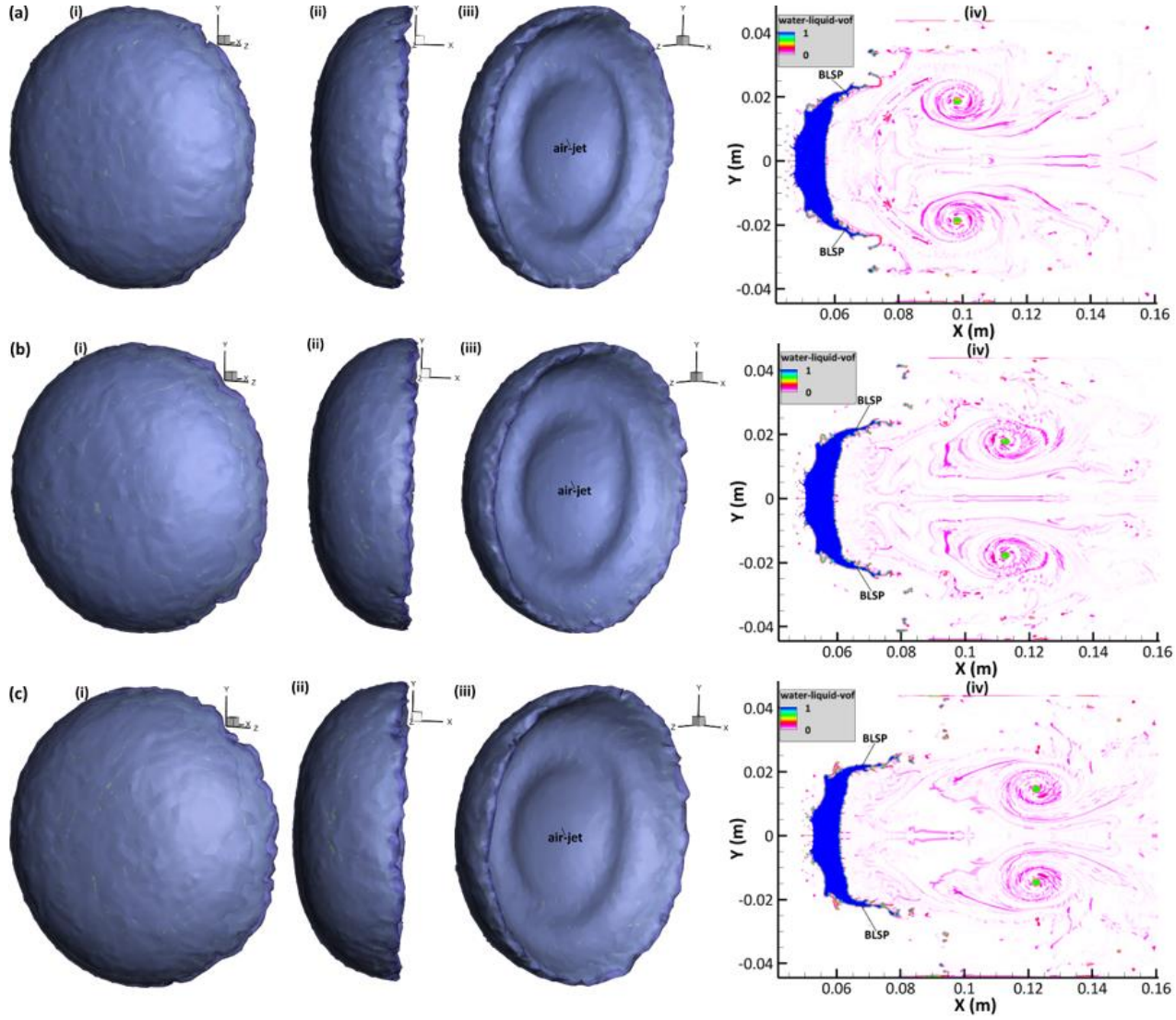

Figure 6.27: (i) – (iii) density iso-surfaces illustrating late time BLSP stripping at (a) $\tau = 0.60$; (b) $\tau = 0.64$; and (c) $\tau = 0.68$; (iv) volume fraction contours on the central x-y plane revealing late time stripping at BLSP at (a) $\tau = 0.60$; (b) $\tau = 0.64$; and (c) $\tau = 0.68$.

Fig. 6.27(a)(iv) shows that in the LS of the deformed bubble, more unsteady vortex shedding yields a more chaotic and complex wake compared to Fig. 6.19(h). Fig. 6.27(a)(iii) reveals that the water sheet has become significantly hollow while the jagged edges of the bubble in Figs 6.27(a)(i) and (ii) is proof that a substantial amount of microdrops has been drawn away from BLSP. The thin FS seen travelling downstream in Fig. 6.19(h) is advected further downstream when it is acted upon by strongly fluctuating forces in the wake of the deformed cylinder. This small FS eventually breaks up to yield smaller fluid particles. There is an increase in the compression of the bubble as SBI progresses such that Fig. 6.27(b)(iii) and Fig. 6.27(c)(iii) are significantly more deepened than Fig. 6.27(a)(iii) due to the persistent effect of the air-jet. Similarly, the corrugations of the bubble

periphery in Figs. 6.27(b)(i)(ii) & (iii) and Figs. 6.27(c)(i)(ii) & (iii) appear to be at its most in comparison to the observed border waviness in Figs. 6.27(a)(i)(ii) & (iii).

6.3.13. Analysis of bubble breakup time

Pilch and Erdman (1987) explained that for sheet stripping, the first indication of a sheet being drawn downstream from the bubble denotes breakup initiation. They suggested a simple empirical correlation which sufficiently denotes the required time to induce breakup for viscous and non-viscous bubbles i.e., dimensionless breakup initiation time, τ_i. This is shown in Eq. (6.23).

$$\tau_i = 1.9(We - 12)^{-0.25}(1 + 2.2.On^{1.6}) \tag{6.23}$$

Using Eq. (6.23) yields $\tau_i = 0.14$. For this research, the first indication of fluid materials being drawn from the bubble surface is observed in Fig. 6.19(a) at $\tau = 0.12$. This is close to the computed τ_i derived from Eq. (6.23). This shows the accuracy of the current numerical model.

Liu et al. (2018) defined the non-dimensional breakup time as:

$$\tau_b = \frac{\mathrm{T}_b.U_{g,2}}{\mathrm{d}}\sqrt{\frac{\rho_{g,2}}{\rho_l}} \tag{6.24}$$

where T_b and τ_b denotes the dimensional and dimensionless total breakup time respectively. Pilch and Erdman (1987) described the total breakup time as the time when the bubble (if a 'coherent' one continues downstream) and all its fragments do not suffer any more breakup. Breakup results and definitions vary from one experiment to another depending on the visualization technique employed (see Engel, 1958; Nicholls and Ranger, 1968; Pilch and Erdman, 1987; and Theofanous, 2011). For some of these experiments and depending on the experimental instruments used, it was difficult to differentiate the remaining portion of the liquid bubble from mists which yielded a greater breakup time taking into consideration the streamwise diameter of the deformed bubble. For example, the works of Engel (1958) and Nicholls & Ranger (1968) estimated τ_b to be roughly 5 while Theofanous et al. (2012), who defined the total breakup time as the total loss of the bubble's physical coherence using laser-induced fluorescence (LIF), stated that τ_b varied from 0.6 to 2 in SIE breakup regime under various conditions. From a numerical perspective, Liu et al. (2018), who defined Eq. 6.24, stated that τ_b is approximately 1. To determine τ_b for this numerical research, it is seen that the material fragments that are drawn from the bubble periphery (either at the BLSP and SP) continue to undergo further disintegration and fragmentation as they travel downstream for all the displayed contours of volume fraction (Fig. 6.19). However, at $\tau = 0.68$, it appears like the coherent water sheet and the fragments which have been drawn from the BLSP no longer undergo further breakup i.e., there is little difference between the wake regions observed in Fig. 6.27(b)(iv) and Fig. 6.27(c)(iv). Also, there is little or no difference in the morphology of the deformed bubble observed in Fig. 6.27(b)(i)(ii) & (iii) and Fig. 6.27(c)(i)(ii) & (iii). However, both images (Fig. 6.27(b)(iii) and Fig. 6.27(c)(iii)) show more compression of the LS and waviness of bubble peripheries in comparison to Fig. 6.27(a)(iii). This research then concludes that total breakup occurs at around $\tau = 0.68$. This value for τ_b falls within the range which Theofanous et al. (2012) obtained for the SIE regime under various conditions. This section confirms the thoughts of Liu et al. (2018) who explained that the results for τ_b are not exact in past experimental measurements or numerical simulations and that the reason for defining τ_b is to typically evaluate the bubble disintegration time even though various definitions yield slightly conflicting results. In summary, the bubble breakup procedure has been effectively represented in Figs. 6.15, 6.16, 6.17, 6.18, 6.19 and 6.27. It is also very useful to point out that since the bubble distortion can be characterized as quasi-stable based on the Bo (see Section 6.3.6), there will not be an unstable shattering of the WS. This is supported by the research of Harper et al. (1972) who explained that the unstable shattering of the WS only takes place beyond the quasi-stable regime i.e., $\mathrm{Bo} > 10^5$, where the acceleration effect controls the disintegration of the water bubble. Lastly all the qualitative results presented are 3D as Fig. 6.5

revealed that the 3D simulations have captured the complex shock water bubble interaction more accurately and there was no need to present the 2D results.

6.4. Conclusions

The stripping type breakup regime which is of key interest in this research has been examined using numerical simulations. This breakup mechanism is typified by a distortion of the water bubble into a sheet-like shape. After the shape of the deformed bubble has changed, fluid particles are observed to be dragged away from the bubble's edges at the BLSP close to the equator by the high-speed surrounding air flow. This led to an instability of the BLSP at the distorted bubble's equator where two tips are formed at the top and bottom of the bubble. These tips are dragged into thin filaments which then break as they are advected downstream. Baroclinic mechanism also leads to the production of two counter-rotating vortices after which more vortices are shed. The deformed bubble is then flattened by the pressure gradient between the stagnation points (at the WS and LS of the bubble) and the equator. The emergence of two lips at the SP is also observed after the deformed bubble is flattened. Afterwards, strong inertial forces from the ambient flow drag a thin sheet of fluid (FS) from the edges of the LS of the bubble at the SP. This sheet is accelerated, stretched, and curved in the flow direction and eventually disintegrates into smaller sheets (likened to ligaments by Meng and Colonius (2018)). These sheets then eventually break up and fragments into smaller particles or microdrops. This research also likened the stripping type breakup model to the SIE disintegration regime which Theofanous (2008) described as a mixture of shear-propelled radial movements that lead to compression and flattening as well as instabilities on the elongated liquid sheet. This research also showed that turbulence is relevant when it comes to the breakup of the liquid sheet as well as the subsequent disintegration of the fluid fragments that are entrained from the liquid sheet's periphery.

With respect to quantitative numerical estimations, the predicted displacement/drift, acceleration, distortion in the lateral direction, distortion in flow direction, area variation from bubble distortion, and drag coefficient agree well with experimental data. Qualitative images for pressure, velocity, phase distribution, turbulence intensity and vorticity are also presented. The time dependent mechanisms portrayed by these images are very consistent with process of bubble stripping and breakup available in previous literature. This research summarized the bubble distortion and breakup process into three stages: instability of the bubble surface, compression of the leeward side of the deforming water bubble, and intense entrainment of small masses from liquid sheet as well as the formation of the bowl-shaped sheet. The bubble was also believed to attain total breakup at $\tau = 0.68$ as it appeared like the coherent water sheet and the fragments which had been drawn from the BL no longer underwent further breakup or fragmentation. Generally, this research was able to resolve the terminal disintegration and fragmentation of the thin FS drawn from the SP. Also, the flow structure and evolution of the chaotic wake are also well resolved. Finally, our numerical method and AMR application have reproduced the most resolution dependent features like the fine-scale interfacial instabilities (interface structure) on the WS, entrainment of small-scale liquid structures from bubble periphery, recirculation zones as well as the formation of the hat-like structure at the WS and a water sheet at the LS.

7. Conclusions and Future Work

7.1. Summary and conclusions

This project has investigated pressure gain using shock-bubble (gas and liquid bubble) interaction (SBI). When vorticity is deposited on a bubble surface by a shock wave due to SBI, the bubble surface is distorted which leads to changes in its surface area. As this deformation increases due to shock refraction of any perturbation previously present in the gas interface, the Richtmyer–Meshkov instability (RMI) is formed. This RMI with growing interface distortion leads to secondary instabilities like the Kelvin–Helmholtz shear instability which further evolves to improve mixing and turbulence (Batley et al., 1996). This research has then studied and understood shock wave interaction (with a gas/liquid bubble) via a detailed computational fluid dynamics (CFD) investigation. From a SBI perspective, positive impacts can be achieved for gas turbine engines particularly with respect to a rise in bubble pressure and an increase in turbulence intensity. Increase in bubble stagnation pressure has been presented in Fig. 6.23 where the stagnation pressure within the bubble has been shown to rise across the bubble, from the WS, upon shock impact and propagation (see Fig. 6.23(a) to Fig. 6.23(h). Similarly, increase in turbulence intensity has also been achieved as shown in Figs 4.19, 5.17 and 6.25. The CFD investigations involve the performance of numerical simulations using the Unsteady Reynolds-Averaged Navier-Stokes (URANS) mathematical model and the coupled level set and VOF method within the commercial CFD code, ANSYS FLUENT. A finite volume method (FVM) is employed in FLUENT to solve the governing equations.

These simulations show that the physical mechanisms taking place during the SBI process are very complicated and elucidated certain aspects of SBI which have not been fully researched in previous studies. These areas are the generation and development of turbulence at the SBI later stages as well as the evolution of vortex filaments/vortex rings/vortices from inception to the later phases. From the presented numerical predictions, this research has plugged the knowledge gaps present in these areas. The numerical simulations have been performed in 2D and 3D representations of the shock tube to depict the interaction of a planar shock wave with distinct gas and liquid inhomogeneities. The three scenarios considered cover the interaction of a planar shock wave with: spherical helium bubble; cylindrical helium bubble and cylindrical water bubble. The gas in the spherical (Mach number, Ma = 1.25) and cylindrical gas bubbles (Ma = 1.22) is helium with air serving as the ambient gas. This is in accordance with the experimental work of Haas and Sturtevant (1987). The surrounding gas employed in the cylindrical water bubble (Ma = 1.47) case is air in accordance with the experimental work of Igra et al. (2002).

For the shock spherical helium bubble interaction scenario, the predicted velocities of refracted wave, transmitted wave, upstream interface, downstream interface, jet and vortex ring agree very well with the relevant available experimental data. The predicted non-dimensional bubble and vortex velocities are also in much better agreement with the experiment data than values computed from a simple model of shock-induced Rayleigh-Taylor instability (the Richtmyer–Meshkov instability). Generally, the 2D and 3D results show a good agreement with the theoretical predictions and experiments, but the 3D predictions are much closer to the theoretical estimations and experimental measurements. This strongly indicates that 3D simulations are necessary in order to capture SBI process accurately. Other quantitative assessment conducted involved comparing the predicted temporal variations of the bubble length and width as well as the produced vortex sizes and vortex pair spacing with that measured in past experimental works. A good agreement between the predictions of the current study and the experimental data has been obtained. It is also noticed in this research that the bubble length initially decreases due to bubble compression before increasing due to an increase in the bubble length in the lateral direction after the air-jet pierces the downstream interface and the downstream ring emerges. The upstream ring height initially increases corresponding to the bubble compression which resulted in bubble elongation in the vertical direction. This is followed by a very gradual rise in

this parameter after which it dropped in connection to the increasing height of the downstream ring. The height of the downstream ring continuously increases albeit at different incremental rates. Finally, these sets of comparisons revealed that the upstream ring height, downstream ring height, horizontal upstream ring size, vertical upstream ring size, upstream vortex pair spacing and downstream vortex pair spacing tend towards a constant value. The final quantitative assessment conducted involved comparing the predicted piston and vortex ring circulations to the experimentally measured ones. This research's estimations show a very good agreement with the experimental measurements with the order of the computed Reynolds number i.e., 10^5, proving that the generated vortex rings are turbulent.

For the shock cylindrical helium bubble case, 2D and 3D simulations have been conducted, and this research showed that the 3D predictions are much closer to the experimentally measured data, with an excellent concordance observed between the predicted velocities of the incident wave, refracted wave, transmitted wave, upstream interface, downstream interface, jet, vortex filament and the corresponding measured values. The predicted dimensionless jet interface velocity is also compared with both the Rayleigh Taylor Theory, for estimating the growth rate of small sinusoidal perturbations, and past experimental results. Both the 2D and 3D results show a good agreement with the theoretical predictions and experiments. As in the previous comparisons, the 3D predictions are much closer to the theoretical estimations and experimental measurements. The final quantitative assessment conducted involved comparing the predicted temporal variations of the interfacial characteristic scales, i.e., the length and width of the evolving interface with that measured in past experimental works. There is a good agreement between the 2D/3D predictions and the experimental data, but the 3D estimations are more representative of the early shock acceleration and bubble distortion as they show shorter lengths (hence more compression) during the early SBI phases. A similar trend is noticed for the width of the developing interface where the 3D predictions are greater than the 2D predictions at early SBI times. This indicated that an increased compression would cause the deforming bubble to become vertically elongated hence the greater 3D predictions compared with the 2D predictions.

For the shock cylindrical water bubble interaction case, the predicted displacement/drift, acceleration, distortion in the lateral direction, distortion in flow direction, area variation from bubble distortion, and drag coefficient agree well with experimental data. Qualitative images for pressure, velocity, phase distribution, turbulence intensity and vorticity are also presented. The time dependent mechanisms portrayed by these images are very consistent with the process of bubble stripping and breakup available in previous literature. In summary, the shock/water bubble interaction case shows that the water bubble is preliminarily compressed in the streamwise direction with this compression visible on the downstream (leeward) end of the bubble. The deformed bubble extends along the equator with tips created at the top and bottom of cylinder's edge which are dragged downstream by the ambient air flow. Lips are also formed on the downstream edge of the deforming bubble. This research designated these tips and lips as BLSP and SP respectively. This research also attributes the stripping of material at the liquid column's edge to the presence of recirculation regions at the equator shown clearly on the qualitative images for phase distribution. These recirculation regions are believed to result from interaction of two oppositely directed streams of vorticity created by the effects of baroclinity on the deforming water surface. Finally, this research demonstrates that the bubble distortion can be divided into three phases: instability of the bubble surface; flattening of water bubble; and entrainment of small droplets from the edge of the water sheet up till the total breakup of the bubble.

Finally, this research explores the positive impacts of SBI particularly with respect to a rise in turbulence intensity. To do this, comprehensive flow visualization has been used to explain the shock-bubble interaction (SBI) process i.e., onset of bubble compression, formation of the vortex filaments or vortex rings (for the cylindrical or spherical helium bubble cases respectively), as well as production and distribution of vorticity. For the water bubble case, flow visualisation helps to explain the SBI process i.e., start of bubble compression, entrainment of small subsize droplets from the bubble periphery and total fragmentation of the water bubble. The visualization of turbulence generation and development provides further intricate details of the SBI flowfield such as small flow structures and

turbulent mixing between the helium bubble and air at the later stage of SBI for the spherical and cylindrical helium bubble cases. A comprehensive development of the vortex filaments/vortex rings (for the cylindrical or spherical bubble case respectively) from formation to a full distinctive structure is also illustrated using flow visualisation. In particular, it is demonstrated for the first time that turbulence is generated at the early phase of the shock bubble interaction process before the air jet is formed in all three cases, with the maximum turbulence intensity reaching about 20%, around the vortex filaments/vortex rings regions, and 22% for the water bubble scenario at the later phase of the interaction process.

7.2. Future work

The good agreement levels between the numerical findings presented in this research and previous experimental measurements show that the employed numerical model represent a reliable and effective method to characterise the shock-bubble interaction process. As a result, in the future, an interesting extension of this research would be to perform similar SBI simulations using other readily available hydrocarbon fuels like kerosene that can be utilised in gas turbines. Shock flame interactions (SFI), which represent a sustainable and hugely beneficial technique for achieving pressure gain combustion in gas turbines, is another area that the current research can be extended to. Such research will provide valuable insight into the interaction between a shock wave and a pre-mixed flame. Very limited research exists in this field particularly with respect to the repeated interaction of a shock wave with an already deformed flame which possesses the potential to considerably boost thermodynamic pressure rise. Also, there is a significant variation between the interaction of travelling shock waves with dispersed reactive mixture in comparison to the SFI process involved in pre-mixed combustion. Thus, this necessitates further research which the employed numerical method is capable of handling. Finally, this research can be extended to investigate the impacts of the chemical reactivity of the mixture components on flame structure, development, and distortion as SFI progresses. This could potentially yield beneficial results particularly with respect to the variability of the reactive mixture adopted for SFI.

References

Aalburg, C., van Leer, B. and Faeth, G.M. (2003) 'Deformation and drag properties of round drops subjected to shock-wave disturbances', *AIAA Journal*, Vol. 41(12), 2371 – 2378.

Abd-el-fattah, A.M., Henderson, L.F. and Lozzi, A. (1976) 'Precursor shock waves at a slow-fast Gas interface', *Journal of Fluid Mechanics*, Vol. 76, pp. 157 – 176.

Abd-el-fattah, A.M. and Henderson, L.F. (1978a) 'Shock waves at a fast slow interface', *Journal of Fluid Mechanics*, Vol. 86, pp. 15 – 32.

Abd-el-fattah, A.M. and Henderson, L.F. (1978b) 'Shock waves at a slow fast gas interface', *Journal of Fluid Mechanics*, Vol. 89, pp. 79 – 95.

Anderson Jr, J.D. (1995) Computational Fluid Dynamics: The Basics with Applications, McGraw-Hill, New York.

Anderson Jr, J.D. (2003) Modern compressible flow with historical perspective, 3rd edition, McGraw-Hill Education, New York.

ANSYS (2018) Fluent user's guide, Release 19.0 ANSYS, Inc., Southpointe, 2600 ANSYS Drive, Canonsburg, PA 15317.

ANSYS (2018) Fluent theory guide, Release 19.0 ANSYS, Inc., Southpointe, 2600 ANSYS Drive, Canonsburg, PA 15317.

Akbari, P. and Müller, N. (2003) 'Performance Investigation of Small Gas Turbine Engines Topped with Wave Rotors', 39th AIAA/ASME/SAE/ASEE Joint Propulsion Conference and Exhibit, AIAA 2003-4414, Huntsville, Alabama, USA.

Akbari, P. and Nalim, M.R. (2009) 'Review of recent developments in wave rotor combustion technology', *AIAA Journal of Propulsion and Power*, Vol. 25 (4), pp. 833 – 844.

Anderson Jr, J.D. (1995) Computational fluid dynamics: The basics with applications. McGraw-Hill Education.

Aris, R. (2012) Vectors, tensors and the basic equations of fluid mechanics. Courier Corporation.

Arnett, W.D., Bahcall, J.N., Kirshner, R.P. and Woosley, S.E. (1989), 'Supernova 1987A', *Annual Review of Astronomy and Astrophysics,* Vol. 27, pp. 629 – 700.

Arnett, D. (2000) 'The role of mixing in astrophysics', *Astrophysical Journal Supplement*, Vol. 127, pp. 213 – 217.

Atkins, T. and Escudier, M. (2013) A Dictionary of Mechanical Engineering, 1st Edition, Oxford University Press.

Batchelor, R.K. (2000) An Introduction to Fluid Dynamics. Cambridge University Press.

Bagabir, A. and Drikakis, D. (2001) 'Mach number effects on shock-bubble interaction', *Shock Waves*, Vol. 11, pp. 209 – 18.

Ball, G.J. and East, R.A. (1999) 'Shock and blast attenuation by aqueous foam barriers: influence of barrier geometry', *Shock Waves, Vol.* 9, pp. 37 – 47.

Baltrusaitis, R.M., Gittings, M.L., Weaver, R.P., Benjamin, R.F. and Budzinski, J.M. (1996) 'Simulations of shock-generated instabilities', *Physics of Fluids*, Vol. 8, pp. 2471 – 2483.

Barth, T.J. and Jespersen, D. (1989) 'The design and application of upwind schemes on unstructured meshes'. Technical Report AIAA-89-0366. AIAA 27th Aerospace Sciences Meeting, Reno, Nevada.

Batley, G.A., McIntosh, A.C. and Brindley, J. (1996) 'The baroclinic effect in combustion', *Mathematical and Computer Modelling*, Vol. 24(8), pp. 165 – 176.

Bauer, S.G. (1958) 'Improved gas generator and method for generating combustion gas under pressure', Patent, 858,601.

Bell, J.B., Berger, M.J., Saltzman, J.S. and Welcome, M. (1994) 'Three-dimensional adaptive mesh refinement for hyperbolic conservation laws', *SIAM Journal on Scientific Computing*, Vol. 15, pp. 127– 138.

Berger, M., Aftosmis, M.J. and Allmaras, S.R. (2012) 'Progress towards a cartesian cut-cell methods for viscous compressible flow', 50th AIAA Aerospace Sciences Meeting Including the New Horizons Forum and Aerospace Exposition Jan. 9-12, Nashville, TN.

Berger, M.J. and Colella, P. (1989) 'Local adaptive mesh refinement for shock hydrodynamics', *Journal of Computational Physics*, Vol. 82, pp. 67 – 84.

Berger, M.J. and Oliger, J. (1984) 'Adaptive mesh refinement for hyperbolic partial differential equations', *Journal of Computational Physics*, Vol. 53, pp. 482 – 512.

Betro, V.C. (2010) 'Fully anisotropic split-tree adaptive refinement mesh generation using tetrahedral mesh stitching', Ph.D. thesis, University of Tennessee, Chattanooga.

Brill, D. and Uberall, H. (1970) 'Transmitted waves in the diffraction of sound from liquid cylinders', *The Journal of the Acoustical Society of America*, Vol. 47, pp. 1467 – 1469.

Bockhoff, M. and Rauch, D. (1973) 'Visualization and piezoelectric recording of the ultrasonic field within shock-loaded head- and container-models', 1973 Ultrasonics Symposium Proceedings, IEEE Cat. 73 CHO 807-8SU.

Brackbill, J.U., Kothe, D.B. and Zemach, C. (1992) 'A continuum method for modeling surface tension', *Journal of Computational Physics*, Vol. 100, pp. 335 – 354.

Brouillette M. (2002) 'The Richtmyer-Meshkov instablity', *Annual Review of Fluid Mechanics*, Vol. 34, pp. 445 – 468.

Budzinski, J.M., Benjamin, R.F. and Jacobs, J.W. (1994) 'Influence of initial conditions on the flow patterns of a shock-accelerated thin fluid layer', *Physics of Fluids*, Vol. 6, pp. 3510 – 3512.

Cameron Jr., T.D. (2011) 'An adaptive hybrid mesh generation method for complex geometries', A thesis submitted to the faculty of the University of Tennessee, Chattanooga in Partial fulfilment of the requirements for the Degree of Master of Science in Computational Engineering.

Catherasoo, C.J. and Sturtevant, B. (1983) 'Shock dynamics in non-uniform media', *Journal of Fluid Mechanics*, Vol. 127, pp. 539 – 561.

Chen, H. (2008) 'Two-dimensional simulation of stripping breakup of a water droplet', *AIAA Journal*, Vol. 46(5), pp. 1135 – 1143.

Chen, J., Qu, F., Wu, X., Wang, Z. and Bai, J. (2021) 'Numerical study of interactions between shock waves and a circular or elliptic bubble in air medium', *Physics of Fluids*, Vol. 33, pp. 043301-1 – 043301-15.

Chou, W.-H. and Faeth, G.M. (1998) 'Temporal properties of secondary drop breakup in the bag breakup', *International Journal of Multiphase Flow*, Vol. 24, pp. 889 – 912.

Chou, W.-H., Hsiang, L.P. and Faeth, G.M. (1997) 'Temporal properties of drop breakup in the shear breakup regime', *International Journal of Multiphase Flow*, Vol. 23(4), pp. 651 – 669.

Collins, T.J.B., Poludnenko, A., Cunningham, A. and Frank, A. (2005) 'Shock propagation in deuterium-tritium-saturated foam', *Physics of Plasmas*, Vol. 12, pp. 062705.

Cowperthwaite, N. (1989) 'The interaction of a plane shock and a dense spherical inhomogeneity', *Physica D*, Vol. 37, pp. 264 – 269.

Dai, Z. and Faeth, G.M. (2001) 'Temporal properties of secondary drop breakup in the multimode breakup regime', *International Journal of Multiphase Flow*, Vol. 27(2), pp. 217 – 236.

Dalal, A., Eswaran, V. and Biswas, G. (2008) 'A finite-volume method for Navier-Stokes equations on unstructured meshes', *Numerical Heat Transfer*, Part B, Vol. 54, pp. 238 – 259.

Daly, B.J. and Harlow, F.H. (1970) 'Transport equations in turbulence', *Physics of Fluids*, Vol. 13, pp. 2634 – 2649.

Davidson, L. (1996) 'A pressure correction method for unstructured meshes with arbitrary control volumes', *International Journal for Numerical Methods in Fluids*, Vol. 22, pp. 265 – 281.

Davy, B.A. and Blackstock, D.T. (1971) 'Measurements of the refraction and diffraction of a short N wave by a gas-filled soap bubble', *The Journal of Acoustical Society of America*, Vol. 49, pp. 732 – 737.

Delale, C.F., Nas, S. and Tryggvason, G. (2005) 'Direct numerical simulations of shock propagation in bubbly liquids', *Physics of Fluids*, Vol. 17, pp. 121705.

Delery, J.M. (1983) 'Experimental investigation of turbulence properties in transonic shock wave/boundary-layer interaction', *The American Institute of Aeronautics and Astronautics*, Vol. 21, pp. 180 – 185.

Delius, M., Ueberle, F. and Eisenmenger, W. (1998) 'Extracorporeal shock waves act by shock wave-gas bubble interaction', *Ultrasound in Medicine and Biology*, Vol. 24, pp. 1055 – 59.

Demirdzic, I. and Muzaferija, S. (1995) 'Numerical method for coupled fluid flow, heat transfer and stress analysis using unstructured moving meshes with cells of arbitrary topology', *Computational Methods in Applied Mechanics and Engineering*, Vol. 125, pp. 235 – 255.

Deshpande, K.B. and Zimmerman, W.B. (2006) ‘Simulation of interfacial mass transfer by droplet dynamics using the level set method’, *Chemical Engineering Science*, Vol. 61, pp. 6486 – 6498.

Didden, N. (1979) ‘On the formation of vortex rings: Rolling-up and production of circulation’, *Zeitschrift für angewandte Mathematik und Physik ZAMP*, Vol. 30, pp. 101 – 116.

Diegelmann, F., Hickel, S. and Adams, N.A. (2017) ‘Three-dimensional reacting shock-bubble interaction’, *Combustion and Flame*, Vol. 181, pp. 300 – 314.

Dimotakis, P.E. Samtaney, R. (2006) ‘Planar shock cylindrical focusing by a perfect-gas lens’, *Physics of Fluids*, Vol.18, pp. 031705.

Ding, Z. and Gracewski, S.M. (1996) ‘The behaviour of a gas cavity impacted by a weak or strong shock wave’, *Journal of Fluid Mechanics*, Vol. 309, pp. 183 – 209.

Ding, J., Liang, Y., Chen, M., Zhai, Z., Si, T. and Luo, X. (2108) ‘Interaction of planar shock wave with three-dimensional heavy cylindrical bubble’, *Physics of Fluids*, Vol. 30, pp. 106109-1 – 106109-13.

Ding, J., Si, T., Chen, M., Zhai, Z., Lu, X. and Luo, X. (2017) ‘On the interaction of a planar shock with a three-dimensional light gas cylinder’, *Journal of Fluid Mechanics*, Vol. 828, pp. 289 – 317.

Eisenmenger, W. (2001) ‘The mechanisms of stone fragmentation in ESWL’, *Ultrasound in Medicine and Biology*, Vol. 27, pp. 683 – 693.

Eliasson, P. (2001) ‘EDGE a Navier-Stokes solver for unstructured grids’, Scientific Report, FOI-R-0298-SE.

Emery, M.H., Gardner, J.H., Boris, J.P. and Cooper, A.L. (1984) ‘Vortex shedding due to laser ablation’, *Physics of Fluids*, Vol. 27, pp. 1338.

Engel, O.G. (1958) ‘Fragmentation of water drops in the zone behind an air shock’, *Journal of Research of the National Bureau of Standards*, Vol. 60(3), pp. 245 – 280.

Enright, D., Fedkiw, R. Ferziger, J. and Mitchell. I. (2002) ‘A hybrid particle level set method for improved interface capturing’, *Journal of Computational Physics*, Vol. 183(1), pp. 83 – 116.

Eugen, L. (2014) ‘Pressure-gain combustion for gas turbines based on shock-flame interaction’ AIAA’s Pressure Gain Combustion Program Committee. Available at: https://elib.uni-stuttgart.de/handle/11682/3963. (Accessed: 29 August 2023).

Fan, E., Guan, B., Wen, C.H. and Shen, H. (2019) ‘Numerical study on the jet formation of simple-geometry heavy gas inhomogeneities’, *Physics of Fluids*, Vol. 31, pp. 026103-1 – 026103-11.

Ferziger, J.H. and Peric, M. (2012) Computational methods for fluid dynamics. Springer Science & Business Media.

Fishburn, B.D. (1974) ‘Boundary layer stripping of liquid drops fragmentated by Taylor instability’, *Acta Astronautica*, Vol. 1(9 – 10), pp. 1267 – 1284.

Folds, D.L. (1971) ‘Target strength of focused liquid-filled spherical reflectors’, *The Journal of the Acoustical Society of America,* Vol. 49, pp. 1596 – 1599.

Friedlander, F.G. (1958) Sound Pulses. Cambridge University Press.

Garrick, D.P., Owkes, M. and Regele, J.D. (2017) 'A finite-volume HLLC-based scheme for compressible interfacial flows with surface tension', *Journal of Computational Physics*, Vol. 339, pp. 46 – 67.

Garrick, D.P., Hagen, W.A. and Regele, J.D. (2017) 'An interface capturing scheme for modeling atomization in compressible flows', *Journal of Computational Physics*, Vol. 344, pp. 260 – 280.

Garrick, D.P., Hagen, W.A. and Regele, J.D. (2019) 'Secondary atomization of liquid columns in compressible crossflows', arXiv:1906.04307v2 [physics.flu-dyn].

Gemmen, R.S., Richards, G.A. and Janus, M.C. (1994) 'Development of a pressure gain combustor for improved cycle efficiency', presented at the ASME COGEN Turbo Power '94 Congress and Exposition, IGTI-Vol. 9.

Gemmen, R.S., Janus, M.C., Richards, G.A., Norton, T.S., and Rogers, W.A. (1995) 'Achieving improved cycle efficiency via pressure gain combustors', In ASME Turbo Expo, 95-GT-63: International gas turbine and aeroengine congress and exposition, Houston, Texas, United State, 5 – 8, June. Available at: https://www. https://www.osti.gov/servlets/purl/42810. (Accessed: 20 March 2024)

Gel'fand, B.E. (1996) 'Droplet breakup phenomena in flows with velocity lag', *Progress in Energy and Combustion Science*, Vol. 22, pp. 201 – 265.

George, P.E. and Corliss, J.M. (1988) 'Development of a rotary valve for pulse combustion applications -- Final Report', Gas Research Institute Contract Number 5086-234-1280, October 31.

Georgievskiy, P.Y., Levin, V.A. and Sutyrin, O.G. (2018) 'Shock focusing in the interaction with a local area of increased gas density', *Fluid Dynamics*, Vol. 53(6), pp. 835 – 842.

Gerhold, T., Friedrich, O. Evans, J. and Galle, M. (1997) 'Calculation of complex three-dimensional configurations employing the DLR-TAU code', 35th Aerospace Sciences Meeting and Exhibit, AIAA 97-0167, Reno, NV.

Gibson, M.M. and Launder, B.E. (1978) 'Ground effects on pressure fluctuations in the atmospheric boundary layer', *Journal of Fluid Mechanics*, Vol. 86, pp. 491 – 511.

Giordano, J. and Burtschell, Y. (2006) 'Richtmyer-Meshkov instability induced by shock-bubble interaction: numerical and analytical studies with experimental validation', *Physics of Fluids*, Vol. 18, pp. 036102.

Gordon, S. and McBride, B.J. (1976) 'Computer program for computation of complex chemical equilibrium compositions, rocket performance, incident and reflected shocks, and Chapman–Jouguet detonations', Spec. Publ. SP-273. Lewis Research Center, NASA.

Gracewski, S.M., Dahake, G., Ding, Z., Burns, S.J. and Everbach, E.C. (1993) 'International stress wave measurements in solids subjected to lithotripter pulses', *Journal of the Acoustical Society of America*, Vol. 94, No. 2, Pt. 1, pp. 652 – 661.

Grasso, F. and Pirozzoli, S. (1999) ‘Shock-wave-vortex interactions: shock and vortex deformations, and sound production’, *Theoretical and Computational Fluid Dynamics*, Vol. 13, pp. 421 – 56.

Greenough, J.A. and Jacobs, J.W. (1996) ‘A numerical study of shock-acceleration of a diffuse helium cylinder. In Proceedings of 5th International Workshop for Compressible Turbulent Mixing, ed. Young, R., Glimm, J. and Boston, B. pp. 338 – 345. Singapore: World Sci.

Gulen, S. (2017) ‘Pressure gain combustion advantage in land-driven electric power generation’, *Journal of the Global Power and Propulsion Society*, Vol. 1, pp. 288 – 302.

Haas, J.F.L. (1983) ‘Wave propagation and Rayleigh-Taylor instability in non-uniform gases’, *Bulletin of the American Physical Society*, Vol. 28, pp. 1359.

Haas, J.F.L. (1984) ‘Interaction of weak shock waves and discrete gas inhomogeneities’. Ph.D. Thesis, California Institute of Technology.

Haas, J.F.L. and Sturtevant, B. (1987) ‘Interaction of weak shock waves with cylindrical and spherical inhomogeneities’, *Journal of Fluid Mechanics*, Vol. 181, pp. 41 – 76.

Hanjalic, K. (2005) ‘Will RANS survive LES? a view of perspectives’, *Journal of fluids engineering*, Vol. 127(5), pp. 831 – 839.

Hansen, J.F., Robey, H.F., Klein, R.I. and Miles, A.R. (2007) ‘Experiment on the mass-stripping of an interstellar cloud in a high Mach number post-shock flow’, *Physics of Plasmas*, Vol. 14, pp. 056505.

Hanson, A.R., Domich, E.G. and Adams, H.S. (1963) ‘Shock tube investigation of the breakup of drops by air blasts’, *Physics of Fluids*, Vol. 6, pp. 1070 – 1080.

Harper, E.Y., Grube, G.W. and Chang, I.-D. (1972) ‘On the breakup of accelerating liquid drops’, *Journal of Fluid Mechanics*, Vol. 52(3), pp. 565 – 591.

Harten, A. (1983) ‘High resolution schemes for hyperbolic conservation laws’, *Journal of Computational Physics*, Vol. 49, pp. 357 – 393.

Hasselbacher, A., McGuirk, J.J., and Page, G.J. (1999) ‘Finite volume discretization aspects for viscous flows on mixed unstructured grids’, *AIAA Journal*, Vol. 37(2), pp. 177 – 184.

Heffer, J.H., and Miller, R. (2009) ‘Performance of choked unsteady ejector-nozzles for use in pressure-gain combustors’, 47th AIAA Aerospace Sciences Meeting Including the New Horizons Forum and Aerospace Exposition, Orlando, Florida, US.

Heiser, W.H. and Pratt, D.T. (2002) ‘Thermodynamic cycle analysis of pulse detonation engines’, AIAA *Journal of Propulsion and Power*, Vol. 18(1).

Henderson, L.F. (1966) ‘The refraction of a plane shock wave at a gas interface’, *Journal of Fluid Mechanics*, Vol. 26, pp. 607 – 637.

Henderson, L.F. (1989) ‘On the refraction of shock waves’, *Journal of Fluid Mechanics*, Vol. 198, pp. 365 – 86.

Henderson, L.F., Colella, P. and Puckett, E.G. (1991) ‘On the refraction of shock waves at a slow-fast gas interface’, *Journal of Fluid Mechanics*, Vol. 224, pp. 1 – 27.

Henkes, R.A.W.M., van der Flugt, F.F. and Hoogendoom, C.J. (1991) 'Natural convection flow in a square cavity calculated with low-reynolds-number turbulence models', *International Journal of Heat and Mass Transfer*, Vol. 34, pp. 1543 – 1557.

Hillier, R. (1991) 'Computation of shock wave diffraction at a ninety degrees convex edge', *Shock Waves*, Vol. 1(2), pp. 89 – 98.

Hinze, J.O. (1955) 'Fundamentals of the hydrodynamic mechanism of splitting in dispersion processes', *American Institute of Chemical Engineers Journal*, Vol. 1, pp. 289 – 295.

Hinze, J.O. (1975) Turbulence. McGraw-Hill Publishing Co., New York.

Hirahara, H., and Kawahashi, M., (1992) 'Experimental Investigation of Viscous Effects Upon a Breakup of Droplets in High-Speed Air Flow', *Experiments in Fluids*, Vol. 13(6), pp. 423 – 428.

Holleman, R., Fringer, O. and Stacey, M. (2013) 'Numerical diffusion for flow-aligned unstructured grids with application to estuarine modelling', *International Journal for Numerical Methods in Fluids*, Vol. 72(11), pp. 1117 – 1145.

Houghton, E.L. and Brock, A.E. (1993) Tables for the compressible flow of dry air, 3rd edition, Butterworth-Heinemann. ISBN-13**:** 9780-713133523.

Hsiang, L.-P. and Faeth, G.M. (1992) 'Near-limit drop deformation and secondary breakup," *International Journal of Multiphase Flow,* Vol. 18(5), pp. 635 – 652.

Hsiang, L.-P. and Faeth, G.M. (1995) 'Drop deformation and breakup due to shock wave and steady disturbances', *International Journal of Multiphase Flow*, Vol. 21(4), pp. 545 – 560.

Hwang, U., Flanagan, K. A., and Petre, R. (2005) 'Chandra X-Ray observation of a mature cloud-shock interaction in the bright eastern knot region of puppis A', *The Astrophysical Journal*, Vol. 635, pp. 355.

Igra, D., Ogawa, T. and Takayama, K. (2002) 'A parametric study of water column deformation resulting from shock wave loading', *Atomization and Sprays*, Vol. 12(5–6), pp. 577 – 591.

Igra, D., and Takayama, K. (2001) 'Investigation of aerodynamic breakup of a cylindrical water droplet', *Atomization and Sprays*, Vol. 11(2), pp. 167 – 185.; also Reports of the Institute of Fluid Science, Vol. 11, 1999, pp. 123 – 134.

Igra, D. and Takayama, T. (2003) 'Experimental investigation of two cylindrical water columns subjected to planar shock wave loading', *Journal of Fluids Engineering*, Vol. 125(2), pp. 325 – 331.

Igra, D. and Sun, M. (2010) 'Shock-water column interaction, from initial impact to fragmentation onset', *AIAA Journal*, Vol. 48, pp. 2763 – 2771.

Ingram, D.M., Causon, D.M. and Mingham, C.G. (2013) 'Developments in Cartesian cut cell methods', *Mathematics and Computers in Simulations*, Vol. 61, pp. 561 – 572.

Jacobs, J.W. (1992) 'Shock-induced mixing of a light-gas cylinder', *Journal of Fluid Mechanics*, Vol. 234, pp. 629 – 649.

Jacobs, J.W. (1993) 'The dynamics of shock accelerated light and heavy gas cylinders', *Physics of Fluids*, A5.

Jacobs, J.W., Klein, D.L., Jenkins, D.G. and Benjamin, R.F. (1993) 'Instability growth patterns of a shock-accelerated thin fluid layer', *Physical Review Letters*, Vol. 70, pp. 583 – 586.

Jahn, R.G. (1956) 'The refraction of shock waves at a gaseous interface', *Journal of Fluid Mechanics*, Vol. 1, pp. 457-489.

Jalaal, M. and Mehravaran, K. (2014) 'Transient growth of droplet instabilities in a stream', *Physics of Fluids*, Vol. 26, pp. 721 – 725.

Jamaluddin, A.R., Ball, G.J. and Leighton, T.J. (2005) 'Free-Lagrange simulations of shock/bubble interaction in shock wave lithotripsy. In *Shock Waves: Proc. 24th Int. Symp. Shock Waves*, ed. Jiang, Z.L. pp. 1211–16. Berlin: Springer.

Jameson, A. (1995) 'Positive schemes and shock modelling for compressible flows', *International Journal for Numerical Methods in Fluids*, Vol. 20(8 – 9), pp. 743 – 776.

Jameson, A. and Mavriplis, D. (1986) 'Finite volume solution of the two-dimensional Euler equations on a regular triangular mesh', *AIAA Journal*, Vol. 24(4), pp. 611 – 618.

Jiang Y. and Przekwas, A.J. (1994) 'Implicit pressure-based incompressible navier-stokes equations solver for unstructured meshes', *AIAA-94-0305*.

Johnson, M.W. (2013) 'A novel cartesian CFD cut cell approach', *Computer and Fluids*, Vol. 79, pp. 105 – 119.

Jones, D.S. (1978) 'Acoustic tunnelling', *Proceedings of the Royal Society of Edinburgh Section 81 A*, pp. 1-21.

Joseph, D.D., Belanger, J., and Beavers, G.S. (1999) 'Breakup of a liquid drop suddenly exposed to a high-speed airstream', *International Journal of Multiphase Flow*, Vol. 25 (6 – 7), pp. 1263 – 1303.

Joseph, D.D., Beavers, G.S. and Funada, T. (2002) 'Rayleigh-Taylor instability of viscoelastic drops at high Weber numbers', *Journal of Fluid Mechanics*, Vol. 453, pp. 109 – 132.

Ju, Y., Shimano, A. and Inoue, O. (1998) 'Vorticity generation and flame distortion induced by shock flame interaction', 27th Symponium (International) on Combustion/The Combustion Institute, pp. 735 – 741.

Kaiser, J.W.J, Winter, J.M., Adami, S. and Adams, N.A. (2020) 'Investigation of interface deformation dynamics during high-weber number cylindrical droplet breakup', *International Journal of Multiphase Flow*, Vol. 132, pp. 1 – 15.

Keller, J.B. (1955) 'Diffraction by a convex cylinder'. URSZ Mich. Symposium on Electro Magnetic Wave Propagation.

Keller, J.B. (1958) 'A geometrical theory of diffraction', Proceedings of Symposia in Applied Mathematics, Vol. 7, Calculus of Variations and its Applications. McGraw-Hill.

Kelvin, W.T. (1871) ‘Hydrokinetic solutions and observations’, *Philosophical Magazine*, Vol. 42, pp. 362 – 377.

Kentfield, J.A.C., Rehman, A. and Cronje, J. (1980) ‘Performance of pressure-gain combustor without moving parts’, *AIAA Journal of Energy*, Vol. 4, pp. 56 – 64.

Kentfield, J.A.C. and O'Blenes, M.J. (1987a) ‘Methods for achieving a combustion-driven pressure-gain in gas turbines’, ASME Gas Turbine Conference and Exhibition, Anaheim, US, Paper 87-GT-126.

Kentfield, J.A.C. and O'Blenes, M.J. (1987b) 'The application of a second-generation pulse, pressure-gain, combustor to a small gas turbine’, AIM-87-2156.

Kentfield, J.A.C. and O'Blenes, M.J. (1990) ‘Small gas turbine using a second-generation pulse combustor’, *AIAA Journal of Propulsion and Power*, Vol. 6 (2), pp. 214 – 220.

Kentfield, J.A.C. and Femandes, L.C.V. (1990) ‘Improvements to the performance of a prototype pulse, pressure-gain, gas turbine combustor’, *Journal of Engineering for Gas Turbines and Power*, 112, pp. 67 – 72.

Khokhlov, A.M., Oran, E.S. and Thomas, G.O (1999) ‘Numerical simulation of deflagration to detonation transition: The role of shock flame interactions in turbulent flames’, *Combustion and Flame*, Vol. 117, pp. 323 – 339.

Kilchyk, V., (2009) ‘Pressure-wave amplification of flame area in wave rotor channels’, Ph.D. Dissertation, Mechanical Engineering Dept., Purdue Univ., West Lafayette, IN.

Kim, S.E., Choudhury, D. and Patel, B. (1997) ‘Computations of complex turbulent flows using the commercial code ansys fluent’, In Proceedings of the ICASE/LaRC/AFOSR Symposium on Modeling Complex Turbulent Flows. Hampton, Virginia.

Klein, R.I., Budil, K.S., Perry, T.S. and Bach, D.R. (2000) ‘Interaction of supernova remnants with interstellar clouds: from the NOVA laser to the galaxy’, *The Astrophysical Journal Supplement Series*; Vol. 127, pp. 379 – 83.

Klein, R.I., Budil, K.S., Perry, T.S. and Bach, D.R. (2003) ‘The interaction of supernova remnants with interstellar clouds: experiments on the NOVA laser’. *The Astrophysical Journal*, Vol. 583, pp. 245 – 259.

Klein, R.I., McKee, C.F. and Colella, P. (1994) ‘On the hydrodynamic interaction of shock waves with interstellar clouds. I. Nonradioactive shocks in small clouds’, *The Astrophysical Journal*, Vol. 420, pp. 213 – 236.

Kruggel-Emden, H., Scherer, V. and Wirtz, S. (2004) ‘Thermodynamische Prozessanalyse von Mikrogasturbinenprozessen’, Report, Institut für Energie-, System-, Material- und Umwelttechnik e.V., Ruhr-Universität Bochum.

Krzeczkowski, S.A. (1980) ‘Measurement of liquid droplet disintegration mechanisms’, *International Journal of Multiphase Flow*, Vol. 6(3), pp. 227 – 239.

Kumar, S., Orlicz, G., Tomkins, C., Goodenough, C. and Prestridge K, (2005) ‘Stretching of material lines in shock-accelerated gaseous flows’, *Physics of Fluids*, Vol. 17, pp. 082107-1 – 082107-11.

Kumar, S., Vorobieff, P., Orlicz, G., Palekar, A. and Tomkins, C. (2007) 'Complex flow morphologies in shock-accelerated gaseous flows', *Physica D*, Vol. 235, pp. 21 – 28.

Kupka, F., Happenhofer, N., Higueras, I. and Koch, O. (2012) 'Total-variation-diminishing impulsive-expicit Runge-Kutta methods for the simulation of double-diffusive convection in astrophysics', *Journal of Computational Physics*, Vol. 231(9), pp. 3561 – 3686.

Lamb, H. (1945) Hydrodynamics, p. 202. Dover.

Lampinen, M.J. and Turunen, R. (1992) 'Thermodynamic analysis of a pulse combustion system and its application to a gas turbine', *International Journal of Energy Research*, Vol. 16, pp. 259 – 276.

Launder, B.E. and Spalding, D.B. (1972) Lectures in mathematical models of turbulence. Academic Press, London, England.

Lawson, S.J. and Barakos, G.N. (2011) 'Review of numerical simulations for high-speed, turbulent cavity flows', *Progress in Aerospace Sciences*, Vol. 47(3), pp. 186 – 216.

Layes, G. (2005) Etude exp´erimentale de l'interaction d'une onde de choc avec une bulle de gaz. PhD thesis. Univ. Provence (Aix-Marseille I)

Layes, G., Jourdan, G. and Houas, L. (2003) 'Distortion of a spherical gaseous interface accelerated by a plane shock wave', *Physical Review Letters*, Vol. 91, pp. 174502.

Layes, G., Jourdan, G. and Houas, L. (2005) 'Experimental investigation of the shock wave interaction with a spherical gas inhomogeneity', *Physics of Fluids*, Vol. 17, pp. 028103.

Layes, G., Jourdan, G. and Houas, L. (2009) 'Experimental study on a plane shock wave accelerating a gas bubble', *Physics of Fluids*, Vol. 21, pp. 074102.

Layes, G. and Le Metayer, O. (2007) 'Quantitative numerical and experimental studies of the shock accelerated heterogeneous bubbles motion', *Physics of Fluids*, Vol. 19, pp. 042105.

Lefebvre, A.H. (2010) Gas turbine combustion. Taylor & Francis, United Kingdom.

Lei, X. and Li, J. (2018) 'A non-oscillatory energy-splitting method for the computation of compressible multi-fluid flows', *Physics of Fluids*, Vol. 30, pp. 040906-1 – 040906-14.

Levy, K., Sadot, O., Rikanati, A., Kartoon, D. and Srebro, Y. (2003) 'Scaling in the shock-bubble interaction', *Laser Part. Beams*, Vol. 21, pp. 335 – 39.

Li, H.; Akbari, P. and Nalim, M.R. (2007) 'Air-standard thermodynamic analysis of gas turbine engines using wave rotor combustion', 43rd AIAA/ASME/SAE/ASEE Joint Propulsion Conference & Exhibit, AIAA 2007-5050, Cincinnati, Ohio, USA.

Li, Q., Yokoi, K., Xie, Z., Omar, S. and Xue, J. (2021) 'A fifth-order high-resolution shock-capturing scheme based on modified weighted essentially non-oscillatory method and boundary variation diminishing framework for compressible flows and compressible two-phase flows', *Physics of Fluids*, Vol. 33, pp. 056104-1 – 056104-24.

Liang, Y., Zhai, Z., Luo, X. and Wen, C. (2020) 'Interfacial instability at a heavy/light interface induced by rarefaction waves', *Journal of Fluid Mechanics*, Vol. 885, pp. A42-1 – A42-19.

Liepmann, H.W. and Roshko, A. (1957) Elements of gasdynamics. New York:Wiley & Sons.

Lin, Y., Wang, Z. and Zhu, J. (2023) 'A new type of increasingly higher order finite difference and finite volume MR-WENO schemes with adaptive linear weights for hyperbolic conservation laws', *Journal of Computational Physics*, Vol. 493, pp. 112471-1 – 112471-33.

Lindl, D.L., McCrory, R.L. and Campbell, E.M. (1992) 'Progress toward ignition and burn propagation in inertial confinement fusion', *Physics Today*, pp. 32 – 40.

Lindl, J. (1995) 'Development of the indirect-drive approach to inertial confinement fusion and the target physics basis for ignition and gain', *Physics of Plasmas*, Vol. 2, pp. 3933 – 4024.

Liu, X.D., Osher, S. and Chan, T. (1994) 'Weighted essentially non-oscillatory schemes', *Journal of Computational Physics*, Vol. 115, pp. 200 – 212.

Liu, N., Wang, Z., Sun, M., Wang, H. and Wang, B. (2018) 'Numerical simulation of liquid droplet breakup in supersonic flows', *Acta Astronautica*, Vol. 145, pp. 116 – 130.

Lohner, R. and Parikh, P. (1988) 'Generation of three-dimensional unstructured grids by the advancing-front method', *International Journal for numerical methods in Fluids*, Vol. 8, pp. 1135 – 1149.

Lutoschkin, E., Rose, M.G. and Staudacher, S. (2013) 'Pressure-gain combustion using shock-flame interaction', *Journal of Propulsion and Power*, Vol. 29, No.5, pp. 1181 – 1193.

Madar, C.L. (1965) 'Initiation of detonation by the interaction of shocks with density discontinuities', *Physics of Fluids*, Vol. 8, pp. 1811– 1816.

Marble, F.E., Hendricks, G.J. and Zukoski, E.E. (1987) 'Progress toward shock enhancement of supersonic combustion processes', AZAA Paper 87-1880.

Marble, F.E., Zukoski, E.E., Jacobs, J.W., Hendricks, G.J. and Waitz, I.A. (1990) 'Shock enhancement and control of hypersonic mixing and combustion', The American Institute of Aeronautics and Astronautics, AIAA Paper No. AIAA 90-1981 26th AIAA Joint Propulsion Conference, Orlando, Florida.

Markstein, G.H. (1957a) 'Flow disturbances induced near a slightly wavy contact surface, or flame front, traversed by a shock wave', *Journal of Aerosol Science*, Vol. 24, pp. 238

Markstein, G.H. (1957b) 'A shock tube study of flame front-pressure wave interactions'. In Sixth Symposium (International) on Combustion, pp. 387 – 398. Reinhold.

Marquina A. and Mulet, P. (2003) 'A flux-split algorithm applied to conservative models for multicomponent compressible flows', *Journal of Computational Physics*, Vol. 185, pp.120 – 138.

Marston, P.L. and Kinqsbury, D.L. (1981) 'Acoustic scattering from fluid spheres: diffraction and interference near the critical scattering angle', *The Journal of the Acoustical Society of America,* Vol. 70, pp. 1488-1495.

Marston, P.L and Lanqley, D.S. (1983) 'Glory- and rainbow-enhanced acoustic back-scattering from fluid spheres: Models for diffracted axial focusing', *The Journal of the Acoustical Society of America,* Vol. 73, pp. 1464 – 1475.

Mavriplis, D.J. (1995) ‘A three-dimensional multigrid Reynolds-averaged Navier-Stokes solver for unstructured meshes’, *AIAA Journal*, Vol. 33(3), pp. 445 – 453.

Mavriplis, D.J. (1996) ‘Mesh generation and adaptivity for complex geometries and flows’, in: R. Peyret (Ed.), Handbook of Computational Fluid Mechanics, Academic Press, San Diego, CA, pp. 417 – 459.

Mavriplis, D.J. (1997) ‘Unstructured grid techniques’, *Annual Review of Fluid Mechanics*, Vol. 29, pp. 473 – 514.

Mavriplis, D.J. (1998) ‘Multigrid strategies for viscous flow solvers on anisotropic unstructured meshes’, *Journal of Computational Physics*, Vol. 145(1), pp. 141 – 165.

Mavriplis, D., Jameson, A., and Martinelli, L. (1989) ‘Multigrid solution of the Navier-Stokes equations on triangular meshes’, *AIAA-89-0120*.

Maxworthy, T, (1977) ‘Some experimental studies of vortex rings’, *Journal of Fluid Mechanics*, Vol. 81, pp. 465 – 495.

Meng, J.C. and Colonius, T. (2015) ‘Numerical simulations of the early stages of high-speed droplet breakup’, *Shock Waves*, Vol. 25, pp. 399 – 414.

Meng, J.C. and Colonius, T. (2018) ‘Numerical simulation of the aerobreakup of a water droplet’, *Journal of Fluid Mechanics*, Vol. 835, pp. 1108 – 1135.

Menter, F.R. (2009) ‘Review of the SST Turbulence Model Experience from an Industrial Perspective’, *International Journal of Computational Fluid Dynamics*, Vol. 23(4).

Meshkov, E. (1969) ‘Instability of the interface of two gases accelerated by a shock wave’, *Fluid Dynamics*, Vol. 4, pp. 101 – 104.

Meshkov, Y.Y. (1970) ‘Instability of a shock wave accelerated interface between two gases’. NASA TT F-13, 074.

Moretti, G. (1973) ‘Experiments in multi-dimensional floating shockfitting’. Polytechnic Institute of Brooklyn, Brooklyn, NY, PIBAL, Report No. 73 – 18.

Muller, J.L. (1971) ‘Theoretical and practical aspects of the application of resonant combustion chambers in gas turbines’, *Journal of Mechanical Engineering Science*, Vol. 13(3), pp. 137 – 150.

Murrow, K.R., Franer, M.T. and Giffin, R.G. (2009) ‘Rotary pressure rise combustor for a gas turbine engine’, United States Patent, US 2009/0196733 A1, General Electric Company, US.

Neubauer, W.G. and Draqonette, L.R. (1970) ‘Observation of waves radiated from circular cylinders caused by an incident pulse’, *The Journal of the Acoustical Society of America,* Vol. 48, pp. 1135 – 1149.

Nicholls, J.A. and Ranger, A.A. (1968) ‘Aerodynamic shattering of liquid drops’, *AIAA Journal*, Vol. 7, pp. 285 – 290.

Niederhaus, J.H.J. (2007) ‘A computational parameter study for three-dimensional shock-bubble interactions’. PhD thesis. University of Wisconsin, Madison.

Niederhaus, J.H.J., Greenough, J.A., Oakley, J.G., Ranjan, D., Anderson, M.H. and Bonazza, R. (2008) ‘A computational parameter study for the three-dimensional shock-bubble interaction’, *Journal of Fluid Mechanics*, Vol. 594, pp. 85 – 124.

Noh, W.F. and Woodward, P. (1976) ‘SLIC (Simple line interface calculation)’, In Proceedings of the Fifth International Conference on Numerical Methods: in Fluid Dynamics, June 28 – July 2, Twente University, Enschede, pp. 330 – 340. Springer.

Nonomura, T., Kitamura, K. and Fujii, K. (2014) ‘A simple interface sharpening technique with a hyperbolic tangent function applied to compressible two-fluid modeling’, *Journal of Computational Physics*, Vol. 258, pp. 95 – 117.

Norris, J.W. and Twelves Jr., W.V. (2005) ‘Pulsed Combustion Engine, United States Patent’, US 6,886,325 B2, United Technologies Corporation, USA.

Nourgaliev, R.R., Dinh, T.N. and Theofanous, T.G. (2006) ‘Adaptive characteristics-based matching for compressible multifluid dynamics’, *Journal of Computational Physics*, Vol. 213, pp. 500 – 529.

Offord, T., Miller, R. J. and Dawson, J.R. (2008) ‘Improving the Performance of a Valveless Pulse Combustor Using Unsteady Fuel Injection’, 46th AIAA Aerospace Sciences Meeting and Exhibit, Reno, Nevada, US.

Olsson, E., and Kreiss, G. (2005) ‘A conservative level set method for two phase flow’, *Journal of Computational Physics*, Vol. 210, pp. 225 – 246.

Olsson, E., Kreiss, G. and Zahedi, S. (2007) ‘A Conservative Level Set Method for Two Phase Flow II’, *Journal of Computational Physics*, Vol. 225, pp.785 – 807.

Onwuegbu, S. and Yang, Z. (2022) ‘Numerical analysis of shock interaction with a spherical bubble’, AIP Advances, Vol. 12, pp. 025215/1 – 025215/15.

Osher, S. and Sethian, J.A. (1988) ‘Fronts propagating with curvature-dependent speed: algorithms based on Hamilton–Jacobi formulations’, *Journal of Computational Physics*, Vol. 79, pp. 12 – 49.

Paxson, D.E. (2010) ‘Pressure-gain combustion for gas turbine’, Presentation, Pennsylvania State University, Turbine System Research Workshop.

Paxson, D. (2017) ‘Resonant pulse combustors: a reliable route to practical pressure gain combustion’, International Constant Volume Detonation Combustion Workshop, ICVDCW, Poitiers, France, July 13-16. Available at: https://ntrs.nasa.gov/archive/nasa/casi.ntrs.nasa.gov/20170007284.pdf. (Accessed: 20 March 2024).

Picone, J.M., Boris, J.P., Greig, J.R., Raleigh, M. and Fernsler, R.F. (1981) ‘Convective cooling of lightning channels’, *Journal of Atmospheric Science*, Vol. 38, pp. 2056 – 2062.

Picone, J.M. and Boris, J.P. (1983) ‘Vorticity generation by asymmetric energy deposition in a gaseous medium’, *Physics of Fluids*, Vol. 26, pp. 365 – 382.

Picone, J.M., Oran, E.S., Boris, J.P. and Young, T.R. (1985) 'Theory of vorticity generation by shock wave and flame interactions'. *In Dynamics of Shock Waves, Explosions, and Detonations*, pp. 429 – 448. American Institute of Aeronautics and Astronautics.

Picone, J.M. and Boris, J.P. (1988) 'Vorticity generation by shock propagation through bubbles in a gas', *Journal of Fluid Mechanics*, Vol. 189, pp. 23 – 51.

Pierce, A.D. (1981) Acoustics. McGraw-Hill.

Pilch, M. and Erdman, C.A. (1987) 'Use of breakup time data and velocity history data to predict the maximum size of stable fragments for acceleration induced breakup of a liquid drop', *International Journal of Multiphase Flow*, Vol. 13, pp. 741 – 757.

Pope, S.B. (2000) Turbulent Flows. Cambridge University Press.

Prestridge, K., Vorobieff, P., Rightley, P.M. and Benjamin, R.F. (2001) 'Validation of an instability growth model using particle image velocimetry measurements', *Physical Review Letters*, Vol. 84, pp. 4353 – 4356.

Probst, M. (2002) 'Development of a pressure-gain combustor for use in a gas turbine cycle', Diplomarbeit, ETH Zurich, Zürich.

Quan, S. and Schmidt, D.P. (2006) 'Direct numerical study of a liquid droplet impulsively accelerated by gaseous flow', *Physics of Fluids*, Vol. 18, pp. 102103/1 – 102103/9.

Quirk, J.J. (1991) 'An adaptive mesh refinement algorithm for computational shock hydrodynamics', PhD Thesis, Cranfield Institute of Technology, UK.

Quirk, J.J. and Karni, S. (1996) 'On the dynamics of a shock–bubble interaction', *Journal of Fluid Mechanics*, Vol. 318, pp.129 – 163.

Ranger, A.A. and Nicholls, J.A. (1969) 'Aerodynamic shattering of liquid drops', *AIAA Journal*, Vol. 7(2), pp. 285 – 290.

Ranger, A.A. and Nicholls, J.A. (1972) 'Atomization of liquid droplets in a convective gas stream', *International Journal of Heat and Mass Transfer*, Vol. 15(6), pp. 1203 – 1211.

Ranjan, D., Anderson, M., Oakley, J. and Bonazza, R. (2005) 'Experimental investigation of a strongly shocked gas bubble', *Physical Review Letters*, Vol. 94, pp. 184507.

Ranjan, D., Niederhaus, J., Motl, B., Anderson, M., Oakley, J. and Bonazza, R. (2007) 'Experimental investigation of primary and secondary features in high-Mach-number shock– bubble interaction', *Physical Review Letters*, Vol. 98, pp. 024502.

Ranjan, D., Niederhaus, J.H.J., Oakley, J.G., Anderson, M.H., Bonazza, R, and Greenough, J.A. (2008a) 'Shock-bubble interactions: features of divergent shock-refraction geometry observed in experiments and simulations', *Physics of Fluids*, Vol. 20, pp. 036101.

Ranjan, D., Niederhaus, J.H.J., Oakley, J.G., Anderson, M.H., Greenough, J.A. and Bonazza, R. (2008b) 'Experimental and numerical investigation of shock-induced distortion of a spherical gas inhomogeneity', *Physica Scripta*, Vol. 2008, pp. 014020.

Ranjan, D., Oakley, J. and Bonazza, R. (2011) 'Shock-bubble interactions', *Annual Review of Fluid Mechanics*, Vol. 43, pp 117 – 140.

Ranger, A.A. and Nicholls, J.A. (1969) 'Aerodynamic shattering of liquid drops', *AIAA Journal*, Vol. 7, pp. 285 – 290.

Ray, M.P., Puranik, B.P. and Bhandarkar, U.V. (2019) 'Development of high-resolution methods for analyzing multi-fluid problems', Journal of Physics: Conference Series, Vol. 1240, pp. 012042-1 – 012042-8.

Reynolds, W.C. (1987) 'Fundamentals of turbulence for turbulence modeling and simulation', Lecture notes for Von Karman Institute Agard Report No. 755.

Richtmyer, R.D. (1960) 'Taylor instability in shock acceleration of compressible fluids', *Communications on Pure and Applied Mathematics*, Vol. 23, pp. 297 – 319.

Robey, H.F., Perry, T.S., Klein, R.I., Kane, J.O., Greenough, J.A. and Boehly, T.R. (2002) 'Experimental investigation of the three-dimensional interaction of a strong shock with a spherical density inhomogeneity', *Physical Review Letters*, Vol. 89, pp. 085001.

Roy, G.D., Frolov, S.M., and Borisov, A.A. (2004) 'Pulse detonation propulsion: challenges, current status, and future perspective, *Progress in Energy and Combustion Science'*, Vol. 30, pp. 545 – 672.

Rudinger, G. (1958) 'Shock wave and flame interactions', In Combustion and Propulsion: Third AGARD Colloquium, London, pp. 153 – 182. Pergamon.

Rudinger, G. and Somers, L. (1960) 'Behaviour of small regions of different gases carried in accelerated gas flows', *Journal of Fluid Mechanics*, Vol. 7, pp. 161 – 176.

Sabatiuk, A. (1987) 'Gas turbine engines employing fixed volume combustion', United States Patent, 4,693,075, USA.

Salas, M.D. (2011) 'A brief history of shock-fitting'. In: Kuzmin A, editor. Computational fluid dynamics 2010. Berlin: Springer; pp. 37 – 53.

Sammann, B.C., Twelves Jr., W.V. and Jones, G.D. (2005) 'Pulsed combustion turbine engine', United States Patent, US 6,901,738 B2, United Technologies Corporation, USA.

Samtaney. R. and Zabusky, N.J. (1994) 'Circulation deposition on shock-accelerated planar and curved density-stratified interfaces: models and scaling laws', *Journal of Fluid Mechanics*, Vol. 269, pp. 45 – 78.

Sembian, S., Liverts, M., Tillmark, N. and Apazadis, N. (2016) 'Plane shock wave interaction with a cylindrical column', *Physics of Fluids*, Vol. 28(5), pp. 056102-1 – 056102-16.

Shapiro, A.H., (1983) Dynamics and thermodynamics of compressible fluid flow, Krieger Pub. Co; ed., Reprint with corrections. ISBN 0-89874-566-7.

Shih, T.-H, Liou, W.W., Shabbir, A., Yang, Z and Zhu, J. (1995) 'A new $k-\varepsilon$ eddy-viscosity model for high reynolds number turbulent flows – model development and validation', *Computers Fluids*, Vol. 24(3), pp. 227 – 238.

Shraiber, A.A., Poduystotsky, A.M. and Dubrovsky, V.V. (1996) 'Deformation and breakup of drops by aerodynamic forces', *Atomization Sprays*, Vol. 6, pp. 667 – 692.

Shukla, R.K. (2014) 'Nonlinear preconditioning for efficient and accurate interface capturing in simulation of multicomponent compressible flows', *Journal of Computational Physics*, Vol. 276(1), pp. 508 – 540.

Shukla, R.K., Pantano, C. and Freund, J.B. (2010) 'An interface capturing method for the simulation of multiphase compressible flows', *Journal of Computational Physics*, Vol. 229(19), pp. 7411 – 7439.

Shyue, K.M. (1998) 'An efficient shock-capturing algorithm for compressible multicomponent problems', *Journal of Computational Physics*, Vol. 142(1), pp. 208 – 242.

Simpkins, P.G. and Bales, E.L. (1972) 'Water drop response to sudden accelerations', *Journal of Fluid Mechanics*, Vol. 55(4), pp. 629 – 639.

Singh, S., Battiato, M. and Myong, R.S. (2021) 'Impact of bulk viscosity on flow morphology of shock-accelerated cylindrical light bubble in diatomic and polyatomic gases', *Physics of Fluids*, Vol. 33, pp. 066103-1 – 066103-26.

Sod, G.A. (1978) 'A survey of several finite difference methods for systems of nonlinear hyperbolic conservation laws', *Journal of Computational Physics*, Vol. 27(1), pp. 1 – 31.

Stone, J.M. and Norman, M.L. (1992) 'The three-dimensional interaction of a supernova remnant with an interstellar cloud', *The Astrophysical Journal*, Vol. 390, pp. L17 – L19.

Takayama, K. (1999) 'Application of shock wave research to medicine'. In: Ball, Hillier, Roberts (eds), Proc. of 22nd International Symposium on Shock Waves, Imperial College, London (UK), pp 23 – 32.

Tamagawa, M. and Akamatsu, T. (1999) 'Modeling of deformation for living tissue cells with sub-structure by shock waves'. In: Ball, Hillier, Roberts (eds) Proc. of 22nd International Symposium on Shock Waves, Imperial College, London (UK), pp 595 – 560.

Taniguchi, N., Furuhata, R., Sou, A. and Abe, A. (2014) 'Numerical simulation of shock wave bubble interaction for ballast water treatment', Proceedings of the 3rd International Symposium of Maritime Sciences, Nov. 10 – 14, Kobe, Japan.

Taylor, G.I. (1949) 'The shape and acceleration of a drop in a high-speed air stream', The Scientific Papers of Sir Geoffrey Ingram Taylor, Vol. 3, Batchelor, G. K. (Ed.), University Press, Cambridge, 1963.

Taylor, G.I. (1950) 'The instability of liquid surfaces when accelerated in a direction perpendicular to their planes', Proceedings of the Royal Society of London Series A, Vol. 201, No. 1065, pp. 192 – 196.

Taylor, G.I. (1953) 'Formation of a vortex ring by giving an impulse to a circular disk and then dissolving it away', *Journal of Applied Physics*, Vol. 24, pp. 104.

Temkin, S. and Kim, S.S. (1980) 'Droplet motion induced by weak shock waves', *Journal of Fluid Mechanics*, Vol. 96, pp. 133 – 157.

Terashima, H. and Tryggvason, G. (2009) ‘A front-tracking/ghost-fluid method for fluid interfaces in compressible flows’, *Journal of Computational Physics*, Vol. 228(11), pp. 4012 – 4037.

Terashima, H. and Tryggvason, G. (2010) ‘A front-tracking method with projected interface conditions for compressible multi-fluid flows’, *Computer and Fluids*, Vol. 39(10), pp. 1804 – 1814.

Theofanous, T.G., Li, G.J. and Dinh, T.N. (2004) ‘Aerobreakup in rarefied supersonic gas flows’, *Journal of Fluids Engineering*, Vol. 126(4), pp. 516 – 527.

Theofanous, T.G. and Li, G.J. (2008) ‘On the physics of aerobreakup’, *Physics of Fluids*, Vol. 20(5), 052103/1 – 052103/14.

Theofanous, T.G. (2011) ‘Aerobreakup of Newtonian and viscoelastic liquids’, *Annual Review of Fluid Mechanics*, Vol. 43, pp. 661 – 690.

Theofanous, T.G., Mitkin, T.G., Ng, C.L., Chang, C.H., Deng, X and Sushchikh, S. (2012) ‘The physics of aerobreakup. II. Viscous liquids’, *Physics of Fluids*, Vol. 24(2), pp. 022104/1 – 022104/39.

Theofanous, T.G., Mitkin, T.G. and Ng, C.L. (2013) ‘The physics of aerobreakup. III. Viscoelastic liquids’, *Physics of Fluids*, Vol. 25(3), pp. 032101/1 – 032101/28.

Thompson, P.A. (1984) Compressible-Fluid Dynamics. New York: McGraw-Hill.

Thomadakis, M. and Leschziner, M. (1994) ‘Numerical simulation of viscous incompressible flows using a pressure-correction method and unstructured grids’, in *Computational Fluid Dynamics*, Vol. 94, pp. 325-332, John Wiley and Sons, Chichester, UK.

Thring, M.W. (Ed.), (1961) ‘Pulsating combustion – *the collected works of F.H. Reynst*, Pergamon Press, Oxford.

Tomkins, C., Kumar, S. and Prestridge, G.O.K. (2008) ‘An experimental investigation of mixing mechanisms in shock-accelerated flow’, *Journal of Fluid Mechanics*, Vol. 611, pp. 131 – 150.

Tomkins, C., Prestridge, K., Rightley, P., Marr-Lyon, M., Vorobieff, P. and Benjamin, R. (2003) ‘A quantitative study of the interaction of two Richtmyer-Meshkov-unstable gas cylinders’, *Physics of Fluids*, Vol. 15, pp. 986 – 1004.

Toro, E.F. (2009) Riemann solvers and numerical methods for fluid dynamics: A practical introduction 3rd edition, Springer, Dordrecht, New York.

Van de Hulst, H.C. (1957) Light scattering by small particles. Wiley.

Van Leer, B. (1979) ‘Towards the ultimate conservative difference scheme, a second order sequel to Godunov’s method’, *Journal of Computational Physics*, Vol. 32, pp. 101 – 136.

Venkatakrishnan, V. (1996) ‘A perspective on unstructured grid flow solver’, *AIAA Journal*, Vol. 34(3), pp. 547 – 553.

Versteeg, H.K. and Malalasekera, W. (2007) An introduction to computational fluid dynamics: the finite volume method. Pearson Education.

Waldman, G.D. and Reinecke, W. (1972) ‘Raindrop breakup in the shock layer of a high-speed vehicle’, *AIAA Journal*, Vol. 10(9), pp. 1200 – 1204.

Wang, Z., Yu, B., Chen, H., Zhang, B. and Liu, H. (2018) ‘Scaling vortex breakdown mechanism based on viscous effect in shock cylindrical bubble interaction’, *Physics of Fluids*, Vol. 30, pp.126103-1 – 126103-13.

Welch, G.E., Jones, S.M. and Paxson, D.E. (1997) ‘Wave-rotor-enhanced gas turbine engines’, *ASME Journal of Engineering for Gas Turbines and Power*, Vol. 119, pp. 469 – 477.

Whurr, J. (1997) ‘Aircraft compound cycle propulsion engine’, United States Patent, 5,692,372, Rolls-Royce plc.

Widnall, S.E., Bliss, D.B. and Tsai, C.Y. (1974) ‘The instability of short waves on a vortex ring’, *Journal of Fluid Mechanics*, Vol. 66, pp. 35 – 47.

Wierzba, A. (1990) ‘Deformation and Breakup of liquid drops in a gas stream at nearly critical Weber number’, *Experiments in Fluids*, Vol. 9, pp. 59 – 64.

Wierzba, A., and Takayama, K. (1987) ‘Experimental investigation liquid droplet breakup in a gas stream’, *Reports of the Institute of Fluid Science*, Vol. 53, pp. 1 – 99.

Wierzba, A. and Takayama, K. (1988) ‘Experimental investigation of the aerodynamic breakup of liquid drops’, *AIAA Journal*, Vol. 26(11), pp. 1329 – 1335.

Wilcox, D.C. (1998) ‘Turbulence modeling for CFD’. DCW Industries, Inc. La Canada, California.

Winkler, K.H., Chalmers, J.W., Hodson, S.W., Woodward, P.R. and Zabusky, N.J. (1987) ‘A numerical laboratory’. *Physics Today*, Vol. 40(10), pp. 28 – 37.

Wintenberger, E. and Shepherd, J.E. (2004) ‘Thermodynamic analysis of combustion processes for propulsion systems’, 42nd AIAA Aerospace Sciences Meeting and Exhibit, 4004-1033, Reno, Nevada, USA.

Wu, Y., Ma, F. and Yang, V. (2003) ‘System performance and thermodynamic cycle analysis of airbreathing pulse detonation engines’, *AIAA Journal of Propulsion and Power*, Vol. 19 (4).

Wu, Z., Xu, Y., Wang W. and Hu, R. (2013) ‘Review of shock wave detection method in CFD post-processing’, *Chinese Journal of Aeronautics*, Vol. 26(3), pp. 501 – 503.

Xiang, G. and Wang, B. (2017) ‘Numerical study of a planar shock interacting with a cylindrical water column embedded with an air cavity’, *Journal of Fluid Mechanics*, Vol. 825, pp. 825 – 852.

Xu, z., Wang, T. and Che, Z. (2022) ‘Droplet breakup in airflow with strong shear effect’, *Journal of Fluid Mechanics*, Vol. 941, pp. A54.

Yang, Z. (2014) ‘Assessment of unsteady-RANS approach against steady RANS approach for predicting twin impinging jets in a cross-flow’, *Cogent Engineering*, Vol. 1(1), 936995.

Yang, J., Kubota, T. and Zukoski, E.E. (1993) ‘Applications of shock-induced mixing to supersonic combustion’, *The American Institute of Aeronautics and Astronautics*, AIAA, Journal, Vol. 31, pp. 854 – 862.

Yang, J., Kubota, T. and Zukoski, E.E. (1994) ‘A model for characterization of a vortex pair formed by shock passage over a light-gas inhomogeneity’, *Journal of Fluid Mechanics*, Vol. 258, pp. 217 – 244.

Yoo, Y.L. and Sung, H.G. (2018) ‘Numerical investigation of an interaction between shock waves and bubble in a compressible multiphase flow using a diffuse interface method’, *International Journal of Heat and Mass Transfer*, Vol. 127, pp. 210 – 221.

Yoshida, T. and Takayama, K. (1990) ‘Interaction of liquid droplets with planar shock waves’, *Journal of Fluids Engineering*, Vol. 112(4), pp. 481 – 486.

Yu, Z. and Fan, L.S. (2008) ‘Direct simulation of the buoyant rise of bubbles in infinite liquid using level set method’, *The Canadian Journal of Chemical Engineering*, Vol. 86, pp. 267 – 275.

Zabusky, N.J. (1999) ‘Vortex paradigm for accelerated inhomogeneous flows: visiometrics for the Rayleigh-Taylor and Richtmyer-Meshkov environments’, *Annual Review of Fluid Mechanics*, Vol. 31, pp. 495 – 536

Zabusky, N.J. and Zeng, S.M. (1998) ‘Shock cavity implosion morphologies and vortical projectile generation in axisymmetric shock-spherical fast/slow bubble interactions’, *Journal of Fluid Mechanics*, Vol. 362, pp. 327 – 346.

Zhai, Z., Ou, Z. and Ding, J. (2019) ‘Coupling effect on shocked double-gas cylinder evolution’, *Physics of Fluids*, Vol. 31, pp. 096104-1 – 096104-9.

Zhang, Q. and Graham, M.J. (1997) ‘A numerical study of Richtmyer Meshkov instability driven by cylindrical shocks’, *American Institute of Physics*, Vol. 10, pp. 974 – 993.

Zhang, Y.-T. and Shu, C.W. (2016) ‘ENO and WENO schemes’, Chapter 5. In: Abgrall, R., Shu, C.-W. (eds) Handbook of Numerical Methods for Hyperbolic Problems Basic and Fundamental Issues. Handbook of Numerical Analysis, Vol. 17, pp. 103 – 122. North Holland, Amsterdam.

Zhu, Y., Yang, W., Luo, K., Pan, J. and Pan, Z. (2019) ‘Numerical investigation of planar shock wave impinging on spherical gas bubble with different densities’, *Physics of Fluids*, Vol. 31, pp. 056101/1 – 056101/10.

Zubair, M., Abdullah, M.Z. and Ahmad, K.A. (2013) ‘Hybrid mesh for nasal airflow studies’, *Computational and Mathematical Methods in Medicine*, Vol. 2013, Article ID 727362, pp. 1 – 7.